



## VORTEX INDUCED VIBRATIONS OF LONG FLEXIBLE CYLINDERS WITH AND WITHOUT WAKE INTERFERENCE

**Denise Fischer Hubert**

**Dipòsit Legal: T 992-2015**

**ADVERTIMENT.** L'accés als continguts d'aquesta tesi doctoral i la seva utilització ha de respectar els drets de la persona autora. Pot ser utilitzada per a consulta o estudi personal, així com en activitats o materials d'investigació i docència en els termes establerts a l'art. 32 del Text Refós de la Llei de Propietat Intel·lectual (RDL 1/1996). Per altres utilitzacions es requereix l'autorització prèvia i expressa de la persona autora. En qualsevol cas, en la utilització dels seus continguts caldrà indicar de forma clara el nom i cognoms de la persona autora i el títol de la tesi doctoral. No s'autoritza la seva reproducció o altres formes d'explotació efectuades amb finalitats de lucre ni la seva comunicació pública des d'un lloc aliè al servei TDX. Tampoc s'autoritza la presentació del seu contingut en una finestra o marc aliè a TDX (framing). Aquesta reserva de drets afecta tant als continguts de la tesi com als seus resums i índexs.

**ADVERTENCIA.** El acceso a los contenidos de esta tesis doctoral y su utilización debe respetar los derechos de la persona autora. Puede ser utilizada para consulta o estudio personal, así como en actividades o materiales de investigación y docencia en los términos establecidos en el art. 32 del Texto Refundido de la Ley de Propiedad Intelectual (RDL 1/1996). Para otros usos se requiere la autorización previa y expresa de la persona autora. En cualquier caso, en la utilización de sus contenidos se deberá indicar de forma clara el nombre y apellidos de la persona autora y el título de la tesis doctoral. No se autoriza su reproducción u otras formas de explotación efectuadas con fines lucrativos ni su comunicación pública desde un sitio ajeno al servicio TDR. Tampoco se autoriza la presentación de su contenido en una ventana o marco ajeno a TDR (framing). Esta reserva de derechos afecta tanto al contenido de la tesis como a sus resúmenes e índices.

**WARNING.** Access to the contents of this doctoral thesis and its use must respect the rights of the author. It can be used for reference or private study, as well as research and learning activities or materials in the terms established by the 32nd article of the Spanish Consolidated Copyright Act (RDL 1/1996). Express and previous authorization of the author is required for any other uses. In any case, when using its content, full name of the author and title of the thesis must be clearly indicated. Reproduction or other forms of for profit use or public communication from outside TDX service is not allowed. Presentation of its content in a window or frame external to TDX (framing) is not authorized either. These rights affect both the content of the thesis and its abstracts and indexes.

# Vortex induced vibrations of long flexible cylinders with and without wake interference

Doctoral Thesis

**Zafar Abbas Bangash**

Thesis Supervisor : Prof. Francisco J. Huera Huarte  
Department of Mechanical Engineering  
Universitat Rovira-i-Virgili



UNIVERSITAT ROVIRA I VIRGILI

Tarragona

May 2015

UNIVERSITAT ROVIRA I VIRGILI

VORTEX INDUCED VIBRATIONS OF LONG FLEXIBLE CYLINDERS WITH AND WITHOUT WAKE INTERFERENCE

Denise Fischer Hubert

Dipòsit Legal: T 992-2015

Department of Mechanical Engineering  
Universitat Rovira-i-Virgili  
Avinguda dels Països Catalans, 26  
43007, Tarragona, Spain  
Tel (34) 977 55 96 02  
secmec@urv.cat

Dr. Francisco Huera-Huarte, Professor in the Mechanical Engineering Department of  
Universitat Rovira-i-Virgili

CERTIFY:

That the present study, titled :

**Vortex-induced vibrations of long flexible cylinders with and without  
wake interference**

presented by Mr Zafar Abbas Bangash for the award of the degree of Doctor, has been  
developed under my supervision at the Department of Mechanical Engineering of this  
university and it is fully adequate in scope and quality as a dissertation for the degree  
of Doctor of Philosophy.

And, to inform you of that, and in order for it to have needed effects, I sign this  
certification.

Thesis Supervisor:

Prof. Francisco J. Huera Huarte

Tarragona, April 2015

UNIVERSITAT ROVIRA I VIRGILI

VORTEX INDUCED VIBRATIONS OF LONG FLEXIBLE CYLINDERS WITH AND WITHOUT WAKE INTERFERENCE

Denise Fischer Hubert

Dipòsit Legal: T 992-2015

Dedicated to my father, my inspiration, my role model. Ashraf Hassan Bangash.

UNIVERSITAT ROVIRA I VIRGILI

VORTEX INDUCED VIBRATIONS OF LONG FLEXIBLE CYLINDERS WITH AND WITHOUT WAKE INTERFERENCE

Denise Fischer Hubert

Dipòsit Legal: T 992-2015

## ACKNOWLEDGEMENTS

---

The work presented here is a result of all the help and support, guidance and teaching of my supervisor, Prof. Francisco Huera Huarte. He has been encouraging and driving me, and supervising my progress on this extremely complex subject. The freedom and resources given to me to carry out the experiments, employ state of the art methods for data acquisition, and processing, and giving me the freedom to explore, improvise, and implement new technology and methods was more than I asked for. His help and guidance in designing, and making the models, and hours of explanations while I stumbled through the understanding of the complex phenomenon must have required a lot of patience. I emerge from this endeavour with a great gratitude for him.

My parents, their sacrifice and support for me to achieve this milestone, can not be overstated. They gave me the liberty to explore all avenues, and have always been there for me, to support me emotionally, and when needed, financially. They have been my motivation and drive, when things looked hard.

My wife, Shazia Gulzar, who took this leap of faith with me knowing and understanding that I will be spending more and more evenings and nights at work instead of spending time with my her. She has been there for me through thick and thin, when I felt frustrated, and through little moments of joy. And it was in these tough times that she gave me the greatest gift, my lovely daughter, Aria Zehra. I thank her for every day, for every hour, for every moment through these last 4 years, which were tougher on her than on me. And to my daughter, whose one hug would take away all the worries.

I would like to thank Jordi Polo. His joyful personality was just as helpful in cheering me up as much as his help in fabrication of the models. In addition, everyone working at the *Taller*, that helped me in building the models.

And a special thank you goes to all my colleagues, and friends, specially to Rafael Fernandez Pratz, who helped me feel at home away from my home, and have been like a brother to me in the lab, and outside.



UNIVERSITAT ROVIRA I VIRGILI

VORTEX INDUCED VIBRATIONS OF LONG FLEXIBLE CYLINDERS WITH AND WITHOUT WAKE INTERFERENCE

Denise Fischer Hubert

Dipòsit Legal: T 992-2015

## ABSTRACT

---

The primary objective of this thesis is the characterization of the response of risers at high mode numbers. As a part of this thesis, three separate experiments were planned and executed. The objectives of these tests were to create a set of model response data for realistically low mass ratio risers, and the determination of wake characteristics of flexible risers undergoing multi-mode vibrations.

A set of vertical tension riser models were used to determine their response when subjected to vortex induced vibrations. For this purpose, the risers used were 3m long. The risers were categorized according to the mass ratio (mass of riser / mass of displaced fluid), where one model had a mass ratio of 2.7, and the other had lower mass ratio of 1.1. The models were tested in conditions where the lower 55% of the riser were exposed to a uniform flow, with speeds up to 2m/s. Reynolds number reached were up to 28000 for the high mass ratio case, and 37000 for the low mass ratio model. Both in-line and cross-flow responses were measured using strain gages, where the curvature data, collected from 11 stations along the span of the riser, was converted to displacements.

The high mass ratio riser indicated cross-flow oscillations up to 4<sup>th</sup> mode, and in-line oscillations up to 5<sup>th</sup> mode. The low mass ratio riser response was mostly limited to 2<sup>nd</sup> mode in cross-flow, and 3<sup>rd</sup> mode in-line oscillations. The modal contributions were also determined using blind source separation, and simultaneous presence of multiple modes at multiple frequencies were determined in many cases, while the dominant oscillation mode governed the dominant frequency. Drag coefficients obtained indicated similarity with the cross-flow oscillation, with values reaching 2.5 for the low mass ratio cylinder.

The response of a flexible riser in the wake of a rigid cylinder was determined, using different separation distance from the leading cylinder. The response trend showed significant similarities to those of an isolated flexible cylinder, in form of the response regimes at each structural mode of oscillation with contributions from adjacent modes.

The wake of a flexible riser was analysed at various positions along the span, from node to anti-node, using DPIV and flow visualization techniques. It was observed that the wake at the node comprised of two shed vortices at every cycle (2S mode), whereas at the anti-node, a pair of counter-rotating vortices remained affixed to the cylinder, with no periodic shedding. An interim region of connectivity was observed between the node and anti-node, displaying a shift in the phase of shedding.

## PUBLICATIONS

---

### Indexed publications:

1. F.J. Huera-Huarte, Z.A. Bangash and L.M. Gonzalez. (2014) Towing tank experiments of the vortex-induced vibrations of a low mass ratio long flexible cylinder. *Journal of Fluids and Structures* , 48, 81-92
2. F.J. Huera-Huarte, Z.A. Bangash and L.M. Gonzalez. (2015) Multi-mode vortex and wake-induced vibrations of a flexible cylinder in tandem arrangement. (Submitted)
3. Z.A. Bangash and F.J. Huera-Huarte. (2015) On the flow around the node to anti-node transition of a self-excited oscillating flexible cylinder. (Submitted)

### Conferences (Peer-reviewed) and presentations:

1. F. J. Huera-Huarte and Z. A. Bangash. (2011) The flow around the node to anti-node transition of an oscillating flexible cylinder. 64th American Physical Society – Division of Fluid Dynamics, APS. DFD 2011. Baltimore, MD, USA
2. F. J. Huera-Huarte and Z. A. Bangash. (2012) DPIV Around a Flexible Circular Cylinder Undergoing Cross-Flow Forced Oscillations ASME 2012 Pressure Vessels and Piping Conference, 2012, Toronto, Ontario, Canada (PVP2012-78535)
3. F. J. Huera-Huarte, and Z. A. Bangash. (2012) Vortex dynamics at the node to anti-node transition of a forced oscillating flexible circular cylinder. Fluid and Elasticity FE, 2012 San Diego, CA. USA.
4. F. J. Huera-Huarte, Z. A. Bangash and L. M. Gonzalez. (2013) Towing tank experiments on the vortex-induced vibrations of a long flexible cylinder in a stepped current. Proceedings of ASME 32nd International Conference on Ocean, Offshore and Arctic Engineering. ASME OMAE 2013, Nantes, France. (OMAE2013-10492)

5. F. J. Huera-Huarte, Z. A. Bangash and L. M. Gonzalez. (2014) Towing tank experiments on the vortex-induced vibrations of a long flexible cylinder with wake interference. Proceedings of ASME 33rd International Conference on Ocean, Offshore and Arctic Engineering, ASME OMAE, 2014 , San Francisco, CA, USA. (OMAE2014-23873)
6. Z A. Bangash and F. J. Huera-Huarte. (2014) Vortex structures in the node to anti-node transition of an oscillating Flexible cylinder. 10th European Fluid Mechanics Conference. EFMC10, 2014, Copenhagen, Denmark.

## TABLE OF CONTENTS

---

<b>List of figures</b>	<b>xvii</b>
<b>List of tables</b>	<b>xxi</b>
<b>Nomenclature</b>	<b>xxiii</b>
<b>1 Introduction</b>	<b>1</b>
<b>2 Literature review</b>	<b>5</b>
2.1 General Overview . . . . .	5
2.1.1 Introduction . . . . .	5
2.1.1.1 Historical overview and paternity of Kármán Vortex Street . . . . .	7
2.1.1.2 Formation of vortices in the wake . . . . .	7
2.1.2 Stationary Cylinders, Flow Regimes . . . . .	9
2.2 Vortex Induced Vibrations; Rigid cylinders . . . . .	17
2.2.1 Rigid cylinder with 1 degree of freedom: Motion transverse to the fluid flow . . . . .	18
2.2.1.1 Equations for 1 degree of freedom . . . . .	19
2.2.1.2 Added mass, virtual mass, potential and effective added mass . . . . .	21
2.2.1.3 Effective stiffness, the concept and its formulation . . .	24
2.2.1.4 Phase angle ( $\phi$ ) by force decomposition . . . . .	25
2.2.1.5 A look at the wake: phase jump, timing and modes of vortex shedding . . . . .	28
2.2.1.6 Amplitude Response Branches . . . . .	31
2.2.2 Rigid cylinder with 1 degree of freedom: Motion in-line with the fluid flow . . . . .	35
2.2.3 Rigid cylinder with 2 degree of freedom . . . . .	36

---

2.2.4	Rigid Cylinders with spanwise geometric variations . . . . .	39
2.2.4.1	Tapered cylinders . . . . .	39
2.2.4.2	Wavy, sinusoidal and curved geometries . . . . .	39
2.2.4.3	Flexible cantilevers, pivoted and inclined cylinders . . . . .	42
2.3	Vortex Induced Vibrations; Flexible Cylinders . . . . .	44
2.3.1	Experimental analysis . . . . .	45
2.3.1.1	Resonant Response . . . . .	46
2.3.1.2	Higher harmonics . . . . .	49
2.3.2	Force Distribution and Prediction Models . . . . .	50
2.3.3	Numerical Methods . . . . .	52
2.4	Vortex Induced Vibrations of Cylinders with Wake interference . . . . .	54
2.4.1	Stationary cylinders in tandem arrangement . . . . .	55
2.4.2	Flexibly mounted rigid cylinders in tandem arrangement . . . . .	55
2.4.3	Flexible cylinders in tandem arrangement . . . . .	57
<b>3</b>	<b>Multi-mode VIV of Long Flexible Cylinders :</b>	
	<b>Set-up, measurements, analysis</b>	<b>59</b>
3.1	Introduction . . . . .	59
3.1.1	Experimental set-up . . . . .	59
3.1.1.1	Towing tank . . . . .	59
3.1.1.2	General Description . . . . .	60
3.1.1.3	Support structure . . . . .	61
3.1.2	Riser model . . . . .	61
3.1.2.1	Riser mounting and external instrumentation . . . . .	62
3.1.2.2	Setting up initial tension and end condition . . . . .	65
3.1.2.3	Test parameters . . . . .	66
3.2	Tandem Cylinders . . . . .	66
3.3	Data Acquisition . . . . .	68
3.4	Curvatures and deflections . . . . .	68
3.5	Modal Analysis . . . . .	73
3.5.1	Standard mode shapes matrix . . . . .	74
3.5.2	Blind Source Separation . . . . .	80
3.6	Tension and Drag . . . . .	83
3.7	Natural frequencies and decay characteristics . . . . .	85
3.7.1	Experimental determination of natural frequencies . . . . .	85
3.7.2	Decay tests . . . . .	86
3.7.3	Analytical computation of Natural Frequencies . . . . .	88

Table of contents	xv
-------------------	----

---

<b>4 Multi-mode VIV of Long Flexible Risers; Results</b>	<b>93</b>
4.1 Introduction . . . . .	93
4.2 Analysed sections . . . . .	94
4.3 Synopsis . . . . .	94
4.4 Statistical Parameters . . . . .	97
4.5 Results . . . . .	98
4.6 Modal Analysis . . . . .	106
4.7 Mode shapes from Blind Source Separation . . . . .	109
<b>5 Multimode VIV of Flexible Risers in Tandem; Results</b>	<b>115</b>
5.1 Introduction . . . . .	115
5.2 Synopsis . . . . .	116
5.3 Results . . . . .	116
5.4 Modal Analysis . . . . .	122
5.5 Mode shapes . . . . .	123
5.6 Summary of Results . . . . .	128
<b>6 Wake characteristics of a flexible riser undergoing VIV</b>	<b>129</b>
6.1 Introduction . . . . .	129
6.2 Experimental Setup . . . . .	130
6.2.1 Apparatus . . . . .	130
6.2.2 DPIV and Flow Visualization setup . . . . .	132
6.3 Results and Discussion . . . . .	134
6.4 Summary . . . . .	146
<b>7 Conclusions and Future Work</b>	<b>147</b>
7.1 Conclusions . . . . .	147
7.2 Future Work . . . . .	148
<b>Bibliography</b>	<b>151</b>
<b>Appendix A Analytical Estimation of Natural Frequencies</b>	<b>165</b>
A.1 Introduction . . . . .	165
A.2 Differential Quadrature Method . . . . .	166



UNIVERSITAT ROVIRA I VIRGILI

VORTEX INDUCED VIBRATIONS OF LONG FLEXIBLE CYLINDERS WITH AND WITHOUT WAKE INTERFERENCE

Denise Fischer Hubert

Dipòsit Legal: T 992-2015

## LIST OF FIGURES

---

2.1	Vortex wake pattern of a cylinder . . . . .	6
2.2	Filament sketch of the formation region . . . . .	8
2.3	Base suction coefficient vs Reynolds number . . . . .	10
2.4	Wake transition regime instabilities, Mode A and Mode B . . . . .	12
2.5	Strouhal number vs Reynolds number . . . . .	12
2.6	Instantaneous PIV results at Re=5,000 and 10,000 . . . . .	13
2.7	Fluctuating lift coefficient vs Reynolds number . . . . .	14
2.8	Cylinder moving through fluid . . . . .	22
2.9	Phase angle $\phi$ vs reduced frequency $f^*$ . . . . .	27
2.10	Phase angle $\phi$ vs reduced velocity $U^*$ . . . . .	28
2.11	Phase jump with reduced frequency . . . . .	28
2.12	Map of regimes for vortex modes . . . . .	30
2.13	Transverse response of a vibrating cylinder . . . . .	32
2.14	Amplitude response map of a vibrating cylinder . . . . .	32
2.15	Collapse of amplitude response data by using true normalized velocity . . . . .	33
2.16	Skop-Griffin plot, in Log-Log format . . . . .	34
2.17	Griffin plot of modally normalized maximum amplitudes, with mode factor . . . . .	34
2.18	Preferred modes of near wake structures for in-line oscillation . . . . .	36
2.19	Cylinder trajectories overlaid on the third harmonic magnitude . . . . .	38
2.20	Hybrid Shedding Mode of Tapered Cylinders . . . . .	39
2.21	Modes of shedding of a cylinder with wavy leading edge . . . . .	41
2.22	Vortex shedding from a varicose cylinder . . . . .	42
2.23	Vortex shedding from a pivoted cylinder, showing different shedding modes along the span . . . . .	43
2.24	Drag Coefficient vs Reduced Velocity, From Chaplin <i>et al.</i> . . . . .	48
2.25	Wake and proximity interference boundaries for two staggered cylinders in steady cross-flow, adapted from Zdankovich [177] . . . . .	56

---

3.1	General layout of the setup . . . . .	60
3.2	Isometric view of setup . . . . .	61
3.3	High mass ratio model, close up . . . . .	62
3.4	Mounted configuration of the risers . . . . .	63
3.5	Bottom mounting and instrumentation . . . . .	64
3.6	top mounting and instrumentation . . . . .	64
3.7	Photograph of the top mounting and instrumentation . . . . .	65
3.8	General arrangement of the cylinders in tandem configuration . . . . .	67
3.9	Photograph of cylinders in tandem configuration . . . . .	68
3.10	Sample displacement data . . . . .	71
3.11	contours of displacement data . . . . .	72
3.12	Comparison of computed vs measured displacement . . . . .	73
3.13	Sample modal contribution . . . . .	75
3.14	Sample snapshots of modal contribution fit using pre-defined mode shape matrix . . . . .	78
3.15	Sample representation of modal response amplitudes and frequencies, extracted pre-defined mode shape matrix . . . . .	79
3.16	Mode shapes and frequencies using SOBI algorithm . . . . .	80
3.17	Comparison of the blind source separation mode shapes with the modal responses obtained from sinusoidal mode shapes . . . . .	82
3.18	$\Delta T_t$ measured from load cell, and computed from arc length . . . . .	83
3.19	Drag measurement by drag load cell and tension decomposition . . . . .	84
3.20	Modal frequencies from static testing . . . . .	86
3.21	Decay testing . . . . .	87
3.22	Pinned-pinned beam under load . . . . .	89
4.1	3D trajectory map and deflections, $m^* = 1.1$ at low $U^*$ . . . . .	95
4.2	Example contour plots at low $m^*$ , $U^*$ . . . . .	96
4.3	3D trajectory map and deflections, $m^* = 2.7$ at low $U^*$ . . . . .	96
4.4	Example contour plots for high $m^*$ , low $U^*$ . . . . .	97
4.5	Increase in tension with $U^*$ , for various end conditions . . . . .	99
4.6	Spatio-Temporal RMS of in-line displacements . . . . .	100
4.7	Spatio-Temporal standard deviation of dynamic in-line displacements vs reduced velocity . . . . .	101
4.8	Spatio-Temporal standard deviation of dynamic cross-flow displacements vs reduced velocity . . . . .	101

---

4.9	Spatio-Temporal standard deviation of cross-flow displacements vs reduced velocity based on dominant mode frequency . . . . .	102
4.10	Spatio-Temporal standard deviation of dynamic in-line displacements vs. reduced velocity based on dominant mode frequency . . . . .	102
4.11	In-line dominant frequency vs reduced velocity . . . . .	103
4.12	Cross-flow dominant frequency vs reduced velocity . . . . .	103
4.13	Non-dimensional in-line dominant frequency vs reduced velocity . . . . .	104
4.14	Non-dimensional cross-flow dominant frequency vs reduced velocity . . . . .	104
4.15	Maximum in-line displacement vs $U^*$ . . . . .	105
4.16	Maximum cross-flow displacement vs $U^*$ . . . . .	105
4.17	Drag Coefficient vs $U^*$ . . . . .	106
4.18	Modal contribution vs $U^*$ . . . . .	107
4.19	Probability of mode for high mass ratio riser ( $m^* = 2.7$ ) . . . . .	108
4.20	Probability of mode for low mass ratio riser ( $m^* = 1.1$ ) . . . . .	108
4.21	Modal amplitudes based on blind source separation, vs $U^*$ . . . . .	109
4.22	Progression of cross-flow Modes with reduced velocity for low tension, high mass ratio riser . . . . .	112
4.23	Progression of cross-flow Modes with reduced velocity for high tension, high mass ratio riser . . . . .	113
4.24	Progression of Mode Shape with $U^*$ for $m^* = 1.1$ riser . . . . .	114
5.1	Arrangement of cylinders, Tandem configuration . . . . .	116
5.2	Spatio-temporal RMS of in-line displacement for riser in wake . . . . .	118
5.3	Comparison of spatio-temporal RMS of in-line displacement for riser in wake, with an isolated riser . . . . .	118
5.4	Spatio-temporal standard deviation of in-line displacement, for riser in wake . . . . .	119
5.5	Non-dimensional dominant in-line mode frequency $f_{dx}/f_1$ vs reduced velocity for riser in wake . . . . .	120
5.6	Spatio-temporal RMS of cross-flow displacement for riser in wake . . . . .	120
5.7	Non-dimensional dominant cross-flow mode frequency $f_{dy}/f_1$ vs reduced velocity for riser in wake . . . . .	121
5.8	Maximum non-dimensional in-line displacement for riser in wake . . . . .	121
5.9	Maximum non-dimensional cross-flow displacement for riser in wake . . . . .	122
5.10	Drag Coefficient $C_D$ of a riser in the wake of another riser . . . . .	122
5.11	Modal contribution vs $U^*$ for cylinders in wake . . . . .	123
5.12	Progression of Mode Shape with $U^*$ for riser in the wake . . . . .	125

---

5.13	Progression of Mode Shape with $U^*$ for riser in the wake . . . . .	126
5.14	Progression of Mode Shape with $U^*$ for riser in the wake . . . . .	127
6.1	Front and Top view of experimental setup . . . . .	131
6.2	Position of light sheets for PIV and FV data. . . . .	132
6.3	Non-dimensional cylinder excursion at various heights . . . . .	135
6.4	Vorticity maps ( $\omega_z$ ) for different phases of oscillation, at (a) the anti-node and (b) the node . . . . .	136
6.5	Flow visualization results for all phases ( $\phi$ ) at (a)the anti-node and (b)the node. . . . .	137
6.6	Vorticity maps ( $\omega_z$ ) for phase averaged PIV at minimum excursion . . .	138
6.7	Vorticity maps ( $\omega_z$ ) for phase averaged PIV at minimum excursion . . .	139
6.8	Averaged flow visualization images in $xz$ plane . . . . .	141
6.9	Instantaneous flow visualization images in $xz$ plane . . . . .	142
6.10	POD plots of flow in $xz$ plane at $y/D=0$ , indicating the first four modes for $V_x$ (top) and $V_z$ (bottom). . . . .	144
6.11	Vortex skeleton sketch, reconstructed based on the PIV and FV images	145
A.1	Pinned-pinned beam under load . . . . .	165

## LIST OF TABLES

---

2.1	Flow regimes and states, from Zdarvkovich[178]	16
3.1	Characteristics of the test models	66
3.2	Main parameters of the experiment runs	66
3.3	Experimental and Numerical Frequencies, in air	91
3.4	Experimental and Numerical Frequencies in water	91
4.1	List of tests for isolated cylinders	99
5.1	List of tests in tandem configuration	117
6.1	Experiment Parameters for wake analysis	131
6.2	Details of the analyzed DPIV and FV planes and runs	133

UNIVERSITAT ROVIRA I VIRGILI

VORTEX INDUCED VIBRATIONS OF LONG FLEXIBLE CYLINDERS WITH AND WITHOUT WAKE INTERFERENCE

Denise Fischer Hubert

Dipòsit Legal: T 992-2015

## NOMENCLATURE

---

### Roman Symbols

$C$	Coefficient
$c$	Damping
$c$	Curvature in x or y direction, depending on subscript
$D$	Diameter of the cylinder
$EA$	Axial stiffness
$E$	Modulus of Elasticity
$EI$	Flexural stiffness
$f$	Frequency
$F$	Force
$k$	Spring constant
$KC$	Keulegan-Carpenter number
$L$	Length, Characteristic length
$P$	Pressure
$Re$	Reynolds number
$S$	Center to center distance in tandem arrangement of cylinders
$St$	Strouhal number
$T$	Tension



$U$  Velocity

### Greek Symbols

$\beta$  Frequency parameter

$\lambda$  Wavelength

$\mu$  Viscosity

$\nu$  Kinematic viscosity

$\phi$  Phase angle

$\rho$  Density

$\sigma$  Standard deviation

$\zeta$  Damping ratio

### Superscripts

' Fluctuating component

\*

$\hat{X}$  Maximum, peak value of a variable X

$\tilde{X}$  Root mean square value of a variable X

### Subscripts

1 Based on the fundamental natural frequency (in air)

$A$  Potential added mass

$b$  Base

$D$  Drag, In-line direction

$EA$  Effective added mass

$fx$  Based on the dominant frequency in the x direction

$fy$  Based on the dominant frequency in the y direction

$\infty$  Free-stream

## Nomenclature

---

xxv

$L$	Lift, Cross-flow direction
$s$	Side
$x$	In the inline / flow direction, along x axis
$y$	In the crossflow direction, along y axis
$z$	Along the axis of cylinder, along z axis

UNIVERSITAT ROVIRA I VIRGILI

VORTEX INDUCED VIBRATIONS OF LONG FLEXIBLE CYLINDERS WITH AND WITHOUT WAKE INTERFERENCE

Denise Fischer Hubert

Dipòsit Legal: T 992-2015

# CHAPTER 1

## INTRODUCTION

---

### About Vortex Induced Vibrations

Structures that are in contact with a fluid flow are subject to flow-induced forces. Whenever a bluff body is placed in the flow, vortices are shed downstream of the body. The shed vortices exert an oscillatory external force on the body. A simple case of a flexibly mounted rigid cylinder in the flow results in rich dynamics of interactions, where the flow induces motion in the body, and the motion of the body induces changes in the flow. A case of flexible cylinder in the flow adds another dimension to the complexity. Vortex induced vibrations (VIV) is a cross-discipline field involving fluid dynamics, structural dynamics and vibrations, with complex inter-dependency.

The off-shore applications of structures has largely been the driving force behind this field. The vibrations of mooring lines, drilling risers, marine cables, seabed pipelines and data cables has been a long standing problem in the ocean-current fields. In the last 30 years, the prediction of VIV has greatly improved because of the data collected in the laboratory experiments and information from the risers in the field. There are quite a few VIV prediction programs that help engineers in predicting the VIV response and help in the designs for future underwater applications. The natural resources explored today are in deeper waters, with stronger currents. Additional applications in form of renewable energy extraction in deep oceans have added impetus to the research, as the design with considerations of VIV becomes more important because of the increased risk of fatigue failure.

There are two basic directives in the field of VIV investigations, *i.e.* prediction of the response, and control or suppression of the response, specially without effecting the drag of the riser. These objectives require a thorough understanding of the physics of the vortex induced vibrations. Even with increasing access to computational methods,

faster computers and improved algorithms, the field is still far from being able to contribute substantially to the practical implementation in the field. The empirical codes available for prediction, based on experimental data, are limited by the same restrictions as the experiments themselves. In real life situation, even the flow conditions may not be fully known, whereas the experimental data is restricted to a range of flow conditions, and structural parameters.

This current thesis covers, briefly, the results of vortex induced vibrations of long flexible risers with a significantly low mass ratio. The reason for picking low mass ratio is the lack of any previous documentation regarding vortex induced vibrations of low mass ratio risers, and that the real application of a significant number of marine risers is of the comparable mass ratio. Another area covered in this thesis, that has previously not been covered is the vortex induced vibrations of flexible risers in tandem arrangements, undergoing multi-mode oscillations. Additionally, the wake of a flexible riser undergoing multi-mode oscillations was analysed using Particle image velocimetry and flow visualization techniques. The results indicate three different regimes in the wake, as we investigate along the span of the riser from the structural anti-node, to the node.

## About this thesis

The document contained herein is a compilation of results of three batches of experiments, whereas an effort has been made to keep a continuity of thoughts. The second chapter contains a brief summary of what is called the 'state of the art'. It is an extremely brief summary of the literature on the subject of vortex induced vibrations. In the beginning, the various regimes of the flow around a stationary cylinder are described, briefly, which is followed by a review of vortex induced vibrations. The sequence goes from the simplest case to the more complex cases *i.e.* starting from stationary cylinder, to rigid cylinder with one degree of freedom, and finally a review of some of the key works on flexible risers, and risers within wake of other risers.

Chapter 3 contains the details of the experimental set-up, data acquisition and processing, and the extraction of important parameters from the data. The chapter not only enumerates the well established, standard procedures for extracting useful information from the curvature data of flexible risers, that have been documented previously, but also lists some new and alternative techniques.

Chapter 4 contains the results and discussion on the vortex induced vibrations, for the two different riser models, in isolated configuration. The difference between the

risers was the mass ratio, which is defined as the ratio of the mass of the riser, to the mass of the displaced water. The results are primarily oriented by statistical parameters, in order to cover the entire matrix of experiments, with the intent to give the readers a general response trend for flexible risers undergoing vortex induced vibrations. While similar experiments have been conducted before, all of the documented laboratory experiments have been for risers with mass ratio significantly higher than the low mass ratio tests contained in this thesis, which is the closest mass ratio to the real life applications of flexible offshore risers.

Chapter 5 is dedicated to a brief coverage of the vortex induced vibrations of a flexible riser, in the wake of a fixed cylinder, in tandem arrangement. The statistical parameters presented in this chapter follow the same, established format, in order to facilitate comparisons and understanding. The experiments were novel in the sense that these are the first documented results of multi-mode vortex induced vibrations of flexible risers in the wake of another cylinder.

Chapter 6 details another experiment, where the wake of a flexible riser undergoing multi-mode vortex induced vibrations was analysed using Digital Particle Image Velocimetry. The vortex dynamics at the structural node, the anti-node, and the transition between these two regions has been described in detail. The resulting wake model signifies some important results, such as the absence of vortex shedding at the structural node of the riser. The last chapter covers a brief conclusion of all three experimental campaigns, and suggests further work on the subject.

UNIVERSITAT ROVIRA I VIRGILI

VORTEX INDUCED VIBRATIONS OF LONG FLEXIBLE CYLINDERS WITH AND WITHOUT WAKE INTERFERENCE

Denise Fischer Hubert

Dipòsit Legal: T 992-2015

## CHAPTER 2

### LITERATURE REVIEW

---

The analysis of a coupled system of structural and fluid dynamics is a complex field, incorporating multiple areas of study. Various assumptions and simplifications have been incorporated by numerous researchers in order to present a simplified picture of the otherwise complex phenomena. Here a review of the previous work is briefly presented. The chapter begins with the study of flow around static / stationary cylinders and proceeds to the more complex cases of flexibly mounted cylinders. In the last section the review covers studies of flexible cylinders undergoing multi-mode vibrations.

## 2.1 Flow round a stationary circular cylinder

### 2.1.1 Introduction

Whenever there is a flow over a body, the fluid forms a boundary layer because of no-slip condition on the surface. In case of bluff bodies there are large parts of the body where the flow is characterized by the separated boundary layer. The separation region is dependent on geometric features of the body as well as the flow characteristics. In all cases the wake is defined by the boundary layer separation because of the presence of adverse pressure gradient in the direction of the flow, which is a function of the shape of the bluff body. This adverse pressure gradient causes the separation of the boundary layer and formation of a region of recirculating fluid, thus forming the wake. In case of a circular cylinder the separation phenomena does not occur at a particular position of the cylinder, rather it is dependent on the flow velocity, type of boundary layer and whether the boundary layer reattaches after forming a separation bubble. The flow downstream of the separation point reaches zero velocity at the surface of



the cylinder and a vortex is formed because of the velocity difference in the cross-flow direction. These formed vortices are shed periodically, and apply forces to the cylinder.



Fig. 2.1 Vortex wake pattern of a cylinder

The two important non-dimensional parameters that govern the flow over a cylinder are the flow transition from laminar to turbulent, and the periodicity of the wake. These parameters are, in non-dimensional terms, the Reynolds number and the Strouhal number.

1. When analyzing flow in pipes, Osborne Reynolds[126] discovered that the transition of flow from laminar to turbulent was a function of density, velocity, viscosity and the characteristic length, which in his case was the diameter of the pipe. The idea originated from the works of Gabriel Stokes in mid 1800s. The Reynolds Number  $Re$  is the ratio of the inertial forces of the flow to the viscous forces and is defined by the equation:

$$Re = \frac{\rho_f U L}{\mu} = \frac{V D}{\nu} \quad (2.1)$$

Where  $\rho_f$  is the density of the fluid,  $V$  is the velocity, and  $\mu$  is the viscosity of the fluid.  $L$  is the characteristic length, which in case of flow inside a pipe would be the inner diameter of the pipe, whereas in case of flow around the cylinder it is the diameter  $d$  of the cylinder, and  $\nu$  is the kinematic viscosity of the fluid.

2. While carrying out investigation of aeolian sound generated by wires undergoing vortex induced vibrations, Vincenc Strouhal[142] defined a dimensionless number describing the oscillating flow mechanism. The Strouhal number ( $St$ ) is defined as

$$St = \frac{f L}{U} \quad (2.2)$$

where  $f$  is the vortex shedding frequency,  $L$  and  $U$  are the characteristic length and flow velocity, equivalent to one described in section above.

### 2.1.1.1 Historical overview and paternity of Kármán Vortex Street

The phenomena of vortex shedding has been a topic of scientific research for more than a century. In 1907 Mallock[98] drew different possibilities of vortices emission in the wake of bluff bodies and included the alternating vortices, while he described the drag of various bluff bodies.

In 1908, Bénard[15] carried out detailed investigation of the wake of a cylinder, and documented the presence of “a double trail of alternating vortices in the wake”. He determined that the distance between these alternating vortices depended only on the transverse size of the bluff body. After analysing in excess of 30,000 images Bénard validated the law of frequency as a function of velocity, or Strouhal number and explained the geometrical characteristics of the vortex emission [16, 17].

In 1912 von Kármán[162] analysed the stability of vortex configurations, and established a theoretical link between the vortex street structure and the drag observed by the body. He investigated the linear stability of point vortex configuration and concluded that two rows of oppositely signed vortices were unstable in both symmetric and antisymmetric configuration except for one specific antisymmetric geometry which exhibited neutral stability, where the distance between vortices in the street, divided by the breadth of the street,  $b/h$ , was equal to  $1/0.28$ . That result was of such important consequence that the phenomenon of alternating vortex shedding by a bluff body is christened as the “Kármán Vortex Street”. In his book, Kármán[163] acknowledged that the phenomenon had been documented earlier by both Mallock[98], who drew the possibility of vortex street in the wake, while investigating the drag of bluff bodies, and Bénard, who showed the vortex shedding phenomena using experimental methods. The stability analysis first carried out by von Kármán remains as the definitive work, and has spawned off significant research in the field.

### 2.1.1.2 Formation of vortices in the wake

After the reports by Bénard and von Kármán, many scientists investigated the phenomena of solid bodies wake, and the stability of vortex arrays. While the point vortex analysis carried out first by von Kármán explained the stability of the alternating row of vortices downstream of the cylinder, that is, if such vortices are formed, they will be stable downstream of the cylinder, the process of formation, and its dependence

on various parameters like flow velocity, was the subject of investigation for many researchers.

Gerrard[53] gave the description of the process of formation of vortices close to the cylinder in his description of the formation region of the cylinder. He suggested that the growing vortex is fed by the circulation from the shear layer, until it is strong enough that it draws the opposite shear layer across the wake. Part of the flow from the opposing shear layer is pulled in by the vortex (*a*) and the shear layer that feeds the vortex (*b*), and a part goes towards the cylinder (*c*). When the entrained opposing shear layer reaches significant amount to cut the supply of circulation to the formed vortex, the vortex is detached from the cylinder and part of the entrained fluid, *c*, starts formation of the opposing vortex. The filament line sketch is shown in figure 2.2.

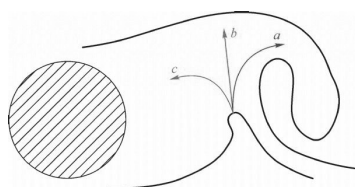


Fig. 2.2 Filament-line sketch of the formation region. Arrows showing entrainment (*a*) and (*b*), and reverse flow (*c*). from Gerrard[53]

The frequency of the shedding process is an important parameter in cases of flow around a cylinder. Different researchers tried to define different characteristic lengths in order to find a Strouhal number relationship that would satisfy a wide range of Reynolds number for flow around a cylinder. In 1954 Anatol Roshko published a pair of technical reports on the subject of frequency and drag of a cylinder in the flow[127, 128], in an attempt to determine a universal Strouhal number for a cylinder in flow,  $S^*$ , to cater for the various flow regimes over Reynolds numbers, defined the characteristic length  $d'$  as the width of the wake defined by his notched-hodograph theory. He acknowledged some discrepancies, as it was insufficient to lump all the Reynolds number effects into one parameter. The problem arose from the point and mechanism of transition in the free shear layers. Bearman [8] defined the characteristic length as the lateral displacement between the vortex rows. Gerrard [52–54] also suggested the presence of two simultaneous characteristic lengths, i.e, the scale of formation length and the width to which the free shear layers diffuse, whereas the formation length showed dramatic changes with increasing Reynolds numbers. In either case, they determined that there is a more complex relationship between the Reynolds number and Strouhal number for flow around a cylinder, which varies differently in

different regimes of the flow. All these regimes definition were suitable for a limited range of Reynolds numbers.

The response of a cylinder in presence of oscillatory forces and pressures can be defined by their respective coefficients in non-dimensional forms as:

- Forces parallel to the flow,  $F_x$ : The force parallel to the flow, drag, is given in the non-dimensional form by:

$$C_D = \frac{F_x}{\frac{1}{2}\rho U_\infty^2 D} \quad (2.3)$$

- Forces perpendicular to the flow,  $F_y$ : The force normal to the flow, lift, is given in the non-dimensional form by:

$$C_L = \frac{F_y}{\frac{1}{2}\rho U_\infty^2 D} \quad (2.4)$$

- Base Pressure,  $P_b$ : The base pressure, which is a predominant factor in drag of a bluff body, is the pressure measured at the point  $180^\circ$  from the front stagnation point. It is given in the non-dimensional form by:

$$C_{pb} = \frac{P_b - P_\infty}{\frac{1}{2}\rho U_\infty^2} \quad (2.5)$$

- Side Pressure,  $P_s$ : The side pressure, a predominant factor in measuring fluctuating lift, is the pressure measured at the point  $90^\circ$  from the front stagnation point is given in the non-dimensional form by:

$$C_{ps} = \frac{P' - P_\infty}{\frac{1}{2}\rho U_\infty^2} \quad (2.6)$$

### 2.1.2 Stationary Cylinders, Flow Regimes

Various attempts at the categorization of flow regimes for flow around a cylinder have been carried out as described above. In almost all cases, Reynolds number is the definitive regime criteria, however it is highlighted that this criteria is valid for undisturbed flow, as disturbances may cause transitions. Even slight variation in background turbulence levels can cause significant differences in flow regimes, specially at the lower and higher limits of each regime. Here we follow the regime definition based on base pressure coefficient ( $C_{pb}$ ) as defined by Williamson[168], and Zdarvkovich[178].

This parameter indicates the most significant changes in different regimes with Reynolds number, and has much better resolution and standardized measurement techniques.

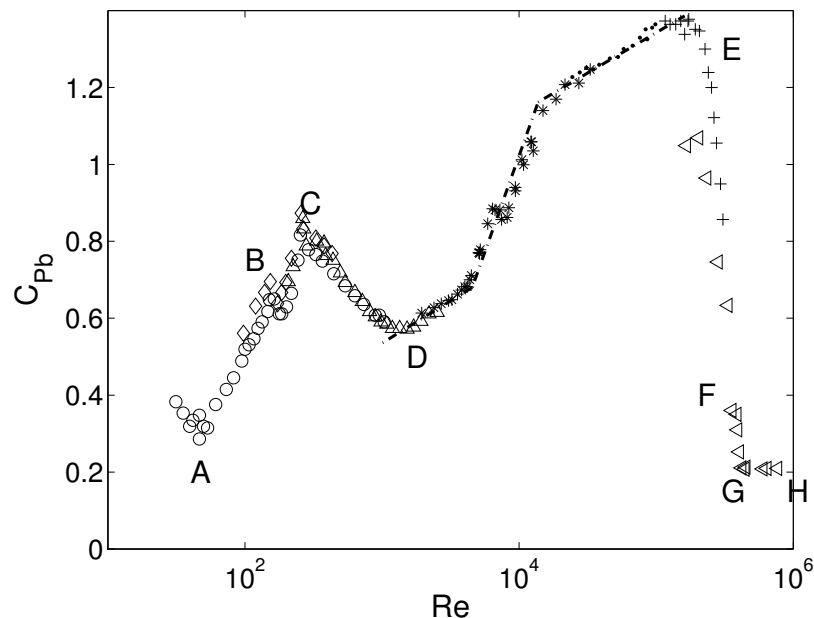


Fig. 2.3 Base suction coefficient as functions of Reynolds number. Plot adopted and reconstructed from Norberg[113]. Dashed lines indicating relatively constant behaviour.

- Regime up to A: Laminar Steady Regime ( $Re < 47$ ):  
 At  $Re$  below 49, the wake comprises a steady recirculation region of two symmetrically placed vortices on each side of the wake, also known as föppl vortices, forming a pseudonamed “steady wake bubble”. Beyond this bubble, the flow appears unaffected by the presence of the cylinder. The base pressure decreases with increasing length of the bubble, due to viscous stresses. The upper limit for this regime was marked by Henderson[61], who determined that at  $Re = 45 - 50$  a Hopf bifurcation occurs beyond which the steady state solution ceased to exist. This position, A, is marked by a sudden change in the base pressure in the  $C_{pb}$  plot.
- Regime A-B: Laminar Vortex Shedding ( $Re \sim 47$  to  $140 - 194$ ):  
 This regime is highlighted by development of wake instabilities. The instabilities develop initially downstream of the bubble in form of a sinuous waves, and with increasing  $Re$  these instabilities amplify in strength and size, and travel towards the bubble as shown by Gerrard[55]. The variation in base suction with  $Re$  show a sharp deviation from the trend seen in regime up to A. At the lower limits the

wake instability is a manifestation of Hopf bifurcation, and with amplification the Reynold stresses increase in the near wake region. Further increase in Reynolds number causes the oscillating recirculation cells to detach from the cylinder and an array of vortices are formed. Increasing the Reynolds number results in a rise in base suction, with monotonic increase in Strouhal number.

The lower limit computed using numerical stability by Jackson[75] and experimentally by Mathis *et al.* [99] for this regime is at  $Re \sim 46$ . The upper limit is defined as a range (140 – 194) because of the sensitivity of the flow towards the end boundary conditions. A good approximation to flow past an infinitely long cylinder has been demonstrated by Williamson[167], and Hammache & Gharib[60], where the three-dimensionality first appears at  $Re \sim 180$ , however with properly set end boundary conditions, the wake is observed to be purely periodic such that the the vortex shedding is completely parallel to the cylinder axis, all the way up to  $Re = 194$ .

- Regime B-C: Wake-Transition Regime ( $Re \sim 190$  to 260):

For  $Re$  between 180 – 200 the vortices are shed in a laminar fashion, however as the vortices travel downstream of the cylinder they become irregular and transitional. This transition is hysteretic, and is indicated with the sudden fall in the Strouhal number as seen in figure 2.5. At the first discontinuity (marked *B*), vortex loops and formation of stream-wise vortex pairs are observed due to the deformation of the primary shed vortices. Zhang *et al.* [180] called it “Hard” transition. These streamwise vortices have a spanwise wavelength of about 3 – 4 diameters, making them scalable to the primary kármán vortices. These appear to be the result of an elliptical instability in the near wake shed vortices, that form a wavy core along the span, which gives rise to the streamwise vortex pairs. These spanwise vortices reduce the coherency in the primary vortex, which results in a decrease in base suction as well as an increase in formation length.

At the higher end of this regime, finer scale stream-wise vortices are observed that at the length scale of about one diameter. This instability takes place through a gradual shift of energy from the previously described mode over a wider range of Reynolds number. These modes were labelled as Mode A and Mode B instabilities by Williamson[167, 168].

The change in the slope of the base pressure curve is evident in the figure 2.3. The review by Roshko[130] and Williamson[169] shows a considerable scatter in the observed values of Reynolds number for the transition to three-dimensionality.

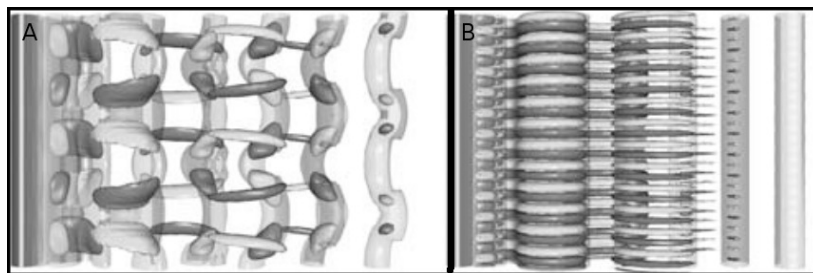


Fig. 2.4 Vorticity isosurface plots for the two wake modes, A (*left*) and B(*right*) from Blackburn *et al.* [20]

Computationally Barkley & Henderson[6] determined that the two-dimensional wake becomes linearly unstable to three-dimensional perturbations at  $Re \sim 189$ , and a secondary instability in form of Mode A is developed in the wake, with a critical wavelength of 3.96. At  $Re \sim 259$  they noticed a secondary bifurcation to Mode B instability. It is easier to compare the computational (linear stability theory based) model of Mode A bifurcation with experimental findings, the task becomes very difficult for Mode B, as at the higher end the flow is already unstable because of Mode A.

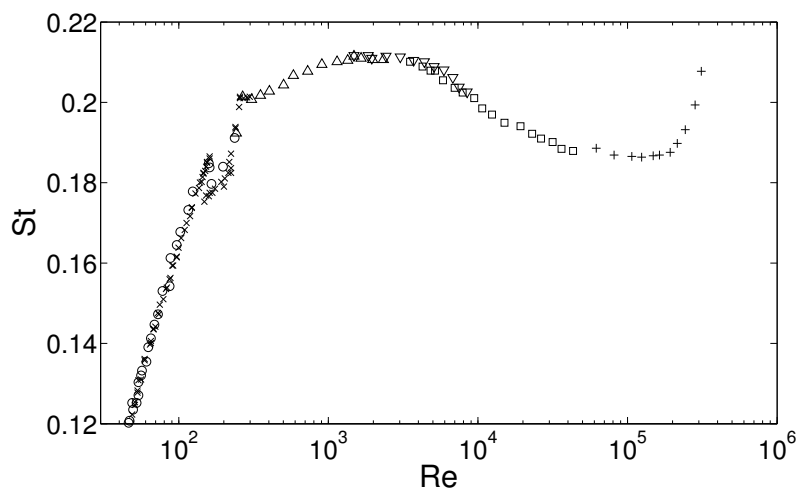


Fig. 2.5 Strouhal number as functions of Reynolds number. Plot reconstructed from Norberg[112]

- Regime C-D: Increasing Disorder in the Fine-Scale Three Dimensionalities ( $Re \sim 260$  to  $\sim 1000$ ):  
 At it's lower end, the primary wake instability (Mode B) behaves like the laminar shedding mode. However slight increase in  $Re$  results in increase in disorder

of the fine-scale three-dimensionalities, which causes a reduction in Reynolds stresses. The base suction reduces and the formation length starts increasing, up until the higher limit where the transition is observed. The two dimensional feature of the vortex shedding seen in the previous regimes is now completely three dimensional (Gerrard[55] and Williamson[172]), and the vortices are shed in cells in span-wise direction.

- Regime D-E: Shear-Layer Transition Regime ( $Re \sim 1000$  to  $2 \cdot 10^5$ )

In the transition regime an increase in the base suction and the two-dimensional Reynold stress level, and a decrease in formation length of main recirculation region, as well as Strouhal number is observed. These variations are caused by developing instability of the separating shear layers from the sides of the body. This regime was first observed by, and thus called the “Schiller-Linke” regime [137]. There is a decrease in Strouhal number as the Reynolds number is increased (Norberg[113]). The instability vortices that appear in the shear layer generate frequencies that vary roughly as  $Re^{3/2}$ (Bloor[24]), rather than as approximately  $Re$ , for the Kármán vortices. This trend can be seen in figure 2.5.

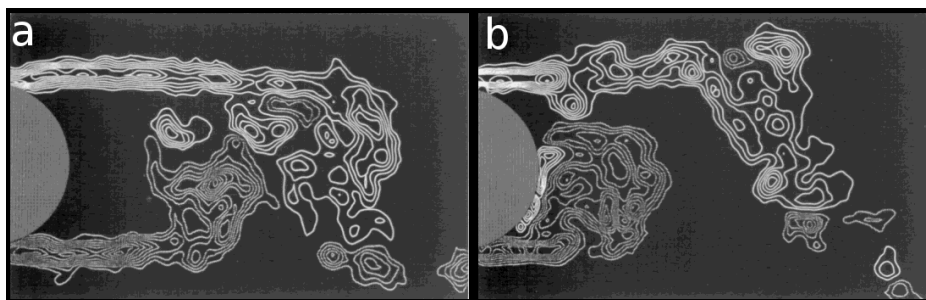


Fig. 2.6 Instantaneous PIV results at (a)  $Re=5,000$  and (b)  $Re=10,000$ , From Lin *et al.* [95]

Another important aspect in this range is that there are three distinct slopes in  $C_{bp}$  vs  $Re$  plot (highlighted by dashed lines in figure 2.3. This is explained by the change in the formation length and the influence of the Kármán vortices on the shear layer. As the  $Re$  is increased from 4,000 to 10,000, as seen in figure 2.6, the formation length reduces drastically. This influences the shear layer and causes dramatic increase in the fluctuating lift coefficient. The  $C_{p'}$  vs  $Re$  plot seen in figure 2.7 (adopted from Norberg[114]) shows that effect. In the range of  $4,000 < Re < 10,000$ , the effect is because of the strength of the formed vortices as well as the reduced formation length. For  $Re > 10000$  the changes in formation length with  $Re$  are not as significant as the formation length reaches



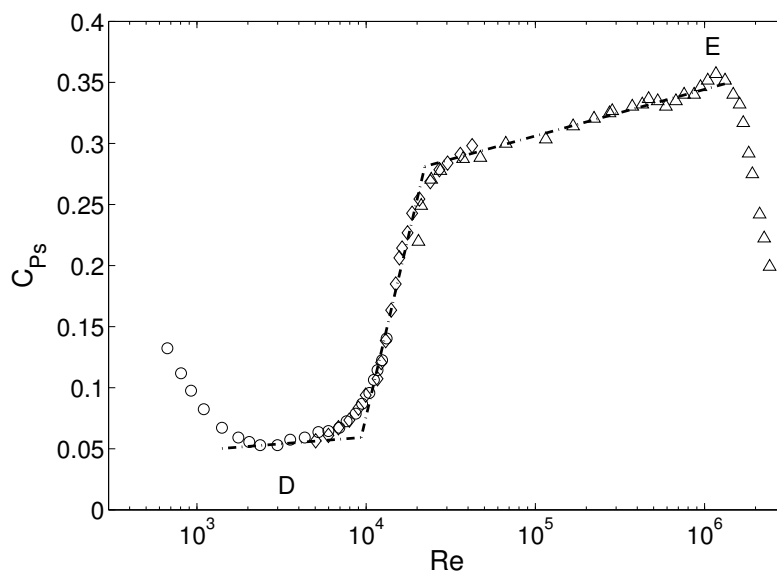


Fig. 2.7 Fluctuating lift coefficient as functions of Reynolds number. Plot reconstructed from Norberg[114],  $\circ$ : $d=4\text{mm}$ ,  $\diamond$ : $d=40\text{mm}$ ,  $\triangle$ : $d=120\text{mm}$

its minimum, therefore the only effect is because of the strength of the formed vortices.

- Regime E-F-G: Asymmetric Reattachment Regime ( $Re \sim 2 \cdot 10^5$  to  $\sim 3 \cdot 10^5$ ):  
 The regime, also called “Critical Regime” is highlighted by drastic reduction of base suction and drag with increasing  $Re$ . This is associated with a separation-reattachment bubble, which leaves a higher energy boundary layer. This results in a delayed separation. The width of the wake is also significantly reduced. The point  $F$  corresponds to the separation-reattachment bubble that remains on one side only, resulting in an unsymmetric, large lift forces (Schewe [136] and Bearman [8])
- Regime G-H: Symmetric Reattachment Regime ( $Re \sim 3 \cdot 10^5$  to  $\sim 5 \cdot 10^5$ ):  
 Also known as the “Supercritical Regime”, the flow is fairly symmetric with two separation-reattachment bubbles on either side of the cylinder, resulting in a relatively thin wake. The Strouhal number rises dramatically (up to 0.4) explained as with the reduced wake width, while maintaining the vortex stability parameter discussed earlier in mind, the distance between successive vortices will be shortened.

- Regime  $>H$ : Boundary-Layer Transition Regime: ( $Re > 5 \cdot 10^5$ ):

In this “Post-critical Regime” the wake downstream of the cylinder re-establishes itself and the Strouhal number drops down to 0.2, as shown by Lienhard[94], and Roshko[129], who had shown presence of periodic vortex shedding re-establish itself in this regime. The separation point moves further upstream till the boundary layer is completely turbulent, and high drag and base suction is observed. While in the  $G - H$  regime the energized post-separation bubble boundary layer was able to withstand the high adverse pressure gradient, here the adverse pressure gradient is significantly higher for the boundary layer to overcome, thus the periodic shedding is re-established.

Zdarvkovich[178] divided the flow regimes into states, as shown in Table 2.1. The details of each state and subdivisions into the regimes are listed in the tabular format. The values have minor differences compared to the regimes defined by Williamson, owing to the slight variations in different experimental set-ups used by various researchers.

It must be noted, however, that while Reynolds number is the key parameter, there are other factors that can cause significantly alter the regimes. Notable factors are the surface roughness, flow turbulence levels, end conditions, aspect ratio, blocking ratio and proximity to walls.

Table 2.1 Flow regimes and states, from Zdarvkovich[178]

State	Reynolds number Range	Properties
Laminar	$0 < Re < 4 - 5$	Non-separation regime
	$4 - 5 < Re < 30 - 48$	Steady separation regime
	$30 - 48 < Re < 180 - 200$	Periodic laminar wake
Transition in Wake	$180 - 200 < Re < 220 - 250$	Far Wake
	$220 - 250 < Re < 350 - 400$	Near wake
Transition in shear layers (subcritical)	$350 - 400 < Re < 1 \cdot 10^3 - 2 \cdot 10^3$	Lower
	$1 \cdot 10^3 - 2 \cdot 10^3 < Re < 2 \cdot 10^4 - 4 \cdot 10^4$	Intermediate
	$2 \cdot 10^4 - 4 \cdot 10^4 < Re < 1 \cdot 10^5 - 2 \cdot 10^5$	Upper
Transition in boundary layers (precritical - postcritical)	$1 \cdot 10^5 - 2 \cdot 10^5 < Re < 3 \cdot 10^5 - 3.4 \cdot 10^5$	Precritical regime
	$3 \cdot 10^5 - 3.4 \cdot 10^5 < Re < 3.8 \cdot 10^5 - 4 \cdot 10^5$	One bubble regime (Critical)
	$3.8 \cdot 10^5 - 4 \cdot 10^5 < Re < 5 \cdot 10^5 - 1 \cdot 10^6$	Two bubble regime (Critical)
	$5 \cdot 10^5 - 1 \cdot 10^6 < Re < 3.4 \cdot 10^6 - 6 \cdot 10^6$	Supercritical regime
	$3.4 \cdot 10^6 - 6 \cdot 10^6 < Re < Unknown$	Postcritical regime

## 2.2 Vortex-Induced Vibrations of Rigid Cylinders

The term Vortex Induced Vibrations (VIV) means that the cylinder undergoes vibrations because of the influence of the Kármán vortices. In case of rigid cylinders these vibrations can be in one dimension (where the rigid cylinder is allowed to oscillate inline, i.e. the direction of the flow or in cross-flow direction) or in two dimensions (where the rigid cylinder is allowed to oscillate in both inline and crossflow directions). In case of VIV, certain other parameters in addition to those described above come into play:

1. Mass Ratio ( $m^*$ ): It is the ratio between the mass per unit length ( $m$ ) of the structure, in our case cylinder, and the mass of the fluid it displaces.

$$m^* = \frac{m}{\rho_f \frac{\pi}{4} D^2} \quad (2.7)$$

Where  $\rho_f$  is the density of the displaced fluid.

2. Reduced Velocity ( $U^*$ ): The velocity of the flow is non-dimensionalized as the ratio of the velocity to the product of frequency and the characteristic length:

$$U^* = \frac{U_\infty}{fD} \quad (2.8)$$

The frequency  $f$  used for non-dimensionalizing velocity can be the fundamental natural frequency in air ( $f_1$ ), where the reduced velocity is indicated by  $U^*$ , or the dominant frequency in the experiment medium in in-line or cross-flow directions ( $f_{x,y}$ ) where the reduced velocity is indicated by  $U_{fx,fy}^*$ .

3. Frequency Ratio ( $f^*$ ): The non-dimensional frequency parameter that is the ratio of the oscillation frequency to the reference frequency, given by:

$$f^* = \frac{f}{f_N} \quad (2.9)$$

If the fundamental natural frequency in air is used, the ratio is represented by  $f^*$ .

4. Keulegan-Carpenter number ( $KC$ ): Keulegan-Carpenter number defines the ratio of drag forces vs inertial forces for bodies in oscillatory flow. Keulegan & Carpenter[79] called it the “period parameter”. This number is defined as:

$$KC = \frac{U'T_m}{L} = \frac{2\pi A_o}{L} \quad (2.10)$$

Where the  $T_m$  is the oscillation time period,  $U'$  is the flow oscillation velocity (or  $A_o$  amplitude of oscillation, in case of an oscillating object) and  $L$  is the characteristic length. This number is related to the oscillation frequency of an unsteady flow around an object.

5. Frequency parameter ( $\beta$ ): It is the ratio of the Reynolds number and the Keulegan-Carpenter number, given by

$$\beta = \frac{Re}{KC} = \frac{fL^2}{\nu} \quad (2.11)$$

6. Added Mass ( $m_a$ ): Whenever a body is oscillating in a fluid, some amount of the fluid surrounding it is forced into oscillation with the body. In case of very light fluids like air, the effect can be ignored. In case of denser fluids like water, the mass of the fluid surrounding the cylinder can cause significant changes in the properties. In case of cylinders at low  $KC$  number, added mass is given by:

$$m_{added} = \rho_f \frac{\pi}{4} D^2 \quad (2.12)$$

7. Damping Ratio ( $\zeta$ ): It is the ratio of the structural damping of the model and the critical damping.

$$\zeta = \frac{c}{c_o} \quad (2.13)$$

where critical damping for simple spring mass damper system is given by  $c_o = 2\sqrt{km}$ .

### 2.2.1 Rigid cylinder with 1 degree of freedom: Motion transverse to the fluid flow

The most basic, and comprehensively studied case of VIV is the case where a rigid cylinder moves in cross-flow  $y$  direction only. It is the fundamental case that isolates the effect of hydrodynamic forces induced by the shedding of vortices, and dynamics of the cylinder-wake system. When a cylinder is immersed in the flow, periodic shedding of vortices are observed that result in induced forces on the cylinder, resulting in the oscillatory motion of the cylinder. As the flow velocity is increased, the shedding frequency increases and a condition reaches where the frequency of vortex shedding ( $f_v$ ) is close enough to the natural frequency of the body ( $f_n$ ), and the system approaches

the state of resonance, and a dramatic increase in the amplitude of oscillation is observed.

### 2.2.1.1 Equations for 1 degree of freedom

In order to understand the phenomena we start with the very basic equation of motion of a body undergoing oscillatory motion:

$$F = m\ddot{y} + c\dot{y} + ky \quad (2.14)$$

Where  $F$  is the applied force,  $m$  is the mass of the structure,  $c$  is the structural damping and  $k$  is the spring constant. Assuming that for large amplitude vortex induced vibrations in steady state, the induced force ( $F(t)$ ) and the motion of the body ( $y(t)$ ) oscillate at a common frequency ( $f$ ), the force and the body response are given by:

$$F(t) = \hat{F}\sin(2\pi ft + \phi) \quad (2.15)$$

$$y(t) = \hat{y}\sin(2\pi ft) \quad (2.16)$$

The term  $\phi$  denoting the phase difference between the induced force and the motion of the body. The force coefficient from equation 2.15 can be written as:

$$C_y = (\hat{C}_y \cos\phi)\sin(2\pi ft) + (\hat{C}_y \sin\phi)\cos(2\pi ft) \quad (2.17)$$

substituting the values of  $c$  from equation 2.13 and  $k$  from the definition of natural frequency,  $\dot{y}$  and  $\ddot{y}$  obtained from differentiating equation 2.16 and  $C_y$  from equation 2.17 in equation 2.14, we obtain:

$$\begin{aligned} & -4m\pi^2 f^2 \hat{y}\sin(2\pi ft) + 8m\pi^2 f_n \zeta f \hat{y}\cos(2\pi ft) + 4m\pi^2 f_n^2 \hat{y}\sin(2\pi ft) \\ & = \frac{1}{2}\rho U_\infty^2 D \hat{C}_y (\cos\phi \sin(2\pi ft) + \sin\phi \cos(2\pi ft)) \end{aligned} \quad (2.18)$$

Here we can equate the sine terms separately, thus getting:

$$4\pi^2 m \hat{y} f^2 - 4\pi^2 m \hat{y} f_n^2 = -\frac{1}{2}\rho U_\infty^2 D \hat{C}_y \cos(\phi)$$

or by rearranging the variables:

$$\begin{aligned} \frac{f}{f_n} &= \left[ 1 - \frac{U_\infty^2 D \hat{C}_y \cos \phi}{4\pi^2 f_n^2 m \hat{y}} \right]^{\frac{1}{2}} \\ &= \left[ 1 - \frac{1}{4\pi^2} \hat{C}_y \cos \phi \left( \frac{U_\infty}{f_n D} \right)^2 \frac{\rho D^2 D}{2m \hat{y}} \right]^{\frac{1}{2}} \\ f^* &= \left[ 1 - \frac{1}{2\pi^3} \hat{C}_y \cos \phi (U^*)^2 \frac{1}{m^* \hat{y}} \right]^{\frac{1}{2}} \end{aligned} \quad (2.19)$$

And equating the cosine terms, we get:

$$8m\pi^2 f_n \zeta f \hat{y} = \frac{1}{2} \rho U_\infty^2 D \hat{C}_y \sin \phi$$

or after rearranging the variables:

$$\frac{\hat{y}}{D} = \frac{1}{4\pi^3} \hat{C}_y \sin \phi (U^*)^2 \frac{1}{m^* \zeta} \frac{1}{f^*} \quad (2.20)$$

Both equations 2.19 and 2.20 can be found in reviews like Bearman[9, 10], Gabbai and Benaroya[51] and Sarpkaya[135]. Others like Khalak & Williamson[80], and Williamson & Govardhan[169, 170] use a slightly different form of the relations as:

$$f^* = \sqrt{\frac{m^* + C_A}{m^* + C_{EA}}} \quad (2.21)$$

$$A^* = \frac{1}{4\pi^3} \frac{\hat{C}_y \sin \phi}{(m^* + C_A) \zeta} \left( \frac{U^*}{f^*} \right)^2 f^* \quad (2.22)$$

Where  $C_A$  is the potential added mass coefficient, and  $C_{EA}$  is an “effective” added mass coefficient, that will be discussed in section 2.2.1.2.

To reach these equations, it is assumed that the force and dislocations on the oscillating cylinder are occurring at the same frequency. Schewe[136] describes that for unforced oscillations the lift, drag, and amplitude time series resemble randomly modulated sinusoidal functions in both frequency and amplitude, and the instantaneous force on a cylinder is a result of a cooperative behaviour of these functions. The assumption of oscillation and the transverse force to be at the same frequency is, thus, an unrealistic one even in the lock-in range, where the shedding frequency matches the structural vibrations for free oscillating cylinder. For experiments with forced

vibrations, these assumptions can be fulfilled by controlling the amplitude and frequency of oscillation. Equations 2.21 and 2.22 show that the frequency is strongly dependent on the effective added mass coefficient, and the amplitude of oscillation is proportional to the transverse force that is in phase with the body velocity ( $\hat{C}_y \cos \phi$ ), and inversely proportional to the mass damping parameter ( $(m^* + C_A)\zeta$ ). For small mass and damping the phase angle ( $\phi$ ) has significant effect on the amplitude of oscillation. We will look at these parameters and their influence in following sections after a brief introduction to some key concepts.

### 2.2.1.2 Added mass, virtual mass, potential and effective added mass

Sarpkaya[135] states, rightly so, that added mass is the best known, least understood and most confused characteristic of fluid dynamics. Added mass is defined as: “Whenever acceleration is imposed on a fluid flow, either by acceleration of a body or by acceleration externally imposed on the fluid, additional fluid forces will act on the surface in contact with the fluid”[28]. It is to be noted that the definition of added mass does not have mass in it, rather it is the forces, which are translated into mass as per Newton’s equation  $F = m \times a$ . The simplest explanation for added mass is that it is that it is the necessary work needed to change the kinetic energy associated with the motion of the surrounding fluid. Supposing that an incompressible fluid of volume  $V$  is moving with velocity  $u_i$ , where  $i = 1, 2, 3$  are the three Cartesian components of velocity, the kinetic energy  $T$  is given by

$$T = \frac{\rho}{2} \int_v (u_1^2 + u_2^2 + u_3^2) dV \quad (2.23)$$

or

$$T = \frac{\rho}{2} I U^2 \quad \text{where } I = \int_v \frac{u_i}{U} \frac{u_i}{U} dV$$

The integral  $I$  is a simple invariant number. This case is valid for potential flow and very low Reynolds numbers only. As the flow is accelerated, the change in the kinetic energy would be  $dT/dt$ . The force, thus, would be given by:

$$F = -\frac{1}{U} \frac{dT}{dt} = -\rho I \frac{dU}{dt} \quad (2.24)$$

The mass of fluid  $\rho I$  is visualized as the “added mass”.

Assuming a cylinder of radius  $R$  moving with a time-varying velocity  $U(t)$ , as shown in figure 2.8, using Laplace equation ( $\nabla^2 \varphi = 0$ ) and considering the relative velocity normal to the surface of the body is zero ( $(U_r)_{r=R} = U \cos \vartheta$ ), the velocity potential is



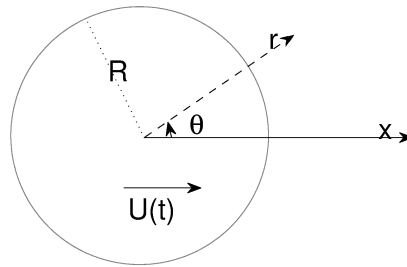


Fig. 2.8 Cylinder of radius  $R$ , moving through fluid with velocity  $U(t)$

given by:

$$\varphi_{cylinder} = -\frac{UR^2}{r} \cos\vartheta$$

The resulting fluid velocities in cylindrical coordinate system,  $u_r$  and  $u_\vartheta$ , are given as:

$$u_r = \frac{\partial\varphi}{\partial r} \quad ; \quad u_\vartheta = \frac{1}{r} \frac{\partial\varphi}{\partial\vartheta}$$

the value of integral,  $I$ , could be evaluated as:

$$I = \int_R^\infty \int_0^{2\pi} \left( \frac{1}{U} \frac{\partial\varphi}{\partial r} \right)^2 + \left( \frac{1}{U_r} \frac{\partial\varphi}{\partial\vartheta} \right)^2 r d\vartheta dr = \pi R^2$$

Consequently, the added mass for a cylinder  $m_{added}$ , which is equivalent of  $-\rho I$  is given by:

$$m_{added} = \rho\pi R^2 \tag{2.25}$$

The potential added mass coefficient ( $C_A$ ) is the non-dimensional added mass parameter from equation 2.25. For circular cylinders, the value of  $C_A$  is equal to 1.0. The added mass can be significantly different from the simplified equation described earlier, depending upon the type of flow, drift, proximity to surfaces or walls etc. For general reference, equation 2.25 is valid for circular cylinders at low Keulegan-Carpenter numbers ( $KC = VT/D$ ) [143]. However Sarpkaya, quoting Stokes, also adds that “in unsteady flows, neither is the drag equal to it’s steady state value, nor is the added mass equal to it’s inviscid flow value, both are affected by viscosity and acceleration”[134, 135].

The cycle averaged added mass coefficient,  $C_a$ , represents the permanently displaced fluid mass for an oscillating cylinder. It is given by  $C_a (= \Delta m / \rho V_b)$  where  $V_b$  is a reference volume.

$$C_a / m^* = (\Delta m / m) = C_a \frac{\rho_f}{\rho_s} \quad (2.26)$$

The normalized virtual mass is given by

$$\frac{m + \Delta m}{m} = \left(1 + \frac{C_a}{m^*}\right) \quad (2.27)$$

With high mass ratio cylinders the effect of change in added mass is not very significant, however for low mass ratio cylinders the cycle averaged added mass coefficient may approach  $-1$ , and the normalized virtual mass may reach zero. The negative value of added mass can be found in the literature [79, 154, 161], and it occurs mostly in the lock-in range, when the phase angle and amplitudes are relatively large.

The effective added mass coefficient, as defined by Williamson & Govardhan[169],  $C_{EA}$  is the added mass coefficient that includes effects due to the total transverse fluid force that is in-phase with the body acceleration:

$$C_{EA} = \frac{1}{2\pi^3} \frac{\hat{C}_y \cos\phi}{A^*} \left(\frac{U^*}{f^*}\right)^2 \quad (2.28)$$

The definition of effective mass coefficient ( $C_{EA}$ ) has, thus, a compensation for the frequency of the oscillation. Sarpkaya[135] determined a posteriori actual added mass by using a compensation factor  $f_{vac}/f_{com}$ , where  $f_{vac}$  is the structural frequency determined in vacuum, and  $f_{com}$  is the actual frequency of oscillation that is either determined experimentally or derived from numerical solutions, where the normalized virtual mass is given by:

$$\Delta m = m \left( (f_{vac}/f_{com})^2 - 1 \right) \quad (2.29)$$

and the added mass coefficient is:

$$C_a = m^* \left( (f_{vac}/f_{com})^2 - 1 \right) \quad (2.30)$$

Thereby, the cycle average value of virtual mass is zero when  $f_{com} = f_{vac}$ . When the oscillation frequency is higher than the natural frequency, the added mass coefficient becomes negative ( $C_a < 0$ ), which implies that the fluid mass displaced during the

acceleration period of the cylinder motion is lesser than the displaced mass during the deceleration.

Both equations for effective added mass, as well as added mass with frequency ratio give rise to the suggestion that a low mass cylinder will have a the lock-in regime encompassing a wider range of reduced velocity based on the natural frequency. In case of using the true natural frequency, the lock-in regime, however, should have similar width for cylinders with different mass ratios. This was noted by Vikestad et al[161], as well as Khalak & Williamson[80] and Govardhan & Williamson[59], and will be described in section 2.2.1.6, where the amplitude response branches are discussed.

### 2.2.1.3 Effective stiffness, the concept and its formulation

In order to explore the concept of effective stiffness, we start by going back to the basic equation of motion 2.14

$$m\ddot{y} + c\dot{y} + ky = \frac{1}{2}C_y(t)\rho_f U_\infty^2 DL \quad (2.31)$$

The non-dimensional temporal and spatial components are given as:

$$Y = \frac{y}{D}, \quad t^* = t \frac{U_\infty}{D}, \quad \frac{\partial}{\partial t} = \left(\frac{\partial t^*}{\partial t}\right) \left(\frac{\partial}{\partial t^*}\right) = \frac{U_\infty}{D} \frac{\partial}{\partial t^*} \quad (2.32)$$

Putting the values from equation 2.32 into 2.31, we get

$$\frac{m/L}{\frac{1}{2}D^2\rho_f} \ddot{Y} + \frac{c/L}{\frac{1}{2}\rho_f U_\infty D} \dot{Y} + \frac{k/L}{\frac{1}{2}\rho_f U_\infty^2} Y = C_y(t) \quad (2.33)$$

Defining the non-dimensional parameters as:

$$m^* = \frac{m/L}{\frac{1}{2}D^2\rho_f}, \quad c^* = \frac{c/L}{\frac{1}{2}\rho_f U_\infty D}, \quad k^* = \frac{k/L}{\frac{1}{2}\rho_f U_\infty^2} \quad (2.34)$$

we can rewrite equation 2.31 as

$$m^* \ddot{Y}^* + c^* \dot{Y}^* + k^* Y^* = C_y(t) \quad (2.35)$$

In case of a pure sinusoidal oscillation, again as discussed earlier, we consider the following identities:

$$Y(t^*) = A^* \sin(\omega^* t^*), \quad C_y(t^*) = \hat{C}_y \sin(\omega^* t^* + \phi)$$

Substituting the values in equation 2.35

$$-\omega^{*2}m^*A^*\sin(\omega^*t^*) + c^*\omega^*A^*\cos(\omega^*t^*) + k^*A^*\sin(\omega^*t^*) = \hat{C}_y\sin(\omega^*t^*)\cos\phi + \hat{C}_y\cos(\omega^*t^*)\sin\phi \quad (2.36)$$

matching the coefficients for  $\sin(\omega^*t^*)$  and  $\cos(\omega^*t^*)$  gives us

$$(-\omega^{*2}m^* + k^*)A^* = \hat{C}_y\cos\phi \quad (2.37)$$

$$c^*\omega^*A^* = \hat{C}_y\sin\phi \quad (2.38)$$

equation 2.37 gives us the effective stiffness. In terms of classical parameters, it is given by:

$$k_{eff}^* = -\omega^{*2}m^* + k^* = \frac{m^*}{U^2} \left( 1 - \left( \frac{f}{f_n} \right)^2 \right) \quad (2.39)$$

In case of no damping, the coefficient  $C_y$  can be given by  $\hat{C}_y = k_{eff}^*A^*$ . Whereas in case of damping  $b^*$ , we get:

$$\hat{C}_y = \sqrt{(k_{eff}^*)^2 + (c^*\omega^*)^2}A^* \quad (2.40)$$

$$\tan\phi = c^*\omega^*/k_{eff}^* \quad (2.41)$$

The concept was initially used by Gharib[56], it was further discussed by Klamo[84, 85] who used it on an extensive amount of experimental data, to collapse the amplitude response profile. The response behaviour was observed to begin and end at approximately the same effective stiffness values. He found that for a majority of cases the maximum amplitude,  $A_{max}^*$  occurred at  $k_{eff}^*|_{A_{max}^*} \approx 2.5$

#### 2.2.1.4 Phase angle ( $\phi$ ) by force decomposition

Khalak & Williamson[80] stated a method of determining the phase angle and force coefficient by using the equations 2.21 and 2.22 in the form:

$$\begin{aligned} \hat{C}_y\sin\phi &= \frac{4\pi^3A^*(m^* + C_A)\zeta}{\left(\frac{U^*}{f^*}\right)^2 f^*} \\ \hat{C}_y\cos\phi &= \frac{2\pi^3A^*}{\left(\frac{U^*}{f^*}\right)^2} C_{EA} \end{aligned} \quad (2.42)$$

With all other variables known, or determined experimentally, the two unknowns can be determined as:

$$\begin{aligned}\hat{C}_y &= \sqrt{(\hat{C}_y \sin \phi)^2 + (\hat{C}_y \cos \phi)^2} \\ \phi &= \tan^{-1} \left( \frac{\hat{C}_y \sin \phi}{\hat{C}_y \cos \phi} \right)\end{aligned}\quad (2.43)$$

Sarpkaya[135] used a slightly different approach based on Morison equation (Morison *et al.* [107]). For a sinusoidally oscillating body, a certain quantity of fluid that is attached to the body is forced into oscillation with the body itself (see definition of added mass above). For such motion, the hydrodynamic force exerted on the body is a linear sum of the drag force that depends on the velocity, and an inertial force because of added mass, which depends on the acceleration. The net force, as a combination of these two forces, is presented by Morison *et al.* [107] and Keulegan & Carpenter[79] as:

$$F(t) = \frac{1}{4}\pi D^2 \rho C_a \dot{U} + \frac{1}{2}\rho D C_D |U| U \quad (2.44)$$

Sarpkaya[133, 135] used the definition of  $U$  and  $y$  as a function of frequency as:

$$\begin{aligned}U &= -U_m \cos(2\pi ft) \\ y &= -A \sin(2\pi ft)\end{aligned}\quad (2.45)$$

in the Morison equation 2.44, to get

$$\begin{aligned}C_L &= C_{mh} \sin(2\pi ft) - C_{dh} \cos(2\pi ft) \\ \text{or} \\ C_L &= -C_a \sin(2\pi ft) + C_D \cos(2\pi ft)\end{aligned}\quad (2.46)$$

Where  $C_{mh}$  and  $C_{dh}$  are the Fourier averages over 100 or more cycles. Equation 2.46 is obtained by using  $y_r = (A/D)\sin(2\pi ft)$  and  $U(t)/U_m = \cos(2\pi ft)$ . Where  $C_a$  is the added mass coefficient, and needs to be replaced by  $1 + C_a$  to cater for the effects of imposed pressure gradient in case the body is at rest and the fluid is oscillating about it. By equating the sine and cosine terms of equation 2.46 and equation 2.17, we obtain:

$$\begin{aligned}C_a &= -C_L \cos \phi \\ C_d &= C_L \sin \phi\end{aligned}\quad (2.47)$$

Giving us

$$\phi = \tan^{-1} \left( -\frac{C_d}{C_a} \right) = \frac{\pi}{2} - \tan^{-1} \left( -\frac{C_a}{C_d} \right) \quad (2.48)$$

Bishop & Hassan[19] found that as  $f^*$  increased through unity, the lift force indicated a sharp increase in amplitude, and the phase  $\phi$  jumped by about  $180^\circ$ . Similar results were documented by many researchers including Sarpkaya[133], Gopalkrishnan[58] and Stabuli[141], who noted during the forced vibrations experiments that in the synchronization range the drag coefficient gradually increased from negative to positive values, and the added mass coefficient decreased, resulting in a change in the phase  $\phi$  at the lock-in. This increase in the transverse force coefficient results in excitation of the cylinder, and the dissipation through the mechanical damping is overcome by the positive transfer of energy from the fluid to the body. Figure 2.9 shows data from these researchers, in addition to data from Mercier[101] and Carberry[35]. The change of phase  $\phi$  as the cylinder oscillations frequency  $f$  approaches and crosses over the natural frequency  $f_n$  is evident in this figure.

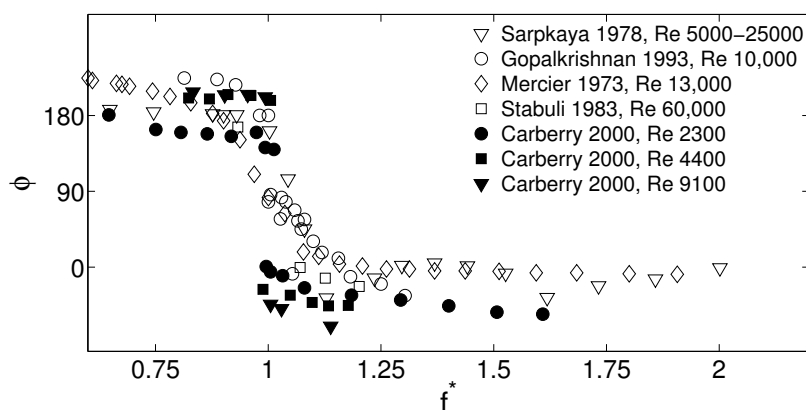


Fig. 2.9 Phase angle  $\phi$  vs reduced frequency  $f^*$ , from Sarpkaya[135]

Sarpkaya[135] also noticed, as per originally stated by Krishnamoorthy *et al.* [88] that the phase change is not sudden or abrupt, rather it happens over a transition period comprising of several cycles of cylinder oscillation, during which both in-phase and out-of-phase shedding occurs.

In case of self-oscillating cylinders, this change of phase difference  $\phi$  is observed when the reduced velocity approaches the lock-in condition. The results of the six tests carried out by Hover *et al.* [62] are shown in figure 2.10

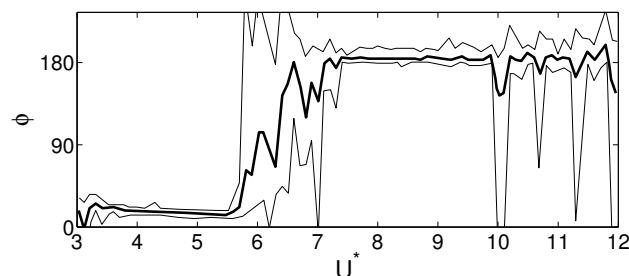


Fig. 2.10 Phase angle  $\phi$  vs reduced velocity  $U^*$ , from Hover *et al.* [62]. Thick line indicates the mean, thin lines show maximum and minimum from six sets of tests

### 2.2.1.5 A look at the wake: phase jump, timing and modes of vortex shedding

The jump in the phase,  $\phi$  has been mentioned repeatedly in the context of the wake of oscillating body. This change in phase, of about  $\pi$ , occurs when the oscillation frequency matches the natural frequency of the structure in the medium. This phenomena has been mentioned by many researchers. Lu & Dalton [96] showed the instantaneous streamlines and the vorticity contours at different frequency ratios, which explained the phase jump as shown in figure 2.11

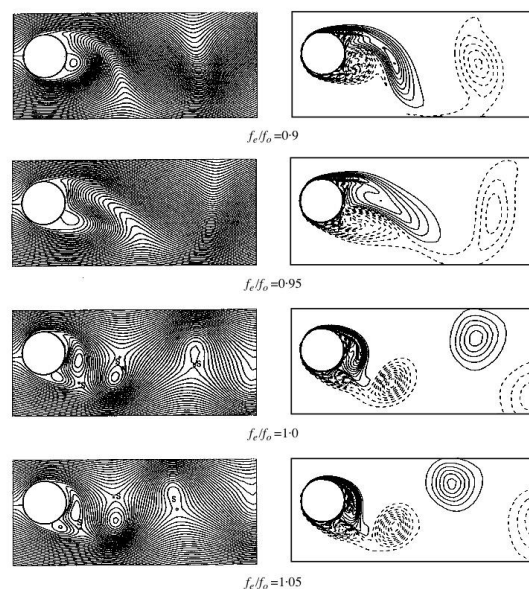


Fig. 2.11 Instantaneous streamlines (left) and vorticity maps (right) for  $A/D=0.4$ ,  $Re=1000$ , indicating increasing excitation frequency from top to bottom. Solid lines indicate negative values and dashed lines indicate positive values in vorticity maps. Cylinder excursion is at it's extreme upper position in all images. From Lu & Dalton [96]

When the frequency of oscillation is below the natural frequency the vortices are shed from one side of the cylinder when the cylinder reaches the maximum displacement on the opposite side of oscillation. As the system reaches the state of resonance, the phase jump is observed and the vortex is shed when the cylinder reaches the maximum displacement on the same side of oscillation.

Ongoren & Rockwell [116] carried out numerous force oscillation tests on cylinders with various cross-section geometries, and found two forms of synchronization. When the excitation frequency was half of the natural frequency, the vortex shedding was found to alternatively phase lock as in-phase and out-of-phase with the cylinder's motion. As the frequency matched the natural frequency, the classic synchronization was observed with alternate vortices shed at corresponding maximum displacements. While both the regimes resulted in classic Kármán type shedding, the relationship between the phase of shedding and the frequency of oscillation is rather complicated. One point they highlighted, however, is that the switching of phase was always associated with attainment of a minimum formation length. This phenomena can also be seen in the figure 2.11. These results confirm the findings by Zdarvkovich[178] that as the frequency of excitation over the Strouhal frequency increases, the concentration of vorticity moves closer to the cylinder until it reaches a limit. Upon reaching that limit, the formation switches to the opposite side of the cylinder. The contraction of the formation region, prior to the phase switching, is attributed to the interaction of the shear layer with the region of base vorticity.

The vortex shedding for a cylinder oscillating in cross-flow direction shows variations from the standard Von Kármán vortex street in certain cases. Brika & Laneville[29, 30] were the first to show the presence of a 2P vortex mode by carrying out VIV wake analysis of a freely vibrating cable in the wind tunnel, when the amplitude of oscillation exceeded  $0.5D$ . Williamson & Roshko[172] presented a map of regimes that show the various types of shedding observed in the wake for oscillating cylinders, corresponding to the amplitude of oscillation and wavelength of the oscillation ( $\lambda/D = U_\infty/f_e D$ ), as shown in figure 2.12:

The 2S mode refers to the vortex pattern of a typical Von Kármán vortex street, where two oppositely signed vortices are shed per cycle. In 2P mode of shedding, two pairs of opposite signed vortices are shed per half cycle. In P+S mode, which is a combination of the previous two regimes, where a single vortex is formed along with a pair of vortices from the opposing side, for each cycle. The region of coalescence indicates a region where the near wake vortices merge / coalesce together to form larger scale structures.



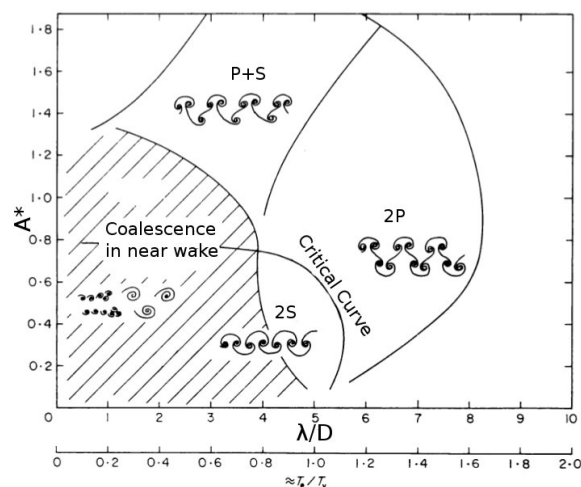


Fig. 2.12 Map of regimes for vortex wake modes, showing various vortex modes corresponding to the oscillation amplitude, and wavelength of cylinder motion. From Williamson & Roshko[172]

Sarpkaya[135], while discussing the frequency corrected added mass as shown in equation 2.30, states that “For cylinders with relatively large  $m^*$ ,  $f_{com} \sim f_{vac}$ , the shedding mode changes from a Kármán-type of vortex shedding (two single vortices per cycle) to two pairs of vortices per cycle, however for small  $m^*$ , the mode of vortex shedding remains essentially the same”.

Williamson[169] states that for low  $m^*\zeta$  systems, there are two jumps in the phase  $\phi$  with increasing  $U^*$ . The first jump is when the oscillation frequency matches the structure’s natural frequency in the medium, where the response branch goes from initial to upper branch. The next jump is when the oscillation frequency matches the structures natural frequency in vacuum, where the response branch moves to the lower branch. The analysis is based on dividing the force component of the equation 2.14 as the total force  $F_{Total}$ , which can be divided into the potential force  $F_{Potential}$  (due to the potential added mass), and vortex force  $F_{Vortex}$  (due only to all the dynamics of the shed vorticity).

Lately Williamson & Jauvtis[171] has shown presence of a triplet type vortex shedding where three vortices are shed every half cycle. This was a result of a presence of super-upper branch, where the amplitude of oscillation  $A_{max}^*/D$  was greater than 1.5.

### 2.2.1.6 Amplitude Response Branches

As described earlier, the amplitude of oscillation in the lock-in regime is inversely proportional to the mass-damping parameter  $((m^* + C_A)\zeta)$ . Some very important experimental and numerical investigations have been carried out in order to determine the relationship between various parameters and the amplitude of oscillation.

One of the pioneers in the research of amplitude and phase analysis of VIV is Feng[48], who mounted a high mass ratio ( $m^* \sim 250$ ) cylinder in flexible mounts that allowed the cylinder to oscillate in cross-flow direction only, in a wind tunnel and measured the amplitudes of oscillation, frequency and phase difference. He carried out his tests by slowly increasing the wind tunnel velocity and measuring the responses, and repeated the tests by slowly decreasing the velocity. He noticed that while reduced velocity reached a critical value of  $U^* \sim 4$ , the amplitude of oscillation started increasing and reached a maximum amplitude at the resonant value of reduced velocity,  $U^* = 2\pi$  for cylinders with very low mass damping. Further increase in  $U^*$  resulted in progressive decrease in the amplitude of oscillation, that continued till  $U^* \sim 8.5$ . The response with ramping down of the velocity did not follow the same trend as ramping up, and followed a different branch. The incrementing velocity branch achieved much higher amplitudes than the decrementing velocity one, and the jump from initial branch to the lower branch with increasing  $U^*$  was noticeably delayed as compared to the jump from the lower branch to the initial branch with reducing  $U^*$ , thus these two branches were hysteretic in nature.

The vortex shedding frequency also showed an interesting trend. In the range of  $5 < U^* < 7$ , the natural frequency of the cylinder took control of the shedding frequency, whereas outside this range the shedding frequency closely followed the Strouhal relationship. The results of one of Feng's tests (with low damping) are shown in figure 2.13.

Williamson & Roshko[172] carried out extensive mapping of the vortex shedding modes. They observed a change in the mode of vortex shedding from  $2S$ , where two single vortices are shed at every oscillation cycle, to  $2P$ , where a pair of vortex is shed from each side at every cycle as the amplitude of oscillation was increased beyond certain critical values. They devised a response map based on the amplitude of oscillation and the pattern of vortex shedding that was observed in that regime. Khalak & Williamson[80] carried out some very interesting tests, where they determined the amplitude response of cylinders with different mass ratios, while keeping the  $m^*\zeta$  constant. The results of some of these tests, in the Williamson-Roshko map, is shown in figure 2.14.

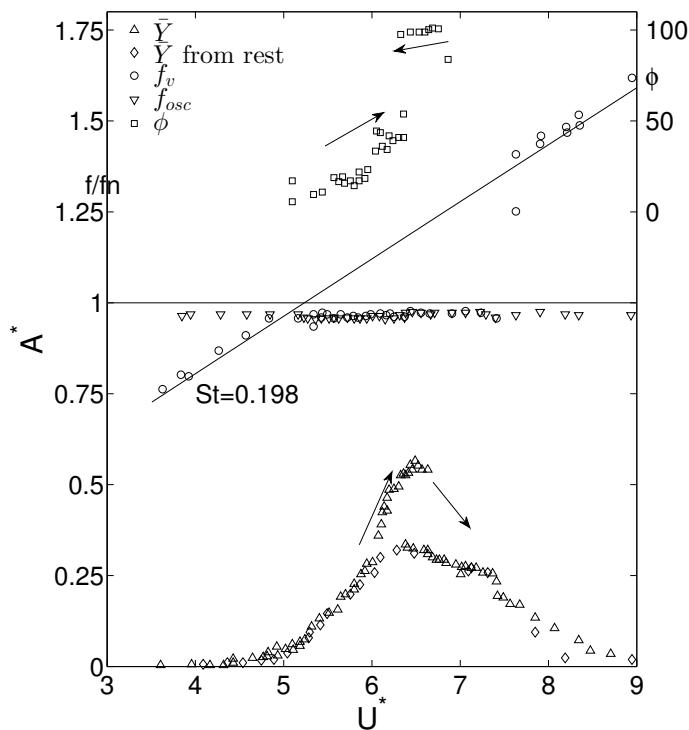


Fig. 2.13 Wake characteristic of an elastically mounted cylinder freely vibrating in air ( $m^* = 248$ ,  $\zeta = 0.00103$  and  $m^*\zeta = 0.255$ ).  $Re$  from  $10^4$  to  $5 \cdot 10^4$  (Feng [48])

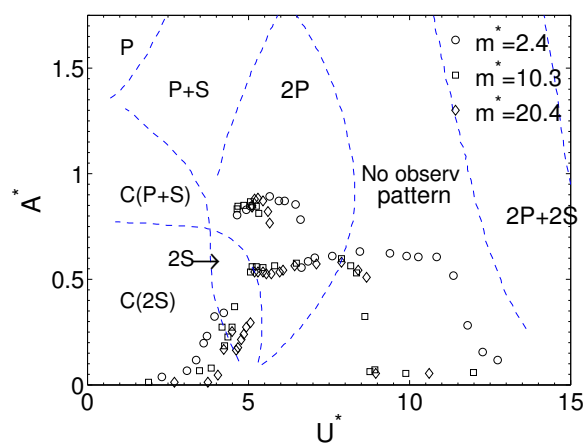


Fig. 2.14 Non-dimensional amplitude response map for constant  $m^*\zeta$ , but for different values of  $m^*$ , from Khalak & Williamson[80]

Khalak & Williamson[80] stated that the peak amplitude of the response is dependent on the mass-damping ( $m^*\zeta$ ), whereas the width of the lock-in region is dependent primarily on the mass ratio  $m^*$ . They compared their results to the data by Feng[48] and justified that the significantly lower amplitude shown by Feng was a consequence of the high  $m^*\zeta$ . A further collapse for different  $m^*$  was observed by Khalak & Williamson[80] as well as Govardhan & Williamson[59] when they used true normalized velocity ( $U^*/f^*$ ), as shown in figure 2.15

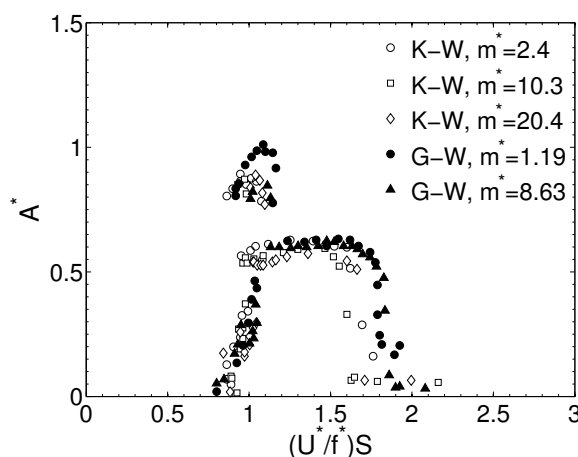


Fig. 2.15 Non-dimensional amplitude response map collapse by using true normalized velocity. Data from Khalak & Williamson[80] marked K-W, and Govardhan & Williamson[59] marked G-W.

Different researchers have used the combined parameter of mass-damping to establish a criteria that would reasonably collapse the peak amplitude data. Vickery & Watkins[160] (as quoted in Blake[22]) used the amplitude response results from the experiments carried out with flexible cantilevers and formed the stability parameter  $K_s$ , as shown in equation 2.49. Skop & Griffin[139] introduced the Skop-Griffin parameter, as shown in equation 2.50. Later Skop & Balasubramanian[140] used the Skop-Griffin parameter to show the collapse of peak amplitude data from a significant number of tests in the form of a log-log plot, as shown in figure 2.16

$$K_s = \pi^2 (m^*\zeta) \quad (2.49)$$

$$S_G = 2\pi^3 St^2 (m^*\zeta) \quad (2.50)$$

Sarpkaya replotted the data compiled by Skop & Balasubramanian[140] using linear axes instead of the log-log axis system and showed that the original data had

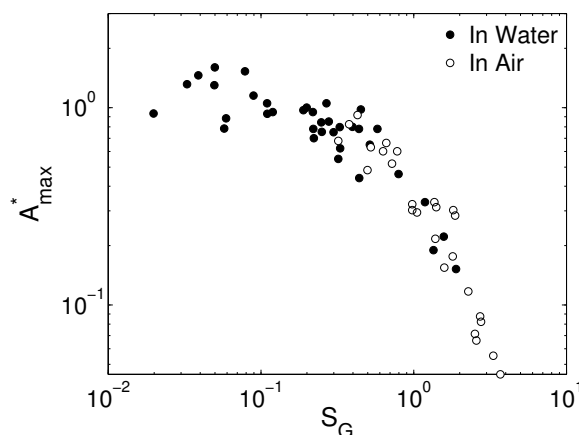


Fig. 2.16 Experimental measurements of the modally normalized maximum amplitudes ( $A_{max}^*$ ) versus the response parameter  $S_G$ , Data from Skop & Balasubramanian[140]

a considerable spread. He devised a curve fit based on mode factor  $\gamma$  as shown in equation 2.51. The resulting plot of  $A_{max}^*/\gamma$  shows a significantly improved collapse of data into one curve. The modally normalized data with, and without the mode factor  $\gamma$  is shown in figure 2.17

$$\left(\frac{A}{D}\right) \frac{1}{\gamma} = 1.12e^{-1.05S_G} = 1.12 \times 0.35^{S_G} \quad (2.51)$$

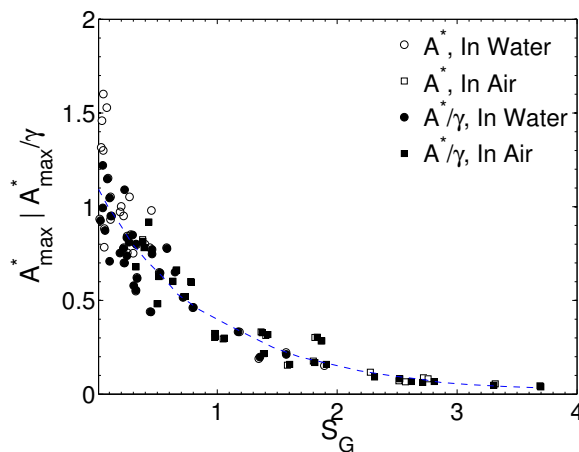


Fig. 2.17 Experimental measurements of the modally normalized maximum amplitudes ( $A_{max}^*$ , shown by hollow symbols), and modally normalized maximum amplitudes corrected by mode factor ( $A_{max}^*/\gamma$ , shown by filled symbols) versus the response parameter  $S_G$ , and the proposed curve-fit from equation 2.51

The value of dimensionless mode factor  $\gamma$  is 1.0 for a rigid cylinder, 1.291 for uniform pivoted rod, 1.155 for taut string, and 1.305 for a cantilever beam.

Some publications show more complex interaction between the cylinder wake and the cylinder undergoing cross-flow oscillation. A special case is presented by Durgin *et al.* [46]. They reported maxima at reduced velocities of 5, and 16. They designated the primary maxima as the “fundamental mode”, which was due to the normal vortex street excitation. The second resonance that they designated as the “lower mode”, occurred when the natural frequency was one-third of the normal vortex shedding frequency. The phenomena was later explored by Dahl *et al.*[41] for cylinders oscillating in two degrees of freedom, as explained in section 2.2.3.

### 2.2.2 Rigid cylinder with 1 degree of freedom: Motion in-line with the fluid flow

The case of cylinder restricted to move only in the in-line direction has seen significantly lesser attention as compared to the cross-flow oscillation, as the practical implementation of pure in-line oscillation, as well as its applicability to the real life cases is significantly limited. King *et al.* [81] carried out experiments on cantilever structures undergoing in-line oscillation and determined some similarities with the cross-flow model described earlier, where the low mass-damping resulted in large amplitudes of oscillation. Okijama *et al.* [108] carried out extensive tests in water tunnel for both cantilever configuration and elastically mounted rigid cylinders, while varying the mass-damping parameter in order to determine the value where in-line oscillation is suppressed. A review of in-line oscillation modes of various kinds of cylinders was carried out by Naudascher[109]. He observed oscillations in the in-line direction when the reduced velocity was close to  $1/2S$ .

Ongoren & Rockwell[116] state that there are two synchronization modes for cylinders oscillating in in-line direction only. The first synchronization occurs when the oscillation frequency is half of the natural vortex shedding frequency ( $f_{com}/f_o^* = 2$ ), where the wake comprises of a pair of vortices emitted from one side, and a single vortex from the other side, resembling the previously described  $P + S$  shedding mode. They defined it as the *AIII* shedding mode. The second synchronization occurs at ( $f_{com}/f_o^* = 3$ ) in which case the wake comprises of a symmetric pair of vortices. Both synchronization modes are shown in figure 2.18

Sumer & Fredsøe[143] designated the in-line VIV into three types:

- First excitation region ( $1.0 < U^* < 2.3$ ) : This region originates from the symmetric vortex shedding in the reduced velocity range  $1.0 < U^* < 2.3$ . The forces

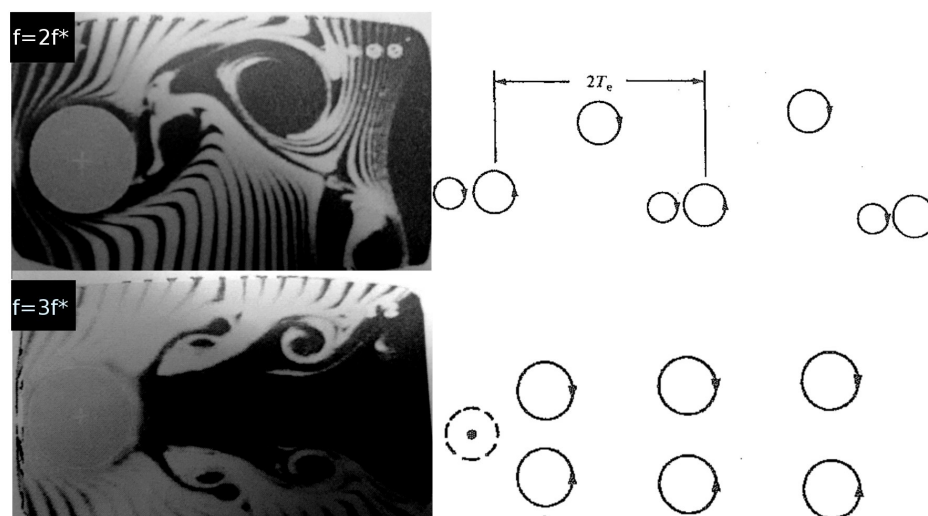


Fig. 2.18 Preferred modes of near wake structures, and corresponding vortex mode sketches for in-line oscillation . Top images show  $f_{com}/f_o^* = 2$ , and bottom shows  $f_{com}/f_o^* = 3$ . From Ongoren & Rockwell[116]

generated in this regime are in-phase with the body velocity. Naudascher[109] and Jauvtis & Williamson[77] found this response range for  $U^*/f^* \simeq 1.5 - 2.5$ .

- Second excitation region ( $2.3 < U^* < 3.8$ ) : This region is signified by alternating vortex shedding, while the oscillation still constitute of pure in-line mode.
- Third excitation region : The third in-line region of oscillation occurs for slender structures, where the cross-flow oscillations have also started. In this case, the in-line oscillations have a significant bearing on the cross-flow oscillation wake, which will be discussed in subsequent section regarding flexible structures.

Cagney & Balabany[32, 33] showed that for most of the first excitation region the vortices are actually shed in an alternating pattern, and at certain reduced velocities, the wake switches between symmetric shedding and alternating shedding in an apparently random manner. It is also noteworthy that the symmetric shedding is inherently unstable keeping in mind the primary stability criteria first discussed by Von Kármán, Cagney & Balabany also found out that the symmetric shed vortices tended to rearrange themselves into an alternating arrangement downstream of the cylinder.

### 2.2.3 Rigid cylinder with 2 degree of freedom

Similar to the case of in-line motion, the cylinders with two degree of freedom do not have as much of literature dedicated to it, primarily because the cross-flow oscillation

results in the simplification of the problem and that the in-line oscillations tend to be an order of magnitude smaller than the cross-flow oscillation.

Sarpkaya[134] carried out experiments on rigid cylinders with XY vibrations using the same natural frequency for both in-line and cross-flow oscillation. He concluded that the amplitude modes displayed, similar to cross-flow oscillation, a broad regime of synchronization. However the synchronization regime did not indicate various response branches as observed in the cross-flow oscillation only. Ongoren & Rockwell[116] carried out similar tests using forced oscillation in in-line direction ( $\alpha = 0^\circ$ ), cross-flow direction ( $\alpha = 90^\circ$ ) and oscillation at an angle ( $\alpha = 45^\circ$  and  $\alpha = 60^\circ$ ). They showed that in cases of oscillation at an angle there is a significant shortening of the formation length. They also showed symmetrical shedding for cylinders oscillating at an angle. They observed symmetrical shedding at  $f_{com}/f_o^* = 3$  for  $\alpha = 0$  and  $45^\circ$ , and at  $f_{com}/f_o^* = 4$  for  $\alpha = 0, 45^\circ$  and  $60^\circ$ .

Jauvtis & Williamson [77] indicated that the response regime of a 2-DOF cylinder was similar to the one observed for cross-flow oscillation only, whereas the freedom to oscillate in the in-line direction did not have a significant effect on the dynamics of the wake. However in their later work, Williamson & Jauvtis[171] they indicated that for cylinder of low mass ratio ( $m^* < 6$ ) there existed a “Super-upper branch”, a response branch that consisted of formation of a triplet of vortices on either side of the cylinder, at every half-cycle of oscillation. This new response branch was attributed to the additional DOF. Sanchis *et al.* [132] indicated that for ( $m^* \leq 5$ ) the 2-DOF cylinder indicated significant increase in the response amplitudes. This behaviour was also noted by Flemming & Williamson[49] for the case of pivoted cylinders.

Jeon & Gharib[78] carried out experiments with circular cylinder in both 1-DOF and 2-DOF oscillations. They used Digital Particle Image Velocimetry (DPIV) and identified vortex structures, and strain gages to determine the forces. They observed the disappearance of the 2P modes of shedding when the cylinder was allowed to oscillate in in-line direction with cross-flow oscillation. The in-line motion influenced the phase  $\phi$ , and resulted in higher circulation in the wake of the cylinder. Recently Cagney & Balabani[34] reported the similarities and differences in the response branches for 1-DOF and 2-DOF oscillation. They said that each case contains two response branches separated by a low amplitude region. They showed negligible transverse motion in the first response branch, with the wake consisting of competing alternate and symmetric vortex shedding. The second response branch showed the figure-of-eight trajectory throughout the lock-in range, and the phase angle between in-line and cross-flow motion decreases linearly with reduced velocity.



Dahl *et al.* [41] indicated presence of stable multi-vortex structures in the wake of a flexibly mounted circular cylinder in cross-flow, where the natural frequencies in the in-line and transverse directions were in a ratio close to 2:1. They showed presence of triplet vortices, as well as quintuplet vortex shedding as observed by PIV images in the wake, at Reynolds number of 10,000. They observed that in the figure 8 trajectory, the cylinder moved upstream just before shedding the vortices, and then downstream while crossing through the center, which brought the cylinder close to the recently shed vortices. The proximity of cylinder to the vortices induced high frequency lift forces on the cylinder, and the lift force indicated a significant third harmonic in the spectrum. The cylinder trajectories overlaid on the third harmonic magnitude of the lift force are shown in figure 2.19

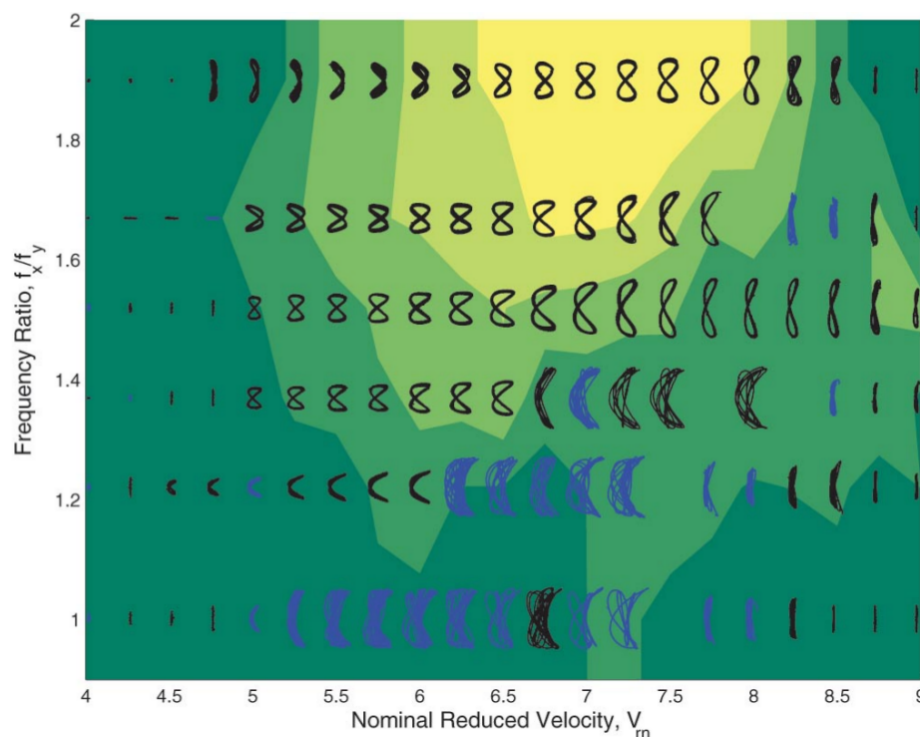


Fig. 2.19 Cylinder trajectories overlaid on the third harmonic magnitude of the lift force. Blue trajectories indicate the cylinder move downstream at the top of figure-eight (C: Clockwise) Black trajectories indicate cylinder moves upstream at the top of figure-eight (CC:Counterclockwise), Flow direction is from left to right. Contours indicate third harmonic lift coefficient magnitude over the total lift coefficient magnitude. Dark green denotes third harmonic less than 25% of the total, lightest yellow indicates third harmonic > 75% of the total. From Dahl *et al.* [41]

## 2.2.4 Rigid Cylinders with spanwise geometric variations

### 2.2.4.1 Tapered cylinders

Hover, Techet & Triantafyllou[64, 148] carried out an extensive analysis of a cylinder that was linearly tapered, with a taper ratio of 4:1, and found a very interesting phenomena. The cylinder wake at regions of larger diameter showed the standard 2S shedding behaviour, whereas at smaller diameter the vortex shedding comprised of a 2P shedding. The two pairs of vortices in the same direction merged along the span of the cylinder to form the 2S mode. The flow visualization and the sketch of what they called the hybrid shedding mode are shown in figure 2.20.

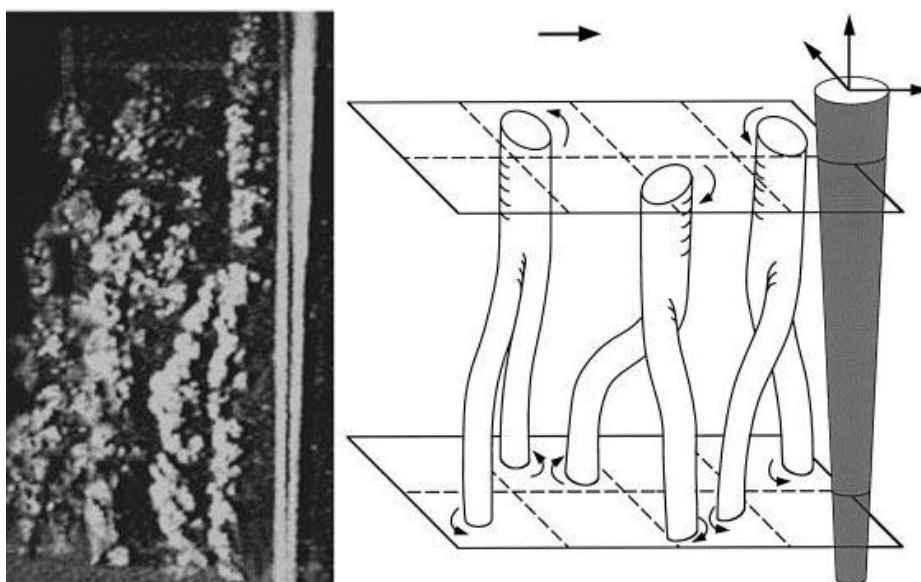


Fig. 2.20 Flow visualization (left) and sketch of 'hybrid' shedding mode topology (right) of vortex reconnection between the '2S' mode at larger diameter, and '2P' mode at the smaller diameter. from Techet et al [148]

Earlier, Piccirillo & Van Atta [121] had documented that for tapered cylinders, the Reynolds number based on the local diameter was the principal criteria for the shedding of the vortices. The shedding was in form of cells, each with a constant frequency. They had noticed vortex splitting and dislocations in the wake, going from the larger diameter towards the smaller diameter.

### 2.2.4.2 Wavy, sinusoidal and curved geometries

The cases of wavy and sinusoidal geometries have seen a surge in interest in the last few years, as there is an added and renewed interest in efforts to reduce drag and

vibrations of cylindrical structures for off-shore applications such as deep sea risers, submarine pipelines and cables. Wavy and sinusoidal geometries are seen as a means to that end. As seen for the tapered cylinders, the vortex shedding forms cells in case of tapered cylinders, it is seen that the wavy cylinders suffer from lesser drag as well as a wider distribution in the power spectrum of shedding frequencies.

Szewczyk & Bearman[146] worked extensively on the effects of imposed three-dimensionality in the shape of the bluff bodies, on the flow. They found that the vortex shedding for a bluff body with a sinusoidal trailing edge occurred in four different modes. The shedding modes, as described by them, are shown in figure 2.21

Bearman & Tombazis[12, 150] extended that work, and documented considerable differences in the wake patterns and the pressure distribution along the span of the cylinder. They found higher base pressures, and longer formation lengths at the valleys, they showed multiple shedding modes and sequence of mode transitions. They observed some similarities with the tapered cylinders where the universal Strouhal number holds, and the shedding at minima (valley) occurs at a higher frequency than the maxima (peaks). Each half wavelength of the cylinder's sinuous shape resulted in two cells of vorticity, corresponding to the base pressure.

Bearman & Owen[11] and Owen *et al.* [117] determined a drag reduction of up to 45% for circular cylinders with a wavy axis, and found out that the shedding could no longer be detected if the wave steepness was increased beyond a certain value.

For the case of varicose cylinders, i.e. cylinders where the diameter sinusoidally varies along the span, some important results have been compiled. Ahmed & Bays-Muchmore[1, 7] measured the surface distribution for cylinders with different axial wavelengths (based on the cylinder diameter). Their results indicated that the separated flow structures near the geometric nodes were distinctly asymmetric, and the sectional drag at the geometric saddles was significantly smaller than that at the geometric nodes. They indicated the presence of trailing stream-wise vortices behind nodal points of separation, resulting in a narrower wake, a rapid wake velocity recovery and suppression of turbulence development. Lam *et al.* [89, 90] carried out DPIV and FV measurements in the wake of a varicose cylinder and found high values of flow in the axial direction, with flow directing from the saddles towards the nodes. as well as indicated significant reduction in drag (up to 20%) depending on the level of obliqueness of the wavy cylinder. The surface streamlines and flow visualization images of the wake at geometric nodes and saddles are shown in figure 2.22

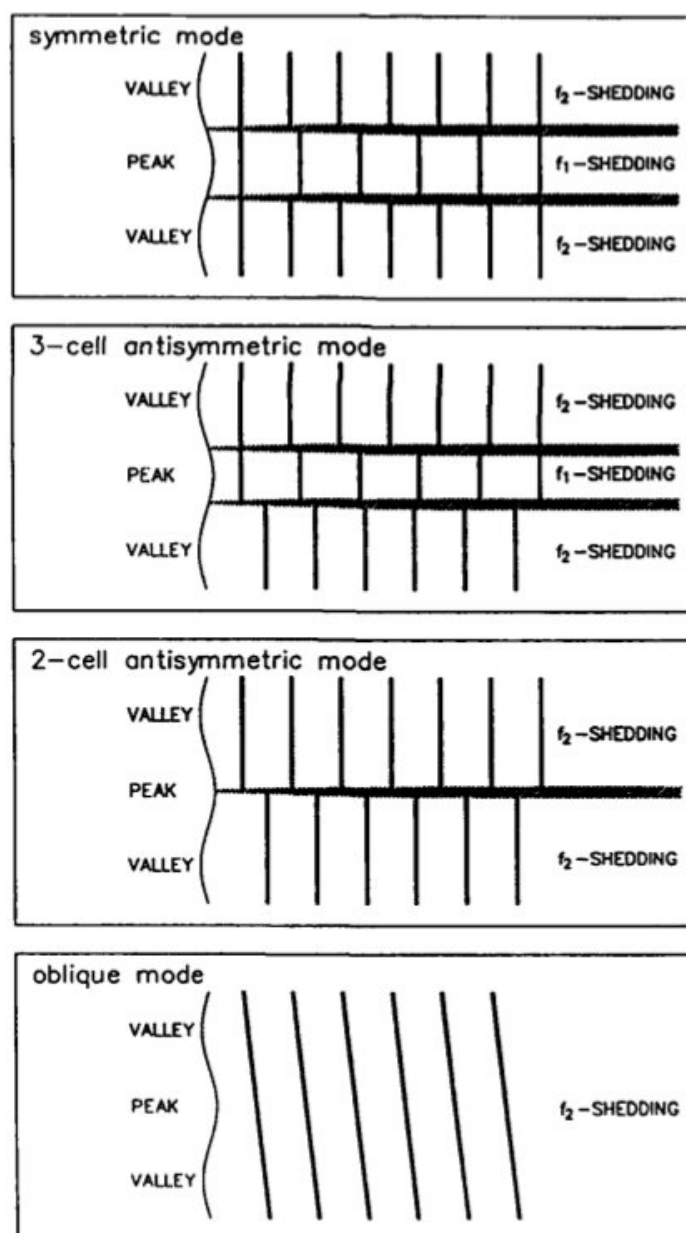


Fig. 2.21 Schematic diagram of different shedding modes of a cylinder with a wavy leading edge and a blunt trailing edge, from Szewczyk & Bearman[146]

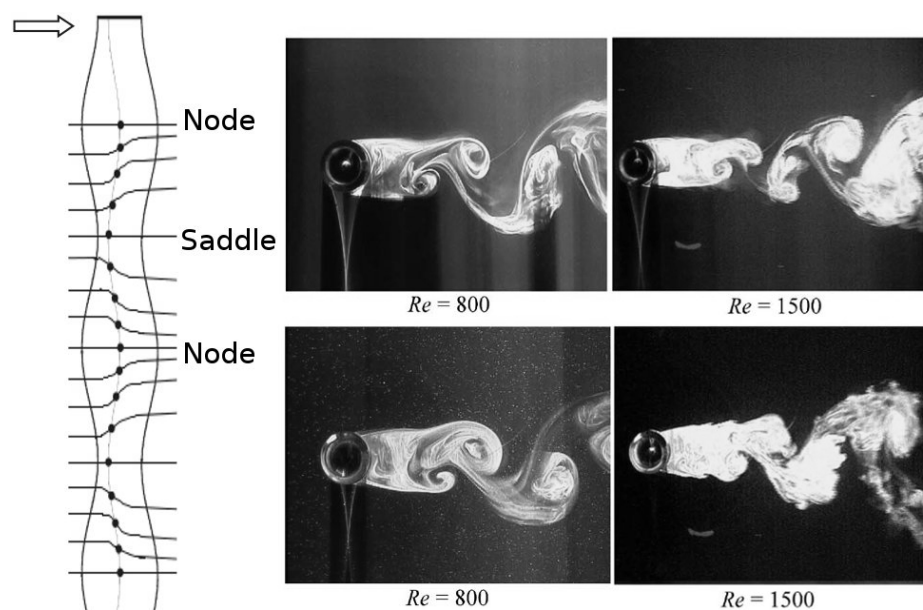


Fig. 2.22 Surface streamlines of 3-D separation (left) and flow visualization images at node (right top) and saddle (right bottom), from Lam *et al.* [89]

### 2.2.4.3 Flexible cantilevers, pivoted and inclined cylinders

Kitagawa *et al.* [82] analysed the vortex induced vibrations on a cantilever cylinder mounted on a leaf spring allowing it to oscillate in transverse direction to the wind (cross-flow). They documented, in addition to the vortex induced vibrations occurring at the lock-in regime, the presence of a response branch at significantly higher reduced velocity. They termed it the “End-cell-induced vibration (ECIV)”. The tip-associated vortex shedding was occurring at a frequency lower than the Kármán vortex shedding, and when the shedding frequency of the tip-associated vortex approached the natural frequency of the model, a significant increase in the amplitude of oscillation was observed.

Fujarra *et al.* [50] carried out experiments with a flexible cantilever undergoing vortex induced vibrations and found out that the response modes were distinctly similar to the response modes seen for an elastically restrained rigid cylinder, despite the fact that the cantilever oscillation amplitude varies along the span. They found two branches in response as opposed to the three branches seen for flexibly mounted cylinders. They also documented the presence of a high-speed mode of large amplitude response, and attributed it to the streamwise-transverse vibration coupling.

Flemming & Williamson[49] used pivoted cylinders with a range of body inertias (equivalent to reduced mass  $m^*$ ) to analyse the shedding modes at various heights along

the span (shown in figure 2.23). They found that for lighter structures the shedding modes resembled the hybrid 2S-2P mode of the tapered cylinders. Structures with very low body inertia also showed presence of another shedding mode, 2C, where two co-rotating vortices were formed at each half cycle.

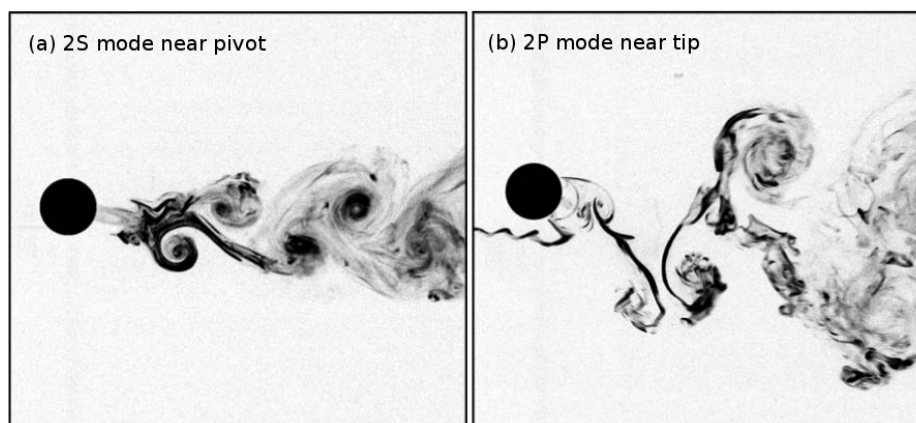


Fig. 2.23 Vortex shedding modes from a pivoted cylinder, indicating 2S shedding mode near the pivot, and 2P shedding mode near the tip, from Flemming & Williamson[49]

For inclined cylinders, a key hypothesis is that the vortex induced vibrations are similar to the case of cylinders with normal axis when only the component of the velocity normal to the cylinder axis ( $U_N = U_\infty \cos\theta$ , where  $\theta$  is the inclination angle) is taken into consideration. This is known as the Independence Principle. It neglects the effects of the axial component for the flow, which may be acceptable for small inclination angle. Various researchers have found different values of inclination angle where the IP is found to be valid. Jain[76] carried out a comprehensive analysis for various inclination angles over a range of Reynolds number, and stated that the IP is valid for angles of inclination up to  $55^\circ$ .

de Vecchi [43] and de Vecchi *et al.* [44] analysed the role played by the curvature of cylinders on the near-wake vortex dynamics. They carried out analysis of curved cylinders in concave and convex configurations, and determined that when a convex cylinder undergoes forced translation, in-phase shedding occurs with bent vortex cores. A concave configuration, which is more likely to be found in case of submarine cables with mean deflection by virtue of its drag, was also tested. In case of no forced oscillation, a suppression of vortex shedding was observed in the wake. For oscillating concave cylinders they observed a disruption of the stabilizing mechanism triggered by the curvature, and a wide wake with staggered arrays of vortices shed from either side of the cylinders.

## 2.3 Vortex Induced Vibrations; Flexible Cylinders

One of the biggest motivation for analysis of Vortex Induced Vibrations is the fatigue of structural elements used in offshore oil production. There is an added interest in the field with the advent and proliferation of offshore wind turbines. Both these industries use various types of platforms, both for temporary applications like exploratory drilling and development wells, and for permanent placement as offshore production platform, or offshore wind turbine. These platforms are broadly categorized as fixed structures, and compliant platforms. As the fixed structures are cost prohibitive in deep water installations, the industry is focused almost entirely on moored floating structures (vertically moored tension leg, and mini-tension leg platforms, spar platforms and semi-submersibles). The structural and mooring elements are exposed to sub-sea currents as well as surge and heave (and surge induced heave) of the floating structures. The mean deflections as well as the vibrations of the elements not only increase the long-term wear and tear, but effect the dynamics and operations of the platforms.

With increasing price of crude oil and the exploration of rich deposits availability in the deep North Sea and the Gulf of Mexico, the offshore oil platforms have progressed from exploring in seas at a depth of a few meters in the beginning of the last century, to over 2000 meters in the last couple of decades. The Semi-submersible offshore rigs like Deepwater Nautilus, and Deepwater Horizon (lost in 2010) are capable of operating at an ocean depth of 2400 meters. In a similar fashion the floating offshore wind turbine technology is progressing and moving into deeper oceans. This has fuelled a surge in the research carried out in the field of vortex induced vibrations of cylindrical structures.

The response data of short rigid, and flexible cylinders has been obtained in wind and water tunnels, and the data are valid for those particular cases. However the theoretical treatment of correlating the laboratory data, by the process of extrapolation from those short lengths to the behaviour of long cables in the field, is not adequate. The case of flexible cylinder presents added complexities. In case of rigid cylinders the lock-in condition is rather simple, whereas in flexible cylinder cases there can be multiple lock-ins based on the multiple modal frequencies, temporal and spatial sharing of multiple frequencies as well as travelling waves. The limited literature available targets specific questions for specific cases. The multi-dimensional domain of variables along with complexities involved in experimental and numerical research to determine the response based on changes in each variable makes it almost impossible to populate a global response domain.

The main foci of interest for VIV of flexible cylinders are:

- Estimation of mean drag,
- Cross-flow and in-line oscillation amplitudes,
- Frequency response analysis of lock-in,
- Different modes of standing waves and travelling waves, wake analysis,
- Dependence on mass ratio,
- Variation in added mass because of oscillation frequencies and amplitudes,
- Dependence on tension,
- Dependence on Reynolds number and reduced velocity.

One simplification that comes from similarities with the earlier discussed cases of rigid cylinders is that the wake resembles that of a rigid cylinders in regions between two structural nodes. Some reported experiments using vibrating cables, for example, Ramberg & Griffin[124], and Brika & Laneville[29, 30] indicate nearly perfect correlation in the wake, for all points between two successive nodes of the vibrating cables. This resembles the response of a rigid cylinder. Hover *et al.* [63] used a novel laboratory apparatus that combined force-feedback with on-line numerical simulation. They were able to establish good correlation with published single-mode free vibration data for lift coefficient, phase and peak amplitudes. However higher modes of oscillation, travelling waves, transients and multiple harmonics add significant complexity to the subject.

### 2.3.1 Experimental analysis

The experimental analysis of VIV of long flexible risers is a highly complex and resource intensive work, which requires fabrication and instrumentation of models that approximate the aspect ratio, and the mass ratio of the real-life application. At minimum, the models are a few meters in length, and instrumented with enough measurement stations to resolve for multiple mode structural oscillation. The test facility typically involves towing tanks that are large enough to accommodate large apparatus. Such tests have also been carried out in lakes and oceans, in which case the local flow conditions, or the variations of the velocity along the span of the risers are not well known. The literature on the field is extremely limited, and most of the reviews of vortex induced vibrations of cylinders cover the introductory thoughts on the



subject. Here we attempt to cover some of the important aspects of the vortex-induced vibrations of long, flexible cylinders undergoing multi-mode vibrations

### 2.3.1.1 Resonant Response

The distinct feature of the VIV of rigid, as well as flexible cylinders is the lock-in phenomena. The case of rigid cylinders undergoing 1 DOF oscillation has been discussed in detail in section 2.2.1. For the case of rigid cylinders, the classical value of Strouhal number is 0.21. For flexible cylinders undergoing multi-mode oscillation, the Strouhal number based on the dominant mode oscillation frequency ranges from 0.16-0.18 (Vandiver & Mazel[158]).

Vandiver & Mazel[158] carried out vortex induced oscillations measurements using a 23 meter long horizontal cable. They found that the lock-in occurred when the preferred shedding frequency is within a few percent of one of the first four, or five natural frequencies. They observed an amplitude response of up to  $\pm 0.7$  diameters. They mention the presence of very regular motion when the Strouhal frequency coincides with one of the first four, or five natural frequencies of the cable, and the cable response shows sinusoidal structural vibrations. The spectrum indicated a sharp peak at the frequency of vibration. In a later publication, Vandiver[153] reported the results of experiments on long flexible cylinders with high aspect ratio at Reynolds number up to 10,000. He observed drag coefficients higher than 3 under lock-in conditions, and a ratio of 3 between in-line and cross-flow oscillation frequencies. Under lock-in conditions an amplitude response of  $\pm 1$  diameter was observed, and in non-lock-in conditions, the response was composed of a contribution of up to 4 in-line and cross-flow modes.

Vandiver[154] also produced an important paper discussing the non-dimensional parameters that play a key role in the response of flexible cylinders undergoing VIV. Some important conclusions from that paper, which condensed over 17 years of experimental data, were that the highest drag and responses are observed in the lock-in conditions. He commented on the mass ratio's role, similar to the rigid cylinders as discussed in section 2.2.1.6, was that smaller values results in a broader lock-in range. He explained the widening effect as the contribution of added mass, which is more significant for lower mass ratio cylinders. The added mass contributes to changes the resonant frequency with increasing flow speed. Similar explanation was provided by Sarpkaya[135] as discussed in section 2.2.1.2. While discussing the lock-in phenomena in case of sheared flow, Vandiver[154] writes that the most important parameters for prediction of lock-in are the shear fraction ( $\Delta V/V_{max}$ , which defines the shear

flow profile) and the number of resident natural modes,  $N_s$ , that lie within the shear excitation bandwidth.

Brika & Laneville[29] carried out analysis of long slender cylinders with many closely-spaced natural frequencies, where the frequency interval between adjacent modes is small. In such cases, the cylinder excitation is usually in multiple, and higher modes. The lock-in is defined as the response range where a single mode is dominant, *i.e.* the mode has enough energy, and competing modes are not participating in the oscillation. Vandiver *et al.* [155] mentioned that in case of strongly sheared flows, one mode may have greater input power than the others. The response of that mode prevents the lesser excited modes from extracting significant power from the wake. This results in a single response frequency domination.

Tognarelli *et al.* [149] published the results of a densely instrumented riser and indicated that the general lock-in VIV response of long flexible risers in laboratory experiments is dominated by standing wave behaviour, and indicate distinct nodes and anti-nodes. In such cases, the VIV response is at a single frequency, in a standing wave mode shape. The multi-mode response, thus, is categorized as the superposition of individual modes; where each mode corresponds to a standing wave mode shape at a distinct frequency. In case of sheared currents, they indicate that for cylinders with long aspect ratio, the general response is in form of travelling waves.

A high quality data was published by Chaplin *et al.* [39], that documents the results of multi-mode vibrations of a 13m long flexible cylinder, instrumented with 32 strain gauge stations and 3 accelerometers. In addition to the curvature and acceleration measurement hardware, they had installed tension and drag load cells at both top and bottom of the riser. The riser, with the mass ratio of 3.0, was towed at very small velocity increments in a stepped current. They documented that with increasing the reduced velocity, the dominant frequency of response advanced in distinct steps, marking the switching from one dominant mode of oscillation to the next. The lock-in phenomena, thus, was defined as the presence of a significantly dominant mode. They reported a monotonic increase in the amplitude of oscillation within each lock-in range, which was followed by a reduction in the amplitude that was in one or two broken rising sequences as the next mode became dominant. They mentioned a significant contribution from two or more modes, with the combination persisting over a range of reduced velocities. These ranges overlapped such that a given reduced velocity resulted in more than one pattern of modal contributions. The drag coefficient, shown in figure 2.24 indicated a strong dependence on the growth and attenuation of successive modes within each series of tests.

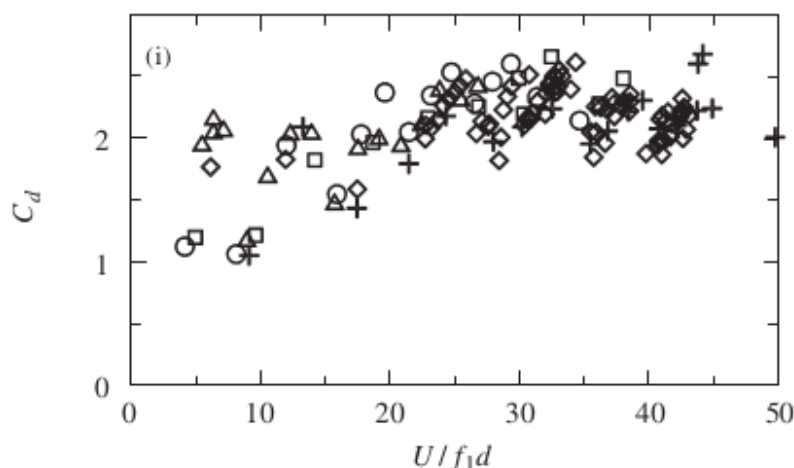


Fig. 2.24 Drag coefficient progression vs reduced velocity ( $U/f_1D$ ), for a flexible cylinder. Symbols indicating the starting tension at the top of the riser. + : 389N,  $\diamond$  : 813N,  $\square$  : 1185N,  $\circ$  : 1546N, and  $\triangle$  : 1925N. From Chaplin *et al.* [39]

Huera-Huarte[65] published the results of the above-mentioned experiments in greater detail. He indicated the presence of up to 14th mode in-line, and 8th mode cross-flow vibrations, where the response included significant contributions from several modes, however the response frequency was controlled by the lock-in of the dominant mode. The largest values of  $C_d$  and  $C_l$  were observed at the largest combined  $xy$  motions (about 4.5). The publication details the development of an indirect finite element technique, that, in conjunction with the experimental response data, computes the in-line and cross-flow force distribution along the axis of the riser (Brief results were also presented in a separate publication by Huera-Huarte *et al.* [71]). He also mentioned the critical importance of taking the in-line oscillations into account when measuring for fatigue damage, as, though previously ignored, these oscillations have a significant amplitude and can contribute to the fatigue of the riser on same order of magnitude as the cross-flow oscillations. Similar conclusion regarding the importance of in-line response was given by Trim *et al.* [152], who published the results of the tests of a densely instrumented flexible cylinder undergoing vortex induced vibrations in sheared, as well as smooth flow.

Huera-Huarte & Bearman[67, 68] published a series of papers on a flexible circular cylinder responding in its' first structural mode. They found out that at lowest tensions the cylinder's dynamic response was very similar to rigid bodies, with clearly defined branches of response. With increased tension the cylinder behaved as a tensioned cable, where under the lock-in condition, the lower branch disappeared and the response was concentrated in the initial and upper branches. The response frequencies were equal to

the natural frequencies of the responding mode, and the Strouhal number was about 0.16. They found drag coefficient up to 3, significantly higher than expected for a stationary cylinder. The drag amplification was observed with the increasing amplitude of oscillation. The entire cylinder shedding was observed to be predominantly 2S mode, while the 2P mode intermittently appeared intermittently in the upper and lower branches, related to largest  $xy$  synchronized motions.

The extensive reports by Huera-Huarte *et al.* [71], and Trim *et al.* [152] have indicated the significance of the in-line response, and its contribution to the fatigue of the riser when the response was dominated by the lower order modes. The presence of in-line oscillations cause a significant change in the vortex pattern behind the cylinder. For the case of rigid cylinders, Jauvtis & Williamson[77] showed the increase in the VIV response when the cylinder was allowed to oscillate in both in-line and cross-flow directions. For the case of flexible cylinders, as the oscillations are almost always in both in-line and cross-flow direction, the in-line response usually occurs at a higher mode than the cross-flow response.

### 2.3.1.2 Higher harmonics

In order to simulate the response of flexible cylinders, some researchers employed an apparatus using flexibly mounted rigid cylinders, by configuring the end condition such that the cylinder has different natural frequencies for in-line and cross-flow direction. Sarpkaya[134] and Dahl[42] have shown that when the nominal frequency ratio, *i.e.* the ratio between the in-line natural frequency, and cross-flow natural frequency is 2, a case of dual resonance of cylinders takes place. Studies by Jeon & Gharib [78] and Blevins & Coughran[23] have shown that the case of dual resonance is accompanied by the figure eight orbits for rigid cylinder. This orbit shape is seen frequently in the case of flexible cylinders, as the in-line oscillations are often at the twice the cross-flow oscillation modes. Zimmer[183], under supervision of Dahl, studied the vortex induced vibrations of flexible cylinders with various mode ratios. For a mode ratio of 1:1, the oscillations were very similar to those observed for free vibrations of rigid cylinders. For a 1:2 mode ratio he noticed that the first mode was being excited in both cross-flow and in-line directions, and effective frequency that was in the middle of the two modal frequencies was observed.

The indication of third harmonics in the response of rigid cylinders has been documented by Dahl [41], and Jauvtis & Williamson[77], among others. The reason, or the mechanism behind this has been briefly explained (see section 2.2.3). Modarres-Sadeghi *et al.* [106] published a report indicating the presence of the third harmonic

force component for flexible cylinders. His analysis of data from Norwegian Deep Water Program (NDP) indicate that when the structural oscillation frequency ( $f_{cf}$ ) is in the neighbourhood of the expected Strouhal shedding frequency, a large (up to 70% of the total acceleration) third harmonic ( $3f_{cf}$ ) is observed in the cross-flow strains and acceleration signals. The presence of a smaller fifth harmonic ( $5f_{cf}$ ) was also noted. In a later publication, Modarres-Sadeghi *et al.* [105] indicated that the vortex induced vibrations of long flexible cylinders are characterised by time intervals of chaotic response, followed or preceded by periods of statistically stationary response. They observed three types of VIV behaviour, namely cases where the entire signal is mainly quasi-periodic, cases where the quasi-periodic oscillations are periodically interrupted by chaotic oscillations, and where the entire signal is chaotic, with even the smallest sub-signals confirm chaotic behaviour. Vandiver *et al.* [157] indicated that during the vortex induced vibrations analysis of a 22m long steel pipe, he observed that at certain span-wise locations a very strong presence of third harmonic was observed. The contribution from the third harmonic force on the entire strain response was even larger than that of the fundamental component of response.

### 2.3.2 Force Distribution and Prediction Models

There are a quite a few semi-empirical prediction models for VIV analysis. Some models are based on pure analytical solution, for example Iwan[74] extended the Iwan-Blevins model of rigid elastically supported cylindrical element to elastic structural elements, and formulated an analytical relationship predicting the maximum amplitudes of response for various types of elements. The fit is given in equation 2.52

$$\left(\frac{Y_{max}}{D}\right) \frac{1}{\gamma_n} = \frac{1}{1 + 1.60(M^*\zeta_n)^{1.80}} \quad (2.52)$$

The values of  $\gamma_n$  for various model types are listed in section 2.2.1.6.

Skop and Balasubramanian[140] presented a modified variation of the Skop-Griffin model, that primarily focuses on the self-limiting structural response of models that have near-zero structural damping. More, slightly altered variations of models based on SDOF differential equations were given by Bearman[9] among many others.

Vandiver & Chung[156] proposed a stochastic model for prediction of vortex induced vibrations of flexible cylinders, and compared it with experimental results. An important step in this model was the prediction outside of the lock-in modes. They determined that with exception of pure lock-in modes, the hydrodynamic damping plays an important role in determining the VIV response, where it is 10 to 100 times greater

than the structural damping. The product  $n\zeta_n$ , where  $n$  is the mode number and  $\zeta_n$  is the damping ratio, when greater than 3, resulted in a response similar to an infinite length cable, and for less than 0.2, a single mode dominated the response.

Gopalkrishnan[58] collected a large amount of data, via forced oscillation experiments of a rigid cylinder undergoing sinusoidal and amplitude modulated oscillations. This data formed the basis of prediction model from the Vandiver group. Venugopal[159] provided a fluid damping model that was valid over a wide range of reduced velocities and amplitudes of oscillations, and compared the response prediction models with measured response of flexible cylinders, for lengths up to 1000 meters. Later that data, alongwith significant amounts of results from other experiments were used in the prediction models (SHEAR7, and SHEAR3D) developed by Vandiver. It has been widely used for determination of likely excited modes, and the amplitude response in uniform and sheared flows.

Hover *et al.* [63] used a combination of numerical methods with forced feedback experimental apparatus, which was an adaptation of the one used by Gopalkrishnan[58]. The apparatus was based on a rigid cylinder, however the combination of numerical method and the force-feedback mechanism incorporated in the experimental set-up gave them a platform to determine response modes for a flexible cylinder. They determined that their numerical models and force feedback apparatus results for single mode response were in good agreement with existing data in terms of lift coefficient, phase and peak amplitudes. Correlation to the multi-mode response, they mention, could be compared to single mode compliant structures with proper frequency scaling which accounts for structural zeros.

Triantafyllou *et al.* [151] presented a way of determining a linear hydrodynamic damping term that could be obtained from forced-motion tests on rigid cylinders, to predict the vortex induced response under lock-in conditions for cylinders. They analysed data from various experiments, including results from cables exceeding 1000 meters in length, and used their prediction method to determine drag coefficient values. The predicted values are shown to match the experimental results within an acceptable limit.

The other set of prediction models use experimental data from measurements on cylinders undergoing vortex induced vibrations, or forced oscillations. Some of the notable codes are:

- VIVANA: A software to calculate VIV of marine risers. It applies frequency domain method for dynamic analysis. The code is limited to cross-flow oscillations only.

- ABAVIV: A time domain program for evaluation of VIV. The code is based on ABAQUS as the core program, with published models for VIV methodology.
- VICoMo: VICoMo uses data from section model tests on forced harmonic motions of cylinders. Identical to strip theory model, the spanwise component of flow is neglected.
- SHEAR7 and SHEAR3D: A mode superposition program, evaluates which modes are likely to be excited by vortex shedding and estimates steady state cross-flow VIV response. SHEAR7 focuses on cross-flow only, and the SHEAR3D variant is for cross-flow as well as in-line oscillations.

A comparison of these prediction models, in addition to others, was carried out by Chaplin *et al.* [39]. He compared the results from a comprehensive experimental dataset against 11 different methods. The predicted response results were within 85% to 105% of the laboratory measurements. With addition of newer datasets in these prediction models, further improvements are expected in future.

Huera-Huarte *et al.* [71] used experimental response data from a densely instrumented riser undergoing vortex induced vibrations and linked to a finite element method code to analyse the instantaneous distributed in-line and cross-flow forces acting along the span of the riser. They documented a strong correlation between the RMS of the cross-flow deflection and the drag distribution. At the anti-nodes, local instantaneous coefficient of drag values up to 4.5 were found, whereas at the nodes, the value of drag coefficient was comparable to stationary (rigid, non-oscillating) cylinders at the same Reynolds numbers. Further work in prediction of modal response was carried out by Huera-Huarte & González [72], that used a quadratic eigenvalue approach to estimate the modal frequencies of flexible cylinder in cross-flow with a current dependent form of damping. The predicted modal frequencies matched the experimental results with good accuracy.

### 2.3.3 Numerical Methods

There are a significant number of numerical methods used for VIV analysis. The methods can be divided into time-marching schemes, direct numerical simulations, and vortex-in-cell methods. Most of the present numerical methods are based on strip theory, where the computations are carried out for planes along the span of the cylinder, and the flow along the span of the cylinder is ignored. Newer codes are being

developed that tackle full three-dimensional FSI problems as coupled solvers for fluids and solids, for example the OpenFOAM FSI solver and ANSYS Fluent FSI.

Blackburn & Karniadakis[21], followed by Newman & Karniadakis[110, 111] carried out extensive numerical evaluation of laminar flows past a flexible cable (in free vibration, as well as in forced oscillation) at low to moderate Reynolds number. Some patterns that they identified consisted of standard Kármán vortex street seen at the anti-nodes, and periodic shedding of symmetric vortex pairs at the nodes for free oscillation simulations. In case of forced oscillation they noticed higher shedding modes at the anti-nodes. The code was further developed into one of the most frequently cited spectral / hp code, suitable for unstructured grids for VIV analysis, called NekTar. Evangelinos *et al.* [47] carried out extensive tests for various types of cylinders (stationary, rigid, short and long beams), and were able to simulate both standing wave responses as well as travelling waves, with cylinders peak displacements of about  $0.9D$ . Lucor *et al.* [97] carried out spectral DNS of flexible cylinders at Reynolds number of 1000, with linear and exponentially sheared flows. The NekTar code was used later by Bourguet[27] in order to explain the phasing mechanism between in-line and cross-flow VIV of long flexible cylinders related to the sectional lock-in phenomena.

Willden & Graham[165] carried out two-dimensional and quasi-three-dimensional simulations of VIV of a flexible cylinder. Similar to experimental results they found that for low mass ratio cylinder, the oscillatory frequency was controlled by the fluid, via the added mass, far from body's natural frequency. The cells of vorticity were observed in the wake. They found the free transverse flexible vibration to exhibit spanwise correlation, similar to rigid bodies, even in case of highly sheared flows. Wang *et al.* [164] modelled the structural vibrations of a fixed-fixed elastic cylinder as an Euler-Bernoulli beam, and resolved the flow field using finite element method. The resulting forces were input into the beam model to resolve the deformation, revise the map and carry out flow field computation, following the time-marching technique. The results matched well with experimental results.

Yamamoto *et al.* [174] applied strip theory with Lagrangian numerical technique, the discrete vortex method coupled with Euler-Bernoulli equations for the cylinder. The results indicated clearly defined spectra peaks corresponding to the shedding frequencies and peak amplitudes up to  $0.6D$  in up to fourth mode of oscillation. Using the same discrete vortex method, Meneghini *et al.*

Bourguet *et al.* [26] carried out numerical analysis with the intention of localization and extent of the lock-in region and regarding the vortical patterns in the wake. The standing waves appeared predominantly near the ends of the cylinder, whereas in case



of sheared flow, the travelling waves moved from the high velocity regions towards the low velocity regions. They found both mono-frequency as well as multi-frequency responses along the cylinder span, while each excited frequency was associated with a single structural mode. The wake in both lock-in and non-lock-in region mostly comprised of oblique vortex shedding. Some more additional features were detailed, for example the multi-frequency responses consisted of several locally and instantaneously mono-frequency events. They state that the multi-frequency character was due to a temporal drift in the excited frequency. In a subsequent publication[25] they clarified the relationship between lock-in and the phase difference between in-line and cross-flow oscillation for a cylinder oscillating with a frequency ratio of 2 between in-line and cross-flow oscillation. They state that for phase difference within the range of  $0 - 180^\circ$  corresponds to the trajectories where the cylinder moves upstream when reaching the cross-flow oscillation maxima, or counter-clockwise, and indicates a lock-in region. At nodes they observed a switching between counter-clockwise and clockwise trajectories.

There are a few publications on the integrated FSI applications, and as the field progresses many additions are expected in the application. Chen *et al.* [40] published results using ANSYS MFX solution strategy, which is a Fluid Structure Interaction (FSI) problem solver, and compared the results with LES modelling as well as experimental tests. They show that with proper mesh density the solution from both FSI solver as well as LES modelling matched well with the experimental results.

## 2.4 Vortex Induced Vibrations of Cylinders with Wake interference

The study of cylinders in tandem configuration has almost entirely been focused on the cases of stationary rigid cylinders, or flexibly mounted rigid cylinders. There are very limited cases of analysis of flexible cylinders in tandem configuration, and even those cases have been studied in first mode of oscillation only, a response regime that is fairly closely associated with flexibly mounted rigid cylinders.

The experimental analysis of cylinders in tandem arrangement started in early 20<sup>th</sup> century with advent of flight. Pannell & Griffiths[119] in 1915 measured drag of two chords in staggered and tandem arrangements, and found out that for tandem arrangements the distance between the chords,  $S_x/D < 4.5$ , caused a reduction in the drag. When the wires were in contact, the minimum drag on two wires was 40% of the drag of individual wire. They attributed this result to the improved streaming of the incident flow over upstream wire because of the wake of the downstream wire.

Biermann & Herrnstien published the results of interference effects of tandem structures in flow for  $S_x$  up to 7.5 with similar results. [18].

### 2.4.1 Stationary cylinders in tandem arrangement

Zdarvkovich *et al.* [175, 179] determined that for tandem cylinders a critical spacing  $S_x$  exists at which the base pressure, lift and drag coefficients have a discontinuous change, and attributed it to the two different flow patterns around the cylinders as a result of an abrupt change from one stable flow pattern to another in the gap between the two cylinders. For side by side arrangement they found two alternative values of drag and lift forces based on the bistable nature of the asymmetric flow pattern around each cylinder. For staggered cylinders they found two distinct regimes, one in which the lift of the downstream cylinder is directed towards the wake of the upstream cylinder due to the entrainment of flow of the upstream cylinder, and the second regime where the very small space between two cylinders cause intense gap flow and results in large lift force. In case of side by side cylinders. Later Zdarvkovich [176, 177] classified the flow around multiple cylinders into two categories, i.e with and without interference, with an interference boundary dividing the regimes, and classified the interference as wake interference for tandem cylinders, and proximity interference for side by side or staggered cylinders, shown in 2.25.

Bearman & Wadcock [13] found that the drag of the cylinders in combination was lesser than the drag of individual cylinders when the gap flow acted as the base bleed. They also found repulsive force between cylinders for a particular range of gap spacing. In similar experiments, Williamson [166] determined that for a certain range of gap between the cylinders, the wakes were synchronized either in-phase or anti-phase. The in-phase wake vortices formed by each cylinder rotate around one another to form a binary vortex street. In case of anti-phase oscillation the shedding frequency on one side of the wake was multiple of the other side.

### 2.4.2 Flexibly mounted rigid cylinders in tandem arrangement

Tanida *et al.* [147] carried out experimental analysis of single and tandem cylinders over a wide range of Reynolds numbers, and observed a discontinuity in lift, drag and Strouhal numbers starting at the center to center distance  $S_x/D \sim 3.9$ . Brika & Laneville [31] in their experiments, showed that the steady state response of a cylinder downstream of a stationary cylinder is represented by a single branch and shows a wider

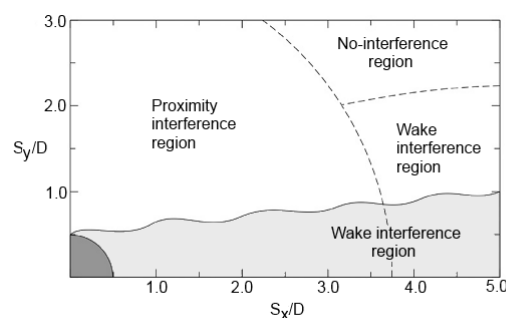


Fig. 2.25 Wake and proximity interference boundaries for two staggered cylinders in steady cross-flow, adapted from Zdarkovich [177]

synchronization region that decreases with increasing space between the cylinders. In case of the upstream cylinder that is free to oscillate the downstream cylinder response becomes hysteretic, characterized with two branches and two discontinuities.

Sumner *et al.* [145], and later Li and Sumner [92] determined that the Strouhal number behaviour can be categorized based on the gap as closely spaced, moderately spaced and widely spaced configurations. Okijama *et al.* [115] determined that if the upstream cylinder is free to oscillate there are two excitation regimes. For small gaps and low reduced velocities,  $0.3 < S_x/D < 3$ ,  $1.4 \leq U^* \leq 2.5$  the vibration is due to the movement-induced excitation accompanied by symmetrical vortex shedding, whereas for  $1.75 < S_x/D < 3$  and  $2.7 \leq U^* \leq 3.7$  the excitation is due to alternate Kármán vortex shedding. When the downstream cylinder is free to oscillate there are two excitation regimes, with a dead water region, for  $2 \leq Vr \leq 4$  and  $0.3 \leq S_x/D \leq 0.75$ , followed by second excitation region due to symmetrical vortex shedding for  $0.75 \leq S_x/D \leq 2$ . They documented buffeting by downstream cylinder for  $S_x > 2.5$ .

Mittal & Kumar [103] used stabilized finite element formulation at low Reynolds numbers for tandem and staggered cylinders, with  $S_x/D$  greater than 5, resulting in an unsteady inflow without proximity interference. and determined that when the downstream cylinder is in symmetric wake (with  $S_y/D = 0$ ) both upstream and downstream cylinders have similar trajectories, i.e forming the *lissajous figure of 8*. In presence of unsymmetrical wake (with  $S_y/D > 0$ ) the downstream cylinder follows a tilted oval trajectory because of the lift in the direction of the upstream cylinder wake. Prasanth & Mittal [122] showed large amplitude oscillations for downstream cylinder in both transverse and streamwise directions for larger gap, and divided the flow range into five sub-regions based on the flow patterns and the phase difference of vibrations.

Mizushima & Suehiro [104] carried out numerical analysis of flow past two circular cylinders at low *Reynolds* numbers, and found the same abrupt changes with  $S_x/D$  over the range of  $3.4 \sim 3.6$ , and attributed those changes to the existence of multiple stable solutions of the flow. Meneghini *et al.* [100], using a 2-D finite element method, observed that for  $S_x/D < 3$  the vortex shedding occurs from the downstream cylinder, which experienced a negative drag force, whereas for  $S_x/D > 3$  the shedding occurred from both cylinders and a positive drag force seen by the downstream cylinder. In case of staggered cylinders they confirmed the repulsive force for low  $S_y/D$  as seen in the experimental results of Bearmann & Wadcock [13].

Dehkordi *et al.* [45] in their numerical analysis showed that for low *Reynolds* numbers (100), the reattachment without formation of counter-rotating vortices in the gap, and negative drag on downstream cylinder occur at  $S_x/D = 2.5$ . At  $S_x/D = 5.5$  the flow behind the downstream cylinder shows unstable behavior, as the vortices from upstream cylinder are fully formed and impinging on the downstream cylinder, causing greater fluctuations in lift. Whereas for high *Reynolds* numbers (turbulent regime,  $Re = 2.2e^4$ ), at  $S_x/D = 2$  the shear layer reattach alternatively on either side of the downstream cylinder, while at  $S_x/D = 3$  the reattachment is symmetric. For greater gap both cylinders shed vortices that amalgamate in the proximity of downstream cylinder resulting in lift fluctuations of the downstream cylinder. Kitagawa & Ohta [83] found the critical gap spacing of  $S_x/D = 3.25$ . Akbari & Price [2] carried out numerical investigation of two staggered cylinders in cross-flow at low subcritical *Reynolds* numbers and determined five distinct flow regimes based on the geometrical arrangements of the cylinders. The shear layer reattachment regime and the vortex impinging regime being relevant for tandem cylinders with increasing  $S_x/D$ , and base-bleed, vortex pairing and enveloping, and complete vortex shedding regimes for staggered cylinders with increasing  $S_x/D$  and  $S_y/D$ .

Assi *et al.* [5] showed that for a rigid cylinder in tandem arrangement, the response regime consists of a single branch of consistently increasing amplitude of oscillation for medium to high gap spacing. For low gap spacing they show a peak at the resonant case, followed by a decreasing trend, that is followed by an increase in amplitude similar to larger gaps. These authors (Assi *et al.* [3, 4]) introduced the concept of wake stiffness to explain their frequency response observations.

### 2.4.3 Flexible cylinders in tandem arrangement

Huera-Huarte & Gharib[70] published the results of the vortex induced vibrations of a tandem arrangement of flexible cylinders, placed in close proximity ( $2 < S_x/D < 4$ ).

The facility limitations allowed, for almost all cases, only first mode of structural oscillation. Some important conclusions could be ascertained from the results. The response regime, due to the fact that it was limited to the first mode of oscillation, appear to have some similarities with the case of flexibly mounted rigid cylinders (Assi *et al.* [5]), where the lock-in regime results in increased response, and subsequently fall with increasing reduced velocity. Within the range of  $2 < S_x/D < 4$ , both cylinders response show classical VIV resonance when the reduced velocity is near to the lock-in. This behaviour was independent of the distance between the cylinders. At higher reduced velocities, the behaviour of the two cylinders was different, depending on the separation. For low separations, the response of the upstream cylinder indicated larger oscillations, whereas for higher separation, both cylinders acted as isolated cylinders. The higher reduced velocity resulted in large oscillations in the downstream cylinder. In case of tandem cylinders, the wake induced vibrations are considered as the primary source of excitation, however it did not appear so for small gap distances. The response was largely dependent on the existence, or not, of the vortices between the gap of the two risers. A subsequent publication by Huera-Huarte & Gharib[69] dealt with the similar apparatus, however the cylinder placement was for larger separation ( $4 < S_x/D < 8$ ). The results indicated that the response primarily is similar to classic VIV response within the lock-in regime, and that of wake induced vibrations (WIV) if the reduced velocities are outside of the lock-in regime.

## CHAPTER 3

# MULTI-MODE VIV OF LONG FLEXIBLE CYLINDERS : SET-UP, MEASUREMENTS, ANALYSIS

---

### 3.1 Introduction

The vortex induced vibrations of a long flexible cylinder were analysed as a part of the investigation. The premise of the experiments was to study the response regimes of long flexible cylinders. For analysis, risers of two different mass ratios were used. The mounting and instrumentation of both riser models were identical. In this chapter the experimental set-up, instrumentation, data collection, determination of structural parameters, and general processing is discussed briefly. The set-up and instrumentation, both external as well as the dense instrumentation of the riser itself were based on the designs used in previous experiments of Chaplin *et al.* [39], and Huera-Huarte *et al.* [71].

#### 3.1.1 Experimental set-up

Two riser models were developed for the experiments. The models, identical in length and instrumentation, had difference in construction, and different mass ratios. The models were mounted in rigid mounting system that was constructed from Aluminium profiles. The mass of the mounting system was kept heavy enough so the structural vibrations were minimized and would have no influence on the vibrations of the model.

##### 3.1.1.1 Towing tank

The experiments were conducted in the still water towing facility of the Institute of Naval Engineering, Madrid Polytechnic University (Canal de Ensayos Hidrodinámicos, Escuela Técnica Superior de Ingenieros Navales, Universidad Politécnica de Madrid).

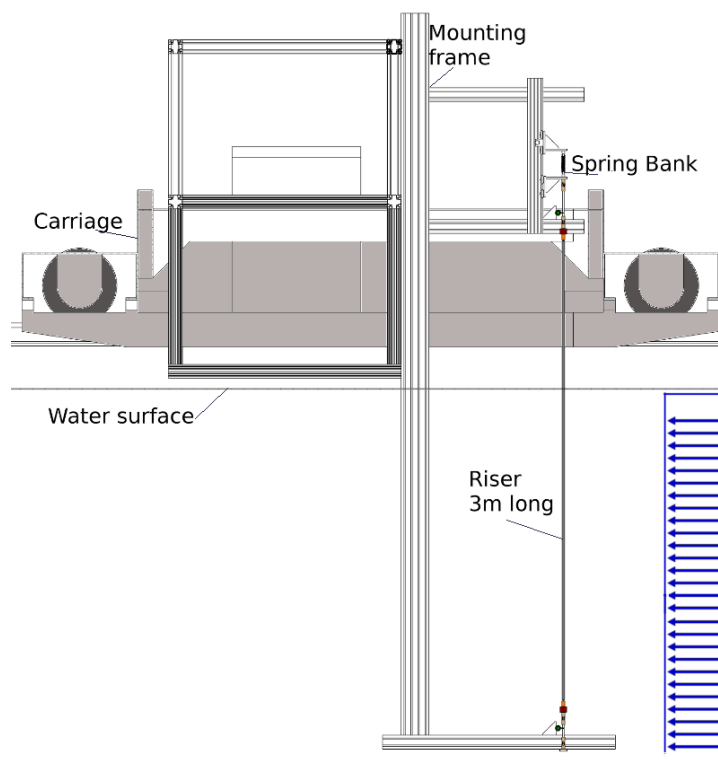


Fig. 3.1 General layout of the experimental setup

The basin is 100 m long, 2.2 m deep and 3.2 m in width, and equipped with a state of the art towing carriage running on top of very smooth rails. The velocity of towing is controlled by a closed loop computerized system and capable of operating up to 4.5 m/s.

### 3.1.1.2 General Description

The riser model was installed in a frame, that was mounted in a carriage as shown in the layout figure 3.1. The lower 55% of the model was submerged in the water, thus subjected to a uniform current. The top 45% of the model was in air. The frame was fixed to the carriage using multiple clamps, ensuring firm and secure hold. The riser model was mounted in the frame using a pair of universal joints at each end, that allowed for a pinned-pinned end conditions in both in-line and cross-flow direction. Each pair of universal joints had a steel rod between them, which was affixed to the drag load cells. The towing speeds were kept constant during the runs, and were kept within a range of 0.1 m/s to 2 m/s. Figure 3.2 shows the cutaway isometric rendering of the experimental set-up.

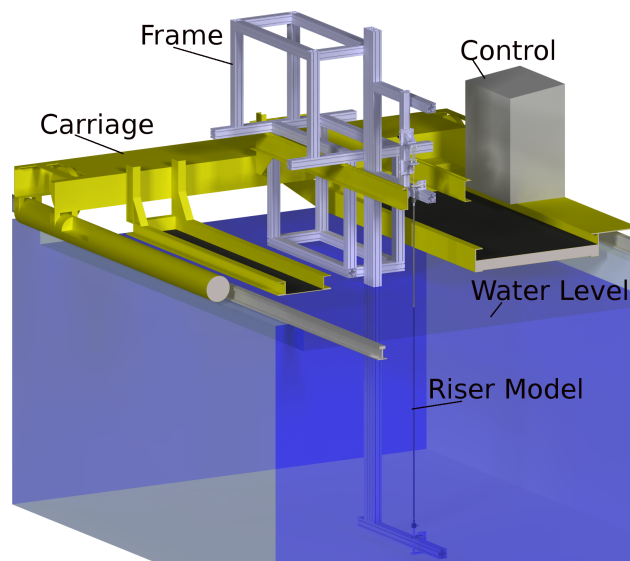


Fig. 3.2 Isometric view (rendered) of the experimental setup. Front part of carriage is cut-off for unobstructed view of the riser model

### 3.1.1.3 Support structure

The supporting structure was specifically designed and fabricated for this experiment. The structure consisted of a primary beam, 4.6 m in length, made of  $90 \times 180$  mm aluminium profiles, mounted vertically in a frame of  $90 \times 90$  mm aluminium profiles. A horizontal bar at the bottom formed the base on which the bottom end of the cylinder was mounted. The mechanism on top consisted of a frame with a set of sliders mounted on a smooth rail, that allowed for vertical motion of the top end of the cylinder. This set-up gave us the capability of applying different end conditions and set the initial tension.

### 3.1.2 Riser model

Both riser models were based on 6 mm diameter brass core, 3 m in length. The instrumentation of the riser models were similar. The riser instrumentation consisted of 11 strain gage stations. The strain gages were mounted using cyanoacrylate adhesive. At each station four (two pairs) of strain gages were mounted, each at  $90^\circ$ , to form two half bridge for measuring the curvature in two directions, at specified locations. Utmost care was taken to ensure that the stations were perfectly aligned. The distance between two consecutive stations was 270 mm, with the first and last stations positioned at 150 mm from the ends. Four wires were marked and soldered to each half-bridge station. After soldering, each strain gage station was covered in polyurethane lacquer



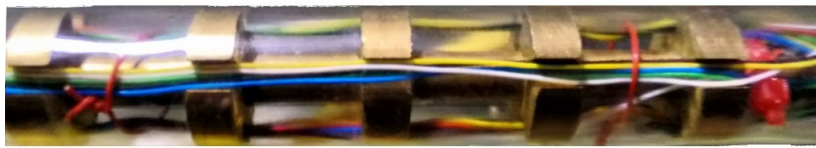


Fig. 3.3 A close-up photograph of model with mass ratio  $m^* = 2.70$

for protection. This particular distribution enabled us to measure up to 13 displacement modes, even though the preliminary numerical estimation forecast indicated that the structural vibrations will be of significantly lower modes.

The lighter model was covered in low density foam sleeve, similar to the sleeves generally used for thermal pipe insulation, with 6mm inner diameter and 20mm outer diameter. The model along with the foam sleeve was passed through a polyolefin heat shrink tubing. The heat shrink tubing was carefully warmed up, resulting in a snug fit. The resulting cylinder had a smooth external surface, with 19 mm diameter. The 3 meter long model had a mass of 0.313 kg/m, and thus mass ratio  $m^* = 1.10$ .

The second model was based on the design previously used by Chaplin *et al.* [39] and Huera-Huarte & Bearman[67]. A total of 154 brass diaphragms, with 15mm outside diameter and 6mm inside diameter and 5mm length, were machined from brass stock. 4 cut-outs were made in the diaphragms in order to allow passage of instrumentation wires. The diaphragms were slid on on the brass rod and mounted with cyanoacrylate adhesive, keeping 15mm distance between two consecutive diaphragms. After routing the wires through the cut-outs, the skeleton structure was passed through a transparent flexible PVC tubing. The end result was a 16 mm diameter, 3 meter long riser model that had a mass of 0.543 kg/m, and the mass ratio  $m^* = 2.70$ . A close up photograph of the high mass ratio model is shown in figure 3.3. For both models, the ends were sealed against ingress of water using epoxy adhesive. Figure 3.4 shows the mounted models in the apparatus. The low mass ratio ( $m^* = 1.1$ ) model is shown in the left column, and the high mass ratio riser ( $m^* = 2.7$ ) shown in the right column.

### 3.1.2.1 Riser mounting and external instrumentation

At both ends of the risers a tension load cell was mounted, aligned with the riser. The other end of the tension load cell was fixed in a universal joint. An extension bar went from the universal joint, passing through a shaft-coupling attached to a drag load cell. The extension bar terminated in another universal joint at each end.

The bottom end was affixed with a plate to the aluminium profile, that connected to the main vertical beam. On top end a special arrangement was designed that allowed

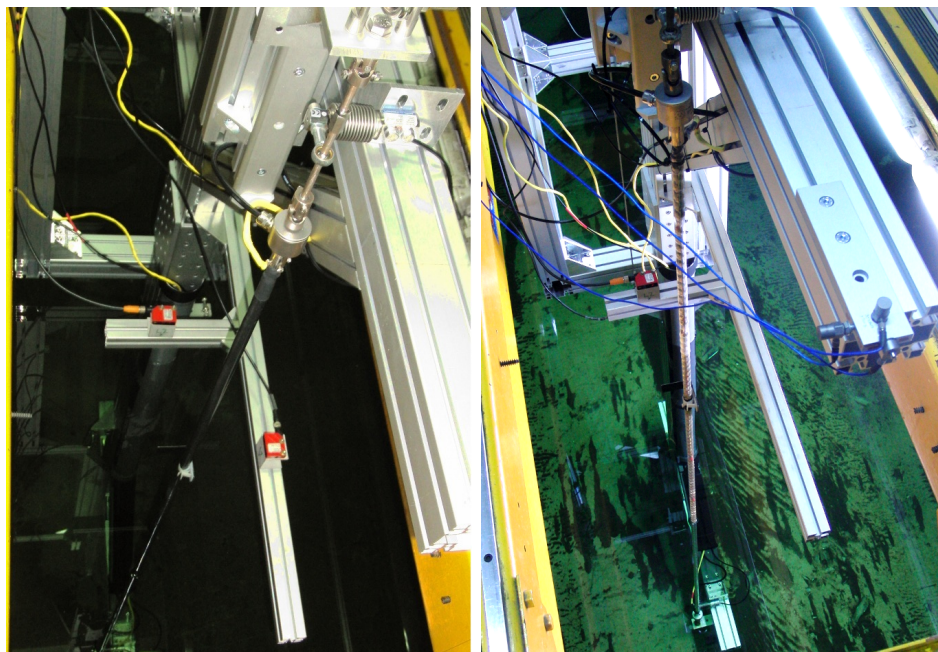


Fig. 3.4 Low mass ratio riser ( $m^* = 1.1$ ) on the left, and high mass ratio riser ( $m^* = 2.70$ ) on the right

for installation of a spring bank, allowing the possibility of affixing the top spring constant to desired value. Figure 3.5 shows the bottom mounting of the riser model.

The top end of the riser model was, in a similar way, mounted to the spring bank assembly. The top end set-up is shown in figure 3.6. The two sliders with the spring-bank gave us the opportunity to use different end conditions for the tests, *i.e.* runs with fixed tension, as well as runs with a knowing starting tension and a fixed spring constant. Figure 3.7 shows the photograph of the top mounting, including the drag and tension load cells and the spring bank.

The two drag load cells were used to directly measure the drag in the system. Necessary corrections were made, keeping in view the geometric configurations of the load cells. Additionally the force measured by the tension load cells was resolved into the force components, giving us redundancy in drag measurement.

Additionally, three precision accelerometers were mounted on the frame, near the top mounting point of the riser model. The purpose of these accelerometers was to monitor the vibration of the whole structure, to determine the structure's vibration frequencies in all three axes, in order to ensure that the vibrations of the structure were not influencing the riser vibrations.

In addition to the above mentioned instrumentation, an independent laser displacement measuring sensor was used for validation of the strain gage measurement. For

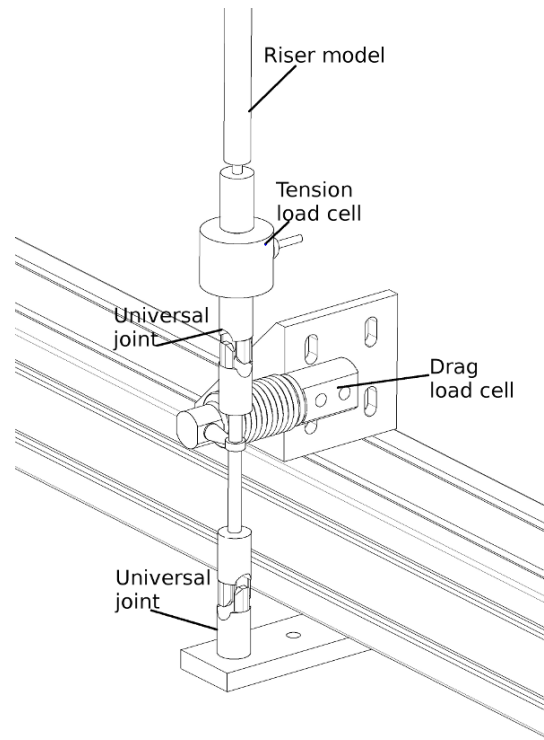


Fig. 3.5 Riser bottom mounting and instrumentation

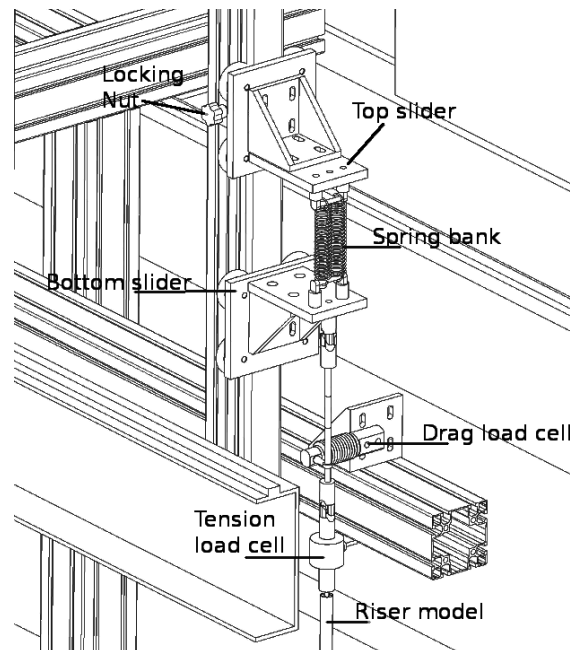


Fig. 3.6 Riser top mounting and instrumentation

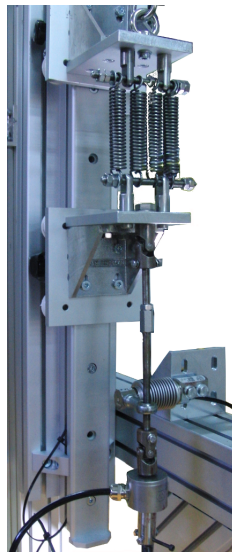


Fig. 3.7 Photograph of the riser top mounting, spring bank and instrumentation

this purpose, the laser sensor was mounted on the supporting frame, and two small reflective plates were attached to the cylinder, axially positioned atop a strain gage measuring station.

### 3.1.2.2 Setting up initial tension and end condition

The tests were carried out using two types of boundary conditions. The first type of condition was keeping the tension constant during the tests. For this the lower slider was connected to a cable passing over a pulley, with calibrated weights hanging from the other side. Thanks to the almost frictionless design of the slider, it enabled us to test the model response with constant applied tension, independent of the forces acting on the cylinder or the curvature of the model. For the second end condition, a spring bank was connected between the two sliders. A known tension was applied to the springs and model by hanging the weights, this time connected to the top slider. Before the run the weights were removed and the locking mechanism was deployed to hold the upper slider in place. The spring boundary condition allowed for a constant  $k$  for the tests. The curvature of the model, along with the spring constant of the spring bank governed the applied tension.

The set-up allowed, thus, a total of three different end conditions. the constant tension boundary condition and the constant spring stiffness of  $K_1 = 17.1N/mm$  and  $K_2 = 41.1N/mm$ . The initial tension for each boundary condition was varied as per previously described. For tests, 4 different initial top tensions were investigated ( $T_1 = 200N$ ,  $T_2 = 397N$ ,  $T_3 = 595N$  and  $T_4 = 795N$ ). The friction in the cable-pulley

system as well as that of the slider mechanisms resulted in lower initial tension as read by the top tension load cell. During the run, the mean in-line curvature of the cylinder results in an increase in tension for the constant spring stiffness cases. Therefore, the top tension measured by the tension load cell is used for subsequent analysis.

### 3.1.2.3 Test parameters

The main parameters and specifications of the test models are listed in table 3.1

Table 3.1 Characteristics of the test models

Parameter	Nomenclature	Units	$m^* = 1.10$	$m^* = 2.70$
Core diameter	d	m	0.006	0.006
External diameter	D	m	0.019	0.016
Length	L	m	3.0	3.0
Aspect ratio	$AR_s = L/D$		158	187
Submerged length	$L_s$	m	1.59	1.59
Flexural stiffness	EI	N m <sup>2</sup>	6.04	6.04
Axial stiffness	EA	N	2.69E6	2.69E6

The lower mass ratio model ( $m^* = 1.10$ ) was tested with three types of end conditions, namely fixed tension, and fixed spring stiffness  $K_1$  and  $K_2$ . The higher mass ratio model ( $m^* = 2.70$ ) was tested with the low fixed spring stiffness end condition. The experiment parameters are listed in table 3.2

Table 3.2 Main parameters of the experiment runs

Parameter	Model	Min	Max
Flow speed	U m/s	0.2	2.0
Reynolds Number	Re	$m^* = 1.10$ $m^* = 2.70$	3740 2800 28000
Starting Tension	$T_s$ N	200	795
Spring stiffness	$K_s$ N/mm	17.1	41.1

## 3.2 Tandem Cylinders

A set of experiments that were carried out in continuation, involved determining the response of the risers in tandem arrangements. For this purpose, the trailing cylinder used was the high mass ratio riser ( $m^* = 2.7$ ), with no variation in the installation or

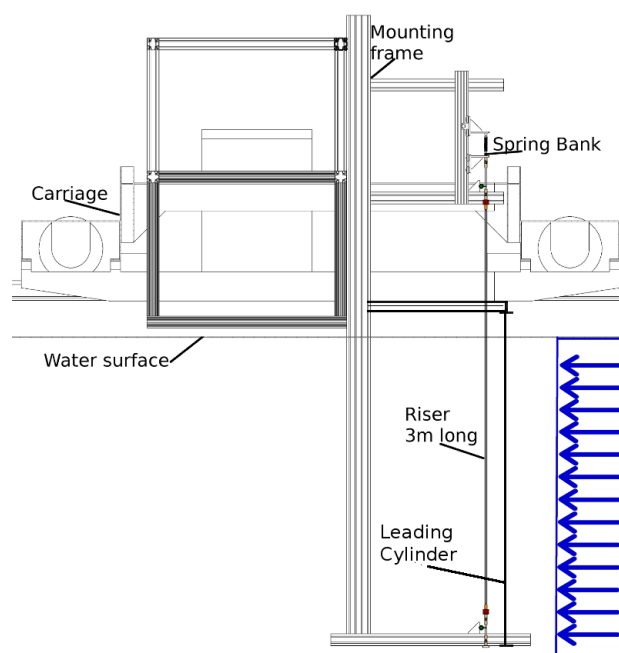


Fig. 3.8 General arrangement of the cylinders in tandem configuration

the external instrumentation. A 20mm external diameter rigid cylinder was mounted in the front of the riser, such that the two cylinders formed a tandem arrangement. The leading cylinder was rigid, and not instrumented. The gap between the two cylinders could be adjusted by moving the leading cylinder mountings in the fore- or aft- directions. The gap spacing ( $S_x$ ) could be adjusted from  $1.5D$  to any prescribed length from the trailing, instrumented flexible riser. The gap spacings ( $S_x/D$ ) were set from 2 to 6 for the runs.

The general arrangement of the tandem cylinders is shown in figure 3.8. Figure 3.9 shows a photograph of the tandem arrangement of cylinders, mounted in the carriage, and set up at a center to center distance of  $S_x/D = 4$ .



Fig. 3.9 Photograph of the cylinders in tandem configuration, To the right is a rigid leading cylinder, whereas the on the left is the flexible, densely instrumented trailing cylinder with mass ratio  $m^* = 2.7$

### 3.3 Data Acquisition

The 22 half bridge strain gage stations were all connected via National Instruments NI 9949 terminal blocks to 6 NI 9237 modules ( $\pm 25$  mV/V Bridge Analogue Input, 50 kS/s/ch, 4 channels/module). The modules provide power to the strain gage stations, as well as acquire, filter and amplify the voltage according to the calibration specifications of the strain gages. Similarly the tension and drag load cells were connected to another NI 9237 module. The data from Laser displacement module was routed through an NI 9205 analogue input module, and the data from the three accelerometers was acquired through an NI 9234 analogue input module. All the modules were mounted in an NI cDAQ chassis, connected to the data acquisition pc through USB. All data was collected at a rate of 2000 samples per second, resulting in the Nyquist frequency of 1000Hz.

### 3.4 Curvatures and deflections

After applying the gage factors to the voltages obtained from the strain gages, the data was converted to strains, which were processed to obtain local curvatures at each strain gage station. With the data from 11 strain gage stations, it was assumed that the curvature varied linearly between consecutive measurement points.

For reference axis, a Cartesian frame of reference is considered where  $x$  axis is along the flow direction (opposite of travel direction),  $z$  axis is along the span of the riser and  $y$  axis is normal to both, satisfying right hand rule. The origin of the reference axis is positioned at the bottom universal joint of the riser assembly.

The curvature of the riser can be written as:

$$\begin{aligned} c_x(z, t) &= \frac{\partial^2 u(z, t)}{\partial z^2} \\ c_y(z, t) &= \frac{\partial^2 v(z, t)}{\partial z^2} \end{aligned} \quad (3.1)$$

Where  $c_x$  and  $c_y$  are the curvatures at each point, and  $u$  and  $v$  are the in-line, and transverse displacements at each point. The displacements, thus, are obtained by double integration of the measured curvatures.

$$\begin{aligned} u(z, t) &= \int_0^L \int_0^L \frac{\partial^2 u(z, t)}{\partial z^2} dz dz \\ v(z, t) &= \int_0^L \int_0^L \frac{\partial^2 v(z, t)}{\partial z^2} dz dz \end{aligned}$$

Where  $L$  is the total length of the riser model. As both ends of the riser model were connected to the frame using universal joints, the pinned-pinned boundary conditions are applied to the beam. The universal joints allowed rotation about  $x$  and  $y$  axis, and restricting the rotation about  $z$  axis, thereby no torsion was allowed in the riser. The displacements and the curvatures at the ends were zero. *i.e.*

$$\begin{aligned} u(0, t) = v(0, t) = 0 \quad , \quad u(L, t) = v(L, t) = 0 \quad \forall t \\ \frac{\partial^2 u(0, t)}{\partial z^2} = \frac{\partial^2 v(0, t)}{\partial z^2} = 0 \quad , \quad \frac{\partial^2 u(L, t)}{\partial z^2} = \frac{\partial^2 v(L, t)}{\partial z^2} = 0 \quad \forall t \end{aligned} \quad (3.2)$$

In addition to the double integration method described above, the curvature data was converted into displacements using the Ko displacement theory [86, 87], which carries out step-by-step deflection analysis assuming the curvatures between two measuring stations as constant:



$$\tan\theta_n = \frac{\Delta l}{2c} \left( \epsilon_0 + 2 \sum_{i=1}^{n-1} \epsilon_i + \epsilon_n \right) + \tan\theta_0$$

$$v_n = \frac{(\Delta l)^2}{6c} \left( (3n-1)\epsilon_0 + 6 \sum_{i=1}^{n-1} (n-i)\epsilon_i + \epsilon_n \right) + n\Delta l \tan\theta_0 \quad (3.3)$$

$$(3.4)$$

Where  $\theta$  is the slope of the beam at each point  $(1-n)$ ,  $\Delta l$  is the distance between two measuring stations,  $\epsilon_i$  and  $v_i$  are the measured strains, and the computed deflections at station  $i$ .

For a pinned-pinned end condition, the slope at the end is not zero ( $\tan\theta_0 \neq 0$ ), whereas  $v_0 = v_n = \epsilon_0 = \epsilon_n = 0$ . The value of  $\tan\theta_0$  is calculated by setting  $v_n = 0$  in equation 3.3, or

$$\tan\theta_0 = -\frac{1}{n(\Delta l)}v_n$$

The complete derivation of the Ko displacement theory is given in Ko *et al.* [87]. The procedure is repeated for both in-line and transverse stations to find the displacements  $u(z, t)$  and  $v(z, t)$  for each measurement. As opposed to the double-integration method, this method computes deflections between two consecutive stations with spline fitting. The results from both methods yielded identical results with less than 5% difference as both methods are based on almost similar assumptions.

A sample of one run in-line and cross-flow displacements at five spanwise locations for an example case, along with the close up of two seconds of data, and the frequency response of at that spanwise location are given in figure 3.10. The in-line oscillation comprises of two components, one being the mean deflection, which is the result of the mean drag acting on the cylinder, and the dynamic component, which is the oscillation about the mean deflection as a result of the vortex shedding. In order to determine the frequency response, the mean deflection values are subtracted from the in-line oscillation data, thereby giving us the dynamic oscillation in the in-line direction.

A sample of 2 seconds data of the instantaneous in-line oscillations about the mean deflection, and the transverse oscillations for the same example case are shown in the form of contours in figure 3.11. As seen in the figure, the in-line oscillations are in predominantly first structural mode, and the cross-flow oscillations are in the second structural mode of oscillation.

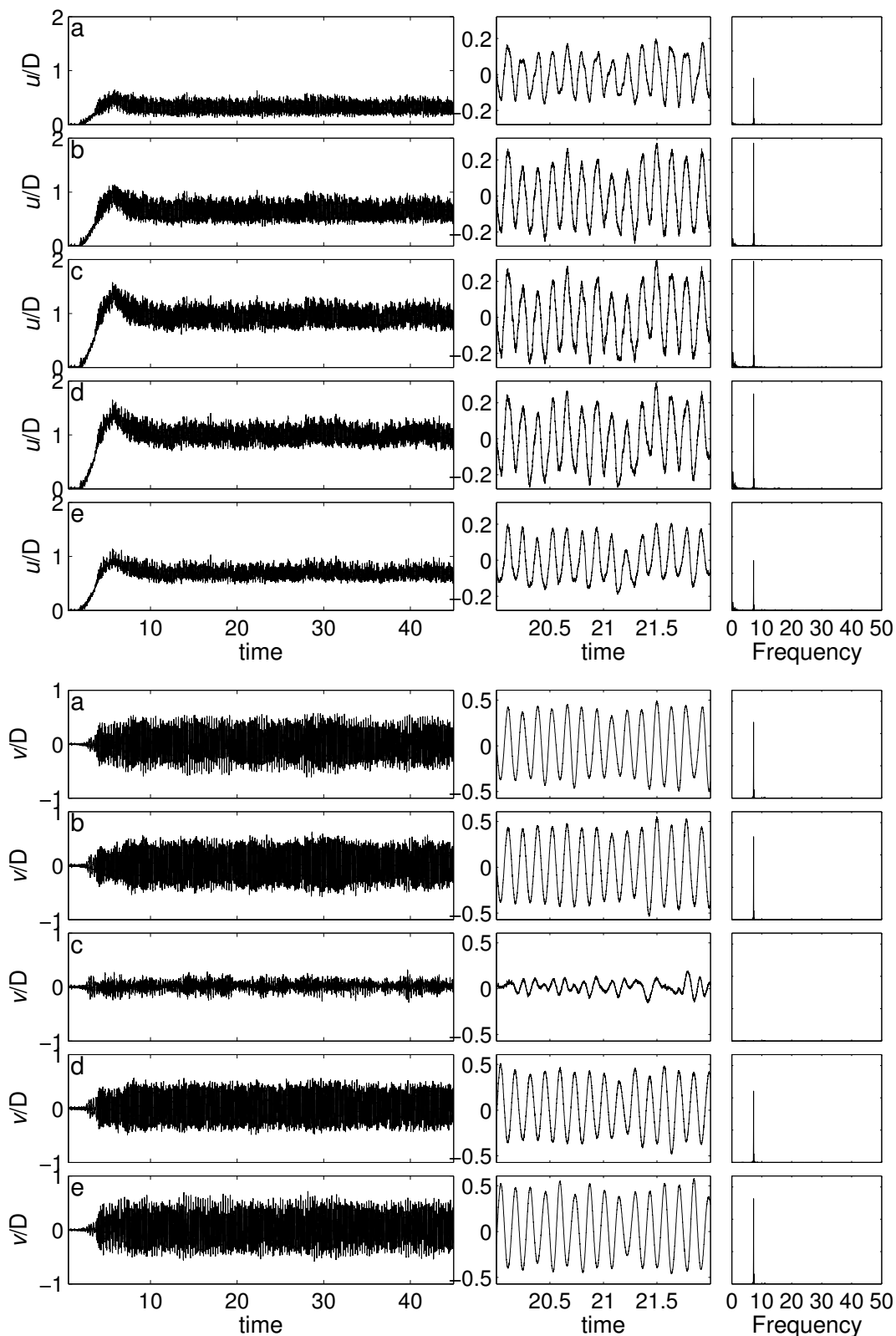


Fig. 3.10 Sample of displacements shown in the left column, a close up of 2 second data of oscillation about the mean deflection in the middle, and the frequency response at specified heights on the right. Top: In-line, Bottom: cross-flow. (a):  $z/L=0.786$ , (b):  $z/L=0.643$ , (c):  $z/L=0.5$ , (d):  $z/L=0.357$  and (e):  $z/L=0.214$ . Data acquired for  $m^*=2.70$ , with fixed end stiffness  $k_2 = 17.1N/mm$ , starting tension  $T_2 = 397N$ .  $U_\infty = 0.8m/s$

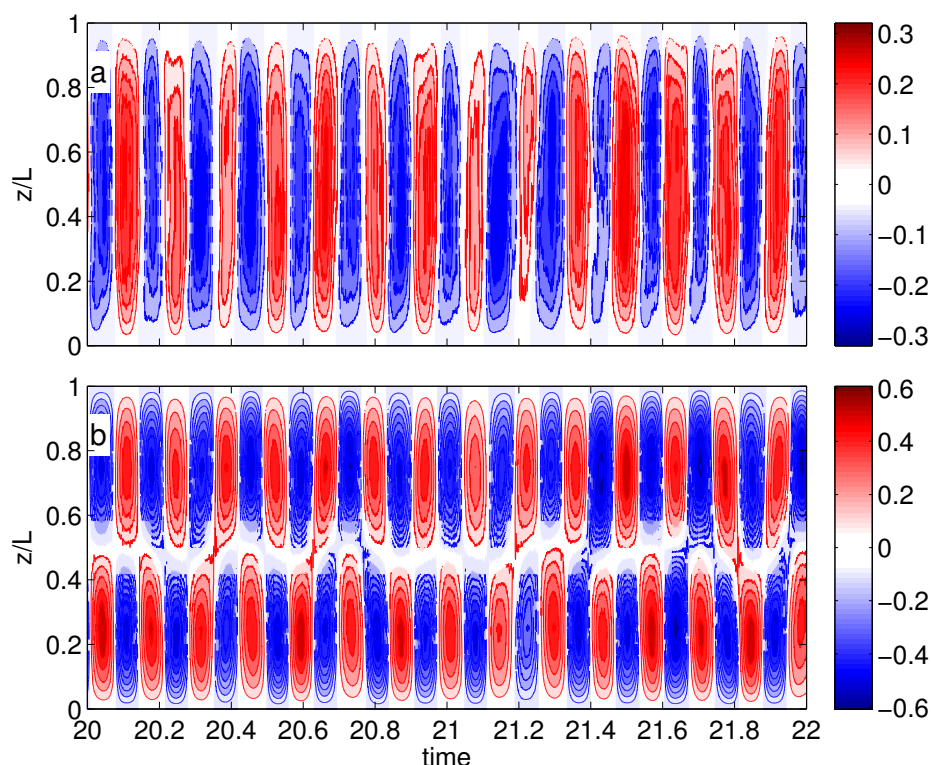


Fig. 3.11 Sample of 2 seconds of displacement data, shown in form of the contours, encompassing the entire span of the riser. (a): In-line, and (b): Transverse displacement. Data for  $m^*=2.70$ , with  $k_2 = 17.1N/mm$ , starting tension  $T_s = 397N$ .  $U_\infty = 0.8m/s$

As mentioned in section 3.1.2.1, an external distance measuring system comprising of a high precision LDMS, in conjunction with a reflector strip was used for independent verification of the displacement data. The sensor plate was positioned above the water level, corresponding to  $z/L = 0.76$ . The sample matching of data for one time series is shown in figure 3.12. This verification process was part of analysis for every run, in order to determine if any of the strain gages had malfunctioned during the tests. The results were found to match satisfactorily.

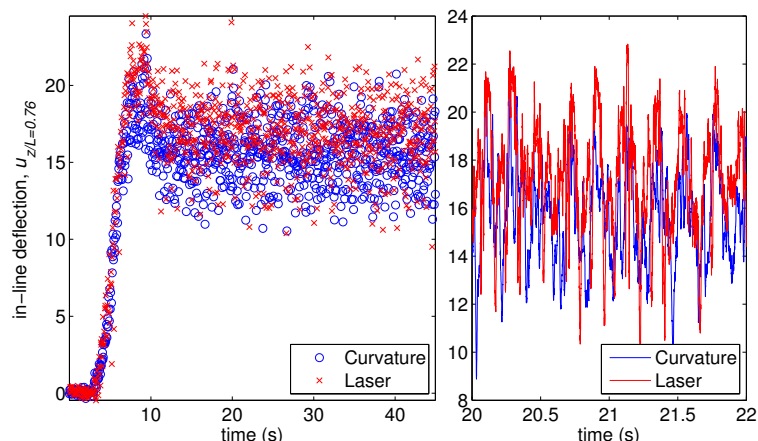


Fig. 3.12 Example of deflection computed from curvature data, and measured through laser sensor. Left shows an entire run, and right shows two seconds of data. Data for  $m^*=2.70$ , with fixed end stiffness  $k_2 = 17.1N/mm$ ,  $T_s = 397N$ .  $U_\infty = 1.2m/s$

### 3.5 Modal Analysis

Operational Modal Analysis is the identification of modal properties of a structure, based on the vibration data. This exercise can be carried out by either assuming the mode shapes based on the theoretical assessment of the structure, and determine the contribution of each of those assumed mode shapes from the response of the riser, or the dominant structural mode shapes can be determined from the time domain data by various means, and the contributions of those dominant mode shapes can be calculated. The purpose of this analysis is to identify the dominant modes of oscillation, as well as the contribution of non-dominant modes to the overall vibration characteristics of the structure.

The deflection, at any instant in time, along the span of the cylinder can be given as:

$$\mathbf{U}(z, t) = \mathbf{\Phi}(z)\mathbf{A}_x(t) \quad (3.5)$$

Where  $\mathbf{U}(x, t)$  is the displacement matrix.  $\mathbf{A}_x(t)$  is the amplitude matrix of the displacement modes.  $\mathbf{\Phi} = [\phi_1, \phi_2, \phi_3, \dots, \phi_n]$  is the modal shapes matrix representing the displacement modes. This method has commonly been used for structural modal analysis. In case of VIV, this method has been employed by many researchers like Lie & Kaasen[93], Willden & Graham[165] and Chaplin *et al.* [38]. In order to determine the in-line modal responses the mean displacement is removed from the measurements for

the in-line direction. A pre-defined, standard mode shapes matrix can be formulated that generally conforms to the displacements matrix for all runs, which will make the statistical comparison possible for various run conditions. Alternatively, the displacement matrix can be used to formulate mode shapes matrix for each individual run, by using one of the various algorithms devised for modal identification.

### 3.5.1 Standard mode shapes matrix

It is predicted by the beam theory that a pinned-pinned beam under uniform tension, when forced to oscillate, will result in sinusoidal mode shapes. Using that assumption, we can say that the modal shapes matrix could be constructed using sinusoidal mode shapes normalized to 1. The components  $\phi_n$  are given by equation:

$$\phi_n = \sin\left(\frac{n\pi z}{L}\right) \quad (3.6)$$

Looking back at the conversion of the curvature data obtained from the strain gages, it is apparent that the curvature data could be converted directly into the modal shapes matrix and analytical integration can be carried out to yield the similar results as obtained from numerical integration indicated in equation 3.2, or from Ko's theory 3.3, as

$$\mathbf{C}_x(z, t) = \frac{\partial^2(\mathbf{U}(z))}{\partial z^2} = \frac{\partial^2\Phi(z)}{\partial z^2}\mathbf{A}_x(t) \quad (3.7)$$

giving us

$$\mathbf{A}_{x,y}(t) = \Phi_c^{-1}(z)\mathbf{C}_{x,y}(z, t) \quad (3.8)$$

where

$$\Phi_c(z) = \frac{\partial^2\Phi(z)}{\partial z^2} \quad (3.9)$$

The matrix  $\Phi_c(z) = [\phi_{c1}, \phi_{c2}, \dots, \phi_{cn}]$  is the curvature mode shape matrix, where the columns are non-dimensional curvature mode shapes. The sinusoidal curvature mode shapes are given by:

$$\phi(z) = \sin\left(\frac{n\pi z}{L}\right) \quad (3.10)$$

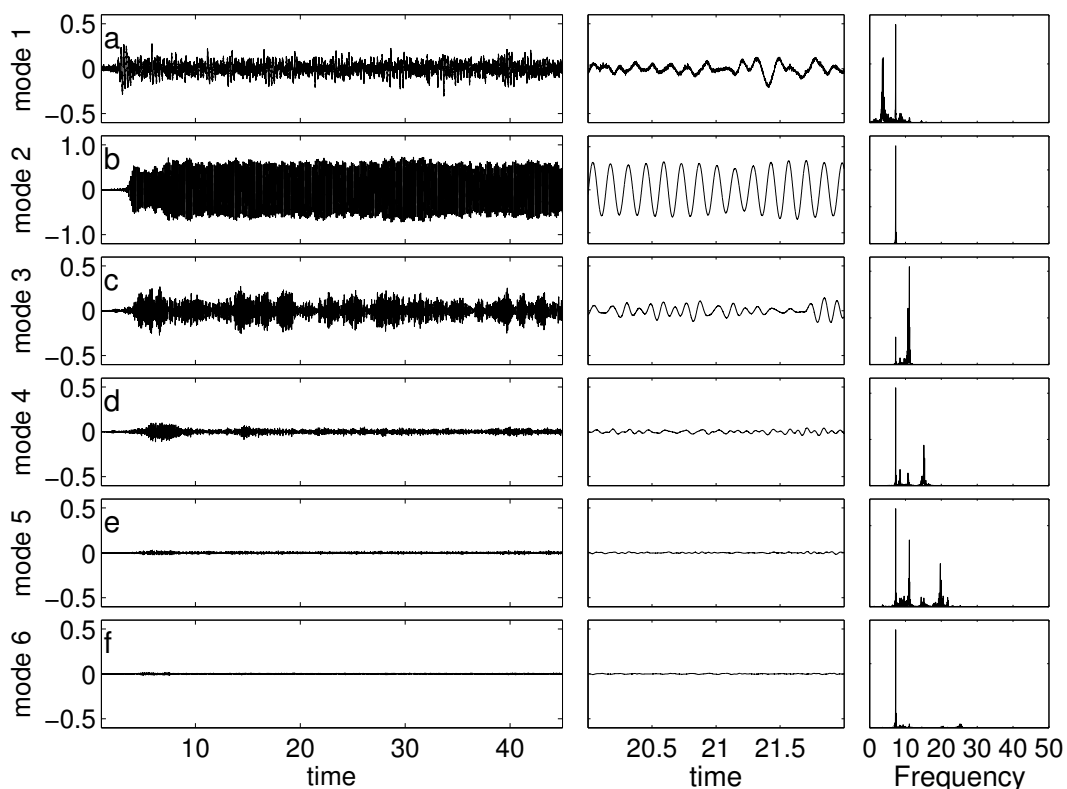


Fig. 3.13 Sample of Non-dimensional transverse modal amplitudes shown in the left column, a close up of 2 second data shown in the middle, and the frequency response at each mode on the right. (a):Mode 1, (b):Mode 2, (c):Mode 3, (d):Mode 4 and (e):Mode 5 and (f):Mode 6. Data acquired for  $m^*=2.70$ , with fixed end stiffness  $k_2 = 17.1N/mm$ , starting tension  $T_2 = 397N$ .  $U_\infty = 0.8m/s$

And the second derivative results in:

$$\frac{\partial^2 \phi_n(z)}{\partial z^2} = - \left( \frac{n\pi}{L} \right)^2 \sin \left( \frac{n\pi z}{L} \right) \quad (3.11)$$

Using a fairly high value of the number of modes,  $n$ , it is expected that the total modal amplitudes determined using the displacements, or the curvatures should give us a very close approximation of the displacements of the cylinder. In almost all cases of the conducted experiments, the modal response beyond 6<sup>th</sup> mode was observed to be negligibly small. An example of the first 6 transverse modal amplitudes ( $A_{x,y,i}, i = 1, 2, \dots, 6$ ) for the entire length of the run, and a sample 2 second data are shown in figure 3.13. The column on the right shows the frequency response for the particular mode. These modal responses are before any data filtering.

The modal contribution plot shown in figure 3.13 is for the same case as shown in form of contours in figure 3.11. The highest modal contribution, clearly, is in the second mode. As for all the real riser cases, the riser oscillation is not purely sinusoidal. The practical limitations of implementing a pre-defined mode shape matrix arise from the following issues:

1. As observed in the equation 3.11, each modal amplitude is multiplied by the square of the mode number. The curvature of low mode shapes could be so low that it is obscured by the electrical noise, or that the electrical noise may be picked up as a low mode shape oscillation.
2. For non-uniform tension cases, which are most common in vertically mounted risers, or in case of the riser immersed in sheared flow, the riser deflection may vary from the assumed sinusoidal mode shapes. In that case, the modal contributions are indicated in higher, or lower modes.

For the resolution of the first issue, a procedure originally proposed by Huera-Huarte[71] was employed to eliminate the lower spurious modes. It consists of finding the ratio of the standard deviation of mode  $i$  to the summation of the standard deviation of all the modes, and if the ratio is below a certain threshold, the lower modes could be discarded by setting the corresponding  $\phi_{ci}$  equal to zero in the  $\Phi_c$  matrix. This criteria was set at 5%, as this resulted in cleaner, well defined modal amplitudes with insignificant alteration of the resulting deflection shapes. For cross-flow modes this process was carried out only for the first mode, as the higher modes in cross-flow oscillation were mostly unaffected. For in-line oscillation, as the mode shapes are influenced by the flow, the procedure was carried out for the first two modes.

The second issue is the deviation from pure sinusoidal mode shapes. When considering real life situation, both the in-line and the cross-flow deflections are significantly altered from the pure sinusoidal shapes due to non-uniform tension (by virtue of the weight), added mass variation along the span, mean curvature, and sheared flow. The in-line oscillations have additional contributing factors such as the drag differential in the upstream ( $-x$ ) and downstream ( $x$ ) direction. In practical application of using the pre-defined mode shape matrix, the shape of the riser at each snapshot in time is correctly approximated as the summation of the sinusoidal mode shapes. A few snapshots of the actual displacements, and the displacements from the modal contribution for the high mass ratio ( $m^* = 2.7$ ) riser and low mass ratio ( $m^* = 1.1$ ) risers are shown in figure 3.14.

---

As seen in these figures, the modal contributions sum up to a perfect match. However both these cases are for almost pure  $2^{nd}$  mode cross-flow oscillation, and the modal contributions indicate presence of  $1^{st}$ ,  $3^{rd}$  and higher modes, as the shape is altered from the assumed pure sinusoidal shapes. The low mass ratio riser response showed greater difference from the assumed sinusoidal mode shapes, resulting in greater chances of indicating spurious modes. For overall statistical results, this issue is of less importance as the general mode of oscillation, and the dominant frequency can be extracted from the modal contributions matrix, and the shape of modal response can be reconstructed from the amplitudes of the fast fourier transform (FFT) at the dominant frequencies, an example of which is shown in figure 3.15.



Multi-mode VIV of Long Flexible Cylinders :  
 Set-up, measurements, analysis

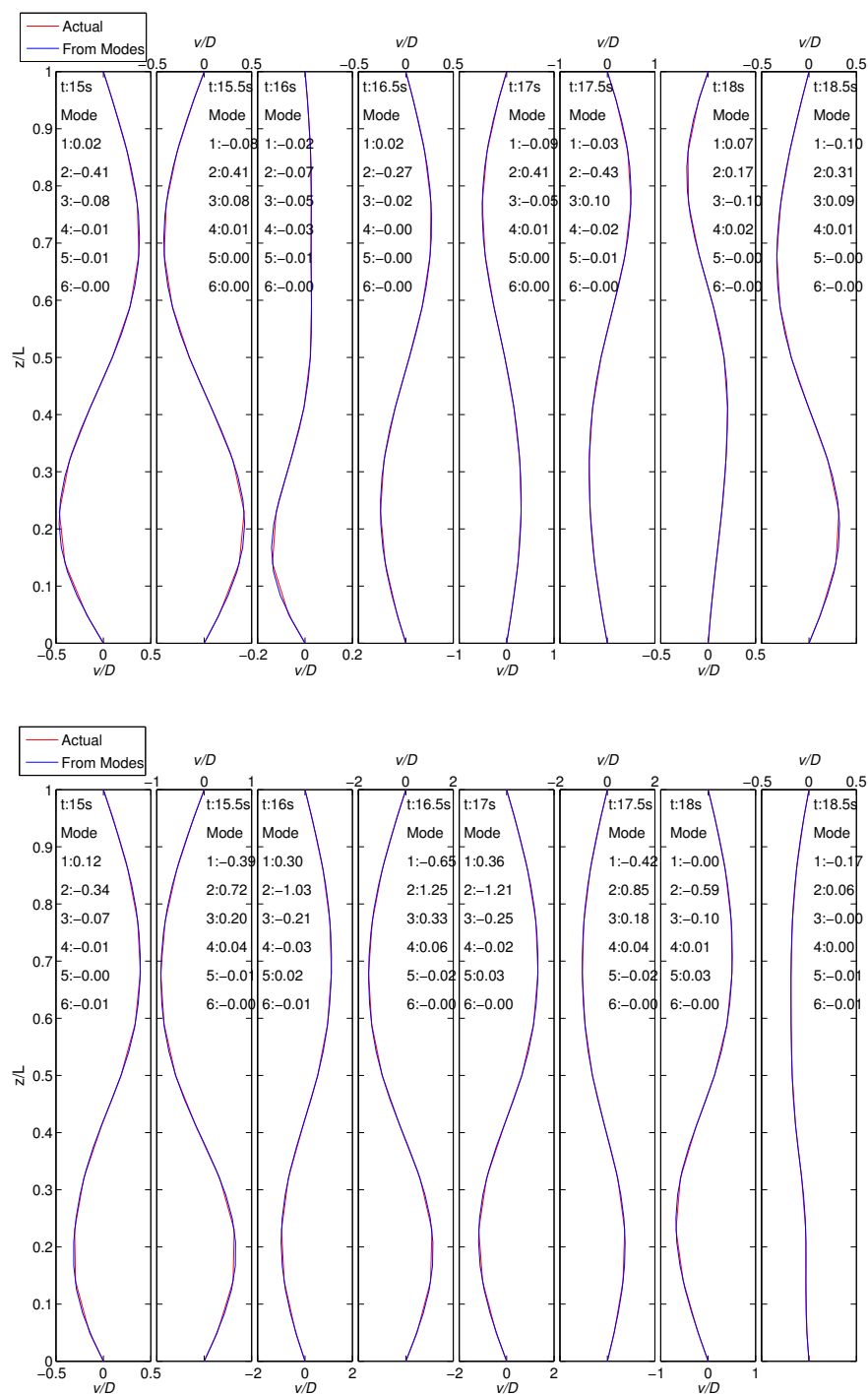


Fig. 3.14 Sample snapshots of the modal contribution fit of the high mass ratio riser ( $m^* = 2.7$ ) (top) and low mass ratio ( $m^* = 1.1$ ) (bottom). Time of snapshot and the contributing modes listed in tabular form for each plot. red line indicates actual displacement and blue indicate mode shape fit.

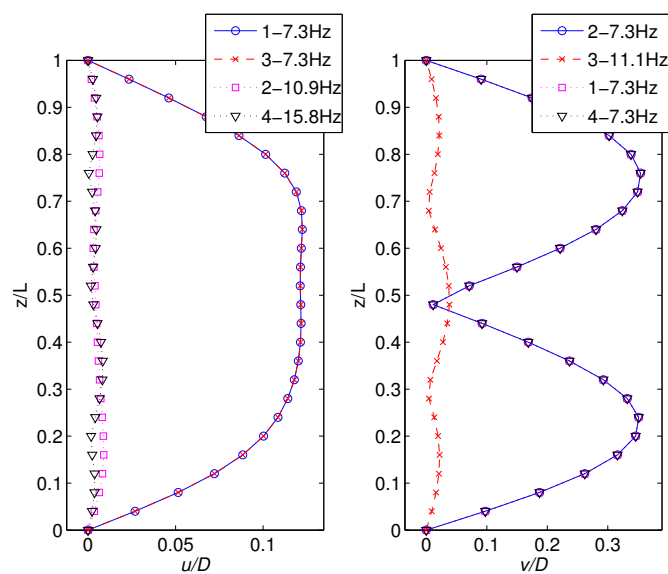


Fig. 3.15 Sample representation of in-line and crossflow non-dimensional modal amplitude, along the span of the riser, extracted using pre-defined mode shape matrix. Data for  $m^*=2.70$ , with fixed end stiffness  $k_2 = 17.1N/mm$ , starting tension  $T_2 = 397N$ .  $U_\infty = 0.8m/s$ .

### 3.5.2 Blind Source Separation

Blind source separation deals with recovering a set of underlying sources from observation, without knowing the mixing process processing and the sources [181]. In simpler terms, this means extracting the mode shape matrix from the observed displacements, without assuming the shapes. There are several methods such as the *Algorithm for multiple unknown signals extraction* (AMUSE)[91], *Temporal decorrelation separation* (TDSEP)[182], and *Second order blind identification* (SOBI)[14] among many others. These methods generally use auto- and cross-covariance matrices. We used SOBI method, where the displacement matrices are first converted into several time-delayed covariance matrices, and the mode shapes are extracted by simultaneously diagonalizing these matrices.

The results of SOBI based mode shapes and the corresponding frequencies for the case shown in figure 3.15 are shown in figure 3.16

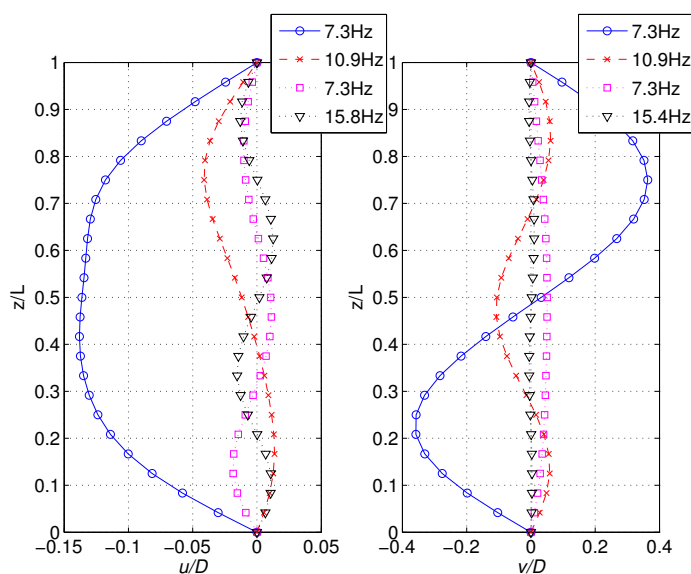


Fig. 3.16 Sample of in-line and crossflow mode shapes using blind source separation. Data for  $m^*=2.70$ , with fixed end stiffness  $k_2 = 17.1N/mm$ , starting tension  $T_2 = 397N$ .  $U_\infty = 0.8m/s$ .

For an individual case, SOBI, or any BSS methodology is an excellent method to determine the dominant mode shapes. The frequency of each mode is determined by FFT of amplitude matrices, and the contribution of each mode shape are determined by normalizing the contribution matrices to the non-dimensional length (1D). Each run results in a unique mode shape matrix.

In order to define statistical similarity, the mode shapes from BSS techniques have to be categorized by some standard criteria that is applicable to all the run cases. An obvious choice is comparing the extracted mode shapes to the standard, sinusoidal mode shapes, however in many cases there are more than one BSS mode shapes in a single mode shape matrix that can be categorized in each sinusoidal mode shape.

An obvious point here is that the validity of the modal contributions obtained from pre-defined mode shapes matrix is dependent on how suitable are the predefined mode shapes, that are used in the  $\Phi$  matrix. In case of a close fit, the results from both methods are almost identical. The amplitude of the response along the span of the riser extracted from the power distribution at highest modal frequencies, shown in figure 3.15 are the almost identical (albeit these are absolute values) to the mode shapes determined from BSS as shown in figure 3.16. It is clear that either method can be used, with proper elimination techniques, for true mode shape identification provided a reasonably valid assumption is made for the pre-defined mode shape matrix. Generally, in all the runs, the largest oscillations were comprised of sinusoidal mode shapes, whereas higher, or lower harmonics at lower amplitudes showed differences from the results obtained by the two methods. A comparative look at both methods can also be seen in figure 3.17.

As evident from the two plots, there are significant similarities when considering the biggest contributing modes to the structural response- The maximum oscillation response is comparable to the second sinusoidal mode of oscillation, for both in-line and cross-flow oscillation using either method. The differences are that in case of in-line oscillation, the blind source separation indicates a teardrop-shaped mode at 3.4 Hz. That response does not stand out when using sinusoidal mode shapes matrix. In case of cross-flow oscillation, the modal response from sinusoidal mode shapes matrix comprises of significant contributions of 1st and 3rd modes at the dominant frequency of the 2nd mode. Blind source separation indicates just one mode shape that is comparable to 2nd sinusoidal mode of response, and almost negligible response at other modes.

As evident from the above examples, both methods are effective at identifying the contribution of significant modes, and both methods have their own limitations. In case of pre-determined mode shapes matrix, the issue arises when the actual oscillation mode is not close to the assumed mode shapes used in the matrix. The blind source separation results in mode shapes that fit the data, however the mode shapes are different for every test case and can not be properly standardized for statistical references.

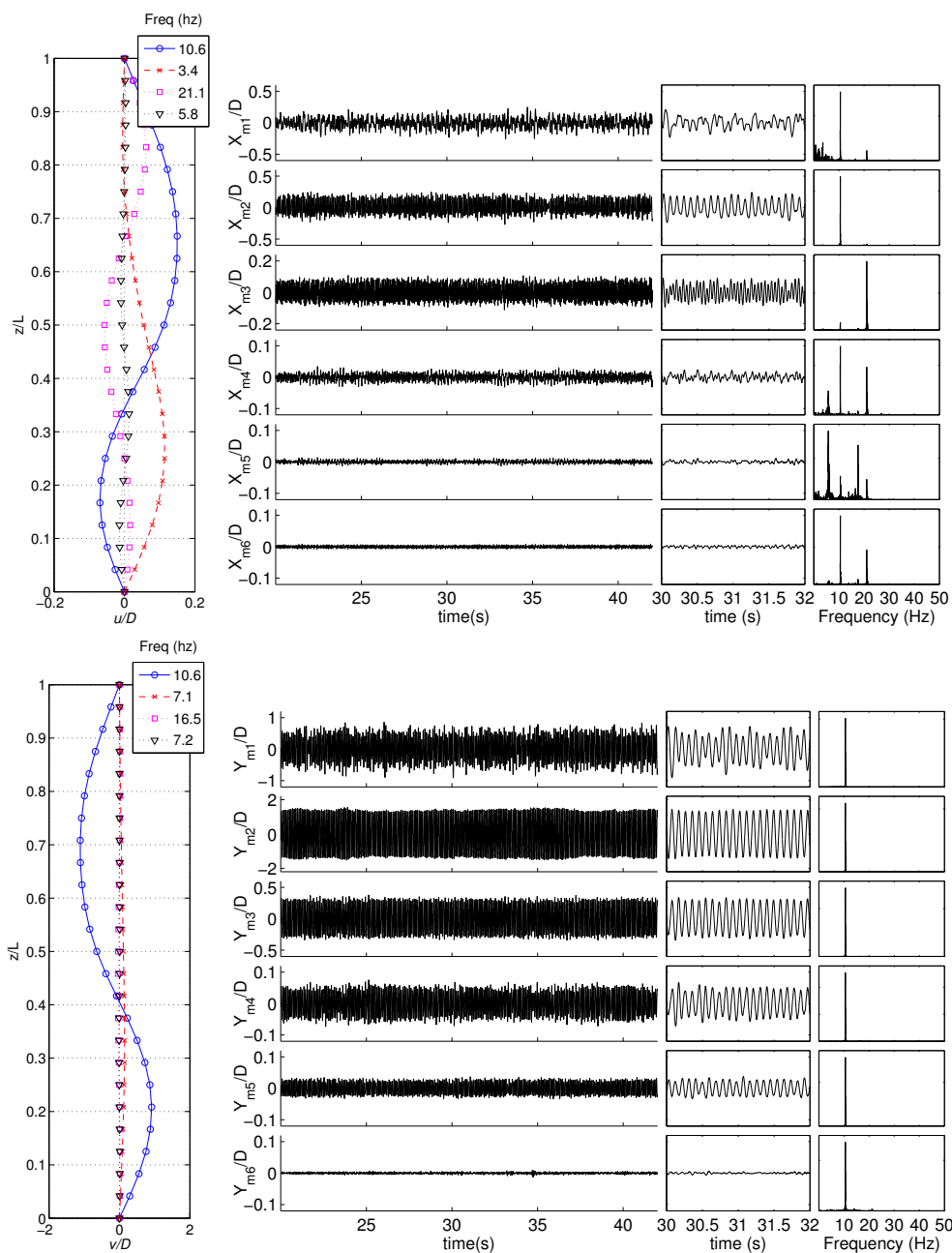


Fig. 3.17 Comparison of the blind source separation mode shapes, and frequencies (left) to the modal contribution obtained using the sinusoidal mode shapes matrix (right). Top row indicates in-line and bottom row indicates cross-flow oscillations. Case  $U^* = 11.5$   $m^* = 1.1$   $T = 560N$

The modal contributions, as they have to be standardized, were computed using pre-defined modal shapes matrix. The blind source separation method was used for

validation of the dominant frequency and mode shape, and for analysis of multiple modes.

## 3.6 Tension and Drag

The processing of data acquired from both tension load cells and drag load cells was straightforward. The load cells came pre-calibrated, and the calibrations were checked by hanging known weights from the load cells. The results from confirmation tests showed that the load cells performed accurately.

The tension data, acquired in millivolts, was converted into physical values based on the conversion factor provided by the manufacturer. During tests, as the carriage is accelerated the riser pipe undergoes a mean deflection as a result of the drag. This mean deflection results in the extension of the springs mounted on the top of the cylinder. As the end spring stiffness,  $k$  is known, the extension of the spring and the resulting increase in the tension can be calculated by determining the change in the distance between the top universal joint and the bottom universal joint, which is equal to the difference of the nominal length of the riser and the arc length formed because of the deflected shape. Figure 3.18 shows a sample of the change in tension over the entire length of the run, as measured using the load cell, and how it matches the values computed using the arc length with the known spring stiffness.

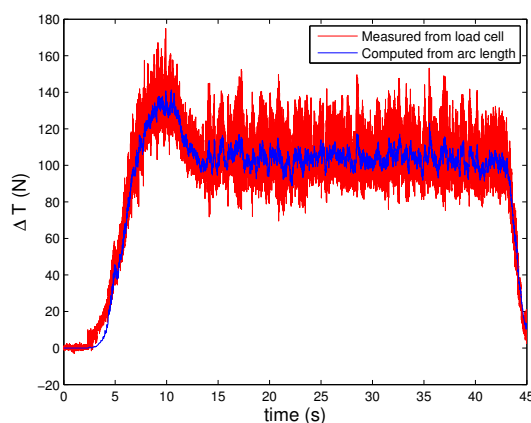


Fig. 3.18 Sample of  $\Delta T_t$  measured from load cell, and computed from arc length. Data for  $m^*=2.70$ , with fixed end stiffness  $k_2 = 17.1N/mm$ , starting tension  $T_2 = 397N$ .  $U_\infty = 1.6m/s$ .

Computations of drag values involved a slight complication. There are two ways to determine the drag of the riser pipe, *i.e.* (a) using the drag load cell directly, and (b)

by resolving the measured tension into components based on the curvature of the riser. This method has been successfully used before by Huera-Huarte [65].

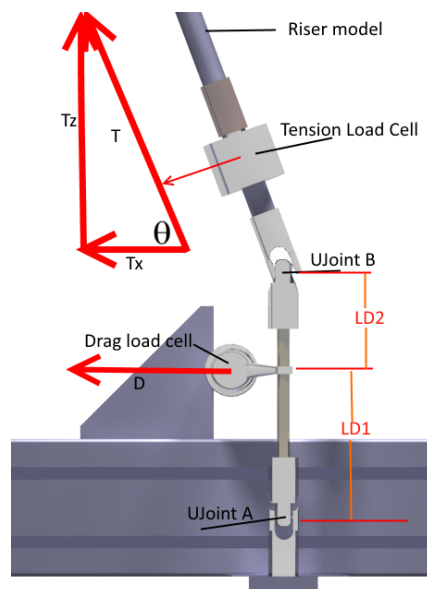


Fig. 3.19 Drag load cell measurement, and tension decomposition into drag

As seen in figure 3.19, the value of drag can be measured by both these methods. The drag load cell is positioned between the two universal joints. The distances LD1 and LD2 are the distances between the load cell and the bottom universal joint and the top universal joint. The measurement from drag load cell is corrected for the lever effect by using the following equation:

$$F x_{dlc} = \frac{F x_m \cdot LD1}{LD1 + LD2}$$

For the bottom drag load cell, the distances LD1 and LD2 were fixed, which makes the computation straightforward. The top drag load cell was fixed in the frame, whereas the universal joint B moved as riser adopted the mean deflection, resulting in the extension of the spring bank. This caused the ratio of LD1 and LD2 to change. In order to determine correct drag, LD1 and LD2 were determined by computing the change in the length of the spring bank according to the procedure explained earlier.

The tension load component in the  $x$  direction could be determined by resolving the total tension into the two components based on the previously computed riser deflection at the bottom end and the top end.

$$T_{tx} = T_t \cos \theta_t = T_t \cdot \cos \left( \operatorname{atan} \left( \frac{du}{dx} \right)_{z=l} \right)$$

$$T_{bx} = T_b \cos \theta_b = T_b \cdot \cos \left( \operatorname{atan} \left( \frac{du}{dx} \right)_{z=0} \right)$$

After applying the necessary corrections to the top and bottom drag load cells data, the results obtained from both methods were practically identical.

The drag forces were converted into non-dimensional coefficient forms ( $C_D$ ) as

$$C_D = \frac{D_{top} + D_{bottom}}{\frac{1}{2} U_\infty^2 L_s D} \quad (3.12)$$

## 3.7 Natural frequencies and decay characteristics

Before the series of tests carried out at ETSIN, the riser damping characteristics in air, and in submerged state were determined experimentally. For this purpose, a mechanical oscillator was designed to convert the rotation of a motor, using a disk mounted with an offset of 1cm, acting as a cam. This cam was inserted in a slider, which was connected near the top end of the riser model with a rigid rod. The geometry of the cam and slider resulted in a pure sinusoidal oscillation at the end of the riser. The motor speed was controlled using a frequency controller. This enabled us to impart forced oscillations of known frequencies on the riser model.

### 3.7.1 Experimental determination of natural frequencies

The data acquisition was started when the model achieved a stable mode of oscillation, normally the highest that could be achieved by the motor. The speed was gradually reduced, and sustained at the frequency where the model displayed the next lower mode of oscillation. A sample of the full length of the acquired data, with a 0.5 second window, shown for clarity of the waveform, and the FFT chart indicating the frequency at the maximum amplitude are shown in figure 3.20.

The results obtained during modal testing were used for validation of the analytical models. The actual run tension varied significantly from these pre-set tensions, and the analytical models were used to determine the fundamental modal frequencies.



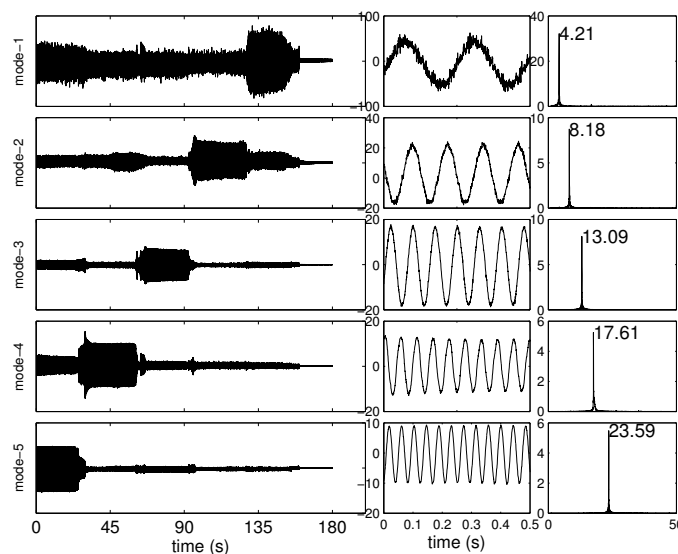


Fig. 3.20 Sample of modal frequency tests, for riser with  $m^* = 2.70$ ,  $k_2 = 17.1N/mm$ , starting tension  $T_2 = 397N$ .

### 3.7.2 Decay tests

The natural frequency of a riser, like all flexible beams, is characterised by the mode shape and the modal damping ratio. In order to determine the damping characteristics, the structural damping in air was tested for both riser models. These tests were carried out at various applied tensions, and results were obtained for up to 4<sup>th</sup> mode, and in some cases up to 5<sup>th</sup> mode of structural oscillation.

In order to determine the decay characteristics the same driving mechanism as described in the previous section was used to excite the riser by imparting sinusoidal oscillation at the end, matching the frequency that resulted in the desired vibration mode shape. Once a stable mode shape was achieved, the driving motor was stopped. The data was acquired as the model oscillations decayed to almost zero, and the riser approached the natural position. An example of the decay characteristics are shown in figure 3.21.

For this test, the riser model was excited at 9.6 Hz (60.59 Radians/s) vibrations at an amplitude of 0.8 diameters. Once the stable mode shape was achieved the motor was stopped and the riser vibrations decayed till the cylinder achieved almost neutral position. As decay is exponential, the vibrations continue at a very low amplitude for many seconds. The envelope edges were obtained using a simple script written in matlab, and were given by:

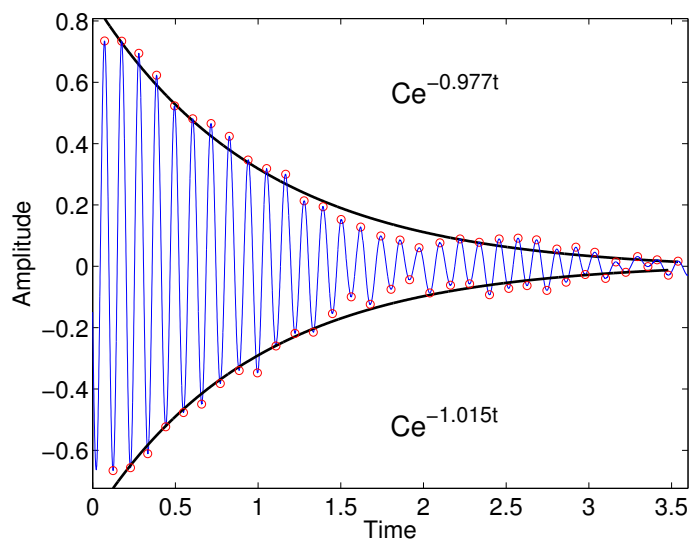


Fig. 3.21 Sample of modal decay tests, for riser in 3<sup>rd</sup> structural mode of vibration.  $m^* = 2.70$ ,  $k_2 = 17.1N/mm$ , starting tension  $T_2 = 397N$ .

$$e(t)_3^{up} = Ce^{-0.977t}$$

$$e(t)_3^{dn} = Ce^{-1.015t}$$

The damping ratio, which is the ratio of the structural damping to the critical damping is given by

$$\zeta_6 = \frac{0.977 + 1.015}{2 \cdot \omega_i} = 0.0164$$

In all the cases, the structural damping remained significantly lower than 3% of the critical damping. The effect of damping on natural vibration is given by

$$\omega_{id} = \left( \omega_i^2 - \left( \frac{\bar{C}_i}{2M_i} \right)^2 \right)^{\frac{1}{2}}$$

where C is the damping matrix. For classical normal modes, Rayleigh showed that the damping matrix is a linear combination of the stiffness and inertia matrices, or

$$C = \alpha M + \beta K$$

where the coefficients  $\alpha$  and  $\beta$  are computed from the modal structural damping ratios, and the corresponding frequencies as

$$\alpha + \beta\omega_i^2 = 2\omega_i\zeta_i$$

The resulting  $\alpha$  was always less than 0.1, and  $\beta$  remained below 0.005 even for the lowest tension cases. It was concluded that for such low damping, the effects on the lower mode natural frequencies is insignificant, and it can be ignored for all practical purposes.

### 3.7.3 Analytical computation of Natural Frequencies

There are various analytical models that can be used to determine the natural frequencies for various modes for the model under tension. The analysis was carried out using two different methods to estimate the natural frequencies of a pinned-pinned tensioned beam. In order to perform accurate analytical estimation, the damping characteristics have to be determined at each tension, which is a formidable task considering that the tension at every run was different. As described earlier, the experimentally determined damping characteristics even at the lowest tension revealed very low damping, the analytical modelling became significantly straightforward.

in case of a pinned pinned beam under tension, P, as shown in figure A.1, considering the equations of motion for an element of the beam, for motion along  $x$  axis:

From the elementary theory of bending beams, we have:

$$M(z, t) = EI \frac{\partial^2 u}{\partial z^2}(z, t) \quad (3.13)$$

where  $u$  is the response of the beam in  $x$  direction. The forces in  $x$  direction are:

$$-(V + dV) + fdz + V + (T + dT)\sin(\theta + d\theta) - T\sin\theta = \rho Adz \frac{\partial^2 u}{\partial t^2} \quad (3.14)$$

The moments about the bottom middle of the segment are given by:

$$(M + dM) - (V + dV)dz + fdz \frac{dz}{2} - M = 0 \quad (3.15)$$

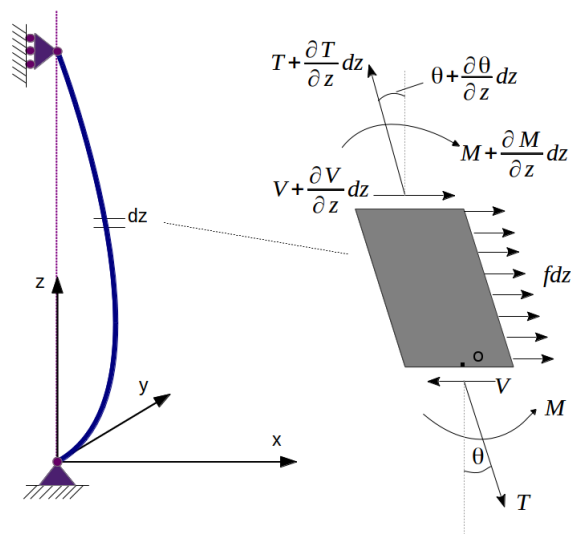


Fig. 3.22 Pinned-pinned beam under tension with load  $f(z,t)$ , from Rao[125], Huera-Huarte & Gonzalez[72]

For very small deflections the value of  $\sin(\theta + d\theta)$  is given as:

$$\begin{aligned} \sin(\theta + d\theta) &\approx \theta + d\theta = \theta + \frac{\partial\theta}{\partial z} dz \\ &= \frac{\partial u}{\partial z} + \frac{\partial^2 u}{\partial z^2} dz \end{aligned}$$

The above equations can be combined to yield a single differential equation of motion:

$$\frac{\partial^2}{\partial z^2} \left( EI \frac{\partial^2 u}{\partial z^2} \right) + \rho A \frac{\partial^2 u}{\partial t^2} - T \frac{\partial^2 u}{\partial z^2} = f \quad (3.16)$$

In case of free vibrations ( $f = 0$ ) of a uniform beam under constant tension, the solution can be determined by separation of variables. After a few simple steps and applying the necessary boundary conditions, the natural frequencies are, as given by Rao[125] :

$$f_n = \sqrt{\frac{n^4 \pi^2 EI}{4L^2 M} + \frac{T n^2}{4L^2 M}} \quad (3.17)$$

Where  $f_n$  is the  $n^{th}$  mode natural frequency,  $EI$  is the stiffness coefficient, which is the product of modulus of elasticity  $E$  and the area moment of inertia,  $I$ ,  $M$  is the mass per unit length,  $L$  is the model length and  $T$  is the tension.

In addition to neglecting the damping, which causes a slightly lowered natural frequency, the effects of non-uniform tension along the span of the riser, by virtue of the weight of the riser are also considered negligible. The tension used in the equation is the average of the tension measured at the top and bottom of the riser.

In order to consider the effects of non-uniform tension, and the added mass over the wetted area of the riser the equation 3.16 is converted into corresponding discrete forms using Differential Quadrature method [123, 138], and resolved for the eigenvalues. The process is briefly explained in Appendix A. The added mass, as explained in section 2.2.1.2, was idealized based on the equation:

$$m_{added} = \rho_{water} \frac{\pi}{4} D^2 \quad (3.18)$$

The frequencies obtained thus, theoretically, have compensation for the idealized added mass over the wetted region of the riser, as well as the variation of tension along the span of the riser. Some of the results from the experimental determination of frequencies in air, compared with the numerical method described above, are presented in table 3.3. Table 3.4 shows some of the results for wetted configuration. In light of these results, it is a reasonable assumption that the numerical method using DQM can predict the modal frequencies of the riser submerged in water with reasonable accuracy. Additionally the structural damping coefficients are low enough that they can be neglected.

Table 3.3 Experimental and Numerical Frequencies, in air

Model	Tension (N)	Mode	Exp. f(Hz)	Num. f(Hz)
$m^* = 2.70$	176	1	2.8	2.75
		2	6.16	5.9
		3	9.9	9.6
		4	14.01	14.23
		5	19.4	19.8
$m^* = 2.70$	333	1	4.2	4.04
		2	8.18	8.14
		3	13.09	12.9
		4	17.61	18.1
		5	23.59	24.3
$m^* = 1.10$	343	1	6.07	5.98
		2	10.89	11.07
		3	17.61	17.37
		4	24.32	24.52
$m^* = 1.10$	407	1	6.84	6.32
		2	12.91	12.92
		3	19.68	20.02
		4	26.49	27.8

Table 3.4 Experimental and Numerical Frequencies in water

Model	Tension (N)	Mode	Exp. f(Hz)	Num. f(Hz)
$m^* = 2.70$	274	1	3.48	3.54
		2	7.32	7.37
		3	10.86	11.21
		4	17.12	16.91
$m^* = 2.70$	323	1	3.54	3.88
		2	8.06	8.02
		3	12.27	12.65
		4	18.49	18.05

UNIVERSITAT ROVIRA I VIRGILI

VORTEX INDUCED VIBRATIONS OF LONG FLEXIBLE CYLINDERS WITH AND WITHOUT WAKE INTERFERENCE

Denise Fischer Hubert

Dipòsit Legal: T 992-2015

## CHAPTER 4

### MULTI-MODE VIV OF LONG FLEXIBLE RISERS; RESULTS

---

#### 4.1 Introduction

The response of the flexible risers undergoing vortex induced vibrations can be presented in various ways. For the case of rigid cylinders, the most important response parameters are the amplitude of oscillation and the frequency of oscillation. In case of flexible cylinders the results are usually staggered in multiple mode responses. As the flow velocity is increased, the shedding frequency comes close to a modal natural frequency and the resonance results in significantly higher response. Further increase in the flow velocity results in higher shedding frequency, and thus a lower response. As the velocity is increased further, the shedding frequency ends up matching the next modal natural frequency and the process is repeated. If the shedding frequency is between the two modal frequency, the conventional thought is that the response should be minimal.

Some of the result parameters are simpler, such as the maximum deflection and mean drag, whereas other results are complex and vary along the span of the riser for each case. In case of flexible cylinders, as the response may comprise of a single mode single frequency oscillation or a combination of multiple modes and multiple frequencies, the response can be presented in terms of the modal contribution and oscillation frequency breakdown. Statistical parameters are used for general overview of the results.

A concise version of these results have been published in Huera-Huarte *et al.* [66]. the results given in this chapter are presented with some more details.



## 4.2 Analysed sections

The data presented in this chapter mostly comprises of a specific time window from the entire run. All the runs that were carried out contained 45 seconds of acquired data. Nominally the first 1-2 seconds of data was acquired before starting the carriage in order to determine the offset for all channels. After that as the carriage accelerated, the riser vibrations started and reached a peak value as the carriage approached its desired velocity, before settling down to a steady state. For this purpose the first few seconds of the data, where the carriage accelerates to its run velocity, and a few seconds after that till the transient response completely dissipates into a steady state response, are removed from analysis. The time of initial acceleration, and the transient response time varied with the carriage speed, and thus was different for every case. The response curves were first plotted for the entire length, and after individual examination, sections of steady response were picked for evaluation.

## 4.3 Synopsis

Ideally, the response of the riser is assumed to follow a specific pattern of repeated cycles of lock-in conditions as the reduced velocity  $U^*$  is increased, with regions of low response between the lock-in regimes. In real situation, at almost all reduced velocities, the flexible riser response is a combination of mode shapes and frequencies. Complex phenomena like oscillations at multiple frequencies and competing modes were commonly observed. The general response mode trends are described briefly in this section.

At very low reduced velocities, the riser deflection comprised primarily of 1st mode in cross-flow and 2nd mode in-line direction. As  $U^*$  is increased, the cross-flow oscillation switches to 2nd mode, and the in-line oscillation mode reduces from 2nd mode to 1st mode. For low mass ratio ( $m^* = 1.1$ ) riser this jump is observed at  $U^* \approx 2.5$ , which is slightly lower than the corresponding jump for higher mass ratio ( $m^* = 2.7$ ) riser, which was at  $U^* \approx 4.5$ .

The first lock-in regime comprised generally of a stable first mode in the cross-flow direction and second mode in-line response, as shown in figure 4.1. At low tension a significant presence of 3rd mode, at the 3rd harmonic of the natural frequency was observed. The spatio-temporal plot of non-dimensional response for the same case ( $U^* = 5.3$ ,  $m^* = 1.1$ ) is shown in figure 4.2

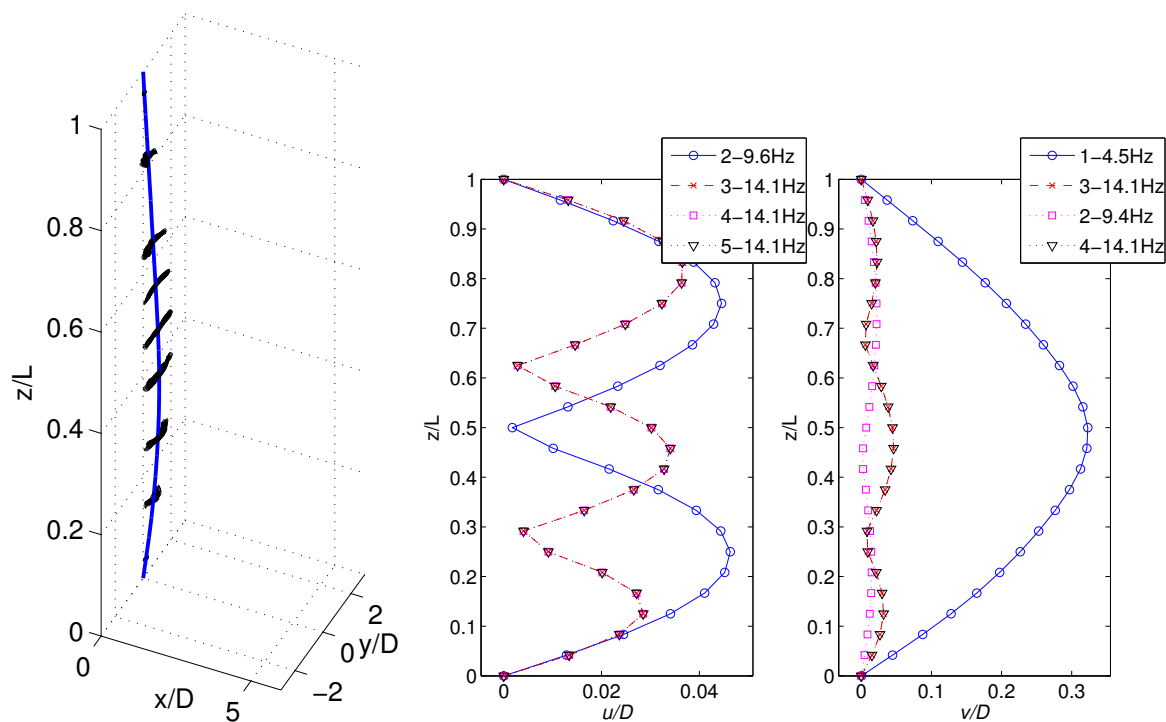


Fig. 4.1 Trajectory map at key spanwise locations, with thick blue line indicating mean deflection (left), non-dimensional modal in-line deflection (center) and cross-flow deflection (right). Case  $U^* = 5.3$   $m^* = 1.1$   $T = 300$  N

The low mass ratio riser indicated a well defined response at lower reduced velocities compared to the high mass ratio riser, and a correspondingly a wider lock-in band as predicted by Khalak & Williamson[80], and Williamson and Govardhan[59] for rigid cylinders. The effect of mass ratio on the width of lock-in region is briefly discussed in the section 2.2.1.6. The three dimensional trajectory map and the in-line and cross-flow deflections for  $m^* = 2.7$  riser are shown in figure 4.3. The contour plots are shown in figure 4.4

With increase in the reduced velocity, the second jump in the cross-flow response mode of both risers was observed at  $U^* \approx 15$ , where the 3rd dominant cross-flow modes were observed. The maximum  $U^*$  for  $m^* = 1.1$  riser was reached before the higher modes of oscillations could become prominent. The high mass ratio riser, by virtue of its higher density, had higher  $U^*$  for the same towing velocity. The results indicated a switch to 4th dominant cross-flow mode at  $U^* \approx 25$ , and 5th dominant cross-flow mode at  $U^* \approx 32$ . Within the range of  $U^*$  common for both risers, the mode jumps were observed to be at almost similar  $U^*$ .

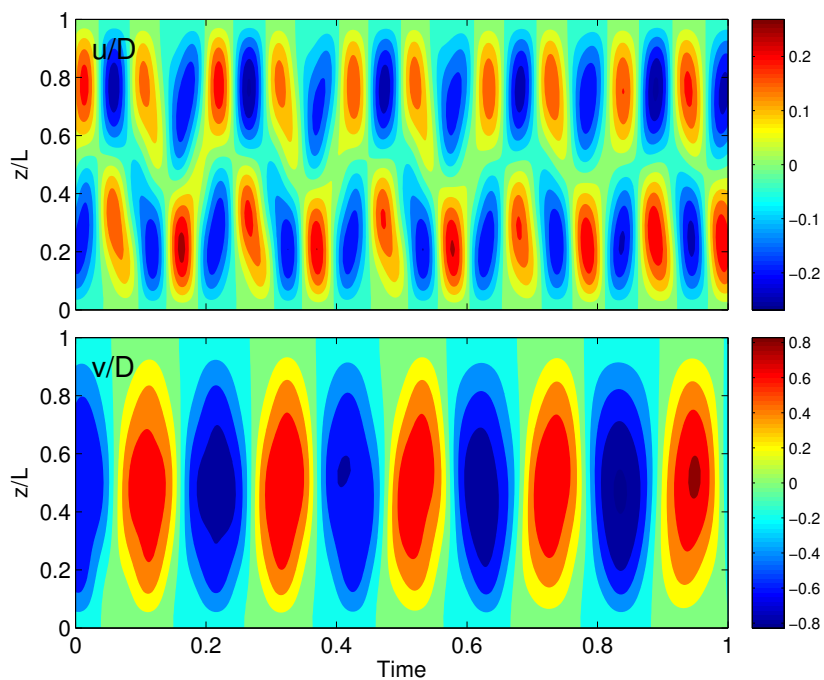


Fig. 4.2 In-line dynamic deflection response (top) and cross-flow deflection response (bottom), for 1 second of data. Case  $U^* = 5.2$   $m^* = 1.1$   $T=300$  N

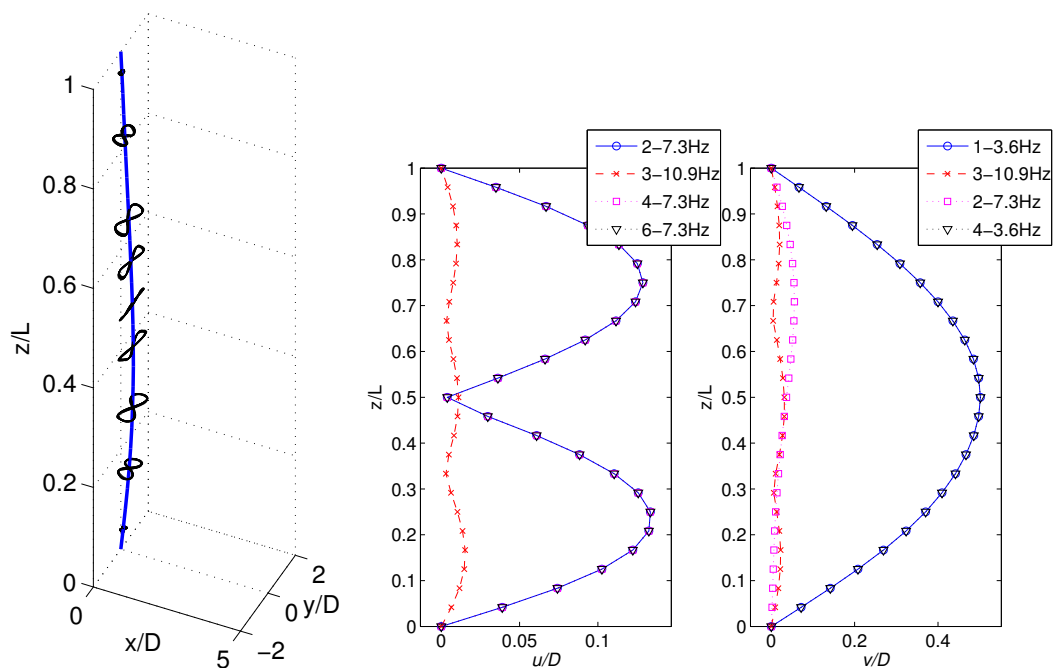


Fig. 4.3 Trajectory map at various spanwise locations, with thick blue line indicating mean deflection (left), non-dimensional modal in-line deflection (center) and cross-flow deflection (right). Case  $U^* = 7.0$   $m^* = 2.7$   $T=300$  N

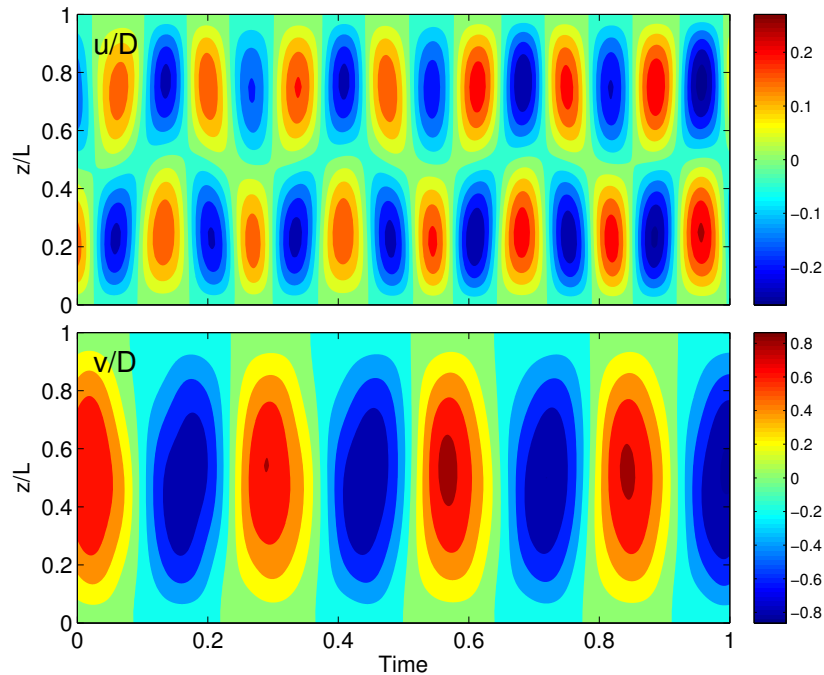


Fig. 4.4 In-line dynamic deflection response (top) and cross-flow deflection response (bottom), for 1 second of data. Case  $U^* = 7.0$   $m^* = 2.7$   $T = 300$  N

## 4.4 Statistical Parameters

Certain properties of the risers' vortex induced vibrations, for example the amplitude of oscillations, are inherently dependent, as the literature suggests, on the reduced velocity parameter as explained in section 2.2. The reduced velocity could be based on the fundamental natural frequency for the submerged riser,  $f_1$ , as per the equation:

$$U^* = \frac{U_\infty}{f_1 D} \quad (4.1)$$

or by the dominant cross-flow modal frequency ( $f_{dx}$ ), and in-line frequency ( $f_{dy}$ ):

$$U_{d_{x,y}}^* = \frac{U_\infty}{f_{d_{x,y}} D} \quad (4.2)$$

The fundamental natural frequency ( $f_1$ ) used in equation 4.1 is the frequency obtained from the Differential Quadrature Method, as explained in section 3.7.3, whereas the dominant cross-flow or in-line frequencies ( $f_{d_{x,y}}$ ), used in equation 4.2 are obtained from the maximum modal amplitude data.

As the risers are flexible in nature, the response is both spatially varying, *i.e.* along the span of the riser, and temporally varying, *i.e.* variation at each measurement station, the statistical representation such as the standard deviations, and means/ root mean square determinations are first carried out along the span of the riser, and then temporally. *ie,*

$$\sigma_x = \sqrt{\frac{1}{S} \sum_{i=1}^S \left( \frac{1}{N} \sum_{j=1}^N (u_{ji}(z, t) - \bar{u}_i(z))^2 \right)} \quad (4.3)$$

$$\tilde{x} = \sqrt{\frac{1}{S} \sum_{i=1}^S \left( \frac{1}{N} \sum_{j=1}^N u_{ji}(z, t) \right)^2} \quad (4.4)$$

$$\sigma_y = \sqrt{\frac{1}{S} \sum_{i=1}^S \left( \frac{1}{N} \sum_{j=1}^N (v_{ji}(z, t))^2 \right)} \quad (4.5)$$

$$(4.6)$$

Where  $N$  is the total number of measuring stations (or the points after curve fitting), and  $S$  is the total number of samples, which is the product of data acquisition rate and the time.

## 4.5 Results

There were, as described in the previous chapter, two different riser assemblies that were tested over a range of initial tension, for a range of test velocities. Majority of the results presented in this section are formatted in the same manner as used by Chaplin *et al.* [39] and Huera-Huarte [65] for compatibility and reference. The test conditions for each riser and the symbols used through the results section are listed in table 4.1.

The drag of the riser results in a mean deflection, causing extension in the springs for the spring end condition. This results in an increase in tension in the riser. The mean deflection is a result of the drag. If the  $C_d$  remains constant, the drag is dependent on the square of the velocity, and thus the mean deflection, and the resultant increase in tension forms a quadratic curve as shown in figure 4.5 for  $m^* = 1.1$  riser and  $m^* = 2.7$  riser. For the cases with constant tension, a higher starting tension shows an increase in tension with increase in  $U^*$ , which is attributed to the friction in the cable and pulley system.

Table 4.1 List of tests for isolated cylinders

Model	End condition	$U_\infty$	Init T (N)	Symbol
$m^* = 1.10$	Const. Tension	0.25...2.0	200	$\triangle$
			397	$\nabla$
			595	$\diamond$
			795	$\square$
$m^* = 1.10$	$k_1(41.1N/mm)$	0.25...2.0	200	$\triangle$
			397	$\nabla$
			595	$\diamond$
			795	$\square$
$m^* = 1.10$	$k_2(17.1N/mm)$	0.25...2.0	200	$\triangle$
			397	$\nabla$
			595	$\diamond$
			795	$\square$
$m^* = 2.70$	$k_2(17.1N/mm)$	0.20...2.0	200	$\blacktriangle$
			397	$\blacktriangledown$
			595	$\blacklozenge$
			795	$\blacksquare$

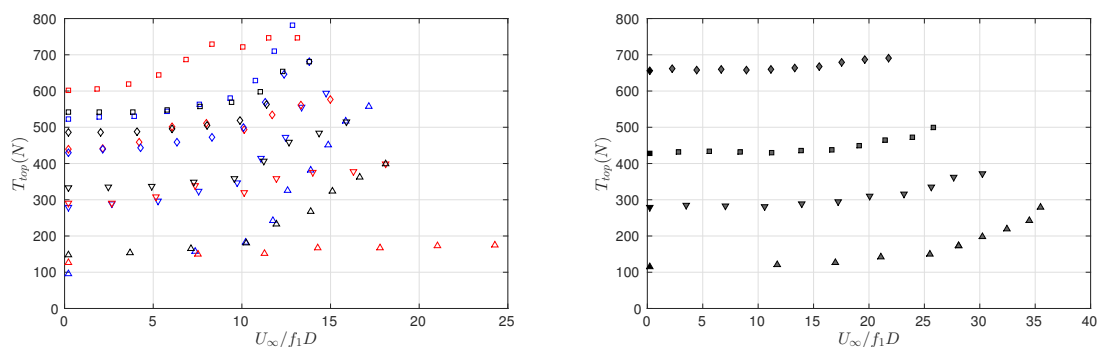


Fig. 4.5 Increase in tension with  $U^*$  for  $m^* = 1.1$  riser (left) and  $m^* = 2.7$  riser (right) for all end conditions. For legend, see table 4.1

The mean of in-line deflection, which is equivalent to the spatio-temporal RMS of the dimensionless in-line displacements is given in figure 4.6. As expected, the RMS of in-line displacement follows the similar quadratic trend as that of the tension curves shown in figure 4.5, for all cases with spring end condition. The fixed tension end condition, having the lowest run tensions, show the highest  $\tilde{x}/D$  as it can reach the highest  $U^*$ . For the  $U^*$  range of all three end conditions, a surprising observation is that the RMS of in-line displacement does not depend on the end condition, rather on the tension, mass ratio and geometry of the riser.

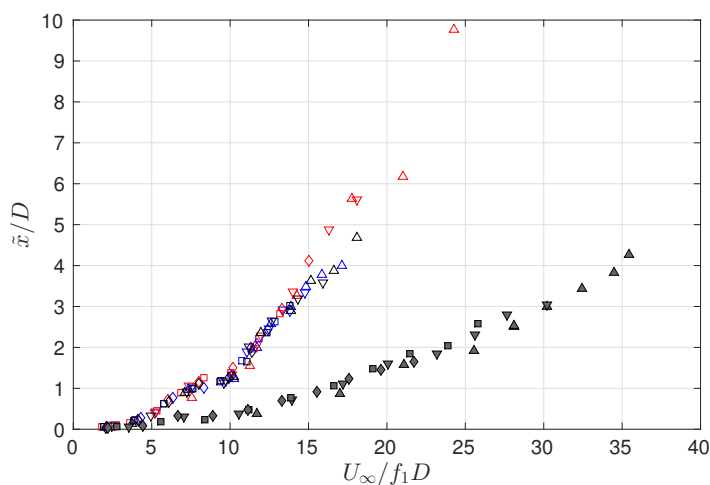


Fig. 4.6 Spatio-temporal RMS of the in-line displacements ( $\tilde{x}/D$ ) vs reduced velocity  $U^*$  ( $= U_\infty/f_1D$ ) for both low and high mass ratio risers. For legend see table 4.1

The standard deviation of in-line displacement,  $\sigma_x$ , is computed after removing the mean deflection of the riser, thus is the measure of the dynamic part of the in-line displacement. As there is no mean displacement in cross-flow direction, so  $\sigma_y$  is equivalent to  $\tilde{y}$ . The standard deviations of the dynamic in-line and cross-flow displacements are shown in figures 4.7 and 4.8 respectively. The in-line values ( $\sigma_x$ ) indicate clear regimes corresponding to modes of oscillation, with highest values for  $m^* = 1.1$  riser approaching  $0.3D$ . The cross-flow oscillations for spring end condition show a similar response behaviour of regimes corresponding to modes, reaching a maximum value of about  $0.9D$ . The fixed tension end condition results in a response pattern that can not be defined in a specific pattern.

If the standard deviation is plotted against the reduced velocity based on the dominant mode frequencies, ( $U_{dx,dy}^*$ ), the cross-flow amplitude response collapses around the non-dimensional reduced velocity range of  $6 - 8$ , as shown in figure 4.9. Instead of separate branches, a general increasing trend is observed. The in-line oscillations, as seen in figure 4.10, collapse in two ranges of reduced velocity, first in the range of  $3 - 4$ , which indicates the in-line oscillation frequency about twice the frequency of cross-flow oscillations ( $f_{dx} \approx 2 \times f_{dy}$ ), resulting in the figure 8 oscillation trajectory, and the second collapse is seen where the in-line oscillation frequency is almost equal to the cross-flow oscillation, at ( $f_{dx} \approx f_{dy}$ ). This indicates a circular trajectory, based on the assumptions that the mode shapes are indicative of the frequency.

The in-line oscillation dominant frequency vs reduced velocity plot, shown in figure 4.11 shows that the in-line oscillation frequency follows two trends, one of which is

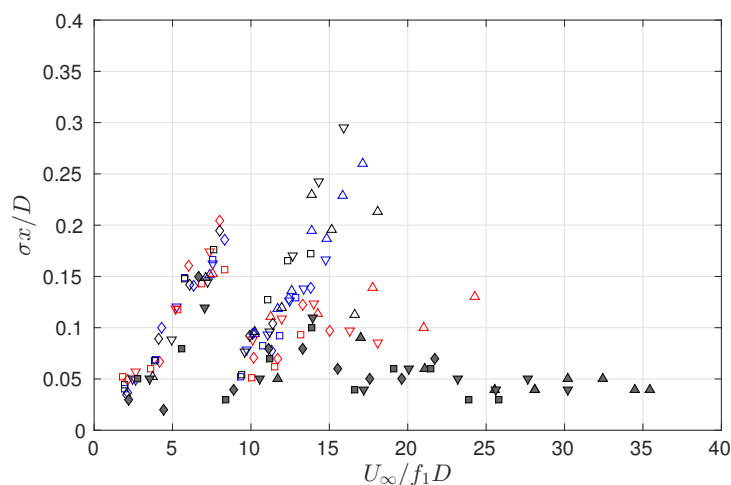


Fig. 4.7 Spatio-temporal standard deviation of dimensionless in-line displacements ( $\sigma_y/D$ ), with mean deflection removed vs reduced velocity ( $U^* = U_\infty/f_1D$ ) for both low and high mass ratio risers. For legend see table 4.1

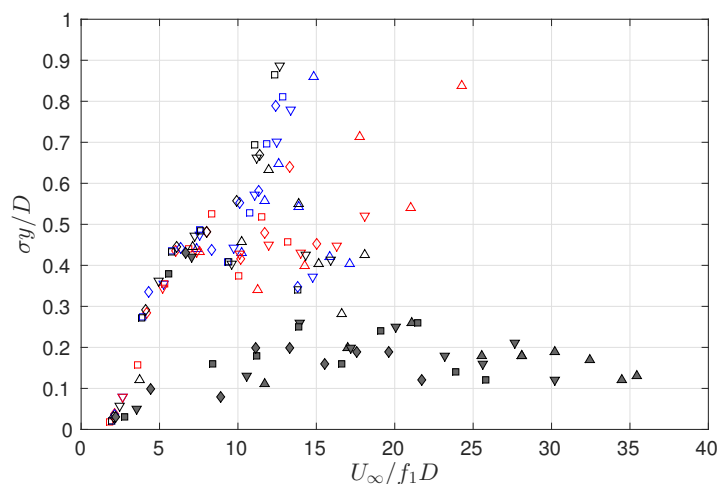


Fig. 4.8 Spatio-temporal standard deviation of dimensionless cross-flow displacements ( $\sigma_x/D$ ) vs reduced velocity ( $U^* = U_\infty/f_1D$ ) for both low and high mass ratio risers. For legend see table 4.1

at twice the Strouhal number of the other ( $St=0.15$ , and  $St=0.3$ ). The cross-flow oscillation dominant frequency, shown in figure 4.12 shows a distinct trend of a single Strouhal number relationship ( $St=0.15$ ). The two trends shown in the in-line oscillation frequency, compared to the single trend in cross-flow oscillation, reaffirm the presence of two distinct regions of collapse of in-line response, shown in figure 4.10.



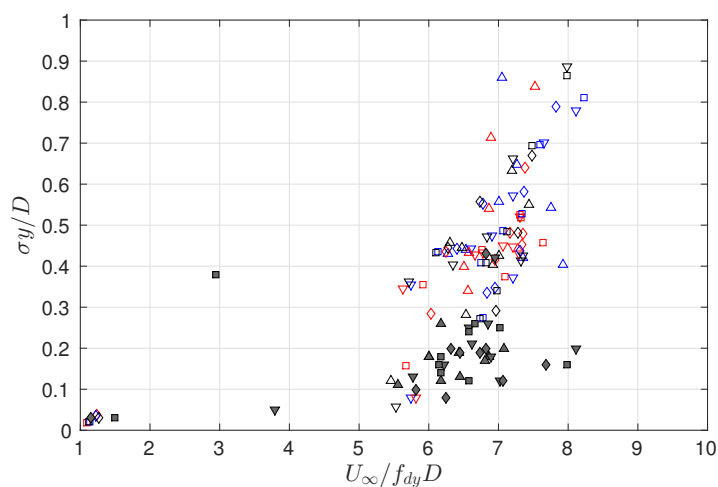


Fig. 4.9 Spatio-temporal standard deviation of dimensionless cross-flow displacements ( $\sigma_x/D$ ) vs reduced velocity ( $U^* = U_\infty/f_{d(y)}D$ ) for both low and high mass ratio risers. For legend see table 4.1

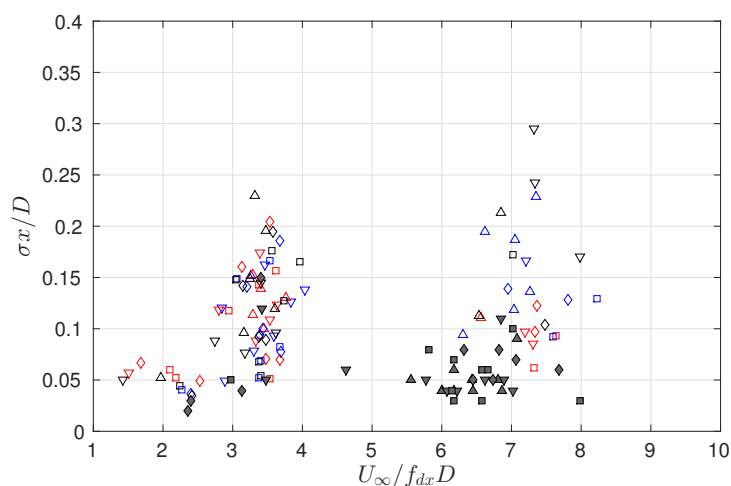


Fig. 4.10 Spatio-temporal standard deviation of dimensionless in-line displacements ( $\sigma_y/D$ ) vs reduced velocity ( $U^* = U_\infty/f_{d(x)}D$ ) for both low and high mass ratio risers. For legend see table 4.1

The non-dimensional dominant frequencies are shown in figure 4.13 for the in-line oscillations and 4.14 for the cross-flow oscillations. These non-dimensional frequencies are equivalent to the Strouhal number, if it is assumed that the shedding frequency is equal to the dominant oscillation frequency. As observed in figure 4.13, two types of in-line oscillation response is evident, and for the reduced velocity  $U^*$  below 20, clear indications of the modal regimes are also prominent. The higher values are where the

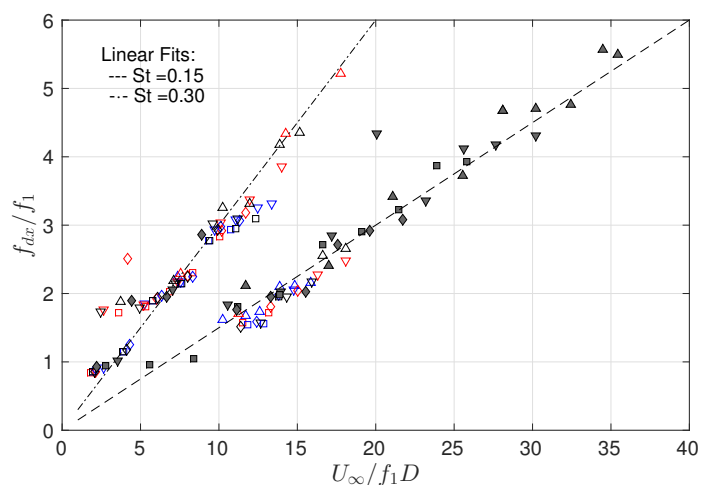


Fig. 4.11 In-line oscillations dominant frequency vs reduced velocity ( $U^* = U_\infty/f_1D$ ) for both low and high mass ratio risers. For legend see table 4.1

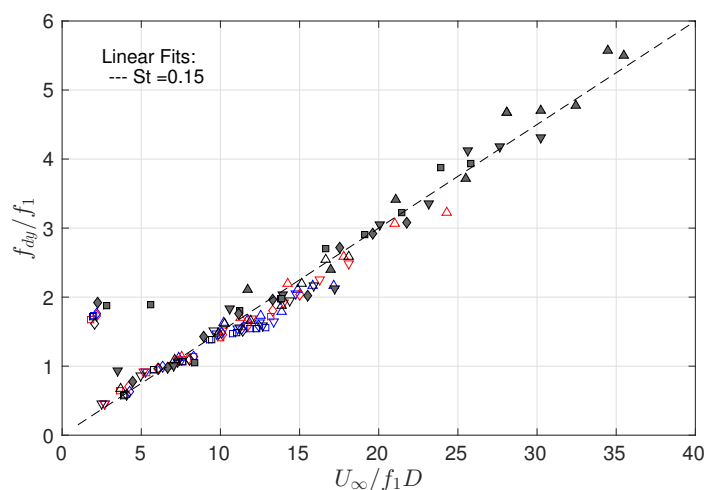


Fig. 4.12 Cross-flow oscillations dominant frequency vs reduced velocity ( $U^* = U_\infty/f_1D$ ) for both low and high mass ratio risers. For legend see table 4.1

in-line oscillation frequency is twice that of the cross-flow oscillation. The cross-flow dominant frequency plots also indicate the regimes of response with increasing  $U^*$ .

The maximum dimensionless in-line displacement ( $x_M/D$ ) and cross-flow displacement ( $y_M/D$ ) are shown in figure 4.15 and 4.16 respectively. The maximum in-line displacements for the low mass ratio risers can reach 1D or higher, whereas the high mass ratio riser has a maximum oscillation amplitude of about 0.4D. The cross-flow oscillation maximas are, similar to the non-dimensional standard deviation plots shown in figure 4.8, about twice the values of maximum in-line amplitudes.

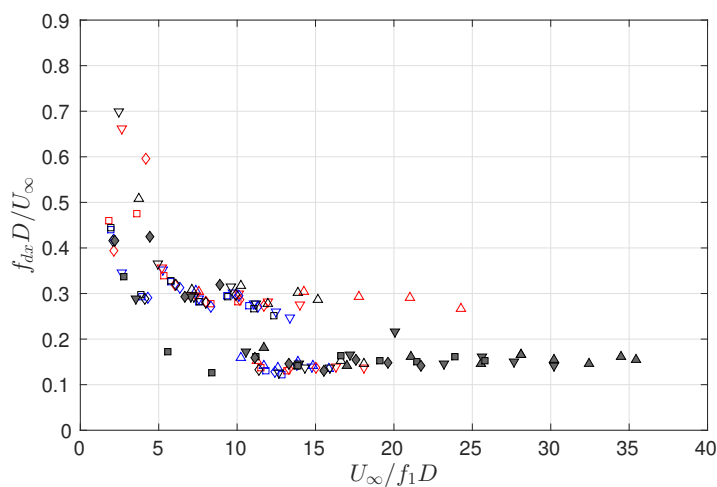


Fig. 4.13 Non-dimensional in-line oscillations dominant frequency vs reduced velocity ( $U^* = U_\infty / f_1 D$ ) for both low and high mass ratio risers. For legend see table 4.1

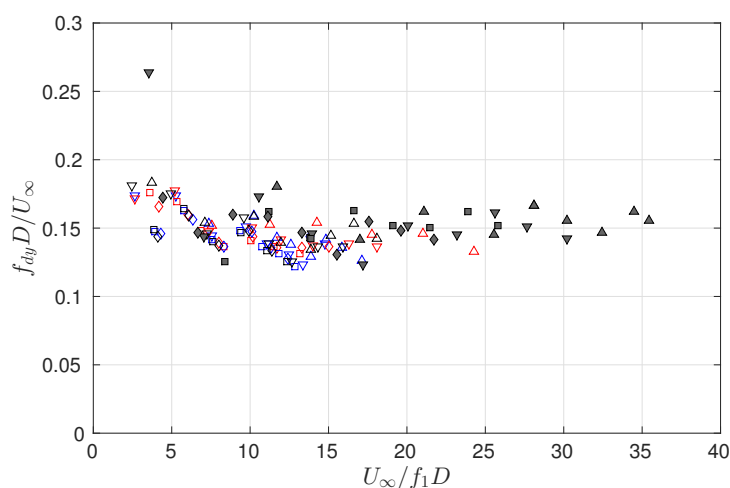


Fig. 4.14 Non-dimensional cross-flow oscillations dominant frequency vs reduced velocity ( $U^* = U_\infty / f_1 D$ ) for both low and high mass ratio risers. For legend see table 4.1

The drag coefficient of the riser,  $C_D$ , plotted against the reduced velocity  $U^*$  is shown in figure 4.17. The modal response regimes, specifically for the low mass ratio riser, are very obvious in this plot. The two modal lock-ins are indicated by the two peaks at  $U^* \approx 7$  and  $U^* \approx 14$ . For the majority of the range, the drag coefficient of the low mass ratio riser remains within a range of 2 – 3, which is significantly higher than that of the high mass ratio riser, or what has been recorded in the existing literature as almost all of the existing literature deals with risers with higher mass ratio. The

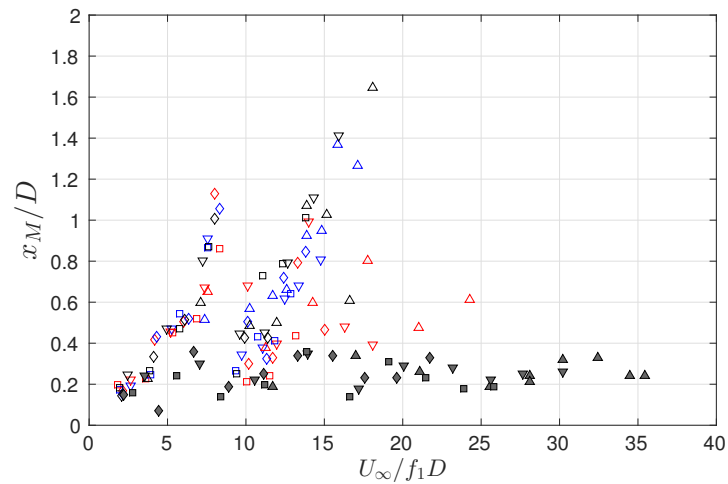


Fig. 4.15 Maximum in-line oscillations displacement vs reduced velocity ( $U^* = U_\infty/f_1D$ ) for both low and high mass ratio risers. For legend see table 4.1

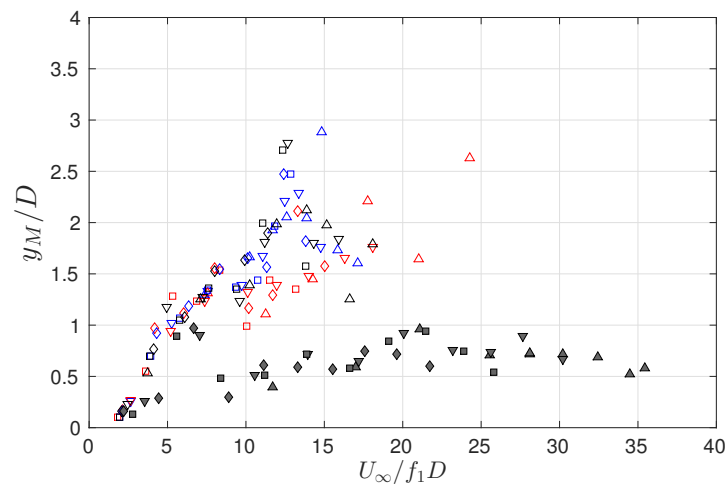


Fig. 4.16 Maximum cross-flow displacement vs reduced velocity ( $U^* = U_\infty/f_1D$ ) for both low and high mass ratio risers. For legend see table 4.1

coefficient for the high mass ratio riser is right in the middle of the range (1-2.5) previously recorded by Chaplin *et al.* [39].

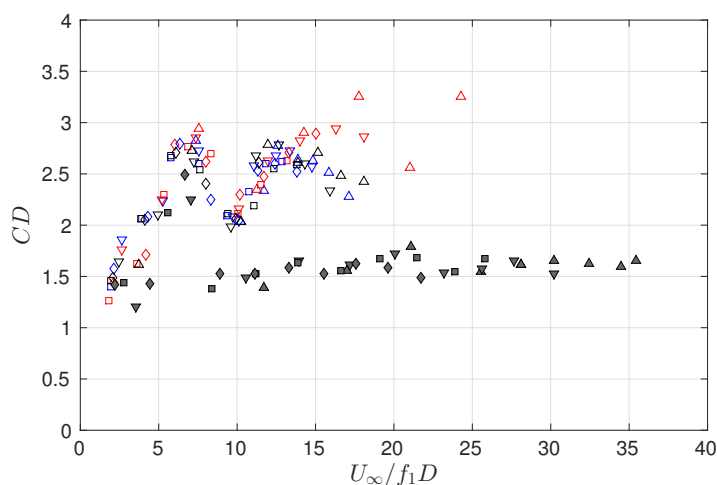


Fig. 4.17 Drag coefficient vs reduced velocity ( $U^* = U_\infty/f_1D$ ) for both low and high mass ratio risers. For legend see table 4.1

## 4.6 Modal Analysis

As described in section 3.5, the modal contributions were analysed using two distinct methods. The first method, utilizing a pre-defined mode shape matrix, resulted in the determination of contributions assuming perfectly sinusoidal mode shapes. Theoretically, the response of the riser can be reconstructed using the sinusoidal contribution values from the modal contribution matrix, and the oscillation assumed to be restricted to the dominant frequencies as shown in figures 4.11 for in-line response and 4.12 for the cross-flow response.

These modal contributions are shown in figure 4.18. The cross-flow oscillations, as expected, show increasing high mode contribution as  $U^*$  is increased, and correspondingly decreasing low mode contributions. The most significant lock-in region is indicated in  $4 < U^* < 8$ , where the cross-flow oscillations show a peak in the first mode and the in-line oscillations are in the second mode. During this range, the magnitude of modal contribution from both low- and high- mass ratio risers is about equal, *i.e.*  $0.8D$ . For higher modes, the low mass ratio riser shows modal values that are twice as much as the higher mass ratio riser. The in-line oscillations indicate the first lock-in in the second mode, whereas subsequent modes are of significantly lower magnitudes.

The non-dimensional modal distribution plots are shown in figures 4.19 for  $m^* = 2.7$  riser, and 4.20 for the low mass ratio,  $m^* = 1.1$  riser. These plots, obtained from interpolation of data shown in figure 4.18, represent the probability of the mode of oscillation for each riser, regardless of the end condition, over the range of reduced

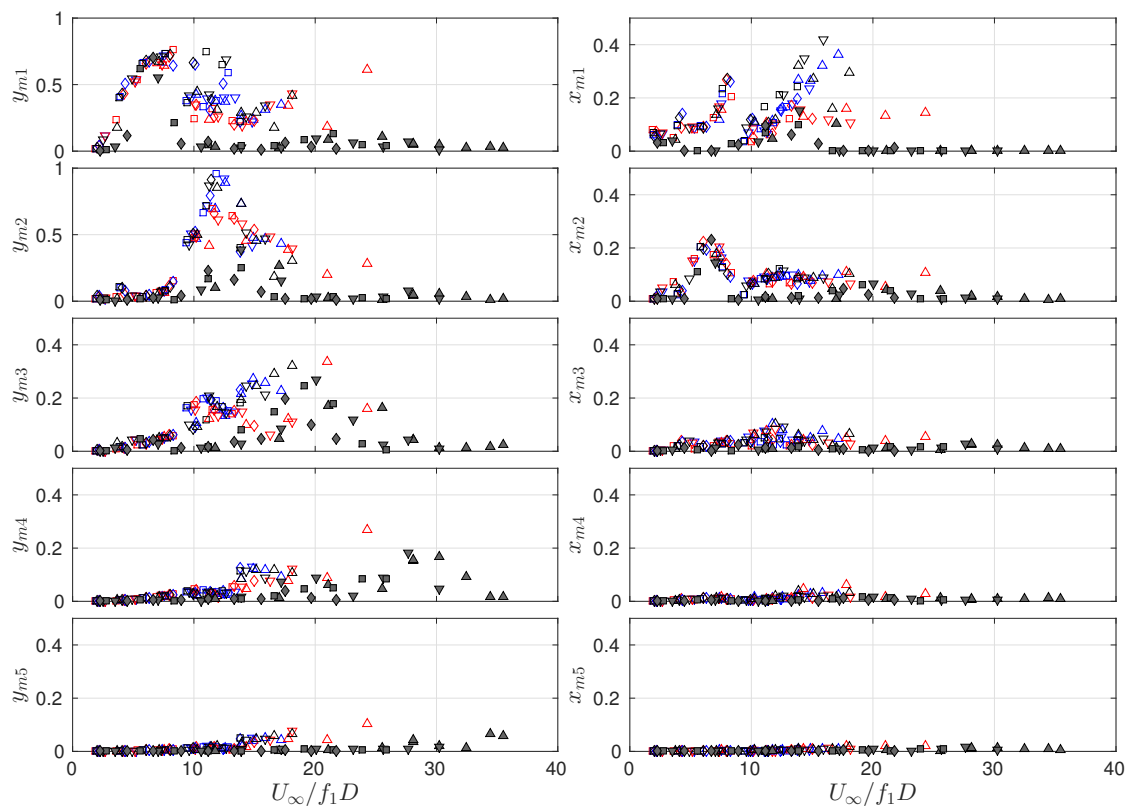


Fig. 4.18 Cross-flow modal amplitudes (left) and in-line modal amplitudes (right) for the first 5 modes vs reduced velocity ( $U^* = U_\infty / f_1 D$ ) for both low and high mass ratio risers. For legend see table 4.1

velocities. For the high mass ratio riser ( $m^* = 2.7$ , figure 4.19), a steadily increasing mode is evident over the range of  $U^*$ . The in-line oscillations usually are at a lower mode than the cross-flow oscillations, exception being the very low  $U^*$ . The low mass ratio riser ( $m^* = 1.1$ , figure 4.20) shows a chaotic trend, and the entire in-line oscillation range is obscured by the significantly higher 1st mode response.

In the blind source separation method, the mode shape matrices are constructed based on the highest to lowest contribution. In other words,  $x_{m1}, y_{m1}$  are the mode shapes that have the highest amplitudes, and  $x_{m7}, y_{m7}$  are the mode shapes with the smallest amplitudes. After some computation, the BSS mode shapes matrix can be sorted according to the approximate sinusoidal shape. One unsolved aspect is that multiple BSS mode shapes can be categorized as a single sinusoidal mode, in which case only the largest value is picked. This results in a loss of data as for each run there would be some mode shapes that are not represented in the statistical modal plots. Generally, the results resemble the modal amplitudes according to sinusoidal mode

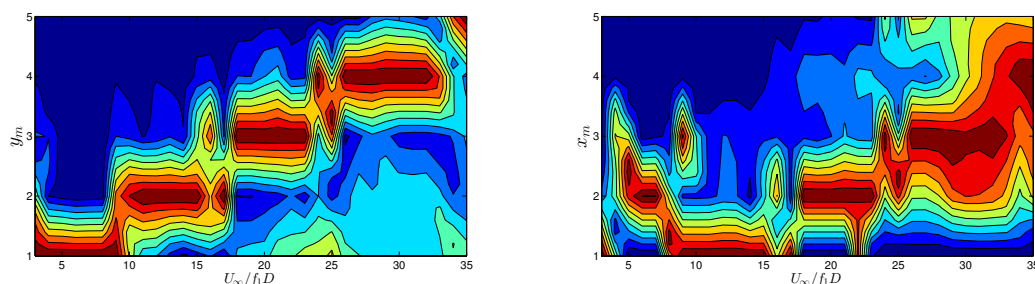


Fig. 4.19 Probability of cross-flow mode (left) and in-line mode (right) for the first 5 modes, vs reduced velocity ( $U^* = U_\infty / f_1 D$ ), for the high mass ratio riser ( $m^* = 2.7$ ). Values range from 0 (blue) to 1 (red)

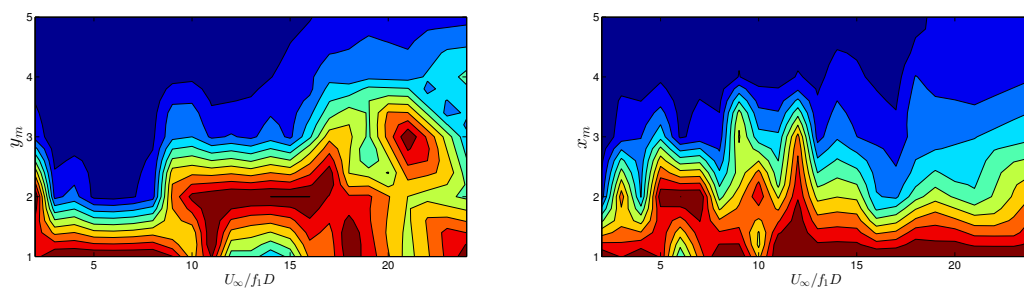


Fig. 4.20 Probability of the cross-flow mode (left) and in-line mode (right) for the first 5 modes, vs reduced velocity ( $U^* = U_\infty / f_1 D$ ), for the low mass ratio riser ( $m^* = 1.1$ ). Values range from 0 (blue) to 1 (red)

shapes matrix shown in figure 4.18. The SOBI algorithm also involves an extensive data whitening. A lot of the first mode in-line response, specifically for the low mass ratio case, is cleansed in the process. The results from blind source separation are shown in figure 4.21.

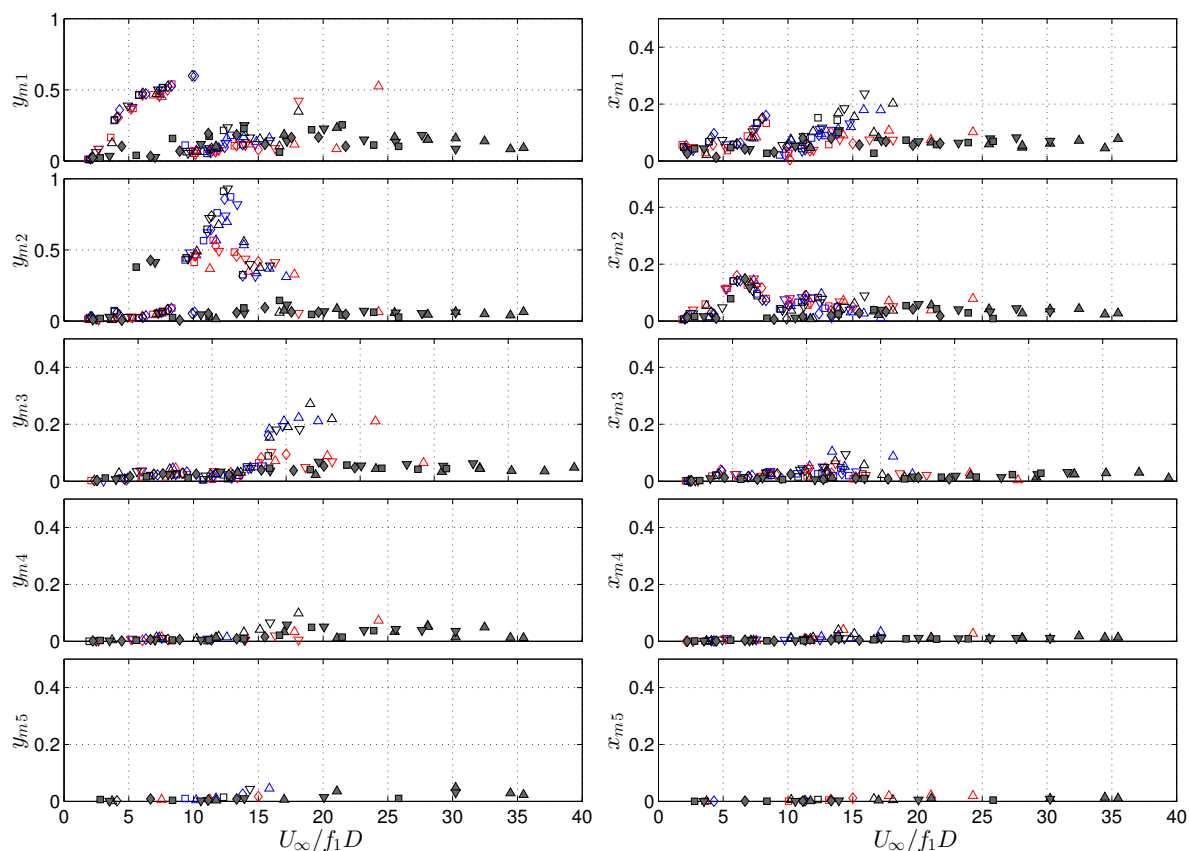


Fig. 4.21 Cross-flow modal amplitudes (left) and in-line modal amplitudes (right) for the first 5 modes vs reduced velocity ( $U^* = U_\infty/f_1D$ ) for both low and high mass ratio risers, based on blind source separation. For legend see table 4.1

## 4.7 Mode shapes from Blind Source Separation

The response regimes, as mentioned in the previous sections, have broadly been categorized by sinusoidal modes with increasing amplitudes in corresponding lock-in branches. The response of high mass ratio risers have been shown to follow those trends in a significant number of experimental and numerical studies. However in many cases, the oscillations were fairly broadband, indicating the simultaneous presence of multiple frequencies and mode shapes.

Blind source separation, as described in section 3.5.2, was used to resolve the mode shapes for each case, and give us an idea of the different modes and/or frequencies that either occur simultaneously, or during different times in a run.



At low reduced velocities, the cross-flow mode shapes obtained from BSS indicate that the response regime consists of a single dominant mode, which matches very well with the sinusoidal mode shape. This trend was more obvious for the high mass ratio riser, a sample of which is shown in figure 4.22 for the low tension case with high modal density. With increase in reduced velocity, simultaneous presence of two competing modes are observed, both contributing almost equally to the response. Further increase in the reduced velocity results in the higher mode response becoming dominant, with the next higher mode showing smaller contribution. This simultaneous presence of multiple modes for vertical tension risers at higher structural modes in the lock-in condition, is similar to the response presented by Chaplin *et al.* [39].

An increase in tension results in wider separation between the natural frequencies of the riser, resulting in lower modal density. In such a case, sample of which is shown in figure 4.23, the progression of modes with increase in reduced velocity shows, with an exception of  $U^* = 15.5$ , that the response is primarily dominated by a single mode, whereas the competing modes have much lower contribution. The way the energy cascades into the competing modes is largely dependent on the modal density, and whether the shedding can contribute to those modes or not. It is clear that the modes whose frequency is far away from the shedding frequency stand to gain the least, whereas those in the vicinity of the shedding frequency extract the most energy. The case of  $U^* = 15.5$  lies between two lock-in regimes, where the net response is much lower than both the neighbouring cases, and the response is dominated by two competing modes.

For the case of low mass ratio riser, the modal density is significantly lower. It is expected that the response regime, because of the low modal density, will show significant presence of a single dominant mode. The cross-flow response for the low mass ratio showed exactly that trend. The response, almost entirely, consisted of a single dominant mode. The response amplitudes are significantly higher than those seen for high mass ratio riser. An example of the dynamics of low mass ratio riser is shown in figure 4.24. The top row shows the cross-flow response of the riser, and the bottom row plots are those of the in-line response. The reduced velocity is listed under each column. The cross-flow response indicates progression from 1st mode to the 2nd mode, and the frequency increments are just as expected.

The in-line response, in the bottom row of figure 4.24 indicate a complex picture. For the first lock-in regime, the maximum contributing in-line mode is equivalent to the 2nd sinusoidal mode, and is at twice the dominant cross-flow oscillation frequency ( $2 \times f_{cf}$ ) as expected. For higher reduced velocity, there is a significant contribution

of non-sinusoidal mode shapes, that match the cross-flow response frequency. These mode shapes, seen in the in-line response are attributed to the fluctuations in the mean deflection shape due to the dynamic component of the drag, which is influenced by the high amplitudes of cross-flow oscillation (see Huera-Huarte[71]). Buried underneath the 1st mode response, one can see the presence of modes at twice the cross-flow oscillation frequency ( $2 \times f_{cf}$ ) and matching the 3rd sinusoidal response mode. The amplitude of in-line oscillations at all modes are significantly lower than the cross-flow oscillations in all the cases, and the fluctuations in the mean deflections are even higher than the higher modes response. These fluctuations are identified as the first mode oscillations when the analysis are carried out using pre-determined mode shapes matrix, and that is the reason for the anomaly in figure 4.20, where the in-line oscillations are shown to be in the first mode for the whole range of reduced velocities higher than the first lock-in mode.

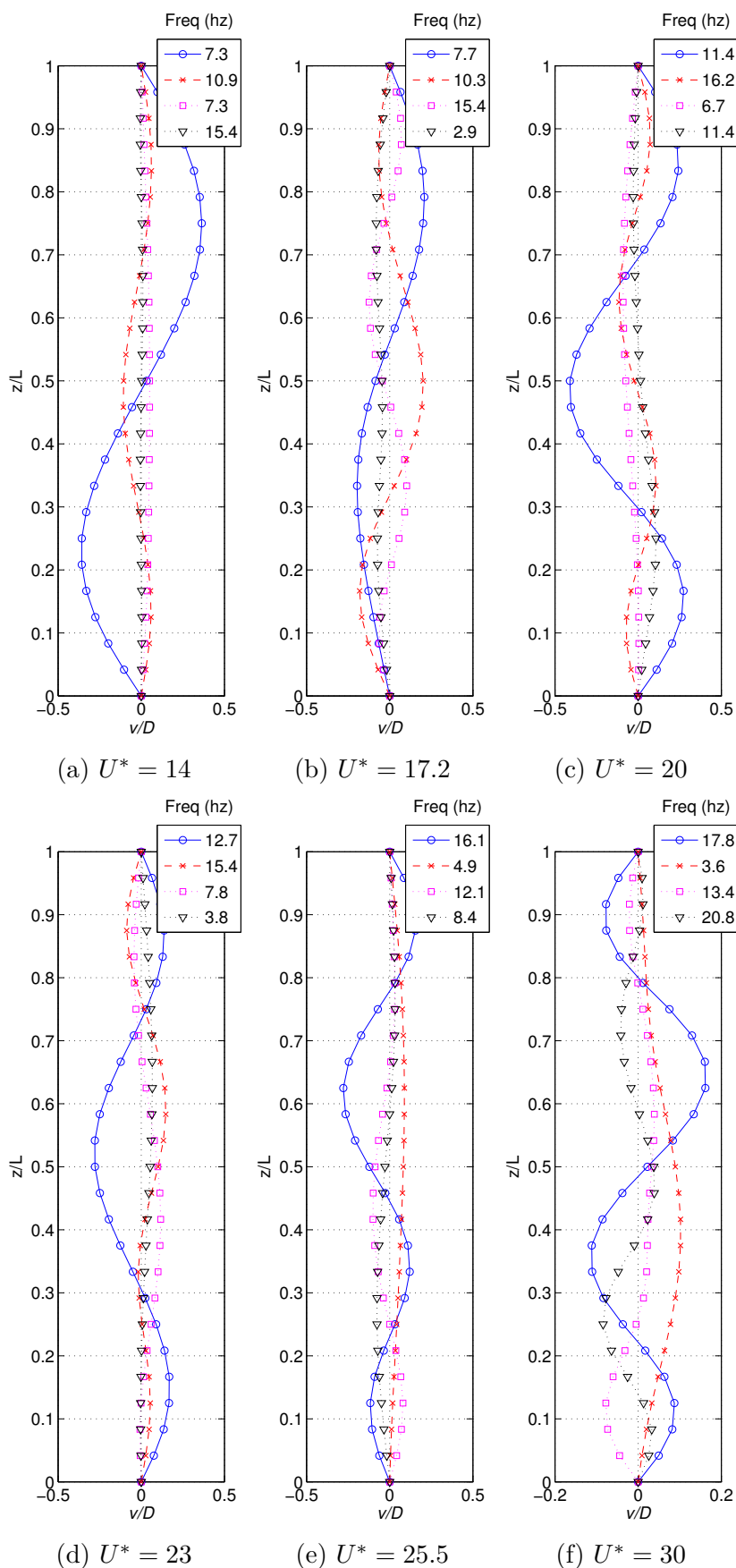


Fig. 4.22 Progression of cross-flow mode shapes and frequencies, with mode competitions with increasing  $U^*$ . Data for  $m^* = 2.7$ , starting tension  $T_{st} = 280N$ .

### 4.7 Mode shapes from Blind Source Separation

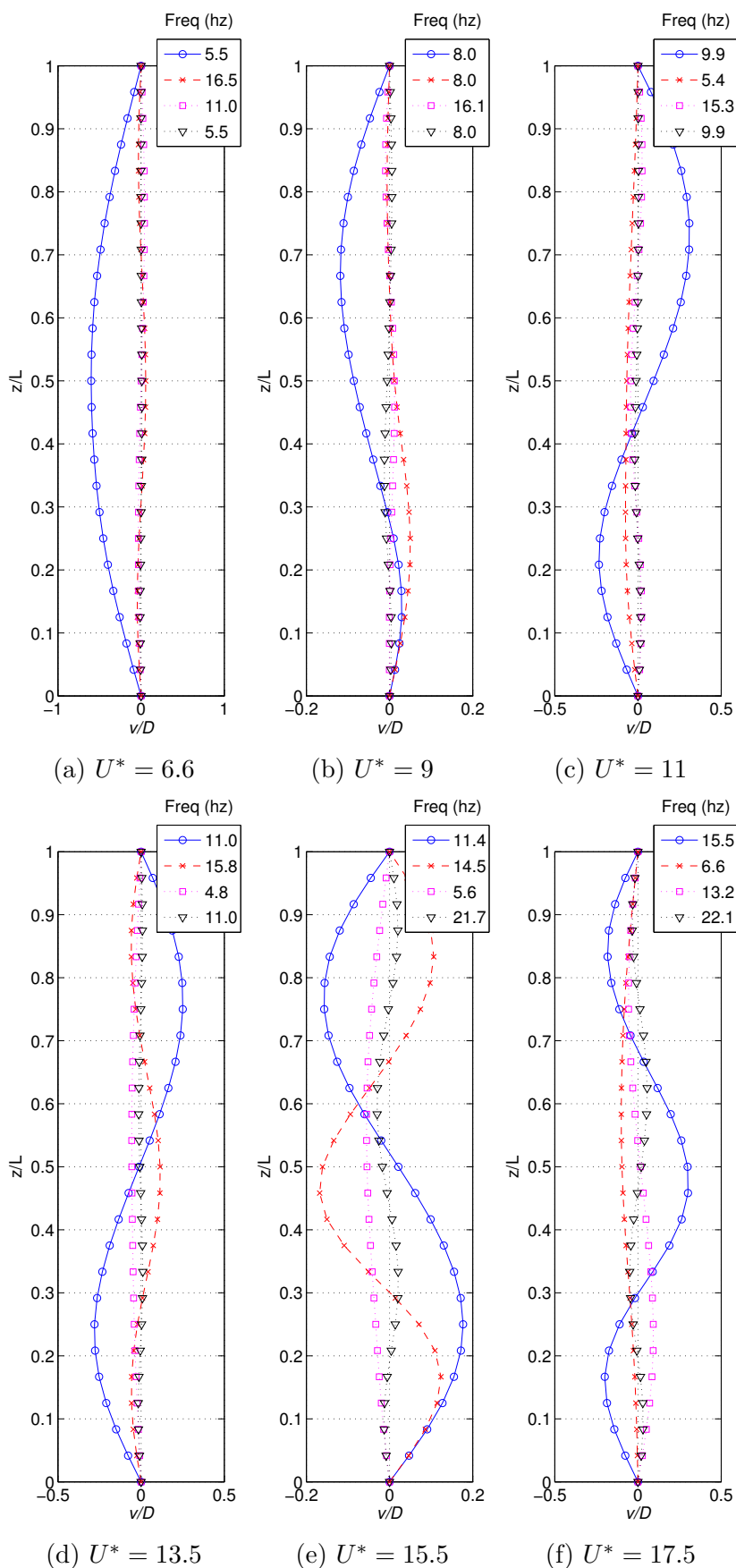


Fig. 4.23 Progression of cross-flow mode shapes and frequencies, with mode competitions with increasing  $U^*$ . Data for  $m^* = 2.7$ , starting tension  $T_{st} = 650N$ .

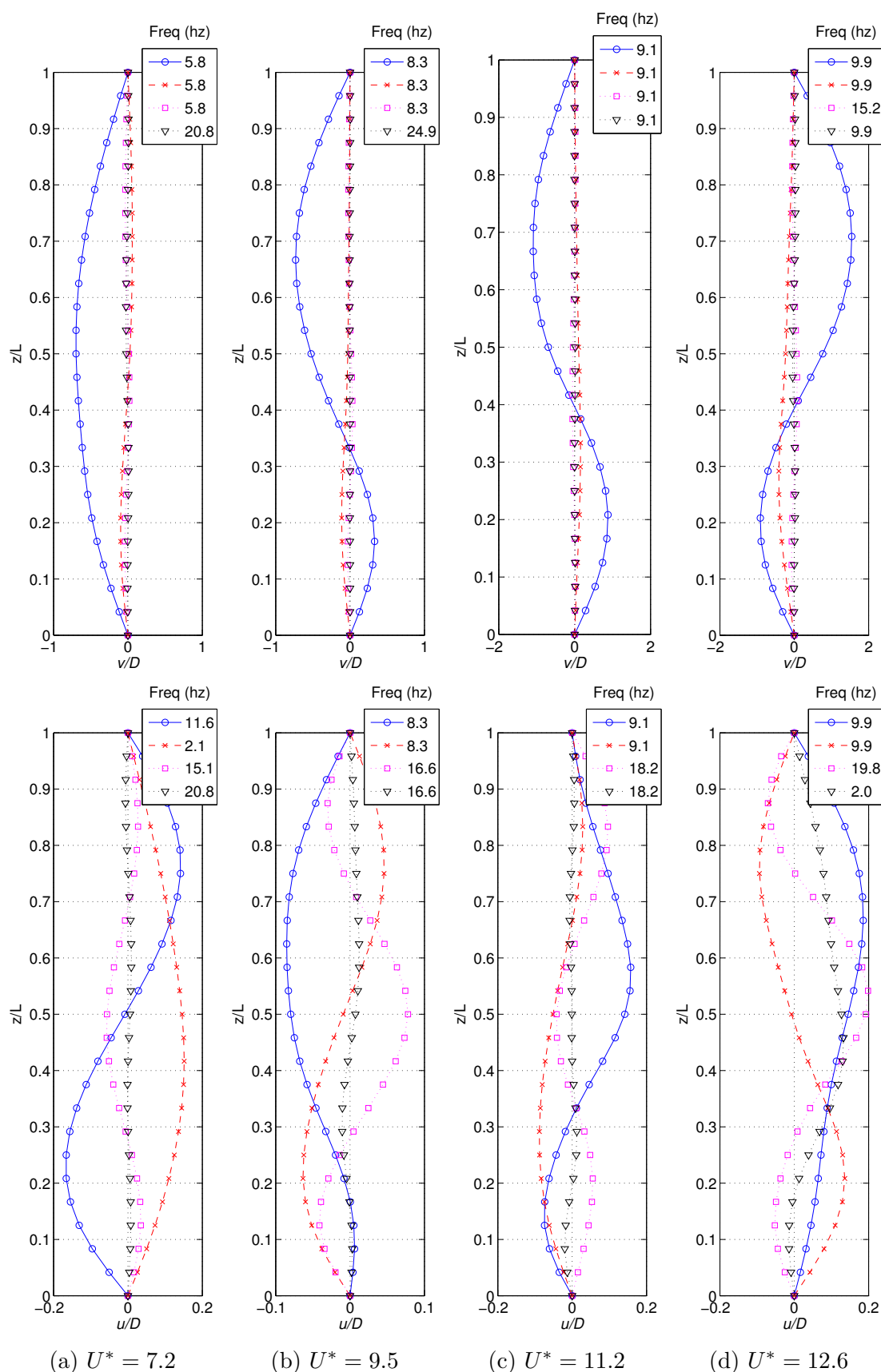


Fig. 4.24 Progression of mode shape and mode competitions with increasing  $U^*$  for low mass ratio riser. Cross-flow modes (top) and in-line modes (bottom) at indicated  $U^*$ . For  $m^* = 1.1$ , starting tension  $T_{st} = 330N$ .

## CHAPTER 5

# MULTIMODE VIV OF FLEXIBLE RISERS IN TANDEM; RESULTS

---

## 5.1 Introduction

The flow around a circular cylinder has been studied extensively. In real world applications, structures are often found in groups. The examples vary from miniature applications such as cooling fins on electronic devices, to large structures such as chimneys, buildings, power lines and offshore risers. When two or more cylindrical structures are placed in proximity, the changes in the flow structures involve complex interactions between shear layers, vortices, and Kármán vortex streets.

In case of bluff bodies the most commonly applied model to study the effect of proximity interference is by putting two identical circular cylinders in tandem arrangement. Such an arrangement has been widely used for experimental and numerical analysis by many researchers. There is a significant amount of literature on the subject, with a recent surge, as more advanced numerical methods are being employed to investigate the phenomena. Section 2.4 briefly covers the state of the art on the subject. An excellent review on the subject was compiled by Sumner[144]. The focus of almost the entirety of the literature on tandem arrangement of bluff bodies is directed at the effects of distance  $S_x$  on the drag characteristics, various states of flow in the gap, forces, frequency and Strouhal number relationships for rigid cylinders in fixed, or flexible mounted configurations. The research on the wake interference effects using flexible risers is scarce, and the case of multi-mode response is non-existent. The objective of the current endeavour was to explore the characteristics of a flexible riser, able to undergo multi-mode vibrations, immersed in the wake of a rigid cylinder.

## 5.2 Synopsis

Similar to the response shown by isolated risers, the tandem cylinders displayed response branches based on increasing mode numbers. The results show modal regions with growing amplitudes, Unlike rigid cylinders, the amplitude of flexible risers grow inside each responding modal region, with cross-flow oscillations showing significant amplitudes up to third mode. In almost all cases, the cross-flow oscillation modes and amplitudes appeared to be unaffected by the distance  $S_x$  between the riser and the rigid cylinder in front. The mean deflection was observed to be significantly smaller for all the cases, as compared to an isolated riser. The cross-flow oscillations of up to 5th mode and in-line up to 4th mode were observed. the range of reduced velocity for each mode was significantly well defined for the in-line modes, however the cross-flow modes were fairly scattered over the range of reduced velocities. The drag, compared to the isolated riser, was measurably less for the entire range. The lowest drag values were observed for the minimum center to center distance  $S_x$ . For the distance larger than  $S_x = 2D$ , the response, largely appeared unaffected.

## 5.3 Results

The tests were carried out for a total of 5 configurations, with the center to center distance ( $S_x$ ) ranging from  $2D$  to  $6D$ , as shown in figure 5.1. A total of 200+ tests were carried out for a range of initial (starting) tension  $T_s$ , while the end condition was with spring constant  $k_2 = 41.7N/mm$ . The rigid cylinder in front of the flexible riser was not instrumented, and was only used to impart the wake influence on the instrumented riser.

The statistical parameters used for flexible risers are previously described in section 4.4, and the same definitions and equations are used for the tandem configurations.

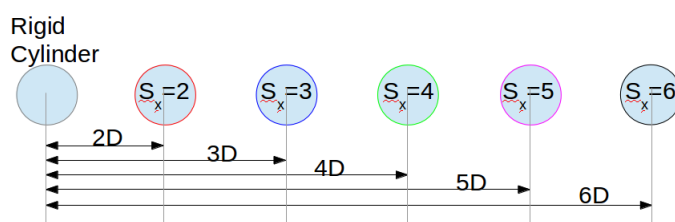























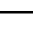


Fig. 5.1 Arrangement of cylinders in tandem configuration

Table 5.1 List of tests in tandem configuration

Case	Distance $S_x$	$U_\infty$	Init T (N)	Symbol
Tandem	2D	0.2...2.0	200	
			397	
			595	
			795	
Tandem	3D	0.2...2.0	200	
			397	
			595	
			795	
Tandem	4D	0.2...2.0	200	
			397	
			595	
			795	
Tandem	5D	0.2...2.0	200	
			397	
			595	
			795	
Tandem	6D	0.2...2.0	200	
			397	
			595	
			795	
Single	---	0.20...2.0	200	
			397	
			595	
			795	



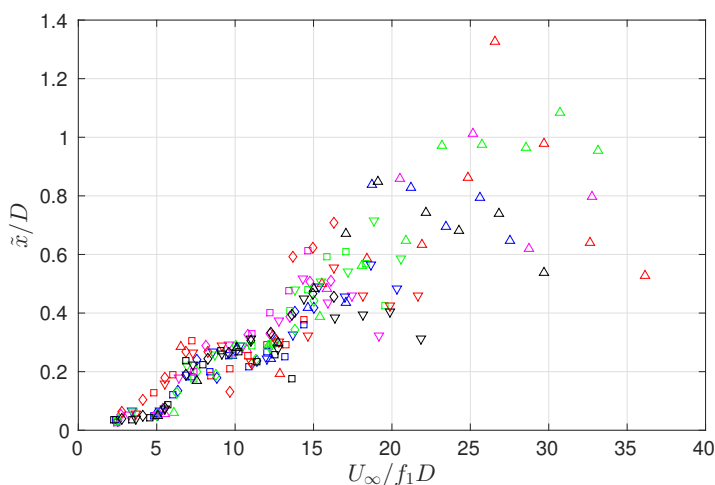


Fig. 5.2 Spatio-temporal RMS of in-line displacement vs reduced velocity for riser in the wake of a cylinder. Colors and symbols defined in table 5.1

The dimensionless in-line deflection, or equivalent spatio-temporal RMS of in-line displacement shows a general quadratic trend with increasing  $U^*$ , as shown in figure 5.3. The lock-in regimes for lower modes are very clear, where the plot shows plateaus for a range of reduced velocities. The amplitudes are significantly smaller than what's observed for an isolated riser case. For the sake of comparison, the values of  $\tilde{x}/D$  for tandem cylinders are shown along with the isolated cylinder in figure

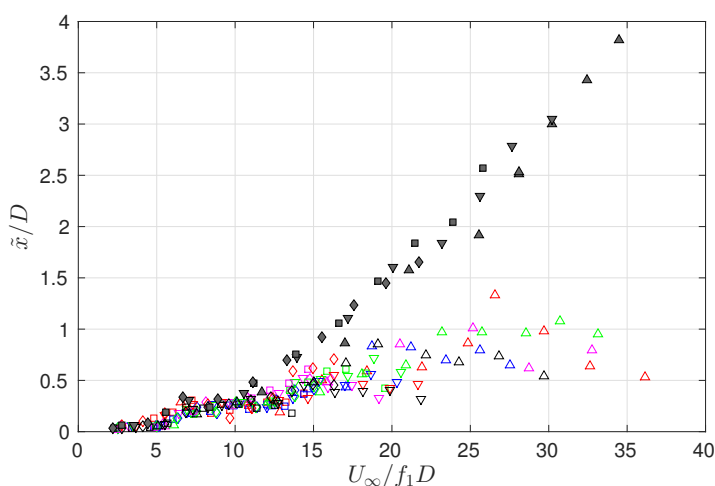


Fig. 5.3 Spatio-temporal RMS of in-line displacement vs reduced velocity for riser in the wake of a cylinder. Colors and symbols defined in table 5.1. Solid symbols indicate spatio-temporal RMS of an isolated riser

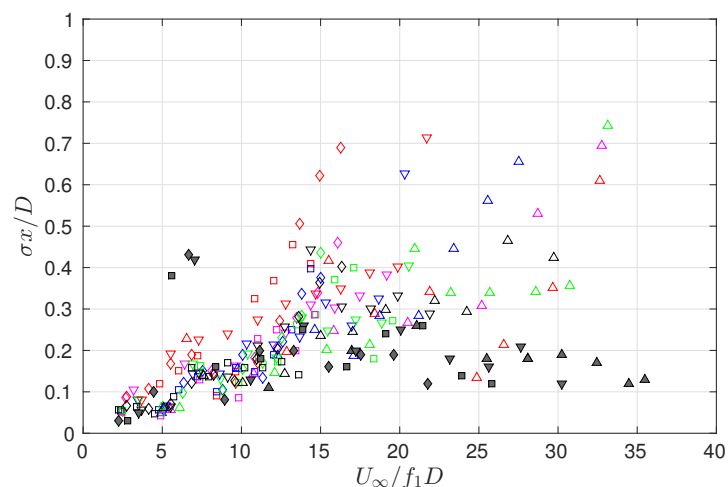


Fig. 5.4 Spatio-temporal standard deviation of in-line displacement vs reduced velocity for riser in the wake of a cylinder. Colors and symbols are defined in table 5.1

The low reduced velocity response, including the presence of the plateaus at ranges of reduced velocity normally expected for lock-in regimes of flexible risers, show almost identical values for isolated riser and riser in the influence of a wake. For all  $S_x > 2D$  the response is almost identical, for all  $S_x \leq 6D$  when  $U^* < 15$ .

The dimensionless spatio-temporal standard deviation of in-line displacement, indicating the dynamic response after removal of mean displacement, plotted against the reduced velocity, is shown in figure 5.4. At very low reduced velocities the values are almost equal to that of an isolated riser, however at higher  $U^*$ , in-line oscillations are almost twice as high as that of an isolated riser. The non-dimensional dominant in-line oscillation frequency, *i.e.* the dominant in-line mode frequency ratio with the fundamental frequency  $f_{dx}/f_1$  is shown in figure 5.5.

A very prominent and interesting feature observed in the case of WIV, as opposed to the VIV, is the absence of the higher Strouhal branch in the dominant mode frequency. The dominant frequency of in-line oscillations of isolated risers, shown in figure 4.13, indicate two branches, where one is at  $2 \times$  the dominant cross-flow frequency. In case of long flexible risers there are many publications, for example Chaplin *et al.* [39], Huera-Huarte[65], Bourguet *et al.* [25], etc which show that the in-line oscillations are at twice the frequency of the cross-flow oscillations. In case of tandem flexible risers, the frequency of the dominant in-line mode follows a low Strouhal number, equivalent to the cross-flow oscillations, indicating strong influence of wake. The plateaus formed at each mode lock-in regime are more prominent, which can be attributed to the low mean deflection of the riser.

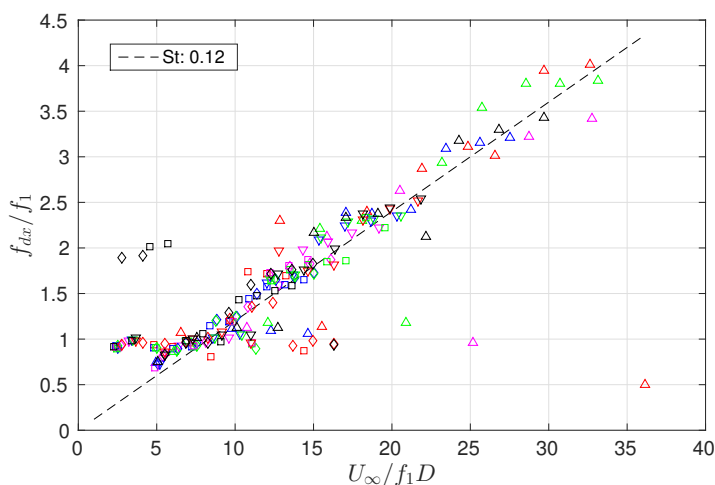


Fig. 5.5 Non-dimensional dominant in-line oscillation frequency ( $f_{dx}/f_1$ ) plotted against reduced velocity ( $U_\infty/f_1D$ ). Colors and symbols are defined in table 5.1

The dimensionless spatio-temporal cross-flow displacements are shown in figure 5.6. Just as the trend observed in the case of in-line oscillations, the cross-flow oscillations also show trend similar to the isolated riser for low reduced velocities. The dominant cross-flow mode frequency, plotted against reduced velocity  $U_\infty/f_1D$  is shown in figure 5.7

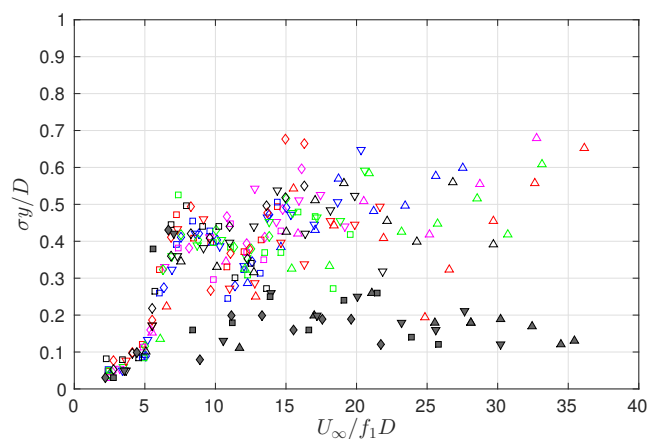


Fig. 5.6 Spatio-temporal RMS of cross-flow displacement vs reduced velocity for riser in the wake of a cylinder. Colors and symbols are defined in table 5.1

The in-line and cross-flow displacement plots, shown in figures 5.4 and 5.6 show a strong resemblance with the case of flexible risers, albeit at significantly higher amplitudes. The results indicate that at for each structural mode, the lock-in condition exists and the response is prominently dominated by the resonance phenomena. The

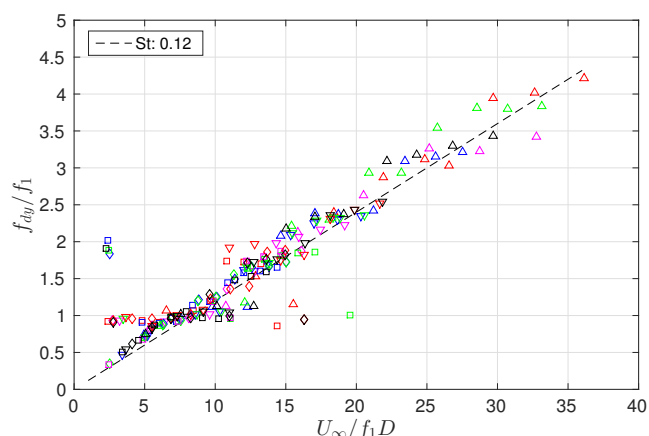


Fig. 5.7 Non-dimensional dominant cross-flow oscillation frequency ( $f_{dy}/f_1$ ) plotted against reduced velocity ( $U_\infty/f_1D$ ). Colors and symbols are defined in table 5.1

maximum non-dimensional in-line oscillation amplitudes are shown in figure 5.8. The values are, surprisingly, about twice as large as the values of the RMS of in-line displacements, shown in figure 5.3.

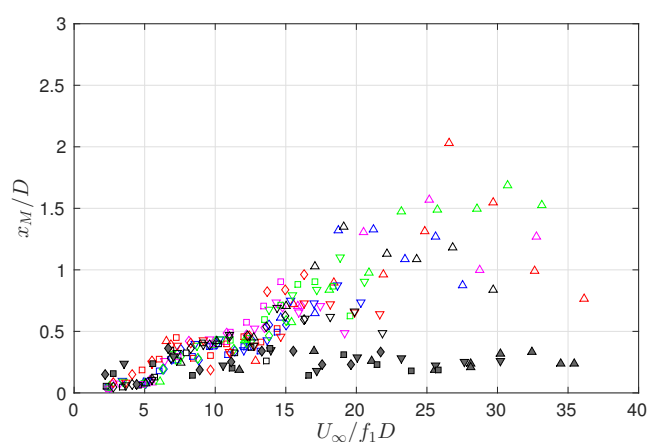


Fig. 5.8 Maximum non-dimensional in-line displacement for riser in wake, plotted against reduced velocity ( $U_\infty/f_1D$ ). Colors and symbols are defined in table 5.1

The maximum cross-flow oscillation amplitudes are shown in figure 5.9. For small values of reduced velocity, the results are similar to the maximum cross-flow oscillations observed by an isolated riser, however for larger reduced velocities ( $U_\infty/f_1D > 12$ ) the cross-flow oscillations can be up to twice as large as that of an isolated riser.

The drag coefficient,  $C_D$  of the riser in the wake of another cylinder is shown in figure 5.10. The plot shows that the drag of the riser in the wake of a cylinder is significantly lesser than the drag of an isolated cylinder. The lowest drag values

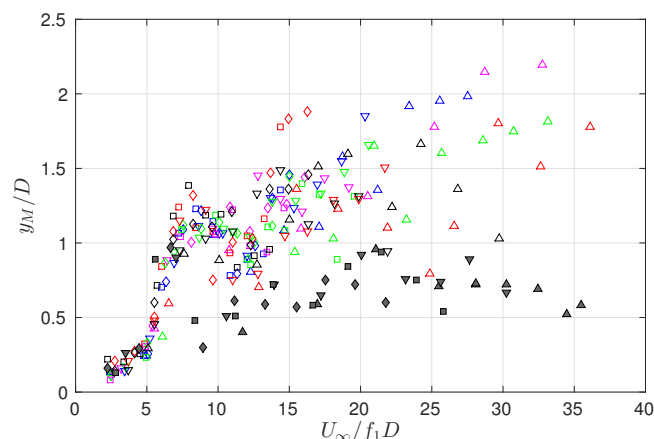


Fig. 5.9 Maximum non-dimensional cross-flow displacement for riser in wake, plotted against reduced velocity ( $U_\infty/f_1D$ ). Colors and symbols are defined in table 5.1

observed are for the case with the smaller  $S_x$ . For the smallest  $U^*$ , negative values of drag are observed for  $S_x = 2$ . For higher values of  $S_x$  show substantially lower drag values.

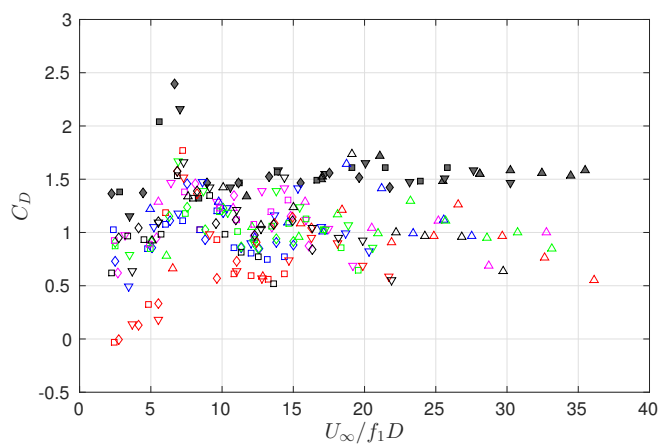


Fig. 5.10 Drag coefficient,  $C_D$  of a riser in the wake of a cylinder, plotted against reduced velocity ( $U_\infty/f_1D$ ). Colors and symbols are defined in table 5.1

## 5.4 Modal Analysis

The modal contribution for each case were determined using the methods described in section 3.5, using sinusoidal mode shapes matrix. The resulting modal distribution, shown in figure 5.11, indicates progression of modal responses as expected from a

flexible riser, albeit at slightly higher reduced velocities as compared to the isolated riser modal responses, shown in figure 4.18. The cross-flow modes are significantly better defined for 1<sup>st</sup> and 2<sup>nd</sup> modes, and are consistent, regardless of the distance from the leading cylinder. The in-line modes are of substantially smaller amplitudes, however clear progression of modes can be observed for in-line oscillation modes, similar to the observation for cross-flow modes. While the wake was produced by a rigid cylinder, the dynamics of the flexible riser in the wake resemble those of a flexible riser without wake interference.

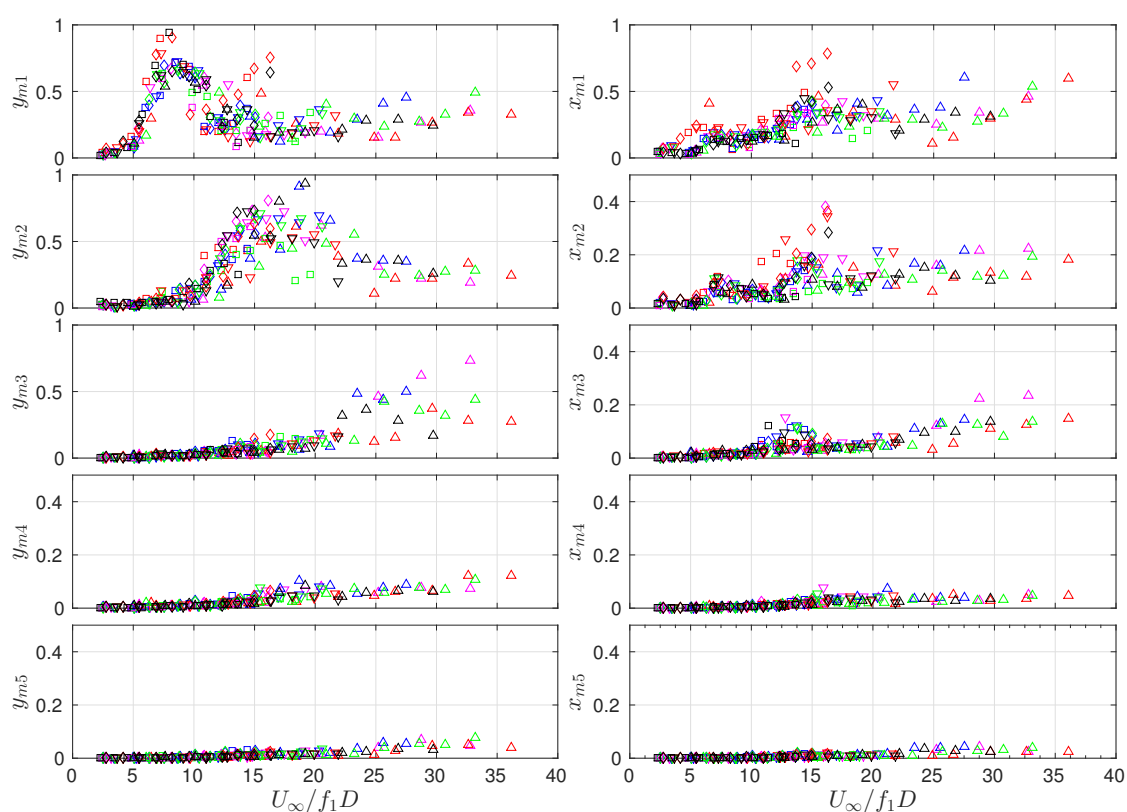


Fig. 5.11 Cross-flow modal amplitudes (left) and in-line modal amplitudes (right) for the first 5 modes vs reduced velocity ( $U^* = U_\infty / f_1 D$ ) for riser in the wake of a cylinder. For legend see table 5.1

## 5.5 Mode shapes

Similar to the case of isolated risers, the mode shape for riser in the wake of a cylinder were also determined using blind source separation. The results indicated, as expected

from a flexible riser, the progression of frequency and corresponding jump in the dominant mode with increasing  $U^*$ . An example case for  $S_x = 4D$  is shown in figure 5.12. It can be observed that at low  $U^*$ , the cross-flow displacement is primarily in the first mode. At slightly higher reduced velocity the cross-flow displacement indicates a significant presence of  $2^{nd}$  mode. Further increase in  $U^*$  results in  $2^{nd}$  mode becoming the dominant mode. This progression of modes can also be seen for a low center to center distance case,  $S_x = 2D$ , as shown in figure 5.13.

The mode shapes plotted in figure 5.12 for  $S_x = 4D$ , and 5.13 for  $S_x = 2D$  indicate identical mode shape progression with  $U^*$ , regardless of  $S_x$  for up to  $4D$ . Many authors have suggested that there is a limiting proximity interference region, for the case of rigid cylinders, which is defined as  $S_x = 3D$  by Meneghini *et al.* [100] and Carmo *et al.* [37], or  $S_x = 3.25D$  as per Kitagawa & Ohta[83], and  $S_x = 3.75$  by Zdarvkovich[179]. All of these studies are based on rigid cylinders. In case of flexible risers, Huera-Huarte & Gharib [70] indicate that for separations below  $S_x/D \leq 3$ , an increase of reduced velocity above the first lock-in regime resulted in an almost disappearance of the amplitudes. They could not analyse the higher lock-in regimes because of the physical limitations of the facility.

A center to center distance  $S_x = 5D$  is an interesting case. The mode shapes are shown in figure 5.14. According to some studies for the case of rigid cylinders,  $S_x = 5.5D$  is the distance at which the vortices formed at the leading cylinder are fully developed, and are impinging on the trailing cylinder, resulting in an unstable behaviour in the wake of the trailing cylinder ( Dehkordi *et al.* [45] ). A previous study on the tandem arrangement of flexible cylinders, carried out by Huera-Huarte & Gharib[69] show that for separation of 3.5 diameters, a bistable regime existed with the vortex wake discontinuously appearing between the cylinders. At 4 diameters separation, they show that the vortex shedding from the leading cylinder appeared continuously in the gap. For larger gap separations, up to 8 diameters, larger amplitudes of oscillations were reported. In our case, the center to center distance of 5 diameters indicate the largest mode of vibrations, This distance corresponds to the gap space where the vortex shedding from the leading cylinder is assumed to be continuously present in the gap between the leading and trailing cylinders.

## 5.5 Mode shapes

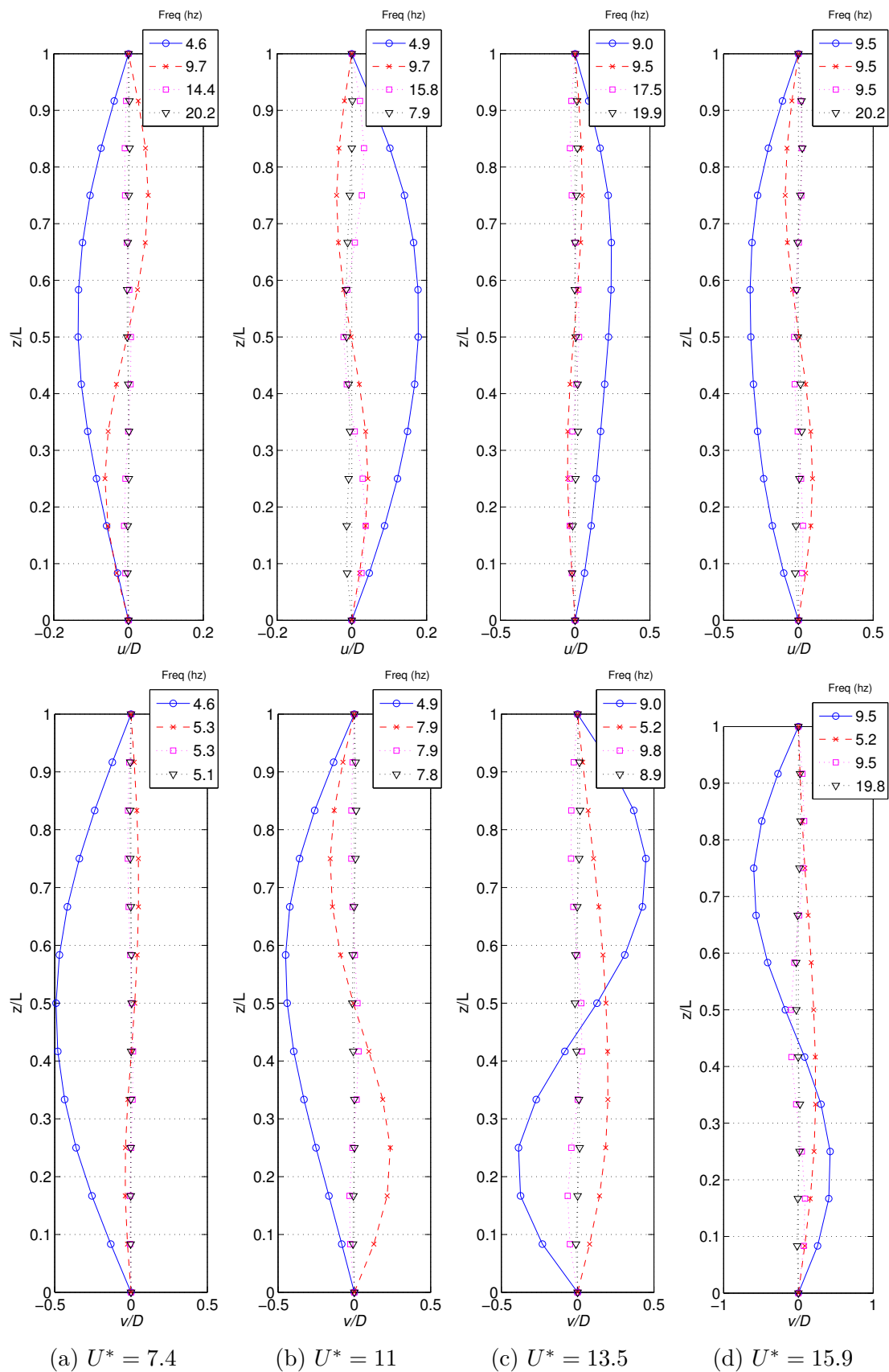


Fig. 5.12 Progression of mode shape and mode competitions with increasing  $U^*$  for riser in the wake. In-line modes (top) and cross-flow modes (bottom) at indicated  $U^*$ . For  $S_x = 4D$ , starting tension  $T_{st} = 520N$ .



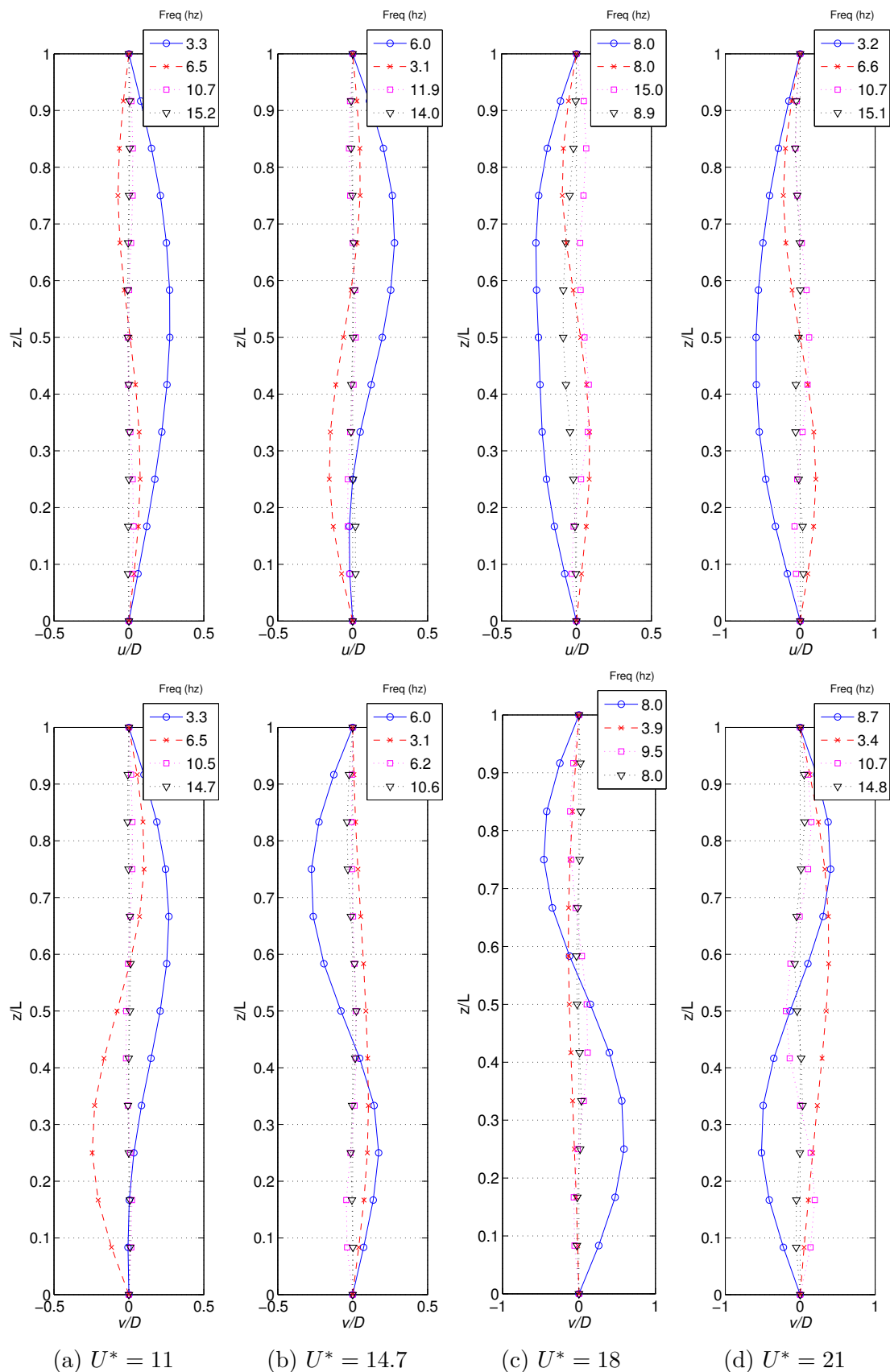


Fig. 5.13 Progression of mode shape and mode competitions with increasing  $U^*$  for riser in the wake. In-line modes (top) and cross-flow modes (bottom) at indicated  $U^*$ . For  $S_x = 2D$ , starting tension  $T_{st} = 205N$ .

## 5.5 Mode shapes

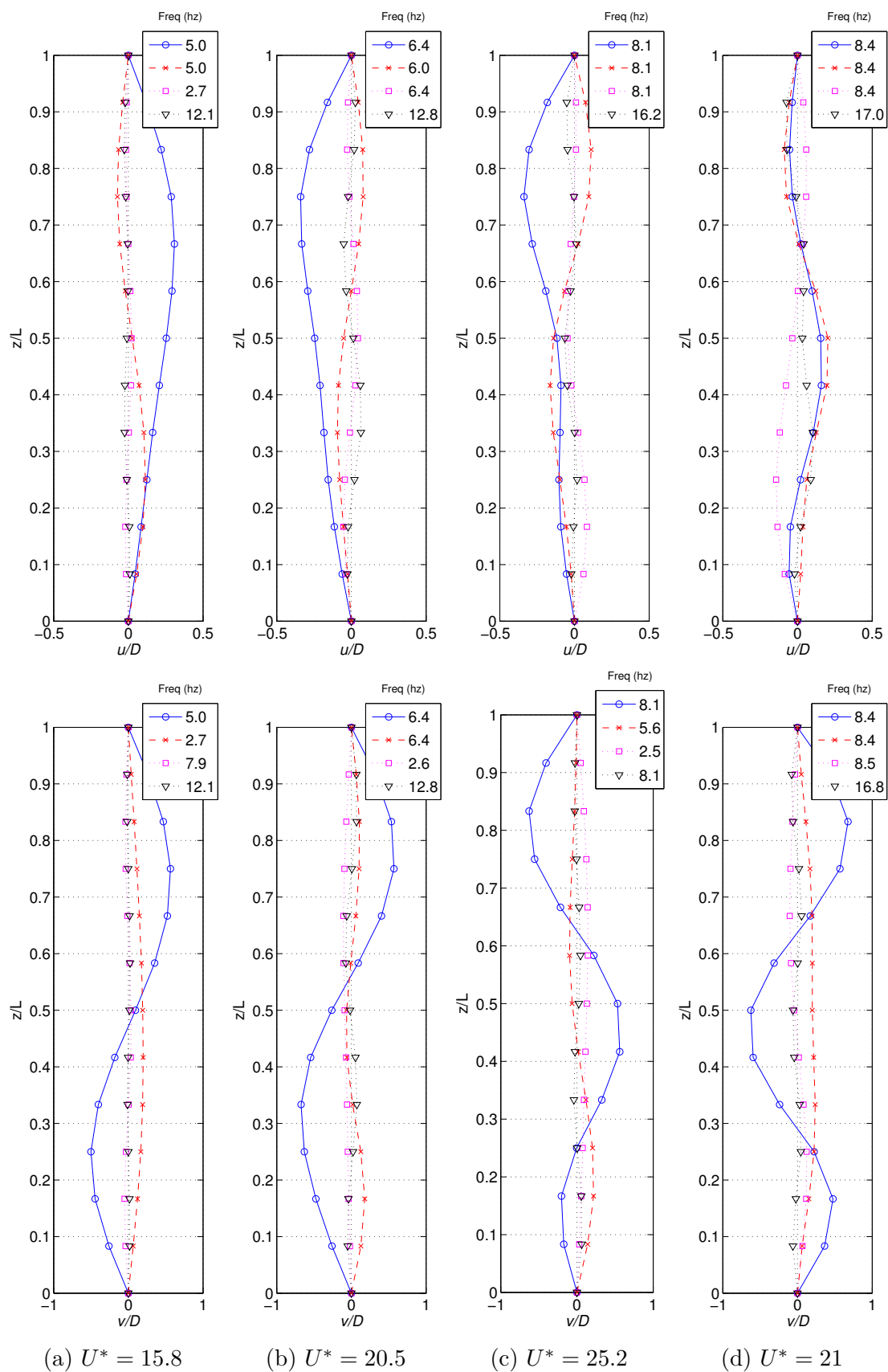


Fig. 5.14 Progression of mode shape and mode competitions with increasing  $U^*$  for riser in the wake. In-line modes (top) and cross-flow modes (bottom) at indicated  $U^*$ . For  $S_x = 5D$ , starting tension  $T_{st} = 170N$ .

## 5.6 Summary of Results

The results presented in this chapter show the dynamic response of a flexible riser immersed in the wake of a stationary cylinder. The novelty of these experiments was that the trailing riser was a flexible cylinder with a relatively high modal density, and the conditions were such that multi-modal response was achieved. Almost all previous literature on the subject comprises of either rigid cylinders (fixed, or flexibly mounted) in the wake of another rigid cylinder (see section 2.4) , or cases of flexible cylinders that are limited to only the first mode of oscillation due to the low modal density (Huera-Huarte & Gharib [69, 70]). In case of flexibly mounted rigid cylinders, the modal response decreases beyond the lock-in region, thus causing a reducing in amplitudes. In case of flexible risers, the modal response continues to grow inside each modal response region, as the effect of modal density, despite the presence of an upstream rigid riser, still dominate the response behaviour of the cylinder.

The mean deflection, and the drag are substantially lower than the case of an isolated riser, specially so for very low center-to-center distance. Some relational concepts in literature, for example, the significantly low drag for center to center distance below  $3D$  are observed similar to the rigid cylinders, however the progression of all parameters, against reduced velocity follow the same trend as that of an isolated flexible riser.

## CHAPTER 6

# WAKE CHARACTERISTICS OF A FLEXIBLE RISER UNDERGOING VIV

---

## 6.1 Introduction

It is well known that for cylinders with variable geometry, the flow pattern in the wake varies along the span of the cylinder. Numerous studies have been carried out for the cases of sinusoidal disturbance along the cylinder span, both numerically (Mittal & Balachandar [102]) and experimentally (Szewczyk & Bearman[146], Bearman & Tombazis[12], Tombazis & Bearman [150], Owen *et al.* [117] etc). These cases have been briefly covered in section 2.2.4.2. In case of tapered cylinders the wake patterns are significantly different at various positions along the cylinder span ( Techet *et al.* [148]). The variations in wake pattern along the span of the cylinder have previously been documented for cases like flexible cantilevers (Fujarra *et al.* [50]) and pivoted cylinders (Flemming & Williamson[49]) (see section 2.2.4.3). In some cases they have shown similarities to the wake of a tapered cylinder in terms of the shedding modes and vortex merging. All these previous works suggest that some of these features may be observed in the VIV of flexible bodies due to the variation of amplitude of oscillation along the span of the cylinder. The work presented here is inspired by the previous results presented by Huera-Huarte *et al.* [71], in which the authors suggested, after Inverse Finite Element Method computations based on the experimental data from Chaplin *et al.* [39], that the instantaneous values of  $C_L$  and instantaneously varying values of  $C_D$  were always zero at the nodes. This zero force would imply that some sort of symmetric flow structures dominate the wake at the nodes, whereas the anti-node has the classic vortex shedding, and a transitional region exists between the node and the anti-node. In those previous works, the flow structures at the nodes were not analysed. Thus, a series of experiments were carried out to better understand

the transition in the wake from the node to the anti-node in an oscillating cylinder. This was done by carrying out planar DPIV at various positions along the span of a vertically mounted flexible cylinder undergoing VIV. Both cross-flow and in-line planes were analysed for prominent flow structures to better understand the flow patterns that characterise the wake of the cylinder from the node to the anti-node.

## 6.2 Experimental Setup

### 6.2.1 Apparatus

The experiments were carried out in a still water tow tank with dimensions of 0.6m x 0.6m x 2.0m, with usable length of 1.7m. The towing carriage was mounted on smooth rails and coupled with an AC motor through a gearbox. The towing speed was controlled by using a variable frequency drive, which was connected to a data acquisition system. A precision potentiometer was used for measurement of position and tow speed.

For the current set of experiments a model was fabricated following the design by Huera-Huarte[66]. A 1m long spring with an external diameter of 6mm was passed through a flexible polyolefin tube with an external diameter  $D$  of 6.5mm. Both ends were sealed with hot glue to avoid ingress of water. The resulting cylinder, 1m in length, had a smooth outer surface. The cylinder had a mass of 64 g/m, resulting in a mass ratio  $m^*$ , defined as the ratio of the mass of the cylinder to the mass of the displaced water, of 1.93. The cylinder was mounted in a rigid frame with pin joints at both ends. The apparatus was installed on the towing carriage in a way that the lower 50% of the cylinder was submerged in the water. The carriage was towed at speeds ranging from 0.25m/s to 0.3m/s, giving Reynolds numbers, based on the external diameter, from 1500 to 2000. The speeds were chosen where the cylinder displayed second mode of cross-flow vibration with a stable structural node located well below the free surface. Ample time was given between the runs to ensure minimal background turbulence. Before the experiments, in order to obtain characteristics of the model, the cylinder was mounted in a rigid frame with a mechanical oscillator connected at one end. The natural frequencies and damping were checked in air and in water with 50% coverage. The tension at the top end was gently incremented. At 3N of applied tension, the second mode natural frequency  $f_2 \approx 8Hz$  was observed. This value was chosen for optimum synchronization of oscillation with the camera frame rate.

The experiment parameters and model details are listed in Table 6.1. The experiment parameters and model details are listed in Table 6.1.

Table 6.1 Experiment Parameters for wake analysis

Parameters	Value
Length (L)	1 m
Diameter (D)	0.0065 m
Aspect Ratio (L/D)	153
Submerged Length	0.50 m
Top Tension	3 N
Tow Velocity	0.25-0.3 m/s
Reynolds Number (Re)	1500-2000
Mass (m)	0.064 kg
Mass Ratio ( $m^*$ )	1.93
Structural Damping $2^{nd}$ mode ( $\zeta_2$ )	1.4 (% of $\zeta_c$ )
Submerged fund. nat. Freq. ( $f_1$ )	3.9 Hz
Submerged $2^{nd}$ mode nat. Freq. ( $f_2$ )	7.9 Hz

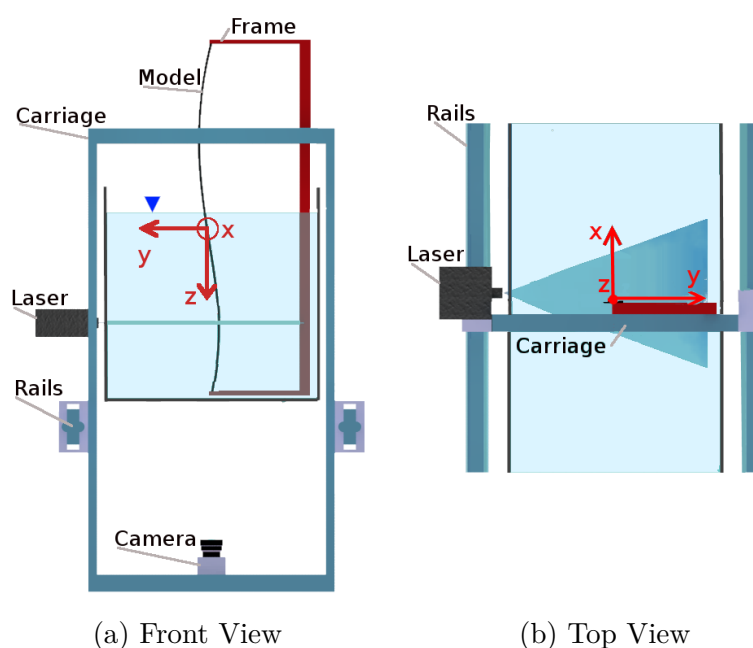


Fig. 6.1 Front and Top view of experimental setup

For ease of understanding the reference coordinate system was fixed at the structural node of the cylinder. The  $x$  axis is in the towing direction of the cylinder,  $z$  axis is along the span of the cylinder, from node towards the anti-node, and  $y$  axis is in the

cross-flow direction satisfying the right hand rule. The schematic of the apparatus installed in the tow tank appears in fig 6.1.

### 6.2.2 DPIV and Flow Visualization setup

The flow visualization and DPIV interrogations were carried out at eight  $xy$  planes at different positions along the axis of the cylinder, and at two  $xz$  planes parallel to both the the axis of the cylinder and the towing direction. The flow patterns near the structural node were considered more critical for analysis, and the measurements were carried out in closer spaced planes near the node. The details of the analysed planes are described in Table 6.2. In order to set up a non-dimensional parameter to standardize the wake characteristics, the axial positions of the planes are described as a ratio of half wavelength of the structural oscillation, centred at the node. This parameter  $\lambda^*$  is thus defined such that the node is at  $\lambda^*=0$  and anti-node is at  $\lambda^*=0.5$

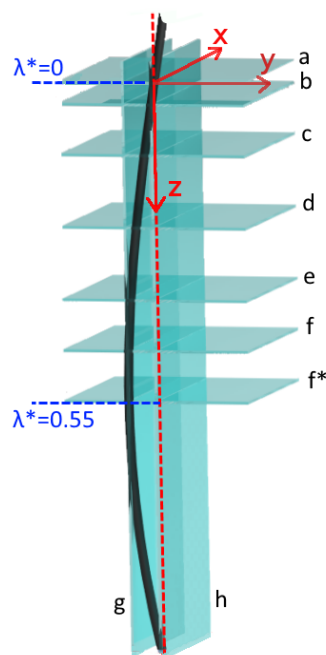


Fig. 6.2 Position of light sheets for PIV and FV data.

For the  $xy$  planes the flow was seeded with polyamide particles of  $0.5\mu\text{m}$  nominal diameter. The planes were illuminated with a 5W continuous wave diode pumped solid state (CW-DPSS) laser. For collection of images, a high speed camera based on 8 bit CMOS sensor with a pixel size of  $5.5\mu\text{m} \times 5.5\mu\text{m}$ , and full resolution of

Table 6.2 Details of the analyzed DPIV and FV planes and runs

Plane	Orient.	$\lambda^*$	Speeds(m/s)
a	xy	0	[0.25:0.05:0.30]
b	xy	0.05	[0.25:0.05:0.30]
c	xy	0.11	[0.25:0.05:0.30]
d	xy	0.24	[0.25:0.05:0.30]
e	xy	0.36	[0.25:0.05:0.30]
f	xy	0.46	[0.25:0.05:0.30]
f*	xy	0.55	[0.25:0.05:0.30]
g	xz (y/D=0.5)	—	[0.25:0.05:0.30]
h	xz (y/D=0.0)	—	[0.25:0.05:0.30]

4MPixel ( $2048 \times 2048$ ) was used. The camera was configured for a smaller region of interest ( $960 \times 640$  pixels), and externally triggered at a fixed frame rate of 440fps. The exposure time was fixed at  $7\mu\text{s}$ . The resulting time step was 2.27 ms. For each plane 11 runs were carried out with towing speed from 0.25m/s to 0.3m/s with 0.05m/s increments. The image frames covered an area from -1D to 8D in the inline direction of the travel, and  $\pm 3D$  along the cross-flow direction. After processing, the flow fields were obtained in the form of matrices with 120x80 vectors. The same setup was used for flow visualization images by reducing the frame rate to 30fps, with a fixed exposure time of 20ms. The particle travel resulted in formation of streaks in collected images, indicating the flow patterns.

For each image the position of the cylinder center and the phase of oscillation were measured by image processing techniques. For planes closer to the anti-node the phase was identified from the position of the center. Even though the amplitude of oscillation was very low at the node, a phase was associated to each snapshot, after image processing, by using the perspective view of the cylinder. This way, the phase averaging was consistent along the span of the cylinder. The oscillation cycle was divided in four phase  $\phi$  positions, from 0 to  $\frac{3}{2}\pi$ . DPIV vector fields were phase averaged accordingly to these phases.

The  $xz$  planes covered the region along the span going from anti-node to node, and -2D to 15D along the  $x$  direction. A hydrogen bubble generator apparatus was devised that comprised of a twisted pair of  $50\mu\text{m}$  steel wire cathode, which was mounted at a distance of  $2D$  in front of the cylinder. A copper plate anode was suspended from the mounting frame, submerged in the water. A 30V DC power source was used for formation of bubbles streamlines from the twisted wire. The region was illuminated using a light sheet generated by the DPSS laser source previously described, and images were collected at 100fps with an exposure time of  $20\mu\text{s}$ .



### 6.3 Results and Discussion

After determination of the position of the center of cylinder, and the phase of oscillation, the shape along the span of the cylinder was reconstructed based on the excursions at each span-wise location. In the range of selected Reynolds numbers the cylinder showed second mode of vibrations in cross-flow direction as expected. The resulting excursion ranged from almost no oscillation at the node, to a straight line of only cross-flow oscillation of magnitude a  $A/D \approx 0.5$  at the anti-node.

We observed identical patterns in all the cases tested. For the sake of brevity only one case is being presented in detail. For this case the flow speed was 0.27m/sec, giving Reynolds number of 1750. The dominant cross-flow frequency of oscillation was 7.8Hz, and the normalized velocity  $U^*$  based on the dominant cross-flow frequency was 5.32, whereas based on the natural frequency the reduced velocity was 10.38. The analysed excursions at various heights and the resulting shape of the cylinder are shown in figure 6.3, where  $A/D$  is the non-dimensional amplitude of oscillation.

It was observed that at the anti-node the cylinder displayed a standard vortex street with a single vortex per cycle, synchronized with the structure's oscillation frequency. The results were identical to the flow patterns shown by Huera-Huarte and Bearman[67]. The distance between successive similar vortices was  $4.5D$  for  $A/D \approx 0.5$ . The vortex structures, as seen in figure 6.4a are similar to the sketches presented by Williamson and Roshko [172] for the corresponding wake wavelength and amplitude.

The shedding pattern was entirely different at the node, as seen in figure 6.4b. There is a significant increase in vortex formation length, as well as absence of coherent shed vortices in the flow downstream of the cylinder. This phenomenon has not been reported in previous studies of cylinders undergoing VIV. The simultaneous presence of counter-rotating vortices formed downstream of the cylinder resemble the numerical analysis presented by Newman & Karniadakis [111], in the matter of the formation of symmetric pair of vortices, however we did not observe the shedding of the symmetric pairs as shown by them. Similarities can also be seen with case of "*stream-wise symmetric*" (*SS*) shedding mode shown by Jauvtis & Williamson [77] for a case of rigid cylinder undergoing pure in-line motion and no cross-flow oscillation. It is emphasized that the *SS* shedding mode is because of inline motion, which was not present in our case. The resulting wake at the node is significantly narrow, similar to the cases shown by Bearman & Owen [11], and Owen *et al.* [118] for a sinuous cylinder, where there

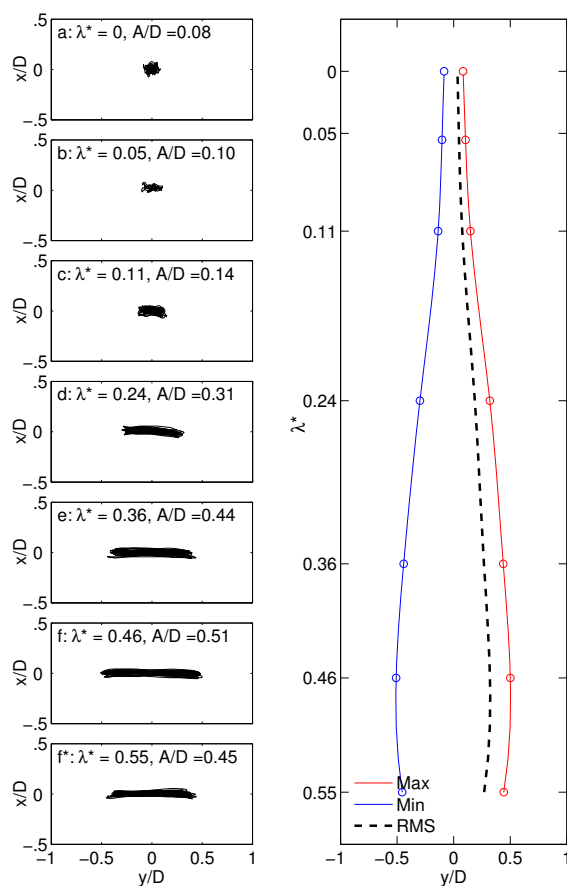


Fig. 6.3 Non-dimensional cylinder excursions at various heights are shown in the left column. The RMS, minimum and maximum excursion cylinder shape is shown in the right column. The position of node is at  $\lambda^*=0$ , and anti-node is at  $\lambda^*=0.5$

was no coherent shedding observed in the valley region defined by them.

The flow visualization results are shown in figure 6.5. The results show perfect correlation to the DPIV results shown in figure 6.4. The anti-node region shows the standard kármán vortex street. The flow behind the node forms a narrow wake, and there is a persistent presence of a symmetric set of counter-rotating vortices.

The phase averaged PIV results for phase with zero excursion and maximum oscillation velocity ( $\phi=0$  and  $\phi=\pi$ ) at all  $\lambda^*$  are shown in figure 6.6. Figure 6.7 depicts the vorticity fields which are phase averaged at maximum excursion and minimum oscillation speed ( $\phi=\pi/2$  and  $\phi=\frac{3}{2}\pi$ ).

Looking at these maps, going from the anti-node to the node (down to up), one can identify significant differences in the regions of wake along the axis of the cylinder. The wake appears to be divisible in three regions:

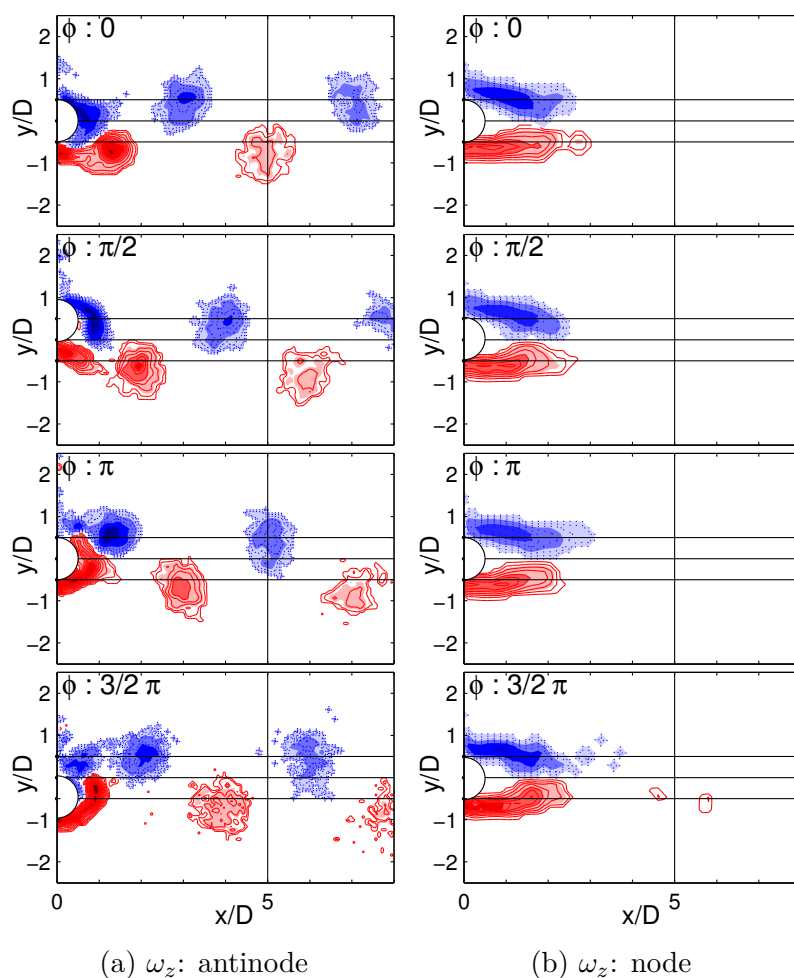


Fig. 6.4 Vorticity maps ( $\omega_z$ ) for different phases of oscillation, at (a) the anti-node and (b) the node. For clarity the horizontal lines are marked to indicate  $y/D = -0.5, 0, 0.5$ , and a vertical line indicates  $x/D = 5$

1. The first is the anti-node region, where  $\lambda^* \gtrsim 0.2$  and corresponding  $A/D \gtrsim 0.3$ , is a region of shear layer interaction. The vortices are formed very close to the surface of the oscillating cylinder. As the cylinder moves to the extreme excursion, the opposing shear layer interact and causes the cut-off of the opposite side shear layer, resulting in the shedding of the vortex, as described by Gerrard [53].
2. The second region is an interim region, where  $0.05 \lesssim \lambda^* \lesssim 0.2$ , with  $0.1 \lesssim A/D \lesssim 0.3$ . This is a transitional region between the node and the anti-node. The vortices appear to have shifted by  $180^\circ$  compared to the anti-node region. Comparing this region to the nodal region where  $\lambda^* = 0.05$ , at  $x/D > 3$  the

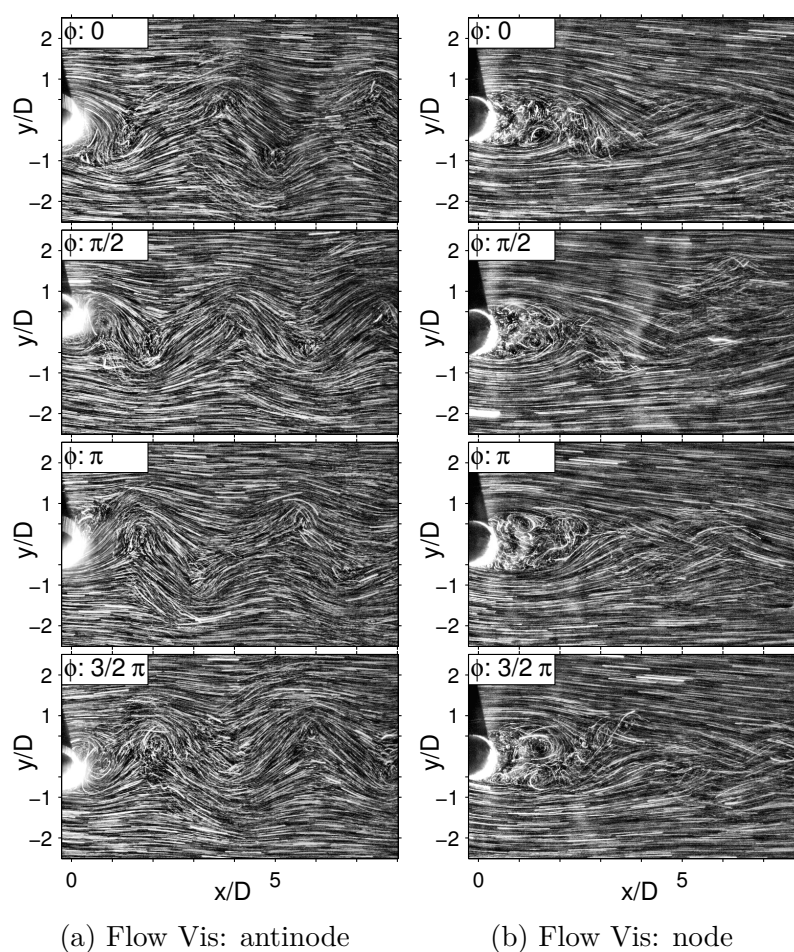


Fig. 6.5 Flow visualization results for all phases ( $\phi$ ) at (a)the anti-node and (b)the node.

coherent shedding has totally vanished. This leads us to think that a vortex connectivity might be taking place in this region.

3. Finally the third region, very near the node where  $\lambda^* \lesssim 0.05$  and  $A/D \lesssim 0.1$ . The vorticity maps indicate the presence of a symmetric pair of vortices. These vortices are formed at a greater distance ( $\approx 1.5D$ ) from the cylinder. There is no cylinder cross-flow motion and no shear layer interaction between opposing shear layers. There are no coherent packages of vorticity downstream beyond  $x/D > 3$ .

The presence of a region where the vortex shedding undergoes a  $180^\circ$  phase shift was observed in all the cases investigated. It is clear that a complex three-dimensional structure should exist around the nodal regions, as the shedding is out-of-phase between two consecutive anti-nodes. Our data shows that at the nodes there is no coherent

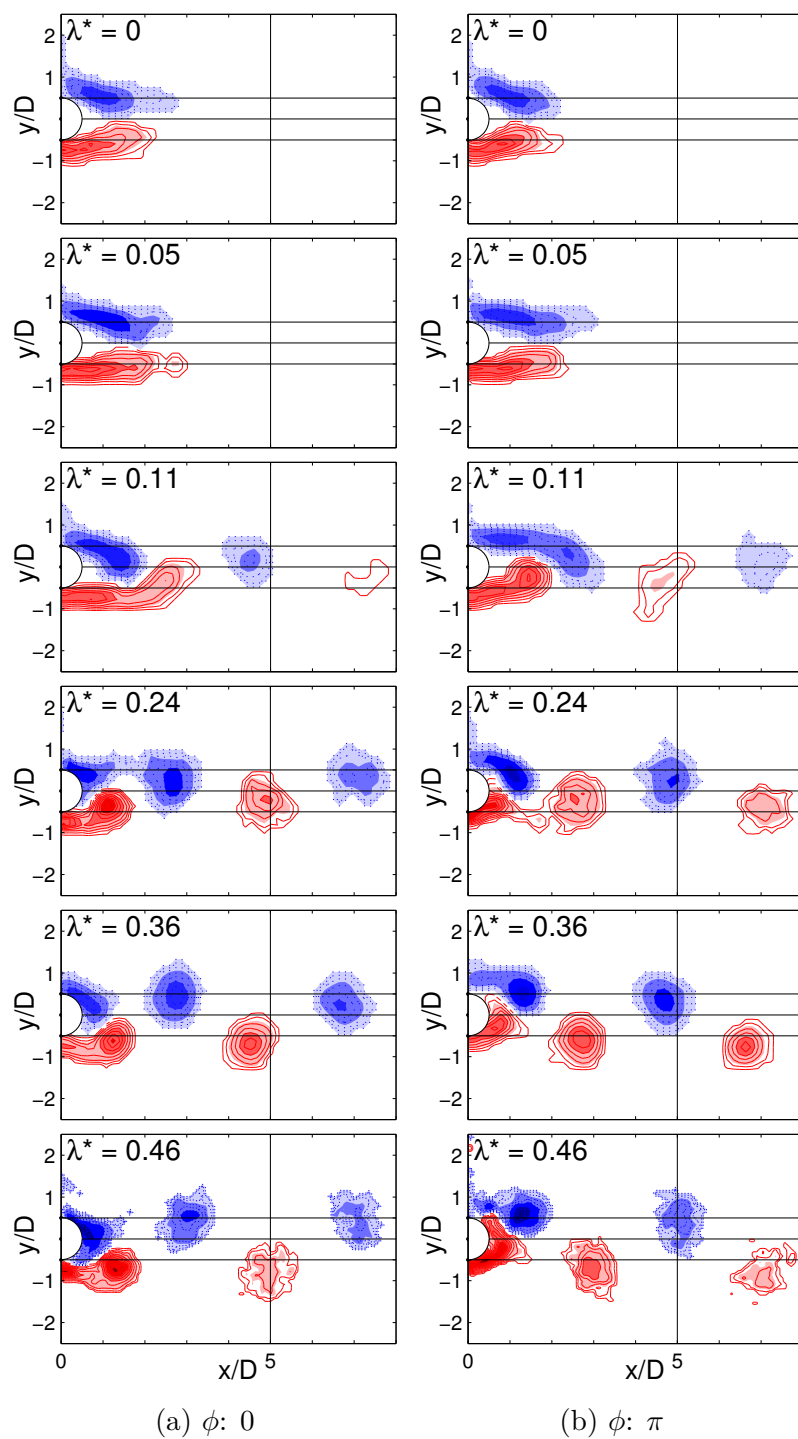


Fig. 6.6 Vorticity maps ( $\omega_z$ ) for phase averaged PIV at minimum excursion,  $\phi: 0$  and  $\phi: \pi$ . For clarity, horizontal lines indicate  $y/D$  of  $-0.5$ ,  $0$  and  $0.5$ , and vertical line indicates  $x/D=5$

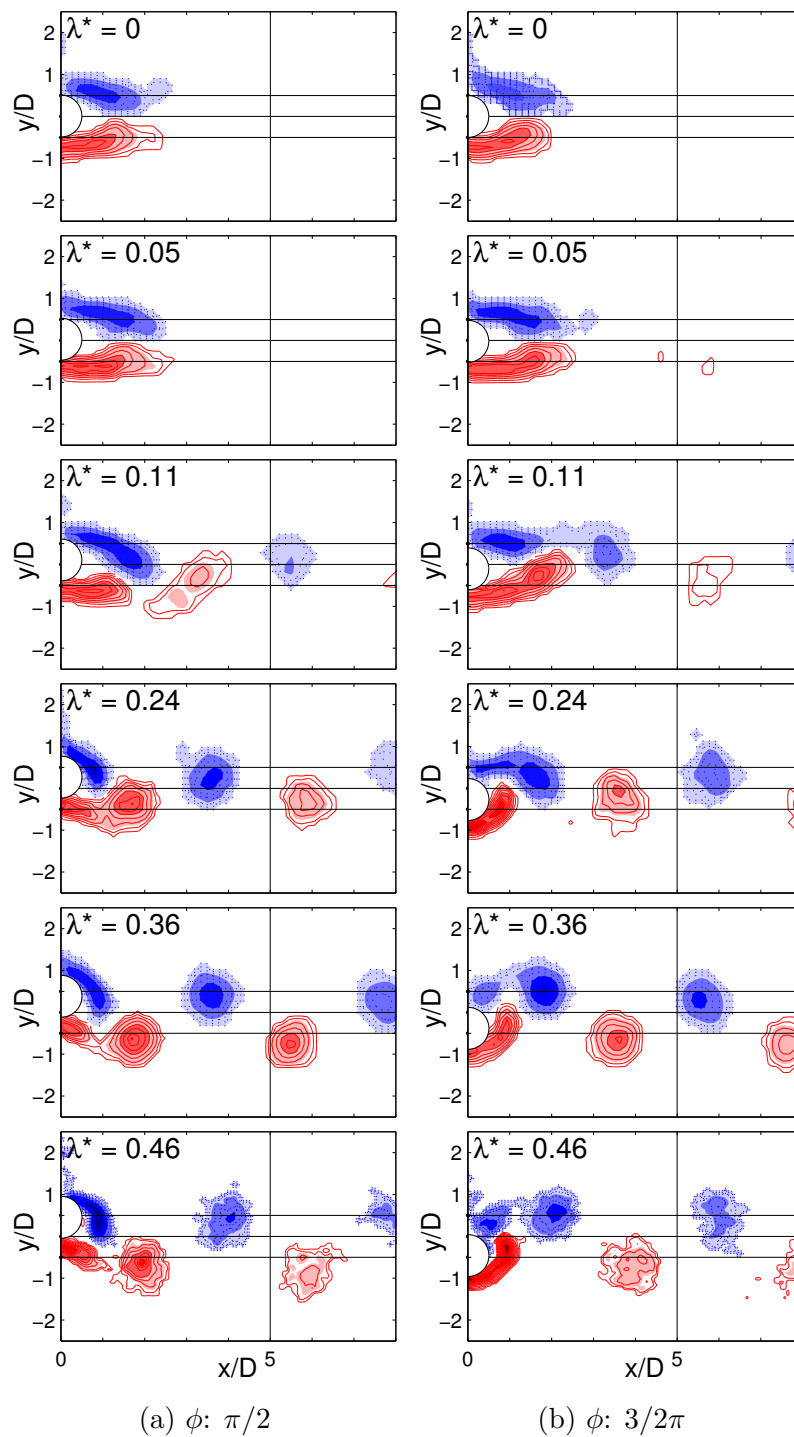


Fig. 6.7 Vorticity maps ( $\omega_z$ ) for phase averaged PIV at minimum excursion,  $\phi: \pi/2$  and  $\phi: \frac{3}{2}\pi$ .

shedding but a symmetrical structure that remains attached to the surface of the cylinder, so a connectivity needs to take place at each side of the node. Conceptually at each anti-node there should be a local lock-in condition that disappears near the node, where there is no motion. The structural oscillation frequency at all other span-wise locations remains close to the shedding frequency under lock-in conditions. The amplitude increases gradually from the node to the anti-node. Accordingly, there is a point between the node, and the anti-node where a phase change is expected to occur. To the knowledge of the authors, there is no existing literature describing this in detail.

In the case of rigid cylinders, in which there are no local changes in frequency and amplitude, a shift in the phase between the vortex shedding and the forced motion, depending on the frequency ratio imposed on the structure and the amplitude has been documented (Lu and Dalton [96]). Moreover, the phase between the lift force and the amplitude in rigid cylinders has been widely studied in the past, by means of force vibration or self-excited set-ups. The focus has been to understand the changes of the phase as a function of the reduced velocity and/or the ratio between oscillation and shedding frequency (Ongoren and Rockwell[116], Carberry and Sheridan[36] and Jeon and Gharib[78]). Again, the relationship between the local shedding or fluid forces and the span-wise varying amplitude in a flexible cylinder at different points along its length has not been investigated.

In order to better understand the mechanism of this switch in the phase of shedding, and how the wake adjusts in the three regions, further analysis was carried out by collecting flow visualization images in the  $xz$  planes. The phase averaged flow visualization images in  $xz$  planes at  $y/D = 0$  are shown in figure 6.8 for cylinder at mean position and at maximum position. The DPIV planes previously presented in figures 6.6 and 6.7 are indicated by red lines and corresponding markings on the right axis of the figures.

The vortices, indicated by the illuminated bubbles, are almost parallel to the cylinder for a range of  $0.15 < \lambda^* < 0.5$ . As already described this is the region where the larger amplitude of oscillation results in entrainment of vortices. At  $\lambda^* < 0.15$  the vortices appear to move away from the cylinder body. Clear signs of connectivity are observed between vortices of opposite rotation at  $\lambda^* \approx 0.12$ . Focusing on the top right corner, i.e. in the wake of the node, one can observe that the structures vanish immediately downstream of the cylinder for  $x/D > 3$ . This dissipation and the subsequent darker region indicate that there are no coherent structures in the flow in the nodal regions. Figure 6.9 shows the instantaneous flow visualization images at two

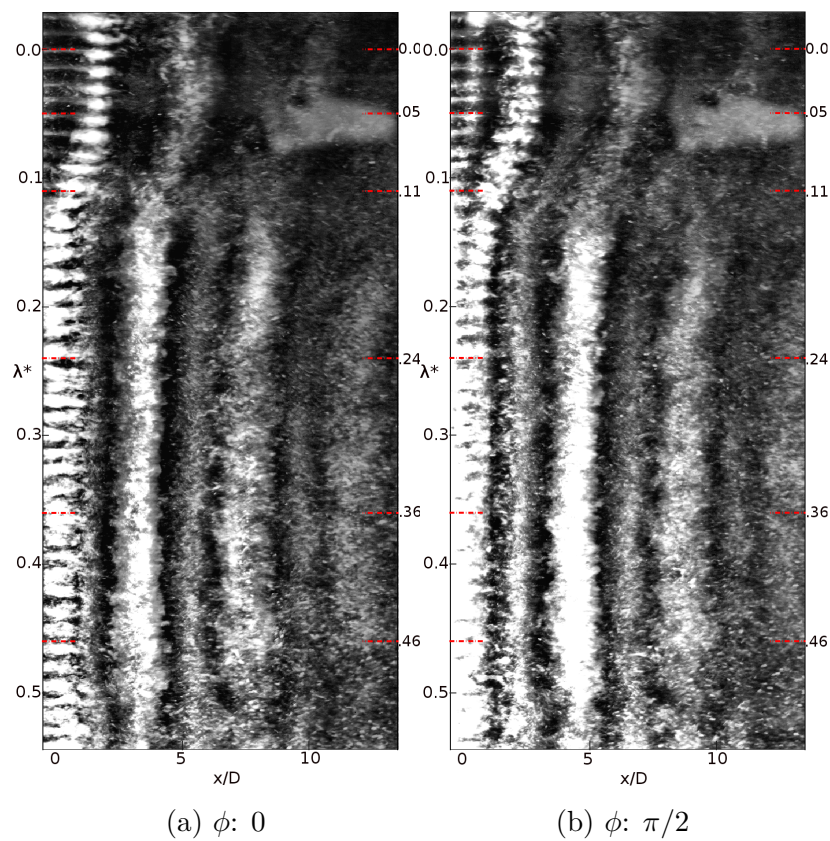


Fig. 6.8 Averaged flow visualization images in  $xz$  plane at  $y/D = 0$ , (a) at  $\phi: 0$  and (b) at  $\phi: \pi/2$ . Vertical axis markers on the left indicate  $\lambda^*$ . DPIV planes are marked on the right vertical axis.



sample points corresponding to the mean position and the maximum excursion. The connectivity between the vortices is even more evident in these images.

The DPIV results seen in figure 6.6 and figure 6.7, at  $\lambda^* = 0.11$  showed the shift in the vortex street, and the first shed vortex appeared to have connectivity to the vortex still attached to the cylinder. Here we have a clearer picture that the subsequent vortex connectivity occurs in the flow. The height at which the opposing vortices connect appears to be within the range of  $0.075 < \lambda^* < 0.15$ , corresponding to the amplitudes of oscillation of the cylinder  $A/D \approx 0.1$ .

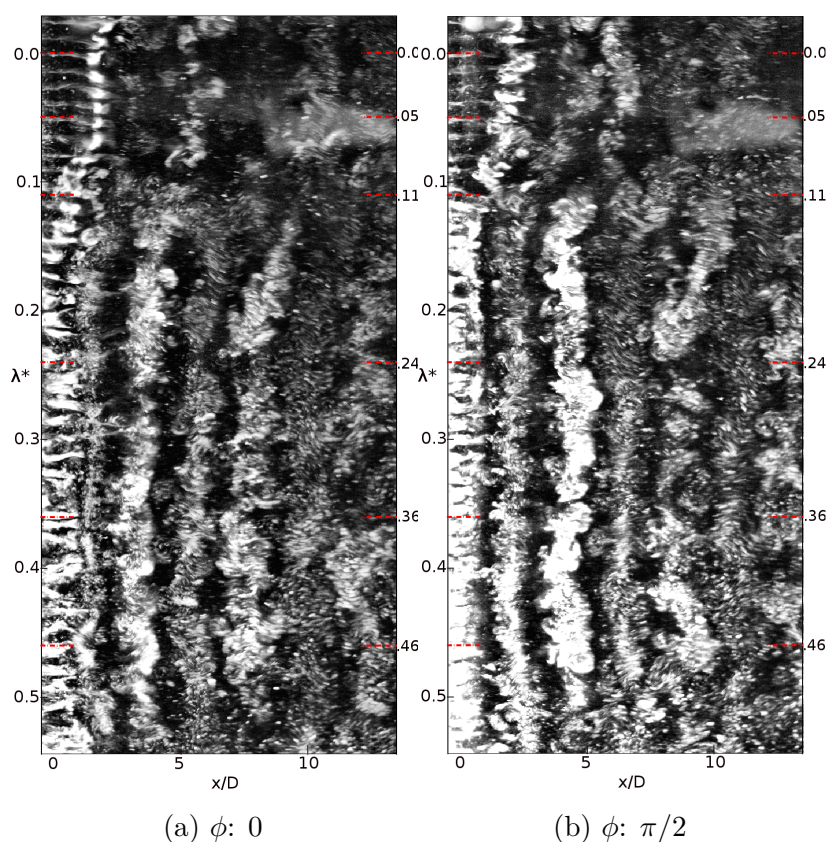


Fig. 6.9 Instantaneous flow visualization images in  $xz$  plane at  $y/D=0$ , (a) at  $\phi: 0$  and (b) at  $\phi: \pi/2$ . Vertical axis markers on the left indicate  $\lambda^*$ . DPIV planes are marked on the right vertical axis.

The phenomenon of vortex connectivity was further explored by application of proper orthogonal decomposition (POD) technique on the DPIV vector fields collected in  $xz$  plane, resulting in the mapping of flow modes. This technique has been previously proven as an alternative to phase averaging [73] in the absence of precise phase data. The results, shown in figure 6.10 indicate clear presence of structures in  $2^{nd}$  and  $3^{rd}$

mode in the flow direction ( $V_x$ ) for  $\lambda^* \gtrsim 0.15$ . For  $\lambda^* < 0.075$  no significant coherent stream-wise structures are observed downstream of the cylinder.

The region of the phase change is seen clearly in the figure 6.10, in the 2nd mode  $V_x$ . From the anti-node to the start of the region 2 ( $0.15 \leq \lambda^* \leq 0.4$ ) the vortices appear parallel to the cylinder axis. The region 2 starts where the vortices appears to move away from the cylinder ( $\lambda^* \approx 0.15$ ), and the vortex shedding resemble an oblique mode of shedding. The phase shift, observed in figure 6.6 and 6.7 is approximately  $180^\circ$ , however the plots for Mode2 and Mode3 of  $V_x$  in figure 6.10 show that the phase change, going from the anti-node towards the node, in region 2 can be slightly more than  $180^\circ$ , And the  $xy$  plane at  $\lambda^* = 0.11$  is at a position where the phase shift is about  $180^\circ$ . The vortices seem to disappear at the upper end of region 2. This leads us to the conclusion that the opposite direction vortices undergo a process of merging and connectivity in this region ( $0.75 \leq \lambda^* \leq 0.15$ ).

The high values in first mode of axial flow  $V_z$ , resulting from the vortex connectivity in the region  $\lambda^* \approx 0.1$  are observed in the lower row of plots in figure 6.10 where the red coloured region indicates the span-wise flow, from the anti-node region, towards the node. The vortex connectivity is also evident in the  $2^{nd}$  mode oscillation of flow in the axial( $z$ ) direction, around the same spanwise location.

For the case of flexible cylinders, the force distribution along the span of a flexible cylinder has not been experimentally documented as it is very difficult to measure, non-intrusively, the local forces along the span. Attempts to obtain the local force distributions have been made in the past[71], but such computations did not allow to conclusively investigate local changes, or phase differences along the span, as the flow dynamics were not described.

Based on the results presented here, the presence of a pinch-off for the first shed vortex and the connectivity between the subsequent vortices, as well as the difference in formation length of the vortices in the nodal and in the anti-nodal region, a vortex skeleton sketch is drawn that satisfies the conditions observed in our experiments. The sketch is shown in figure 6.11. The model proposed here satisfies the previous findings [57, 146] and also satisfies the observations made by Huera-Huarte et.al [71], where they suggested that the  $C_L$  and the instantaneous variations of  $C_D$  were zero in the nodal region of a flexible oscillating cylinder.

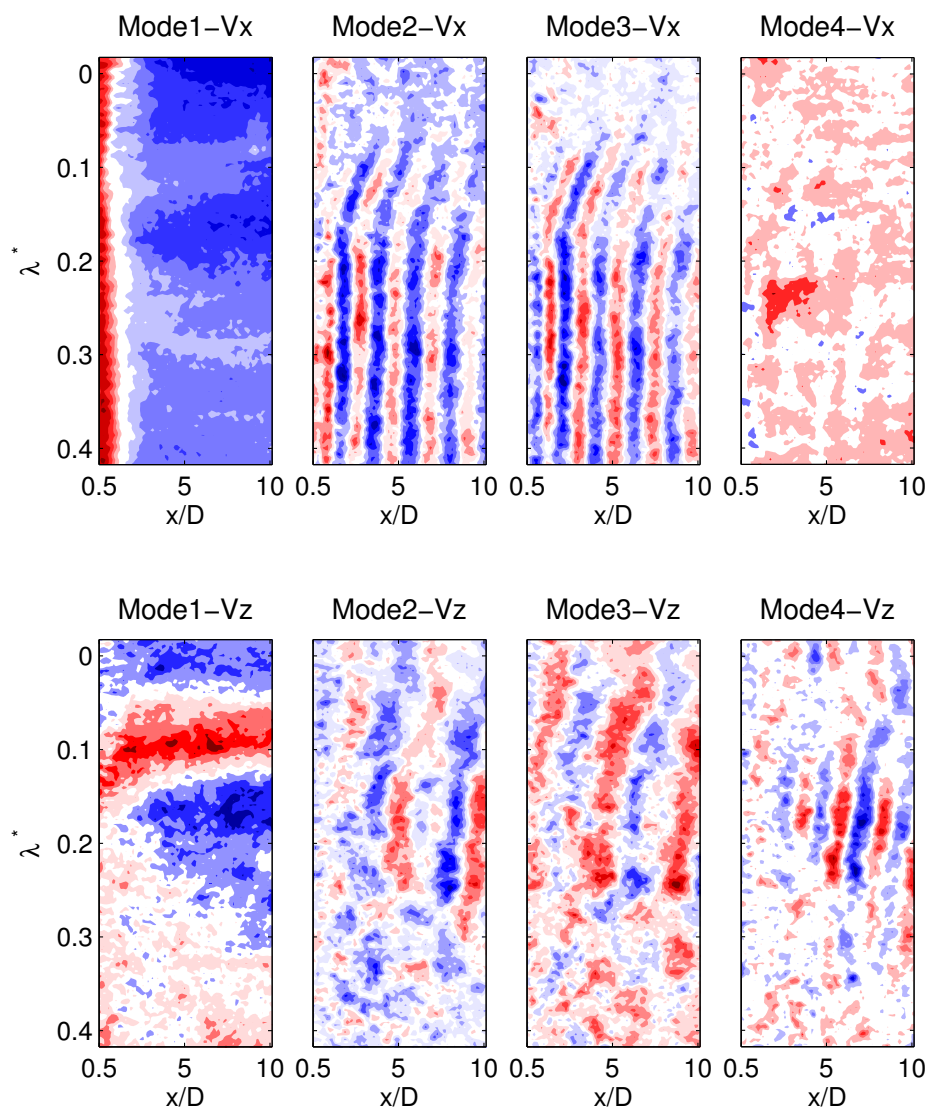


Fig. 6.10 POD plots of flow in  $xz$  plane at  $y/D=0$ , indicating the first four modes for  $V_x$  (top) and  $V_z$  (bottom).

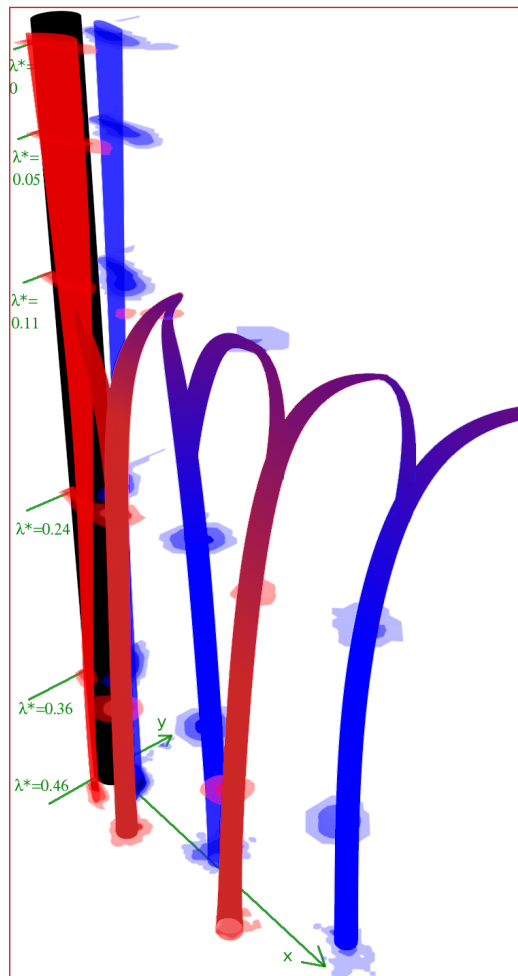


Fig. 6.11 Vortex skeleton sketch, reconstructed based on the PIV and FV images

## 6.4 Summary

We have analysed the flow structures in the wake of a flexible cylinder undergoing an almost pure second mode of cross-flow vortex induced vibrations, using digital particle image velocimetry and flow visualization techniques.

At the anti-node region the opposite signed vortices are shed when the cylinder excursion is near its maximum amplitude points, at  $3/2\pi$  and  $\pi/2$  of the cycle, regularly and predictably, resulting in the classic shedding of 2 vortices per cycle. We have observed in these experiments how the formation length is independent of the amplitude of excursion, as long as the values are higher than a certain minimum amplitude. When the amplitude does not reach this minimum value, approaching the node, conditions exist such that the vortex shedding undergoes a  $180^\circ$  phase shift. As we interrogated positions closer to the node, the formation length increased, and the lack of opposing shear layer interaction resulted in the absence of coherent shedding. The flow at the node forms a symmetric pair of counter-rotating vortices that remain attached to the cylinder body without exhibiting shedding.

We have proposed here a flow structure that shows a vortex connectivity region near the node, in a transitional region from a clear lock-in condition at the anti-nodes to a no shedding situation at the node where there is absence of motion. The consistent symmetric pair of recirculation areas at the node, and the lack of oscillation (in-line and cross-flow), is in agreement with the observations of local force distribution along the length of a flexible cylinder, previously made by Huera-Huarte et.al[71].

## CONCLUSIONS AND FUTURE WORK

---

### 7.1 Conclusions

The thesis covers the experiments carried out to study the multi-mode response of flexible circular cylinders. The two cylinders used for analysis of isolated riser VIV had realistic mass ratios  $m^* = 2.7$ , and  $m^* = 1.1$ . The aspect ratios ( $L/D \approx 190$  and  $L/D \approx 160$ ) and Reynolds numbers ( $Re = 2800-28000$ , and  $Re = 3800-38000$ ), which were limited by the experimental facility, are an order of magnitude smaller than the realistic off-shore values, the experimental results gave us an improved understanding of the physics of vortex induced vibrations.

The experimental set-up design, based on some of the previous successful experimental campaigns in the subject area, proved to be robust and accurate. The use of strain gage based measurement system provides a low cost alternative, with significantly high density, as compared to the accelerometers based measurement systems that are frequently seen in large scale datasets. The data analysis was carried out using two different modal decomposition techniques. The standard modal decomposition technique provided us with excellent statistical foundation for data comparison, whereas blind source separation technique gave a deeper insight to the individual cases where multiple mode responses at multiple frequencies, were separated.

The overall response of isolated flexible cylinder is characterised by lock-in regimes, or branches, and in each regime the response is dominated by a specific mode. Within each branch, the response is somewhat similar to that of a rigid cylinder in its initial branch, however instead of the lower branch as expected from the rigid cylinder, the flexible cylinder jumps to the initial branch of the next mode. The mass ratio, similar to the case of rigid cylinders, plays a significant role in the response regimes. The amplitudes of oscillation for a low mass ratio cylinder was significantly larger than any

of the previously documented results, with values approaching 1D. The drag coefficient values for low mass ratio riser were almost twice the values observed for a higher mass ratio riser, with significant resemblance, or correlation with the amplitudes of oscillation.

For the cylinders installed in tandem arrangement, some interesting results were observed. The response behaviour was a combination of that of a rigid cylinder in tandem arrangement, and that of an isolated flexible cylinder. The drag response, based on the separation distance between the risers, to some extent followed the trend as expected from rigid cylinders. A center to center separation of less than 3 diameters ( $S_x < 3D$ ) showed incredibly low drag, as documented for the case of rigid risers, whereas for the separation larger than 3D, the drag, while significantly larger than the 2D separation, still showed lower values as compared to an isolated cylinder. The largest modes were observed at 5D separation, conforming with the theory regarding rigid cylinders, that it is the distance at which the vortices from the front cylinders have fully developed, and result in the largest interaction with the trailing cylinder. The oscillation response, was characterised by lock-in regimes almost identical to the overall response of a flexible cylinder.

The analysis of the wake of a flexible cylinder, using Particle Image Velocimetry, yielded in some very interesting results. The wake at the node comprised of the shedding patterns as expected from flexibly mounted rigid cylinders, with regular vortices being shed in form of two single vortices per cycle. Closer to the structural node, a phase change was observed in the vortex shedding cycle, associated with the position where the oscillation amplitude was below 0.1D. The most intriguing results were observed at the structural nodes, where instead of a regular shedding pattern, a pair of vortices were observed that consistently remained with the cylinder. The absence of vortex shedding at the node reaffirmed the results shown by Huera-Huarte and Gharib [71], who predicted the absence of periodic oscillatory forces at the structural nodes of a flexible riser undergoing vortex induced vibrations.

## 7.2 Future Work

1. Further work on low mass ratio risers: the analysis of low mass ratio risers was restricted in the cross-flow modes. The drag, and the mean deflection of the riser was significantly higher, compared to the high mass ratio riser, and the corresponding modes achieved were lower. An increase in the tension would have reduced the mean deflection. However it would have resulted in a lower modal

- density, and thus harder to achieve higher modes. The fabrication process for the low mass ratio riser, detailed in chapter 3.1.2, is very simple, economical, and scalable. The same fabrication process can be used to make modes long enough to achieve a very high mode count. The low mass ratio is a very realistic case in real world application, and the results obtained would go a long way in adding to the analytical models for prediction of off-shore risers vortex induced vibrations.
2. Research on tandem cylinders: The cases presented in this thesis comprise of the response of flexible cylinder in the wake of a rigid cylinder. The indication of the mode based response branches is a new addition to the literature on the VIV of cylinders in tandem arrangement. It is recommended that for future work, a tandem arrangement of identical, instrumented flexible cylinders be used, which would match the more realistic, practical scenario.
  3. The wake of a flexible cylinder: The current research was limited to the number of planes analysed to determine the wake characteristics of a flexible cylinder, from node to anti-node. The runs were carried out in a tow tank, where slight variation in the speeds or conditions could cause the position of the node to change. The resulting spanwise position of the planes, while being a good approximation, are not accurate. The three regions of the wake are identified, however the boundaries of these regions are approximated because of these limitations. The best venue for carrying out such an experiment would be a very low turbulence intensity water channel. Once a stable oscillation mode is achieved, the entire wake can be analysed with significantly higher number of planes. It is also suggested that utilizing volumetric methods such as defocusing digital particle image velocimetry (DDPIV) (Pereira & Gharib[120]) could give us significantly better picture of the entire wake of a flexible cylinder.



UNIVERSITAT ROVIRA I VIRGILI

VORTEX INDUCED VIBRATIONS OF LONG FLEXIBLE CYLINDERS WITH AND WITHOUT WAKE INTERFERENCE

Denise Fischer Hubert

Dipòsit Legal: T 992-2015

## BIBLIOGRAPHY

---

- [1] Ahmed, A. and Bays-Muchmore, B. (1992). Transverse flow over a wavy cylinder. *Phys. Fluids*, 4(9)(September):1959–1967.
- [2] Akbari, M. H. and Price, S. J. (2005). Numerical investigation of flow patterns for staggered cylinder pairs in cross-flow. *J. Fluids Struct.*, 20:533–554.
- [3] Assi, G. R. S., Bearman, P. W., Carmo, B. S., Meneghini, J. R., Sherwin, S. J., and Willden, R. H. J. (2013). The role of wake stiffness on the wake-induced vibration of the downstream cylinder of a tandem pair. *J. Fluid Mech.*, 718(Ruscheweyh 1983):210–245.
- [4] Assi, G. R. S., Bearman, P. W., and Meneghini, J. R. (2010). On the wake-induced vibration of tandem circular cylinders: the vortex interaction excitation mechanism. *J. Fluid Mech.*, 661:365–401.
- [5] Assi, G. R. S., Meneghini, J. R., Aranha, J. A. P., Bearman, P. W., and Casaprima, E. (2006). Experimental investigation of flow-induced vibration interference between two circular cylinders. *J. Fluids Struct.*, 22:819–827.
- [6] Barkley, D. and Henderson, R. D. (1996). Three-dimensional Floquet stability analysis of the wake of a circular cylinder. *J. Fluid Mech.*, 322:215–241.
- [7] Bays-Muchmore, B. and Ahmed, A. (1993). On streamwise vortices in turbulent wakes of cylinders. *Phys. Fluids A Fluid Dyn.*, 5(2):387.
- [8] Bearman, P. W. (1969). On vortex shedding from a circular cylinder in the critical Reynolds number regime. *J. Fluid Mech.*, 37.
- [9] Bearman, P. W. (1984). Vortex shedding from oscillating bluff bodies. *Annu. Rev. Fluid Mech.*, 16:195–222.
- [10] Bearman, P. W. (2011). Circular cylinder wakes and vortex-induced vibrations. *J. Fluids Struct.*, 27(5-6):648–658.
- [11] Bearman, P. W. and Owen, J. C. (1998). Reduction of bluff body drag and suppression of vortex shedding by the introduction of wavy separation lines. *J. Fluids Struct.*, 12:123–130.
- [12] Bearman, P. W. and Tombazis, N. (1993). The effects of three-dimensional imposed disturbances on bluff body near wake flows. *J. Wind Eng. Ind. Aerodyn.*, 49:339–349.

- [13] Bearman, P. W. and Wadcock, A. J. (1973). The interaction between a pair of circular cylinders normal to a stream. *J. Fluid Mech.*, 61(3):499–511.
- [14] Belouchrani, a., Abed-Meraim, K., and Cardoso, J.-F. (1993). Second-order blind separation of temporally correlated sources. *Proc. Int. Conf. . . .*, (1):2–7.
- [15] Bénard, H. (1908). Formation périodique de centres de giration à l’arrière d’un obstacle en mouvement. *Comptes rendus l’Académie des Sci.*, 147:839–842.
- [16] Bénard, H. (1913a). Sur la marche des tourbillons alternés derrière un obstacle. *Comptes rendus l’Académie des Sci.*, 156:1225–1228.
- [17] Bénard, H. (1913b). Sur la zone de formation des tourbillons alternés derrière un obstacle. *Comptes rendus l’Académie des Sci.*, 156:1003–1005.
- [18] Biermann, D. and Herrnstein, W. H. (1933). The interference between struts in various combinations. Technical report, NACA.
- [19] Bishop, R. E. D. and Hassan, A. Y. (1964). The Lift and Drag Forces on a Circular Cylinder Oscillating in a Flowing Fluid. *Proc. R. Soc. London, A*, 277:51–75.
- [20] Blackburn, H., Marques, F., and Lopez, J. (2005). Symmetry breaking of two-dimensional time-periodic wakes. *J. Fluid Mech.*, 522:395–411.
- [21] Blackburn, H. M. and Karniadakis, G. E. (1993). Two- and Three-Dimensional Simulations of Vortex-Induced Vibration of a Circular Cylinder. *3rd Int. offshore polar Eng. Conf.*, (1977):715–720.
- [22] Blake, W. K. (1986). *Mechanics of Flow-Induced Sound and Vibration, V1: General Concepts*. Academic Press.
- [23] Blevins, R. D. and Coughran, C. S. (2009). Experimental Investigation of Vortex-Induced Vibration in One and Two Dimensions With Variable Mass, Damping, and Reynolds Number. *J. Fluids Eng.*, 131(October 2009):101202.
- [24] Bloor, M. S. (1964). The transition to turbulence in the wake of a circular cylinder. *J. Fluid Mech.*, 19.
- [25] Bourguet, R., Karniadakis, G. E., and Triantafyllou, M. S. (2011a). Lock-in of the vortex-induced vibrations of a long tensioned beam in shear flow. *J. Fluids Struct.*, 27:838–847.
- [26] Bourguet, R., Karniadakis, G. E., and Triantafyllou, M. S. (2011b). Vortex-induced vibrations of a long flexible cylinder in shear flow. *J. Fluid Mech.*, 677:342–382.
- [27] Bourguet, R., Karniadakis, G. E., and Triantafyllou, M. S. (2013). Phasing mechanisms between the in-line and cross-flow vortex-induced vibrations of a long tensioned beam in shear flow. *Comput. Struct.*, 122:155–163.
- [28] Brennen, C. (1982). A review of added mass and fluid inertial forces. *Ocean Eng.*, (January):50.

- [29] Brika, D. and Laneville, A. (1993). Vortex-induced vibrations of a long flexible circular cylinder. *J. Fluid Mech.*, 250:481–508.
- [30] Brika, D. and Laneville, A. (1995). An Experimental Study of the Aeolian Vibrations of a Flexible Circular Cylinder at Different Incidences.
- [31] Brika, D. and Laneville, A. (1997). Wake interference between two circular cylinders. *J. Wind Eng. Ind. Aerodyn.*, 72:61–70.
- [32] Cagney, N. and Balabani, S. (2013a). Mode competition in streamwise-only vortex induced vibrations. *J. Fluids Struct.*, 41:156–165.
- [33] Cagney, N. and Balabani, S. (2013b). Wake modes of a cylinder undergoing free streamwise vortex-induced vibrations. *J. Fluids Struct.*, 38:127–145.
- [34] Cagney, N. and Balabani, S. (2014). Streamwise vortex-induced vibrations of cylinders with one and two degrees-of-freedom. *J. Fluid Mech.*, 758:702–727.
- [35] Carberry, J. (2000). *Wake states of a submerged oscillating cylinder and of a cylinder beneath a free surface*. Ph.D. Thesis, Monash University, Monash University. Australia.
- [36] Carberry, J. and Sheridan, J. (2001). Forces and wake modes of an oscillating bluff body. *J. Fluids Struct.*, 15:523–532.
- [37] Carmo, B. S., Meneghini, J. R., and Sherwin, S. J. (2010). Possible states in the flow around two circular cylinders in tandem with separations in the vicinity of the drag inversion spacing. *Phys. Fluids*, 22:1–7.
- [38] Chaplin, J. R., Bearman, P. W., Cheng, Y., Fontaine, E., Graham, J. M. R., Herfjord, K., Huera-Huarte, F. J., Isherwood, M., Lambrakos, K., Larsen, C. M., Meneghini, J. R., Moe, G., Pattenden, R. J., Triantafyllou, M. S., and Willden, R. H. J. (2005a). Blind predictions of laboratory measurements of vortex-induced vibrations of a tension riser. *J. Fluids Struct.*, 21:25–40.
- [39] Chaplin, J. R., Bearman, P. W., Huera-Huarte, F. J., and Pattenden, R. J. (2005b). Laboratory measurements of vortex-induced vibrations of a vertical tension riser in a stepped current. *J. Fluids Struct.*, 21:3–24.
- [40] Chen, Kim, and Choi (2009). Numerical simulation of a short flexible pipe subject to forced motion and vortex-induced vibration. *Acta Oceanol. Sin. -English Ed.*, 28(6):70–83.
- [41] Dahl, J. M., Hover, F. S., Triantafyllou, M. S., Dong, S., and Karniadakis, G. E. (2007). Resonant vibrations of bluff bodies cause multivortex shedding and high frequency forces. *Phys. Rev. Lett.*, 99(October):5–8.
- [42] Dahl, J. M., Hover, F. S., Triantafyllou, M. S., and Oakley, O. H. (2010). Dual resonance in vortex-induced vibrations at subcritical and supercritical Reynolds numbers. *J. Fluid Mech.*, 643:395.

- [43] De Vecchi, A. (2009). Wake dynamics of flow past a curved circular cross-section body under cross-flow vibration. pages 1–231.
- [44] De Vecchi, A., Sherwin, S. J., and Graham, J. M. R. (2009). Wake dynamics of external flow past a curved circular cylinder with the free-stream aligned to the plane of curvature. *Solid Mech. its Appl.*, 14(June 2008):175–185.
- [45] Dehkordi, B. G., Moghaddam, H. S., and Jafari, H. H. (2011). Numerical simulation of flow over two circular cylinders in tandem arrangement. *J. Hydrodyn.*, 23(1):114–126.
- [46] Durgin, W. W., March, P. A., and Lefebvre, P. J. (1980). Lower Mode Response of Circular Cylinders in Cross-Flow. *J. Fluids Eng.*, 102(June):183.
- [47] Evangelinos, C., Lucor, D., and Karniadakis, G. E. (2000). DNS-derived force distribution on flexible cylinders subject to vortex-induced vibrations. *J. Fluids Struct.*, 14(429-440):429–440.
- [48] Feng, C. C. (1968). The measurement of vortex-induced effects in flow past a stationary and oscillating circular and D-section cylinders. Master’s thesis, University of British Columbia.
- [49] Flemming, F. and Williamson, C. H. K. (2005). Vortex-induced vibrations of a pivoted cylinder. *J. Fluid Mech.*, 522:215–252.
- [50] Fujarra, A. L. C., Pesce, C. P., Fleming, F., and Williamson, C. H. K. (2001). Vortex-Induced vibration of a flexible cantilever. *J. Fluids Struct.*, 15(3-4):651–658.
- [51] Gabbai, R. D. and Benaroya, H. (2005). An overview of modeling and experiments of vortex-induced vibration of circular cylinders. *J Sound Vib*, 282:575–616.
- [52] Gerrard, J. H. (1965). A disturbance sensitive Reynolds number range in the flow past a circular cylinder. *J. Fluid Mech.*, 22:187–196.
- [53] Gerrard, J. H. (1966a). The mechanics of the formation region of vortices behind bluff bodies. *J. Fluid Mech.*, 25:401.
- [54] Gerrard, J. H. (1966b). The three-dimensional structure of the wake of a circular cylinder. *J. Fluid Mech.*, 25:143.
- [55] Gerrard, J. H. (1978). The wakes of cylindrical bluff bodies at low {R}eynolds number. *Philos. Trans. R. Soc. London, Ser. A*, 288:351–382.
- [56] Gharib, M. R. (1999). *Vortex-induced vibration, absence of lock-in and fluid force deduction*. Ph.D. Thesis, California Institute of Technology.
- [57] Gilbert, S. and Sigurdson, L. (2010). The ‘void’ structure in the wake of a self-oscillating flexible circular cylinder. *Exp Fluids*, 48:461–471.

- [58] Gopalkrishnan, R. (1993). *Vortex induced forces on oscillating bluff cylinders*. Ph.D. Thesis, Massachusetts Institute of Technology, Department of Ocean Engineering.
- [59] Govardhan, R. and Williamson, C. H. K. (2000). Modes of vortex formation and frequency response for a freely vibrating cylinder. *J. Fluid Mech.*, 420:85–130.
- [60] Hammache, M. and Gharib, M. (1991). An experimental study of the parallel and oblique vortex shedding from circular cylinders. *J. Fluid Mech.*, 232:567–590.
- [61] Henderson, R. (1995). A study of two-dimensional flow past an oscillating cylinder. *Phys. Fluids*, 7:2012–2014.
- [62] Hover, F. S., Davis, J. T., and Triantafyllou, M. S. (2004). Three-dimensionality of mode transition in vortex-induced vibrations of a circular cylinder. *Eur. J. Mech. B/Fluids*, 23:29–40.
- [63] Hover, F. S., Miller, S. N., and Triantafyllou, M. S. (1997). Vortex-induced vibration of marine cables: experiments using force feedback. *J. Fluids Struct.*, (0889):307–326.
- [64] Hover, F. S., Techet, A. H., and Triantafyllou, M. S. (1998). Forces on oscillating uniform and tapered cylinders in cross flow. *J. Fluid Mech.*, 363:97–114.
- [65] Huera-Huarte, F. J. (2006). *Multi-mode Vortex-Induced Vibrations of a Flexible Circular Cylinder*. Ph.D. Thesis, Department of Aeronautics, Imperial College, London.
- [66] Huera-Huarte, F. J., Bangash, Z. A., and González, L. M. (2014). Towing tank experiments on the vortex-induced vibrations of low mass ratio long flexible cylinders. *J. Fluids Struct.*, 48:81–92.
- [67] Huera-Huarte, F. J. and Bearman, P. W. (2009a). Wake structures and vortex-induced vibrations of a long flexible cylinder - Part 1: Dynamic response. *J. Fluids Struct.*, 25(6):969–990.
- [68] Huera-Huarte, F. J. and Bearman, P. W. (2009b). Wake structures and vortex-induced vibrations of a long flexible cylinder - Part 2 : Drag coefficients and vortex modes. *J. Fluids Struct.*, 25(6):991–1006.
- [69] Huera-Huarte, F. J. and Bearman, P. W. (2011a). Vortex and wake-induced vibrations of a tandem arrangement of two flexible circular cylinders with far wake interference. *J. Fluids Struct.*, 27:824–828.
- [70] Huera-Huarte, F. J. and Bearman, P. W. (2011b). Vortex and wake-induced vibrations of a tandem arrangement of two flexible circular cylinders with near wake interference. *J. Fluids Struct.*, 27:193–211.

- [71] Huera-Huarte, F. J., Bearman, P. W., and Chaplin, J. R. (2006). On the Force Distribution along the Axis of a Flexible Circular Cylinder Undergoing Multi-mode Vortex-Induced Vibrations. *J. Fluids Struct.*, 22:897–903.
- [72] Huera-Huarte, F. J. and González, L. M. (2013). Numerical prediction of the modal response of flexible cylinders in cross-flow with a current dependent form of damping. *J. Mar. Sci. Technol.*, 18:370–380.
- [73] Huera-Huarte, F. J. and Vernet, A. (2010). Vortex modes in the wake of an oscillating long flexible cylinder; combining POD and fuzzy clustering. *Exp Fluids*, 48:999–1013.
- [74] Iwan, W. D. (1975). The vortex induced oscillations of elastic structures. *J. Manuf. Sci. Eng.*, 97(4):1378–1382.
- [75] Jackson, C. P. (1987). A finite-element study of the onset of vortex shedding in flow past variously shaped bodies. *J. Fluid Mech.*, 182:23–45.
- [76] Jain, A. (2012). *Vortex-Induced Vibrations of an Inclined Cylinder in Flow*. Masters thesis, University of Massachusetts-Amherst.
- [77] Jauvtis, N. and Williamson, C. H. K. (2003). Vortex-induced vibration of a cylinder with two degrees of freedom. *J. Fluids Struct.*, 17:1035–1042.
- [78] Jeon, D. and Gharib, M. (2001). On circular cylinders undergoing two-degree-of-freedom forced motions. *J. Fluids Struct.*, 15:533–541.
- [79] Keulegan, G. H. and Carpenter, L. H. (1958). Forces on cylinders and plates in an oscillating fluid. *J Res Nat Bur Stand*, 60(5):423–440.
- [80] Khalak, A. and Williamson, C. H. K. (1999). Motions, forces, and mode transitions in the vortex-induced vibrations at low mass-damping. *J. Fluids Struct.*, 13:813–851.
- [81] King, R., Prosser M. J, and Johns, D. L. (1973). On vortex excitation of model piles in water. *J. Sound Vib.*, 29:169–188.
- [82] Kitagawa, T., Fujino, Y., and Kimura, K. (1999). Effects of Free-End Condition on End-Cell-Induced Vibration. *J. Fluids Struct.*, 13:499–518.
- [83] Kitagawa, T. and Ohta, H. (2008). Numerical investigation on flow around circular cylinders in tandem arrangement at a subcritical Reynolds number. *J. Fluids Struct.*, 24:680–699.
- [84] Klamo, J. T. (2007). *Effects of Damping and Reynolds Number on Vortex-Induced Vibrations*. Ph.D. Thesis, California Institute of Technology.
- [85] Klamo, J. T., Leonard, A., and Roshko, A. (2004). On the maximum amplitude in vortex-induced vibrations. In *Am. Phys. Soc. 57th Annu. Meet. Div. Fluid Dyn.*, Seattle, Washington.

- [86] Ko, W. L. and Fleischer, V. T. (2009). Further Development of Ko Displacement Theory for Deformed Shape Predictions of Nonuniform Aerospace Structures. Technical report, NASA.
- [87] Ko, W. L., Richards, W. L., and Tran, V. T. (2007). Displacement Theories for In-Flight Deformed Shape Predictions of Aerospace Structures. Technical Report October, NASA.
- [88] Krishnamoorthy, S., Price, S. J., and Païdoussis, M. P. (2001). Cross-flow past an oscillating circular cylinder: synchronization phenomena in the near wake. *J. Fluids Struct.*, 15:955–980.
- [89] Lam, K., Jiang, G. D., Liu, Y., and So, R. M. C. (2004a). Grid-free surface vorticity method applied to flow induced vibration of flexible cylinders. *Int. J. Numer. Methods Fluids*, 46(May 2003):289–313.
- [90] Lam, K., Wang, F. H., Li, J. Y., and So, R. M. C. (2004b). Experimental investigation of the mean and fluctuating forces of wavy (varicose) cylinders in a cross-flow. *J. Fluids Struct.*, 19:321–334.
- [91] Lang, T., Soon, V., Liu, R., and Huang, Y. (1990). AMUSE: An Algorithm for Multiple Unknown Signal Extraction. In *Proc. 1990 IEEE Int. Symp. Circuits Syst.*
- [92] Li, H. and Sumner, D. (2009). Vortex shedding from two finite circular cylinders in a staggered configuration. *J. Fluids Struct.*, 25:479–505.
- [93] Lie, H. and Kaasen, K. E. (2006). Modal analysis of measurements from a large-scale VIV model test of a riser in linearly sheared flow. *J. Fluids Struct.*, 22:557–575.
- [94] Lienhard, J. H. (1966). Synopsis of lift, drag, and vortex frequency data for rigid circular cylinders. Technical report.
- [95] Lin, J. C., Towfighi, J., and Rockwell, D. (1995). Instantaneous structure of near-wake of a cylinder: on the effect of  $\{R\}$ eynolds number. *J. Fluids Struct.*, 9:409–418.
- [96] Lu, X. Y. and Dalton, C. (1996). Calculation of the timing of vortex formation from an oscillating cylinder. *J. Fluids Struct.*, 10:527–541.
- [97] Lucor, D., Imas, L., and Karniadakis, G. E. (2001). Vortex dislocations and force distribution of long flexible cylinders subjected to sheared flows. *J. Fluids Struct.*
- [98] Mallock, A. (1907). On the resistance of air. *Proc. R. Soc.*, A79:262–265.
- [99] Mathis, C., Provansal, M., and Boyer, L. (1987). Bénard-von Kármán instability : transient and forced regimes. *J. Fluid Mech.*, 182:1–22.
- [100] Meneghini, J. R., Saltara, F., Siqueria, C. L. R., and Ferrari, J. A. (2001). Numerical simulation of flow interference between two circular cylinders in tandem and side-by-side arrangement. *J. Fluids Struct.*, 15:327–350.



- [101] Mercier, J. A. (1973). *Large amplitude oscillations of a circular cylinder in a low speed stream*. Ph.D. Thesis, Stevens Institute of Technology,, Stevens Institute of Technology, NJ, USA.
- [102] Mittal, R. and Balachandar, S. (1997). On the inclusion of three-dimensional effects in simulations of two-dimensional bluff-body wake flows. *ASME FEDSM'97*.
- [103] Mittal, S. and Kumar, V. (2001). Flow-Induced Vibrations of a Light Circular Cylinder At {R}eynolds Numbers  $10^{\{3\}}$  To  $10^{\{4\}}$ . *J. Sound Vib.*, 245:923–946.
- [104] Mizushima, J. and Suehiro, N. (2005). Instability and transition of flow past two tandem circular cylinders. *Phys. Fluids*, 17:104017.
- [105] Modarres-Sadeghi, Y., Chasparis, F., Triantafyllou, M. S., Tognarelli, M., and Beynet, P. (2011). Chaotic response is a generic feature of vortex-induced vibrations of flexible risers. *J. Sound Vib.*, 330(11):2565–2579.
- [106] Modarres-Sadeghi, Y., Mukundan, H., Dahl, J. M., Hover, F. S., and Triantafyllou, M. S. (2010). The effect of higher harmonic forces on fatigue life of marine risers. *J. Sound Vib.*, 329(1):43–55.
- [107] Morison, J. R., Johnson, J. W., and Schaaf, S. A. (1950). Force exerted by surface waves on piles. Technical Report SPE-950149-G, Society of Petroleum Engineers.
- [108] Nakamura, A., Okijama, A., and Takashi, K. (2001). Experiments on flow-induced in-line oscillation of a circular cylinder in a water tunnel. 2. Influence of the aspect ratio of a cantilevered circular cylinder. *JSME Int. J. B*, 44:705–711.
- [109] Naudascher, E. (1987). Flow-induced streamwise vibrations of structures. *J. Fluids Struct.*, 1(3):265–298.
- [110] Newman, D. (1996). Simulations of Flow Over a Flexible Cable: a Comparison of Forced and Flow-Induced Vibration. *J. Fluids Struct.*, 10:439–453.
- [111] Newman, D. J. and Karniadakis, G. E. (1997). A direct numerical simulation study of flow past a freely vibrating cable. *J. Fluid Mech.*, 344:95–136.
- [112] Norberg, C. (1987). Effects of Reynolds number and a low intensity freestream turbulence on the flow around a circular cylinder. (87):54.
- [113] Norberg, C. (1994). An experimental investigation of the flow around a circular cylinder: influence of aspect ratio. *J. Fluid Mech.*, 258:287–316.
- [114] Norberg, C. (2003). Fluctuating lift on a cylinder: review and new measurements. *J. Fluids Struct.*, 17:57–96.
- [115] Okajima, A., Yasui, S., Kiwata, T., and Kimura, S. (2007). Flow-induced streamwise oscillation of two circular cylinders in tandem arrangement. *Int. J. Heat Fluid Flow*, 28:552–560.

- [116] Ongeron, A. and Rockwell, D. (1988). Flow structures from an oscillating cylinder. Part 1. Mechanics of phase shift and recovery in the near wake. *J. Fluid Mech.*, 191:197–223.
- [117] Owen, J. C., Bearman, P. W., and Szewczyk, A. A. (2001). Passive control of VIV with drag reduction. *J. Fluids Struct.*, 15:597–605.
- [118] Owen, J. C., Szewczyk, A. A., and Bearman, P. W. (2003). Suppression of kármán vortex shedding. *A Gall. Fluid Motion*, M:23.
- [119] Pannel, J. R., Griffiths, E. A., and Coales, J. D. (1915). Experiments on the interference between pairs of aeroplane wires of circular and lenticular cross section. *Advis. Comm. Aeronaut. Reports Memo.*, 208(7):219–221.
- [120] Pereira, F. and Gharib, M. (2002). Defocusing digital particle image velocimetry and the three-dimensional characterization of two-phase flows. *Meas. Sci. Technol.*, 13:683–694.
- [121] Piccirillo, P. and Van Atta, C. W. (1993). An experimental study of vortex shedding behind linearly tapered cylinders at low Reynolds number. *J. Fluid Mech.*, 246:163–195.
- [122] Prasanth, T. K. and Mittal, S. (2009). Flow-induced oscillation of two circular cylinders in tandem arrangement at low Re. *J. Fluids Struct.*, 25(6):1029–1048.
- [123] Rajasekaran, S. (2002). Structural dynamics of earthquake engineering. Number 1971. CRC Press.
- [124] Ramberg, S. E. and Griffin, O. M. (1975). Velocity correlation and vortex spacing in the wake of a vibrating cable. *J. Fluids Eng.*, 98(1):10–18.
- [125] Rao, S. S. (2010). *Mechanical Vibrations*, volume 67.
- [126] Reynolds, O. (1883). An experimental investigation of the circumstances which determine whether the motion of water shall be direct or sinuous, and of the law of resistance in parallel channels. *Philos. Trans. R. Soc.*, 174:935–982.
- [127] Roshko, A. (1954a). A new hodogram for free-streamline theory. Technical report, National Advisory Committee for Aeronautics.
- [128] Roshko, A. (1954b). On the drag and shedding frequency of two-dimensional bluff bodies. Technical report, National Advisory Committee for Aeronautics.
- [129] Roshko, A. (1961). Experiments on the flow past a circular cylinder at very high Reynolds number. *J. Fluid Mech.*, 10(1924):345–356.
- [130] Roshko, A. (1993). Perspectives on bluff body aerodynamics. *J. Wind Eng. Ind. Aerodyn.*, 49:79–100.
- [131] Sadeghian, H., Rezazadeh, G., and Osterberg, P. (2007). Application of the Generalized Differential Quadrature Method to the Study of Pull-In Phenomena of MEMS Switches. *J. Microelectromechanical Syst.*, 16(6):1334–1340.

- [132] Sanchis A, Saelevik G, and Grue, J. (2008). Two-degree-of-freedom vortex induced vibrations of a spring-mounted rigid cylinder with low mass ratio. *J. Fluids Struct.*, 24:907–919.
- [133] Sarpkaya, T. (1978). Fluid forces on oscillating cylinders. *J. Waterw. Port, Coast. Ocean Div.*, 104:275–290.
- [134] Sarpkaya, T. (1995). Hydrodynamic damping, flow-induced oscillations, and biharmonic response. *ASME J. Offshore Mech. Arct. Eng.*, 117:232–238.
- [135] Sarpkaya, T. (2004). A critical review of the intrinsic nature of vortex-induced vibrations. *J. Fluids Struct.*, 19:389–447.
- [136] Schewe, G. (1983). On the force fluctuations acting on a circular cylinder in cross-flow from subcritical up to transcritical Reynolds numbers. *J. Fluid Mech.*, 133:265–285.
- [137] Schiller, L. and Linke, W. (1933). Druck und reibungswiderstand des zylinders bei Reynoldsaachen Zahlen 5,000 bis 40,000,. *Z. Flugtech. Mot.*
- [138] Shu, C. (2000). *Differential Quadrature and Its Application in Engineering*, volume 1. Springer.
- [139] Skop, R. A. and Griffin, O. M. (1973). A model for the vortex-excited resonant response of bluff cylinders. *J. Sound Vib.*, 27(2):225–233.
- [140] Skop R A and Balasubramanian, S. (1997). A new twist on an old model for vortex-excited vibrations. *J. Fluids Struct.*, 11:395–412.
- [141] Stabuli, T. (1983). Calculation of the vibration of an elastically-mounted cylinder using experimental data from forced oscillation. *J. Fluids Eng.*, 105:225–229.
- [142] Strouhal, V. (1878). On an unusual sort of sound excitation. *Ann. der Phys. und Chemie*, 10:216–251.
- [143] Sumer, B. M. and Fredsø e, J. (2006). *Hydrodynamics around cylindrical structures*, volume 26. Advanced Series in Ocean Engineering.
- [144] Sumner, D. (2010). Two circular cylinders in cross-flow: A review. *J. Fluids Struct.*, 26(6):849–899.
- [145] Sumner, D., Richards, M. D., and Akosile, O. O. (2005). Two staggered circular cylinders of equal diameter in cross-flow. *J. Fluids Struct.*, 20:255–276.
- [146] Szewczyk, A. A. and Bearman, P. W. (1992). Imposed 3-D disturbances on bluff body near wake flows. Technical report, Office of Naval Research.
- [147] Tanida, Y., Okajima, A., and Watanabe, Y. (1973). Stability of a circular cylinder oscillating in uniform flow or in a wake. *J. Fluid Mech.*, 61(04):769–784.

- [148] Techet, A. H., Hover, F. S., and Triantafyllou, M. S. (1998). Vortical patterns behind a tapered cylinder oscillating transversely to a uniform flow. *J. Fluid Mech.*, 363:79–96.
- [149] Tognarelli, M. A., Slocum, S. T., Frank, W. R., and Campbell, R. B. (2004). VIV response of a long flexible cylinder in uniform and linearly sheared currents. In *Offshore Technology Conference*, pages OTC – 16338.
- [150] Tombazis, N. and Bearman, P. W. (1997). A study of three-dimensional aspects of vortex shedding from a bluff body with mild geometric disturbance. *J. Fluid Mech.*, 330:85–112.
- [151] Triantafyllou, M. S., Grosenbaugh, M. A., and Gopalkrishnan, R. (1994). Vortex-induced vibrations in a sheared flow: a new predictive method. In *Int. Conf. Hydroelasticity Mar. Technol.*, pages 31–38.
- [152] Trim, A. D., Braaten, H., Lie, H., and Tognarelli, M. A. (2005). Experimental investigation of vortex-induced vibration of long marine risers. *J. Fluids Struct.*, 21:335–361.
- [153] Vandiver, K. J. (1983). Drag coefficients of long flexible cylinders. In *Offshore Technol. Conf.*, page 10, Houston, Texas.
- [154] Vandiver, K. J. (1993). Dimensionless Parameters Important to the Prediction of Vortex Induced Vibrations. *J. Fluids Struct.*, 7:423–455.
- [155] Vandiver, K. J., Allen, D., and L, L. (1996). The occurrence of lock-in under highly sheared conditions. *J. Fluids Struct.*, 10:555–561.
- [156] Vandiver, K. J. and Chung, T. Y. (1988). Predicted and measured Response of flexible cylinders in sheared flow.pdf. In *ASME Winter Annu. Meet. Symp. Flow Induc. Vib.*
- [157] Vandiver, K. J., Jaiswal, V., and Jhingran, V. (2009). Insights on vortex-induced, traveling waves on long risers. *J. Fluids Struct.*, 25(4):641–653.
- [158] Vandiver, K. J. and Mazel, C. H. (1976). A field study of vortex-excited vibrations of marine cables. In *Offshore Technol. Conf.*, page 10.
- [159] Venugopal, M. (1996). *Damping and Response Prediction of a Flexible Cylinder in a Current*. Ph. d. thesis, Massachusetts Institute of Technology.
- [160] Vickery, B. J. and Watkins, R. D. (1964). Flow induced vibrations of cylindrical structures. In *Australas. Conf. Hydraul. Fluid Mech. 1st*, pages 213–241.
- [161] Vikestad, K., Vandiver, K. J., and Larsen, C. M. (2000). Added mass and oscillation frequency for a circular cylinder subjected to vortex-induced vibrations and external disturbance. *J. Fluids Struct.*, 14:1071–1088.
- [162] von Kármán, T. (1912). Über den mechanismus des flüssigkeits und Luftwiderstandes. *Phys. Zeitschrift*, 13:49–59.

- [163] von Kármán, T. (1954). *Aerodynamics: Selected Topics in the Light of Their Historical Development*. Cornell University Press.
- [164] Wang, X., So, R. M. C., and Liu, Y. (2001). Flow-Induced vibration of an Euler-Bernoulli Beam. *J. Sound Vib.*, 243:241–268.
- [165] Willden, R. H. J. and Graham, J. M. R. (2001). Numerical prediction of VIV on long flexible circular cylinders. *J. Fluids Struct.*, 15:659–669.
- [166] Williamson, C. H. K. (1985). Evolution of a single wake behind a pair of bluff bodies. *J. Fluid Mech.*, 159:1–18.
- [167] Williamson, C. H. K. (1989). Oblique and parallel modes of vortex shedding in the wake of a circular cylinder at low Reynolds numbers. *J. Fluid Mech.*, 206:579–627.
- [168] Williamson, C. H. K. (1996). Vortex dynamics in the cylinder wake. *Annu. Rev. Fluid Mech.*, 28:477–539.
- [169] Williamson, C. H. K. and Govardhan, R. (2004). Vortex-Induced Vibrations. *Annu. Rev. Fluid Mech.*, 36(1982):413–455.
- [170] Williamson, C. H. K. and Govardhan, R. (2008). A brief review of recent results in vortex-induced vibrations. *J. Wind Eng. Ind. Aerodyn.*, 96:713–735.
- [171] Williamson, C. H. K. and Jauvtis, N. (2004). A high-amplitude 2T mode of vortex-induced vibration for a light body in XY motion. *Eur. J. Mech. B/Fluids*, 23:107–114.
- [172] Williamson, C. H. K. and Roshko, A. (1988). Vortex formation in the wake of an oscillating cylinder. *J. Fluids Struct.*, 2:355–381.
- [173] Wilson, E. L. (2002). *Three-Dimensional Static and Dynamic Analysis of Structures*. Number January. Computers and Structures, Inc.
- [174] Yamamoto, C. T., Meneghini, J. R., Saltara, F., Fregonesi, R. A., and Ferrari, J. A. (2004). Numerical simulations of vortex-induced vibration on flexible cylinders. *J. Fluids Struct.*, 19:467–489.
- [175] Zdarvkovich, M. M. (1977). Review of flow interference between two circular cylinders in various arrangements. *ASME J. Fluids Eng.*, 99:618–633.
- [176] Zdarvkovich, M. M. (1985). Flow induced oscillations of two interfering circular cylinders. *J. Sound Vib.*, 101:511–521.
- [177] Zdarvkovich, M. M. (1987). The effects of interference between circular cylinders in cross flow. *J. Fluids Struct.*, 1:239–261.
- [178] Zdarvkovich, M. M. (1997). *Flow around cylindrical structures. Vol 1: Fundamentals*. Oxford University Press.

- 
- [179] Zdarvkovich, M. M. and Pridden, D. L. (1977). Interference between two circular cylinders, series of unexpected discontinuities. *J. Ind. Aerodyn.*, 2:255–270.
- [180] Zhang, H., Fey, U., Noack, B., König, M., and Eckelmann, H. (1995). On the transition of the cylinder wake. *Phys. Fluids*, 7:779.
- [181] Zhou, W. and Chelidze, D. (2007). Blind source separation based vibration mode identification. *Mech. Syst. Signal Process.*, 21(8):3072–3087.
- [182] Ziehe, A. and Müller, K.-R. (1998). TDSEP - an efficient algorithm for blind separation using time structure. In *Proc. ICANN, Vol 98*, pages 675–680.
- [183] Zimmer, H. (2014). *Modal excitation of a flexible cylinder undergoing vortex-induced vibration*. M.s. thesis, University of Rhode Island.

UNIVERSITAT ROVIRA I VIRGILI

VORTEX INDUCED VIBRATIONS OF LONG FLEXIBLE CYLINDERS WITH AND WITHOUT WAKE INTERFERENCE

Denise Fischer Hubert

Dipòsit Legal: T 992-2015

## APPENDIX A

### ANALYTICAL ESTIMATION OF NATURAL FREQUENCIES

---

#### A.1 Introduction

As shown in chapter 3 section 3.7.3 the forces and moments on a section of the riser assembly, as shown in figure A.1, can be resolved by Euler-Bernoulli formulation:

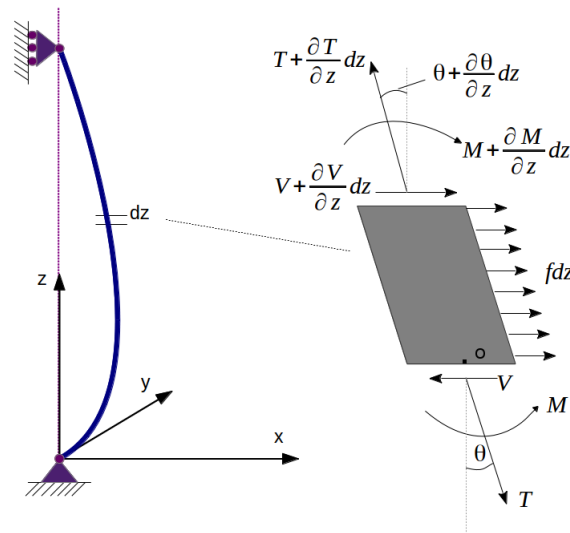


Fig. A.1 Pinned-pinned beam under tension with load  $f(z,t)$

The Euler Bernoulli theory tells us:

$$M(z,t) = EI \frac{\partial^2 u}{\partial z^2}(z,t) \quad (\text{A.1})$$



where  $u$  is the response of the beam in  $x$  direction. The forces in in-line direction and the moments about point  $O$  are given by:

$$-(V + dV) + fdz + V + (T + dT)\sin(\theta + d\theta) - T\sin\theta = \rho Adz \frac{\partial^2 u}{\partial t^2} \quad (\text{A.2})$$

$$(M + dM) - (V + dV)dz + fdz \frac{dz}{2} - M = 0 \quad (\text{A.3})$$

For very small deflections the value of  $\sin(\theta + d\theta)$  is given as:

$$\begin{aligned} \sin(\theta + d\theta) &\approx \theta + d\theta = \theta + \frac{\partial\theta}{\partial z} dz \\ &= \frac{\partial u}{\partial z} + \frac{\partial^2 u}{\partial z^2} dz \end{aligned}$$

The equations A.2, A.3 and A.1 can be combined to yield a single differential equation of motion:

$$\frac{\partial^2}{\partial z^2} \left( EI \frac{\partial^2 u}{\partial z^2} \right) + \rho A \frac{\partial^2 u}{\partial t^2} - T \frac{\partial^2 u}{\partial z^2} = f \quad (\text{A.4})$$

If the values of  $EI$ ,  $\rho A$ , or tension  $T$  are not uniform over the length of the riser, the case can be resolved by using differential quadrature (DQ) method.

## A.2 Differential Quadrature Method

The Generalized Differential Quadrature Method (GQDM) is used to transform non-linear differential equations into the corresponding discrete forms. The methodology is based on the assumption that the different-order partial derivatives of a function at a given point can be approximated by a weighted sum of function values at all discrete points in the variable domain[138]. If discretization is carried out with  $N$  points, the following expressions are obtained:

$$\left. \frac{\partial^m u(z)}{\partial z^m} \right|_{z=z_i} = \sum_{j=1}^N A_{ij}^{(m)} u_j, \quad \text{for } i = 1, 2, \dots, N \quad (\text{A.5})$$

Where  $A_{ij}(m)$  are the weighted coefficients associated with the  $m$ th order derivative, and  $N$  is the grid points in the  $z$  direction.

The evaluation of the function  $A_{ij}$  is, for the non-symmetric part ([131]:

$$A_{ij}^{(1)} = \frac{1}{z_j - z_i} \prod_{\substack{k=1 \\ k \neq j \\ k \neq i}}^N \frac{z_i - z_k}{z_j - z_k} \quad \text{for } i, j = 1, 2, \dots, N. \quad (\text{A.6})$$

and for the symmetric part:

$$A_{ii}^{(1)} = \sum_{\substack{k=1 \\ k \neq i}}^N \frac{1}{z_i - z_k} \quad \text{for } i = 1, 2, \dots, N. \quad (\text{A.7})$$

The weighted coefficients of the higher order derivatives can be determined from the recurrent relationship:

$$A_{ij}^{(r)} = r \left[ A_{ii}^{(r-1)} A_{ij}^{(1)} - \frac{A_{ij}^{(r-1)}}{(z_i - z_j)} \right] \quad i, j = 1, 2, \dots, N, \quad i \neq j, \quad r \geq 2 \quad (\text{A.8})$$

For the sake of simplicity, the weighted coefficients are expressed per unit length. ( $A_{ij}^{(r)} = A_{ij}^{(r)}/L^r$ ). where  $L$  is the length of the riser. The sampling points are determined using Chebychev-Gauss-Lobatto mesh distribution:

$$z_i = \frac{1}{2} \left[ 1 - \cos \frac{i-1}{N-1} \pi \right] \quad (\text{A.9})$$

The equation A.4 for free oscillation, where the elements may have varying  $\rho$ ,  $A$ , or  $T$  along the span of the riser could be written as:

$$\frac{\partial^2}{\partial z^2}(EI\kappa) - [\text{diag } T]\kappa + \rho A \frac{\partial^2 u}{\partial t^2} = f(z, t) \quad (\text{A.10})$$

where

$$\kappa = \frac{\partial^2 u}{\partial z^2} \quad (\text{A.11})$$

Whereas in the above equation the  $u$  at the domain and the boundary points, and  $\kappa$  only on the boundary points are taken as independent degrees of freedom. The general governing equation of an elastic isotropic beam under axial and transverse loading can thus be written as:

$$(EI)_i \left( \sum_{j=1}^N A_{ij}^{(2)} \kappa_j \right) + 2(EI)'_i \left( \sum_{j=1}^N A_{ij}^{(1)} \kappa_j \right) + (EI)''_i \kappa_i - T_i \kappa_i + (\rho A)_i \frac{d^2 u_i}{dt^2} = f(z_i, t) \quad (\text{A.12})$$

where

$$(EI)'_i = \left. \frac{d(EI)}{dz} \right|_{z=z_i}$$

$$(EI)''_i = \left. \frac{d^2(EI)}{dz^2} \right|_{z=z_i}$$

The value of  $\kappa_i$  at any point inside the domain is obtained from

$$\kappa_i = \sum_{k=1}^N A_{ik}^{(2)} u_k \quad i = 2, \dots, N - 1 \quad (\text{A.13})$$

the transverse deflection is assumed to be a temporally harmonic function, or  $u$  can be written as

$$u(z, t) = f(z)g(t) = f(z)\sin(\omega t + \phi)$$

$$\frac{\partial^2 u(z, t)}{\partial t^2} = -\omega^2 f(z)g(t) = -\omega^2 u(z, t) \quad (\text{A.14})$$

After combining the matrices, in absence of an external force ( $f(z, t) = 0$ ) the equation results in:

$$\frac{1}{\omega^2}[G]u = [E]u \quad (\text{A.15})$$

where  $[E]$  is given as  $-(\text{diag } \rho A)u/L^2$ . Both  $[G]$  and  $[E]$  are  $N \times N$  square matrices. The boundary conditions are applied according to Wilson's method [173]. For pinned-pinned configuration we have

$$\begin{aligned} u(0, t) = 0 \quad \text{or} \quad G_1[1, 1] = 1.0 \\ \frac{d^2u(0, t)}{dz^2} = 0 \quad \text{or} \quad G_1[2, 1 : N] = \frac{w_{1j}^{(2)}}{L^2} \\ u(L, t) = 0 \quad \text{or} \quad G_1[3, N] = 1.0 \\ \frac{d^2u(0, t)}{dz^2} = 0 \quad \text{or} \quad G_1[4, 1 : N] = \frac{w_{Nj}^{(2)}}{L^2} \quad \text{for } j = 1 : N \end{aligned} \quad (\text{A.16})$$

In general the boundary conditions are given by:

$$[G]_1u = [E]_1u \quad (\text{A.17})$$

where  $[G]_1$  is a  $4 \times N$  matrix,  $u$  is  $N \times 1$ , and  $[E]_1u$  is  $4 \times 1$ .

The governing equations and the boundary conditions are combined to yield

$$\frac{1}{\omega^2} \begin{bmatrix} [G]_0 \\ [G]_1 \end{bmatrix} \{u\} = \begin{bmatrix} [E] \\ [E]_1 \end{bmatrix} \quad (\text{A.18})$$

Using Lagrange multiplier approach (Wilson [173]) the equation is modified to square matrix:

$$\frac{1}{\omega^2} \begin{bmatrix} [G]_0 & [G]_1^T \\ [G]_1 & [0] \end{bmatrix} \begin{Bmatrix} \{u\} \\ \{\lambda\} \end{Bmatrix} = \begin{bmatrix} [E] & [E]_1^T \\ [E]_1 & [0] \end{bmatrix} \begin{Bmatrix} u \\ \lambda \end{Bmatrix} \quad (\text{A.19})$$

This equation has both equilibrium and equation of geometry. This is an eigenvalue problem and solving this equation results in the natural frequencies of the system.

UNIVERSITAT ROVIRA I VIRGILI

VORTEX INDUCED VIBRATIONS OF LONG FLEXIBLE CYLINDERS WITH AND WITHOUT WAKE INTERFERENCE

Denise Fischer Hubert

Dipòsit Legal: T 992-2015